Sheffield Hallam University

A Sheffield Hallam University thesis

Development of High Temperature/ Oxidation-Resistant PVD Coatings for Cutting Tools Using HIPIMS

Thomas Joseph Morton

A thesis submitted in partial fulfilment of the requirements of

Sheffield Hallam University

for the degree of Doctor of Philosophy

In collaboration with The National HIPIMS technology Centre, UK at Sheffield Hallam

University and Sandvik Coromant

October 2016

Declaration

I hereby declare that this thesis is my own work and effort and that it has not been submitted anywhere for any award apart from that of Doctor of Philosophy at Sheffield Hallam University.

Where other sources of information have been used, they have been acknowledged.

Thomas J. Morton   25.10.2016

Abstract

A series of high temperature and oxidation resistant, nanoscale, multilayer PVD, hard coatings have been developed through combine DC Unbalanced Magnetron (UBM) and High Power Impulse Magnetron Sputtering (HIPIMS) deposition technologies. The properties of the coatings lend themselves to the application of protecting cutting tools exposed to harsh environment such as the dry, high-speed machining of abrasive materials. This thesis discusses the literature supporting the project and pays tribute to the development of coatings that formed the foundation for the CrAlYBCN/AlSiCN coating series.

Plasma diagnostics optimised the process conditions for deposition; a highly ionised metal rich plasma was generated to investigate the effect of process conditions during the pretreatment step. It was found that metal ion implantation into the substrate was successful and that ramping the cathode charge had little effect of the sputter rate of the substrate. Ion etching removed loosely bound surface grain to improve adhesion.

A series of coatings were developed that were deposited at different levels of target poisoning, in an attempt to improve coating properties by process control and stoichiometry. Superhard coatings able to withstand temperatures of over 800 °C were produced. The coatings were subjected to a series of mechanical and thermal testing using pin on disk, microhardness, scratch test, Rockwell indentation, isothermal heat treatment and thermogravimetric analysis. Mechanisms of wear and oxidation process have been proposed based on the evidence given.

Through coating development two coatings were indicated as having the desired chemical, thermal and mechanical properties suitable for cutting tests. The coating that was deposited at higher bias improved the tool lifetime by 5 times.

Acknowledgements

First and foremost I would like to take the time to thank my Director of Studies Professor Arutiun P. Ehiasarian who's expertise and guidance has made this thesis possible. A special mention to his understanding and flexibility around the late mornings and late night working pattern I adopted, it has honestly been a great honour and pleasure learning from you over the years.

In addition, a special mention goes to my second supervisor, Professor Papken Eh. Hovsepian has played an invaluable role in the direction of this project through his vast knowledge of the subject area.

My time at Sheffield Hallam would not have been the same without the support and friendship of my fellow colleagues and PhD students. A big thank you goes to Yash, Gary, Arun, Paranjayee, Danny, Anna, Barnali, Itai and Sampan. Thank you for the all the laughs and the community we built within the department.

Acknowledgements must go to the sponsoring company, Sandvik Coromant, for funding this project and in particular thanks go to Dr. Eleanor Merson who discovered me in Leeds and encouraged me to apply for the PhD, to Johan Bohlmark for initiating the project with Harry, and finally to Dr. Mats Ahlgren, Dr. Carl-Fredrick Carlstrom and the rest of team based in Stockholm for their insightful input and question that have helped the project develop.

I would like to thank the continued and never wavering support of my family; the parents and partners, Sian and John, John and Alison, have always had faith and belief in me, when times have been hard we have all been there

4

together standing tall in the face of the grief of two huge losses during this project, Cath and Eamon.

To my sister Alice, on so many occasions you have kept me sane; the holidays, the events and the laughs are truly treasured.

To my longest and dearest friend Aaron, thank you for always bringing humour, wit and sarcasm to every situation. There is not better security than the solidarity of your friendship.

To my partner in life and partner in crime, Rebecca, without you this piece of work wouldn't have been possible. You allow me to be my best, you pick me up when I'm at my worst and you have helped us build a life together, for that I will be eternally grateful.

The final acknowledgement I would like to include goes to man who has inspired me since I was a child, a man who instilled in me the importance of education and the prestige of attaining knowledge, a man who came from humble beginnings to become a Doctor. To my Grandfather, Peter, you have been and always will be my role model. To use your words one must "Create your own destiny".

Contents

List of Tables

List of Figures

11

1.   Introduction

1.1.   Motivation

With advancements in the materials used in the engineering industries such as automotive and aerospace, there is a continuous parallel requirement for the adaptation, improvement and development of the tools used to machine said materials. Coatings technology has an important role to play within the cutting tool industry as it can provide properties that neither the substrate nor the coating as a bulk material could achieve alone; for example, a hard substrate combined with a wear resistant coating. Combinations such as this and the manipulation of elemental properties can allow bespoke coatings to be produced specifically for the machining requirements.

Many conventional tooling coatings are TiAlN based. Titanium forms a highly porous oxide compared to Chromium [1]–[6] and so Sheffield Hallam University's Nanotechnology and PVD Centre developed Ti-free coatings using conventional magnetron sputtering and HIPIMS with an aim to improve the oxidation resistance of the conventional coating. CrAlN and Carbon-containing CrAlN coatings provided improved oxidation resistance. The architecture of the coating also plays an important role in improving a coating; the group developed nanoscale multilayer coatings which experience improved lifetime by altering the wear mechanism and providing oxygen diffusion barriers at layer interfaces. Dopants such as Yttrium, Silicon, Boron and Carbon aim to improve the high temperature oxidation resistance further by plugging grain boundaries (Yttrium), forming very dense oxides (Silicon and Boron) and improve wear resistance by reducing the coefficient of friction (Carbon).

1.2.   Aims and Objectives

- To develop highly wear resistant PVD coatings for cutting tools to be used in dry high speed machining of hardened steels and other hard alloy materials

- To better understand the effect of the oxidation resistance and high temperature stability of the coating on the lifetime and the quality of the machined surfaces

- To develop new generation Ti-free PVD coatings

- To better understand and exploit the effect of HIPIMS to produce dense, very smooth and highly adherent coatings

- To develop HIPIMS based technology for production of the new coatings on large scale.

2.   Literature Review

2.1.   Physical Vapour Deposition (PVD)

2.1.1.   What is PVD?

Coating methods are divided into a number of fields depending on the substrate, coating type and application requirements; examples of which are electroplating, spray coating, chemical vapour deposition (CVD) and physical vapour deposition (PVD). PVD is the conversion of material into a vapour phase via a physical process [7] and can be divided into two main areas. Thermal evaporation heats a target material until atoms/molecules of material are expelled into the surrounding atmosphere, they then travel through a chamber and condense onto a surface forming a coating. The other type of PVD process involves collisional bombardment of a target material by heavy atoms with sufficient energy to eject a particle from the target surface via transfer of momentum, a process known as sputtering, usually performed in a vacuum to reduce the number of collisions the sputtered particles experience with gas atoms and will be the method used in this project.

The conventional method of sputtering involves attaching the target material to a DC power supply, the target acts as the cathode and the chamber walls as the anode, using an inert gas such as Argon as a sputtering medium. The substrate is either floated or negatively biased. Free electron collisions within the plasma ionises the gas atoms. The positively charged gas ions migrate toward the target cathode, their directed motion also induces further collisions with atoms forming more ions via the process;

$$Atom + e^- \rightarrow Ion + 2e^- \qquad \text{Equation 2.1.}$$
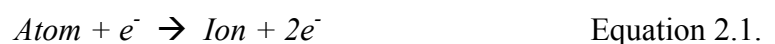
Thus increasing the number of charged and excited particles in the gas and igniting the plasma. The ions form close to the cathode and are accelerated toward the target, they collide with other gas atoms and the target is bombarded with a combination of gas ions and atoms. Dependent on the energy of the bombarding particles they may be backscattered or become embedded into the surface of the target, upon collision secondary electrons are released from the target atoms which are then accelerated toward the anode and collide with gas atoms creating more ions. In addition to this if the bombarding particles have sufficient energy the momentum transfer can occur through the target material, ejecting atoms away from the target and landing on the substrate - sputter deposition [8]–[10].

2.1.2.   DC Magnetron Sputtering

The main disadvantage of DC sputtering is that the emitted secondary electrons can recombine with ions and also are drained from the plasma via the chamber walls, decreasing the electron density of the plasma and hence the ion flux at the substrate. The application of magnets behind the cathode combatted this (magnetron); the magnets are arranged to have one pole on the outside and another in the centre, thus creating closed magnetic field lines just in front of the target material. The benefit of this is electrons will travel along the field lines with helical paths due to the Lorentz force vector, $\boldsymbol{F}$, given in equation 2.2.

$$\boldsymbol{F} = q \ (\boldsymbol{E} + v_{\perp} \times \boldsymbol{B}) \hspace{3cm} \text{Equation. 2.2}$$

Where q is the charge, $\boldsymbol{E}$ is the electric field vector and $v_{\perp}$ is the velocity of the charged particle perpendicular to the magnetic field, $\boldsymbol{B}$. The field lines therefore also increase the probability of electron collision with a gas atom close to the cathode by confining them, increasing the ion flux. The effect of this however is that there is a high electron density in a small area of the target, an erosion path of sputtered material forms

known as the 'racetrack' and therefore only approximately 30% of the target material is useable [11].

Although the sputter rate increases with the application of a closed loop magnetron system, due to the charge on the ions they too become concentrated close to the target and thus reducing ion flux at the substrate. A growing film benefits from the bombardment of ions by improving the density, the removal of any growth defects and inducing a preferred crystal growth orientation, therefore improving the ion flux would be advantageous. Window and Savvides developed a magnetron system that achieved this by altering the magnetic configuration [12]. In the previous discussion the magnetic strengths were balanced, however by increasing the strength of the outer magnets compared to the central magnet forces the field lines away from the target area and into the chamber, thus the charged particles are directed towards the substrate and increases the ion flux. This set-up is known as Unbalanced Magnetron (UBM), an example of the two arrangement types is given below in Figure 2.1.

a)   b)
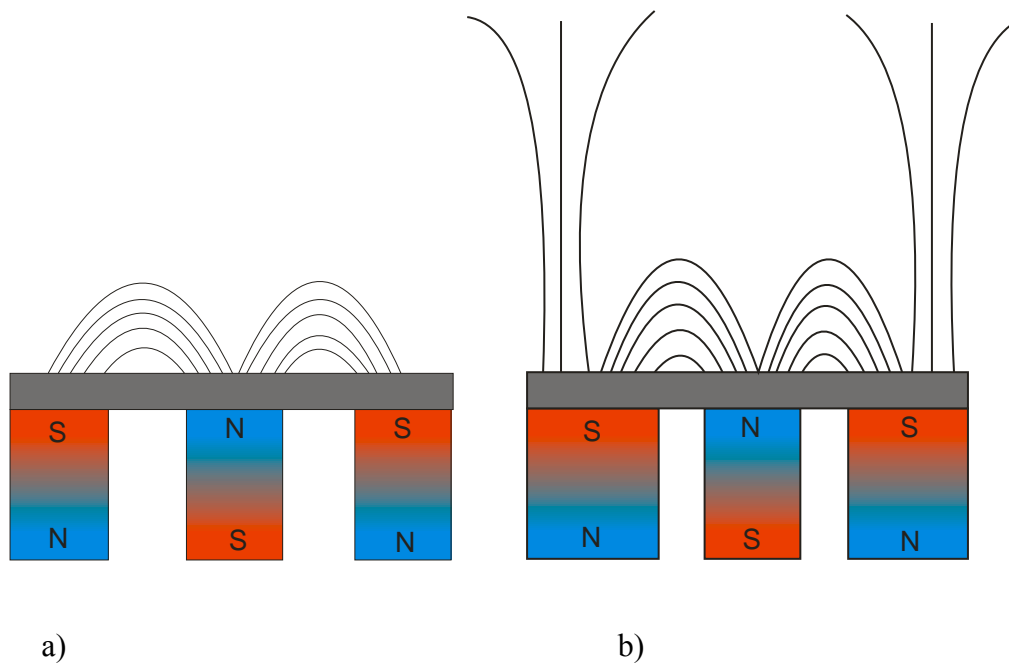
Figure 2.1. Schematics of balanced and unbalanced magnetrons a) and b) respectively, the field lines of a) are closed whereas in the unbalanced arrangement the field lines extent out away from the cathode.

In addition to the advantages of the UBM set up, a combination of UBM cathodes with alternating north south magnetic arrangement can close the extended field lines and thus reducing the electron depletion through the walls of the chamber, as can be seen in Figure 2.2. a four cathode UBM system [13].
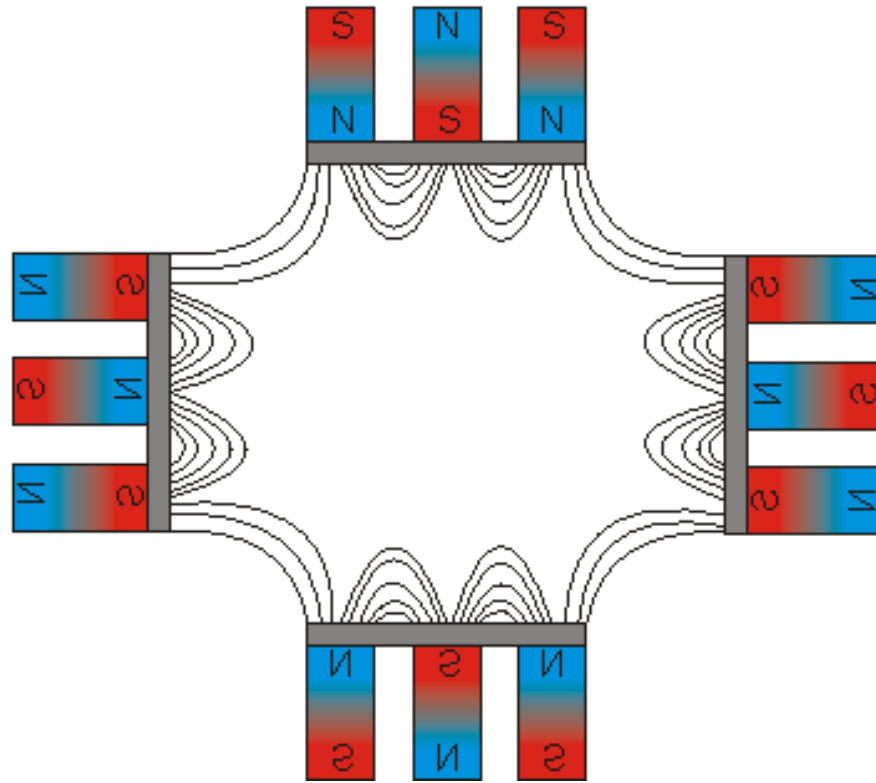
Figure 2.2. A schematic of the magnetic arrangement and fields lines of a 4 target UBM PVD system.

This combination is ideal for trapping electrons close the target to ionise atoms and accelerate them towards the target and intensifying the plasma [14]. Electrons are guided by the magnetic field lines away from the targets, ions are subsequently 'pulled' away from the targets and towards the substrate due to the ambi-polar nature of the plasma. The ions are therefore directed toward the substrates for coating. This can also be aided by applying a bias voltage to the substrate. The unique feature of plasmas is that they form a quasi-neutral environment, the electron and ions are linked electrostatically and so cannot move independent of one another thus creating a system where the diffusion rates of all species is equal and the overall charge is neutral. In light

of this, a bias can be imposed on the substrate with respect to the quasi-neutral plasma accelerating ions close to the substrate across the plasma sheath and toward the substrate surface [8][9].

The DC UBM configuration is widely used but is limited by the average power it can supply. Target materials have a power threshold before they begin to melt meaning that most DC UBM sputtering occurs at powers of up to 15 Wcm^{-2}, this means that there is a low percentage of target material ions within the plasma and ion current at the substrate is of the order mA cm^{-2} [15].

2.1.3. High Power Impulse Magnetron Sputtering (HIPIMS)

The thermal stability of the target material is controlled by the average power across it and not peak power. Khodachenko and Mozgrin in Moscow first reported the use of HIPIMS, which was later described in a seminal paper by Kouznetsov et. al.[15]. HIPIMS applies a large power (MW) for a short period of time (μs) in a pulse with a long 'off' time (ms), there is then sufficient time for the target to cool a thus thermal evaporation does not occur. The large peak power increases the energy of the sputtering atoms, increasing the number of gas and metal ions in the plasma and preventing macroparticle ejection. The main advantage of HIPIMS is that it increases the amount of metal ions in the plasma; 50 - 90% of the sputtered species are ions, resulting in ion current density of the order A cm^{-2}. In addition HIPIMS can produce higher order ions (M^{+1}, M^{+2}, M^{+3}), this has proved successful in the production of fully dense, droplet-free coatings. HIPIMS has low deposition rate due to the ionised sputtered material being accelerated back towards the cathode via the strong electric field applied to create the

high power, this loss can however be partly salvaged by the application of both DC UBM and HIPIMS together during a coating process [11].

The high ionisation of the HIPIMS plasma is very much desirable for pre-treatment steps during coating deposition. Impurities and native oxides must be cleaned off the surface of the substrate prior to deposition to allow good adhesion between coating and substrate, the high energy ions produced with HIPIMS can achieve good surfaces and also can implant into the surface to improve adhesion. The improvements seen through the use of HIPIMS as an etching step will be discussed in a later section of the literature review - 2.4. Previously Established Coatings, and the plasma properties involved during the etching step and the effect on the substrate will form the basis for the experimental work and results in this report.

2.1.4. Edge effects

Applying a negative bias to a sample within a plasma creates a sheath between the quasi-neutral plasma and the negatively charged sample. A potential difference is formed in this space and accelerates ions from the plasma to the surface. The electric field generated by the biased sample is perpendicular to the sample surface, for a flat sample the incident ions arrive normal to the surface. However for 2D and 3D geometries the shape of the sheath changes, thus also altering the angle of incidence of the ions. When considering sharp edges the plasma sheath curves around the edge, this increases the collection area of ions from the plasma and therefore increases the ion flux at the surface of the edge compared to the flat. There are two main effects of the curvature of the plasma sheath, firstly as described, the ion flux increases, this in turn increases the amount of material sputtered from the sample. Secondly the non-uniform sheath alters the trajectories of the ions from normal to perpendicular which again increases the sputtering rate [16]–[18]. Macak et al. confirmed the change in angle of

incidence when approaching the edge by noticing cone-like structures forming in the substrate induced by ion bombardment; the surface features altered their direction in relation to the angle of incidence of the incoming ion flux [18].
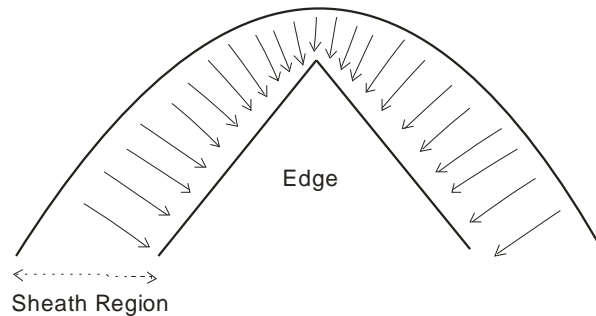
Figure 2.3. A schematic of the plasma sheath shape around an edge, the arrows indicate the direction and angle of incident of incoming ions to the sample surface and the concentration of arrows increases closer to the edge representing the increased ion flux.

Often in applications the geometry of the sample is determined for its application not the coating process; if the geometry is unchangeable then the edge effects must be controlled through process parameters. Increasing the negative bias applied to the sample has the effect of decreasing the sheath thickness and thus increases the sputter rate, illustrated by Figure 2.3, which may cause blunting of the sharp edge [17]. However, the substrate bias is directly proportional to ion implantation, adhesion and also hardness, and so can provide beneficial properties. Therefore optimising the plasma conditions to accommodate the edging effects is essential throughout a coating process; to ensure the required material properties are achieved without blunting the edge during etching or complete re-sputtering during coating.

2.1.5.   Coating Growth

A number of models for coating growth have been proposed and revised, describing the effects of process parameters of grain formation, densification and recrystallisation. The Thornton model [19] shown in Figure 2.4 was the first publication to include the transition zone into coating models and is now widely cited. The study investigates two variables; the effect of T/T_m, where T = substrate temperature and T_m = melting point of the material, and also the effect of Ar pressure for coating growth.

The coatings are separated into four zones; zone 1, at low T/T_m values there is little adatom surface mobility and so coatings grow in the direction of incoming flux. Growth is significantly affected by shading, giving rise to tapered crystallites. The intercolumnar areas are voids rather than grain boundaries which gives the materials poor lateral strength. It was seen that the structure of zone 1 coatings persisted to higher values of T/T_m with increased Ar pressure as Ar limits the adatom mobility.
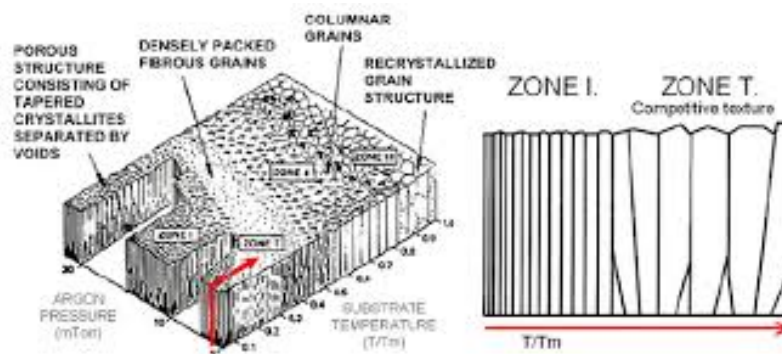
Figure 2.4. Thornton structure zone model correlating the argon pressure and the substrate temperature to the morphological properties of the films. When increasing the substrate temperature from room temperature to 325 °C, at 0.12 Pa, the structure of the film transits from zone 1 to zone T [20].

By increasing T/T_m above 0.1 the microstructure enters what has been termed the transition zone; the inter-grain voids begin to fill due to self-diffusion, creating a dense array of fibrous grains separated conventional-like grain boundaries that are generated from coalescence during growth.

At T/T_m = 0.3 - 0.5, zone 2, columnar grains that extend through the thickness of the coating are observed with faceted column tops; the increased surface mobility due to temperature causes grain boundary migration and begins recrystallisation. Finally, zone 3, with T/T_m > 0.5, the study observed an increase in the grain size and grooved grain boundaries forming as the coasting crystallises and begins to show bulk properties [20].

10 years later in 1984, Messier et. al. revised the Thornton Model to evaluate the effect of increasing the bias voltage on the coating structural zones [21]. It was found that the transition region could be reached at lower temperatures by increasing the substrate bias (Figure 2.5); accelerating ions towards the surface, increasing adatom mobility and hence the density. This increases the ability to deposit dense coatings for applications that require substrates sensitive to high temperatures.
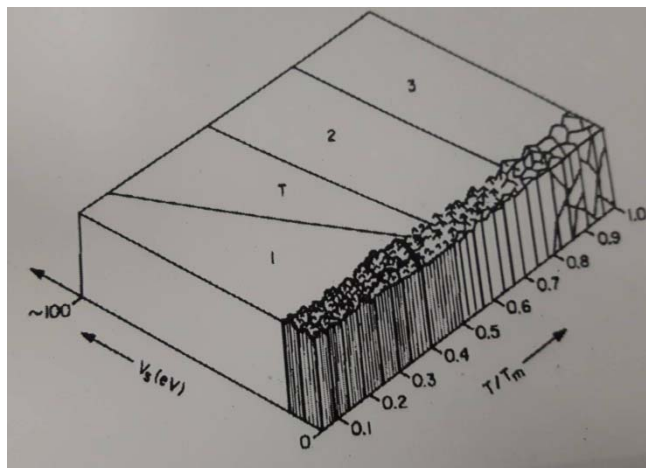
Figure 2.5. Revised structure model for thin film physical structure to include the effect of substrate bias voltage [21].

The increased ion bombardment produces the dense structures observed in the transition zone. The mechanisms of densification arise from: the forward sputtering of coating atoms into the voids, impact induced surface diffusion and localised heating, such that recrystallisation occurs as the coating grows [22].

Increasing the substrate bias induces a higher compressive stress within the coating. Residual stresses arise from growth stresses generated during deposition by the

competitive growth of the columns that make up the microstructure. An increased residual stress is directly correlated to increased coating hardness and an improvement in abrasive wear. However, at high levels, the build-up of stored elastic strain energy at interfaces can reduce adhesion and hence reduces wear resistance [23].
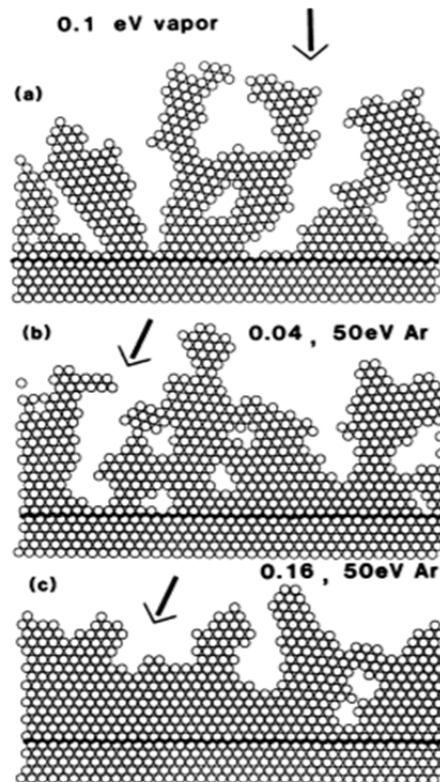
Figure 2.6. Diagram by Muller et. al. illustrating the densification of coatings without ipn bombardment (a) with an ion:neutral ratio of 0.04 (b) and 0.16 (c) [24].

In 1987, Muller et. al. described that increasing the content of ionised Ar leads to densification due to increased adatom surface energy and mobility. Ions have sufficient energy to migrate into voids between islands, significantly reducing shadowing effects and voids. Figure 2.6 is a schematic of atomic coating growth with increasing ion:neutral ratio giving rise to increased densification .

With improved technologies and the development of plasma-based deposition such as HIPIMS another revision to the model was required. This was proposed by

Anders et. al. in 2010, the adjustments made were to generate the diagram as a function of the kinetic energy of bombarding ions and taking into account the effect on coating thickness is the z-axis (Figure 2.7). The diagram shows that with high energy bombardment zone 1 is not possible - coatings automatically enter the dense transition region. The drawback is coating re-sputtering reduces coating thicknesses and there is also an inclusion of the negative region to illustrate the ion etching region [25].
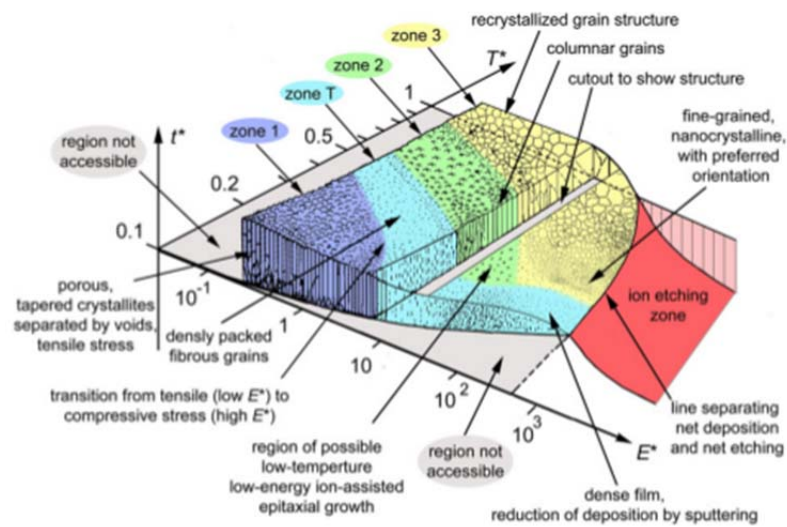
Figure 2.7. Revised Thornton model by Anders et. al. to illustrate coating structure growth for high energy deposition technologies such as HIPIMS[25].

2.1.6.   Reactive Sputtering

Many applications benefit from compound nitride or carbide coatings rather than pure metallic, this has been especially seen in the development of the cutting tools industry which predominantly uses ceramic materials for their increased hardness compared to metallic coatings [26]. As many compound materials are insulating it is not always practical to sputter from compound targets, this will be noted in the results section of this study as a compound layer deposited onto the AlSi target is highly insulating and generates arcing, which (due to the arc-suppression unit) momentarily shuts down the process resulting in interrupted deposition.

Reactive gases such as CH_4 and N_2 introduced to the deposition chamber react with all surfaces: chamber walls, substrate and target. It is at these locations that the formation of compounds is most likely; due to the energy conservation requirement collisional gas phase reactions have a low probability [26]. To ensure reproducibility of the coatings we must have control of the gas species; this is done through the use of a mass flow controller which can be used to set the relative partial pressures of the gas species inlet. With time a compound begins to form in the racetrack of the target material, this results in compound sputtering which generally has much low sputtering yields than metallic [26][27]. Compound formation at the target is called 'poisoning', the high intensity erosion of the racetrack delays the target becoming fully poisoned but with time and increased gas flow this can occur.

Once poisoned, if the gas flow is reduced, the racetrack area will begin to sputter the built-up compound until reaching a stage where it has returned to metallic sputtering. The return however does not follow the same route as the poisoning process and therefore generates a hysteresis curve for poisoning. An example of a hysteresis curve for target poisoning during reactive sputtering is given in Figure 2.8. The target begins

the process free of any compound build-up, this is termed the metallic mode. With increased nitrogen flow (A to B on Figure 2.8) the compound begins to grow around the race track having little effect on the nitrogen partial pressure. Once the compound begins to build up in the racetrack (B to C) the nitrogen partial pressure increases and this is known as the transition region. Further increase (C to D) in nitrogen flow causes the racetrack to be fully poisoned with a compound covering the entire area. It can be seen that reducing the nitrogen flow from this point the nitrogen partial pressure has a much lower gradient on the return [27].
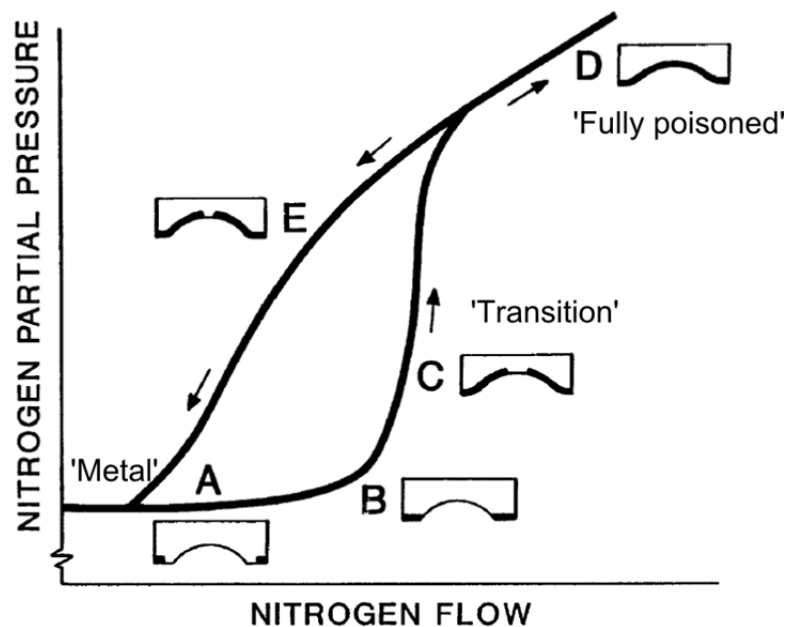
Figure 2.8. Target poisoning during reactive sputtering [27]

For many coatings developments there is a desire to reach compound stoichiometry, e.g. CrN, to improve coating properties such as hardness. The ability to control the gas flow during processes allows for specific positions along the hysteresis curve to be selected as deposition parameters.

2.2.   Novel Elemental Coating Additions

2.2.1.   Boron

Historically pure boron has been very difficult to synthesise, many of the original 'discoveries' of boron were actually compounds containing impurities [28]. The reason for this is boron's extreme sensitivity to reactive elements and readily forms compounds, one of which is the superhard cubic boron nitride (c-BN), first synthesised by Robert Wentorf at General Electric during their research into diamond and other hard materials [28]. c-BN is often compared to diamond and is the hardest material producible, seconded only by diamond. c-BN is considered a reasonable replacement as diamond is expensive to produce and is reactive with ferrous materials; c-BN however, is non-reactive to ferrous materials and can be synthesised using the same apparatus as diamond, so the infrastructure for production is already available, but is less costly [29][30].

The similarities between BN and carbon does not end there; B and N are located either side of C on the periodic table making them isochemical to carbon. BN also has a number of other phases, most notably hexagonal boron nitride (h-BN) and amorphous boron nitride (α-BN). Hexagonal BN contains similar bonding to that of graphite and has been coined the term 'inorganic graphite'; the intra-atomic bonds of the B and N atoms are strong covalent, orientated in planar hexagons that are stacked with weaker Van der Waals forces between the layers, much the same as graphite. This property gives h-BN a low interlayer shear strength allowing layers to be removed easily during wear, improving the wear resistance and friction as it acts as a solid lubricant. The 3rd most useful phase of BN is its amorphous phase; the absence of grain boundaries provides excellent oxidation resistance as there are no oxygen diffusion paths available and thus α-BN is useful in oxidation resistance and thermal barrier applications [30][31].

The properties described make B a highly desirable addition to coatings, controlling the synthesis of the coatings and the phase of BN can allow for tailored, bespoke improvements for applications where high hardness, high temperature stability, oxidation resistance and low friction are essential; leading to the selection of B addition in this project where the applications are centred around the machining of hard, abrasive materials.

2.2.1.1.   Composition, Microstructure and Mechanical properties

The microstructure and phase of B containing coatings depends on the type of deposition, the process parameters and the amount of B included. The c-BN phase has been seen to only be producible if there is stoichiometry, B:N = 1, other ratios allow hexagonal and amorphous phases to form [32]. A review paper in 1994 discussed the different methods of producing c-BN and it concluded that PVD systems provided the best solution; the low operating temperatures and highly energetic ions present produce adhesive BN coatings, the review did however, emphasise that c-BN is not the only phase often forms and that in the most part it is c-BN crystals in a α-BN matrix which acts to lessen the effect of increased hardness. Despite this, c-BN has been shown to be producible if the N content in the gas mix is greater than 10% however if it exceeds 50% the target becomes poisoned and so B sputtering is reduced. The study [29] used a conductive B_4C target for magnetron sputtering to deposit c-BN films, in order to keep the C content low N was used at 20%; IR spectroscopy indicated clear c-BN peaks and indicated a window of operation for the production of c-BN. The peaks started to be visible at a substrate bias voltage of -220 V and tailed off at around -320 V, at higher voltages re-sputtering occurs and so c-BN phase not able to form, this indicates that controlling the bias voltage may allow for cubic phase BN to be repeatedly formed, they do however also report IR spectra for the hexagonal phase indicating a mixture of bond types [29].

Yamamoto et al. [33] studied the effect of cathode power and rotational speeds on the microstructure and architecture of nano-multilayered CrN/BCN coatings; they used a Cr target and a B_4C target in a gas mix of 1:1 $Ar:N_2$ - controlling the UBM power of the B_4C target to vary the B inclusion. They found that a bilayer formed consisting of a thin amorphous BCN layer and a thick crystalline fcc CrN layer, upon increasing the rotation speed of the sample holder both layers decreased in thickness, however, further increase did not allow time for the nanolayer structure to form and a columnar grain growth influenced by the CrN lattice formed, the evolution is shown in Figure 2.9.
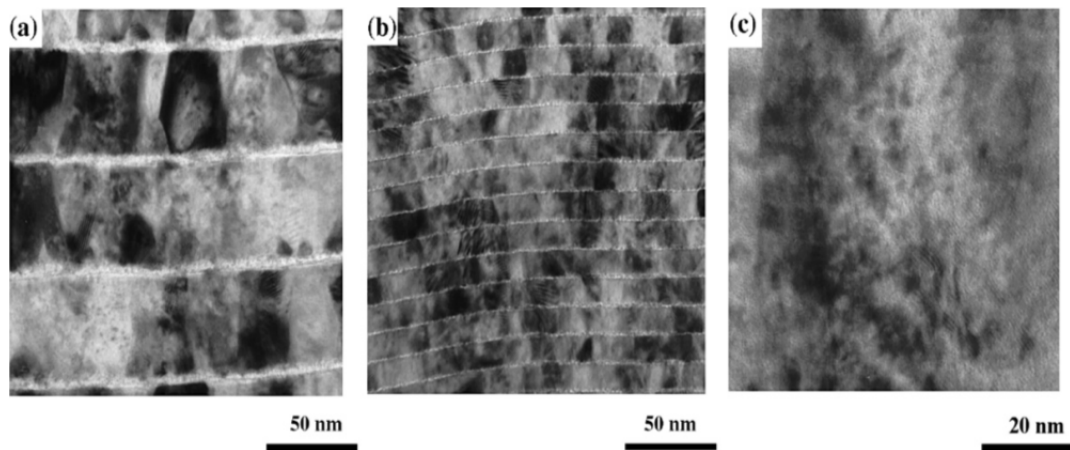
Figure 2.9. The multilayer evolution of CrN/BCN with increased substrate holder rotation speeds. The thin, light contrast layers consist of amorphous BCN and the thicker, darker layer is crystalline CrN. The images a) b) and c) represent 1.5 rpm, 5 rpm and 10 rpm, respectively [33].

It was also found that increasing the UBM power decreased the grain sizes and layer thickness indicating that a layer of BCN inhibits the columnar growth of CrN, this is limited by the layer thickness though, to which a minimum of approximately 1 nm is required [33]. The decreased grain size, by increased UBM power, provided and increase in hardness to 25 GPa. The decrease in layer thickness by increasing the rotation speed inherently increases the number of layers if the process time remains the same. The layers act as interfaces against crack propagation - effectively acting as grain

38

boundaries; this was seen by an increase in the hardness with increased rotational speed (up to a minimum layer size). The effect on the coefficient of friction showed interesting results for Lu et. al. as for CrN $\mu = 0.5$, however using a multilayer structure reduced this from an initial value of 0.4 down to 0.1: the material has become almost self-lubricating. They analysed the residue left on the counterpart after Pin on Disk tests and found that for the CrN/BCN coating h-BN was present; as previously mentioned h-BN is graphite-like having low shear strength between hexagonal layers and thus the formation of this phase during wear explains the reduced coefficient of friction [33].

Another study into the effect of B on the microstructure of coatings was performed by Lu et. al. [34]; they showed that the microstructure of TiN coatings is affected by varying the B content of TiBN. Increasing the voltage of the TiB target sputtered more B and also provided the atoms with high surface mobility at the substrate increasing the deposition rate and increasing the presence of TiB_2. B-free coatings showed a polycrystalline NaCl TiN structure, upon the addition of B a 2 phase nanocomposite forms where there are TiN crystals in a TiB_2 amorphous matrix. It was also seen that increasing the B content had the effect of inhibiting the grain growth of the TiN crystals and thus producing small grains within the matrix [34]. The mechanical properties of these coatings were also tested; the B-free coating has a low residual stress of 1.7GPa, which was seen to increase to 5GPa with increased boron content, in addition to this the hardness increased with increased B from 31GPa (B-free) to 44.2GPa (18.9% B) highlighting the improvements B inclusion can have on a coating. Further increase in B however does cause the structure to become amorphous and therefore reduces the hardness [34].

The effect of grain size on the mechanical properties of a material is well established by the Hall-Petch relationship whereby decreasing the grain size increasing the strain yield of a material and the increased number of grain boundaries act to inhibit dislocation propagation [35]. In addition to B inclusion into coatings reducing grain size, it also stabilises in a number of phases which act to improve mechanical properties.

2.2.2. Yttrium

Yttrium is a rare earth element and has widely been used as a method for improving the oxidation resistance of materials due to some unique properties and is known as a Reactive Element (RE); Yttrium has a high affinity to oxygen and so will readily form Y_2O_3. Yttrium oxide particles at the surface of material containing elements such as Cr or Al then act as nucleation sites for the growth of a protective layer of Cr_2O_3 or Al_2O_3, these oxides are very dense and so inhibit further oxidation of the substrate. In addition to this Y is known to segregate to grain boundaries thus 'plugging' them, limiting/blocking the major oxygen diffusion pathways, and therefore increasing the oxidation resistance of the material. For these reasons Y inclusion is desirable for protective coatings used in high temperature applications such as cutting tools.

2.2.2.1. Scale Growth on Bulk Material

In order to study how yttrium effects scale growth Przybylski [36] implanted a Co-Cr alloy with yttrium and heated the samples to 1000 ˚C in oxygen allowing a 1 μm scale to grow. TEM and EDX analysis was then performed on cross sections of the samples to study the microstructure and yttrium distribution within the scale. It was found that the scale grain size decreased from 300 nm - 50 nm with distance from the substrate towards the scale/gas interface, EDX indicated that yttrium segregates to the grain boundaries of the scale with the yttrium peak disappearing after a distance of 2.5 nm from the grain boundary, this occurs throughout the scale but its predominant towards the scale/gas interface. The authors suggest mechanism for the behaviour of yttrium is the difference in atomic size between Y and Cr - this leads to a high strain energy in the scale and therefore the driving force for Y segregation is to reduce the strain energy by migration of Y to grain boundaries. Oxidation of Cr is dominated by the diffusion of Cr cations out via grain boundaries toward the surface, rather than O anions in; by Y segregating to the diffusion pathways the concentration of Cr cations is significantly reduced and also the presence of large Y atoms increases the activation energy for diffusion. This reduces the Cr cation diffusivity so low that O anion diffusion becomes the driving mechanism for scale growth and hence the oxidation rate is drastically reduced through the presence of Y [37][36].

2.2.2.2.   Effect of Y on Microstructure

Y addition was shown to improve the oxidation resistance of alloys, the logical step was to include it into coatings to produce protective scale such as TiAlN and TiAlCrN. Y incorporation into coatings was studied by varying the target composition to create coatings Y-free, Y deposited in layers and homogeneous Y incorporation [38]. Y inclusion induced a change in grain growth mechanism; Y-free TiAlCrN coatings have columnar growth mechanism with a preferred {111} grain orientation that is driven by a reduction in strain energy and is common in bulk materials. Upon adding Y periodically so that it is included in layers (confirmed by LA XRD) the preferred orientation switches to {100}. The reasoning behind this is that Y acts as nucleation sites for grain growth so each new layer of Y deposited provides fresh nucleation sites and thus preventing columnar growth, in doing so the grain become equi-axed and reduced in size by a factor of approximately 10 times. Homogeneous inclusion resulted in a mixture of {111} and {100} indicating a competitive growth mechanism between nucleation and surface energy caused by distribution of Y inhibiting full {111} development [38]. The number of grain boundaries increases and therefore there is an increase in the grain boundary diffusion rate, it also provides more barriers for inhibiting crack propagation.

$(Ti_{1-x}Al_x)N$ coatings maintain a fcc-NaCl structure up to the maximum solubility of Al in the TiN lattice where x = 0.7, after which they convert to the hexagonal wurtzite structure. The addition of Y into the coatings also affects the crystal structure; a small percentage addition of Y up to 2 atom% still produces the fcc-NaCl structure. However, further increase in the atom% leads to a convergence to the hexagonal wurtzite structure which is inherently weaker and thus detrimental to the protective coating [39]. The addition of Y up to 8 atom% has been shown to yield stoichiometric coatings [40].

2.2.2.3.   Oxidation Resistance

Small additions of Y (2 at. %) into TiAlCrN resulted in an improved oxidation resistance; XRD analysis gave TiO_2 peaks at 920 ˚C for Y-free coatings and 950 ˚C with Y. This is attributed to the smaller grain sizes produced with Y inclusion and Y segregation to grain boundaries blocking diffusion paths, highlighted by the evidence of Y at grain boundaries [38]. In addition, after annealing to 950 ˚C the Y-free coating showed XPS peaks indicative of Iron based oxides; evidence that the oxidation had perturbed down to the substrate whereas these peaks were not visible for the Y-containing coating indicating the improved oxidation resistance [38].

The improved oxidation resistance has also been highlighted by a reduction in the mass gain of (AlTi)Cr coating doped with Y. Increasing the thickness of the (AlTi)Cr coating   from 10 μm to 30 μm reduced the mass gain during oxidation however adding Y decreased it further [41]. A study in 2008 [40] looked at the oxidation resistance of CrAlN coatings with varied Y inclusion from 0 at.% to 8 at.%. Upon annealing to 900 ˚C for 10 hours oxide peaks were visible via XRD for the 0 % and 8% coatings, caused by the release of N_2 through the production of Cr_2O_3 and Al_2O_3, 2% and 4% however only showed CrAlYN peaks. Y acting as nucleation sites for oxidisation forces a thin Cr and Al protective initial oxide layer to form which is below the detection limit of the XRD and thus prevent further oxidation of the coating. The onset of rapid oxidation occurs for CrAlN at a temperature of 1212 ˚C, 2% Y increases this to 1298 ˚C.   The inhibition of Cr ion transport along grain boundaries means that they are limited in their migration to the surface, oxidation of Al however is anion diffusion driven and so the formed oxide scale is a mixed bilayer with a Al scale concentration at the scale/gas interface and a high Cr oxide scale towards the coating/scale interface, these two scale regions are crystalline and very dense and provide excellent oxidation protection of the coating underneath [40].

43

As a comparison to other rare earth, reactive elements, the oxidation resistance of 20Cr-25Ni-Nb stainless steel (where the composition is in weight per cent) implantation with yttrium and cerium ions was studied [42]. Figures 2.10 and 2.11 show the mass gain in carbon dioxide at elevated temperatures for the implanted materials.
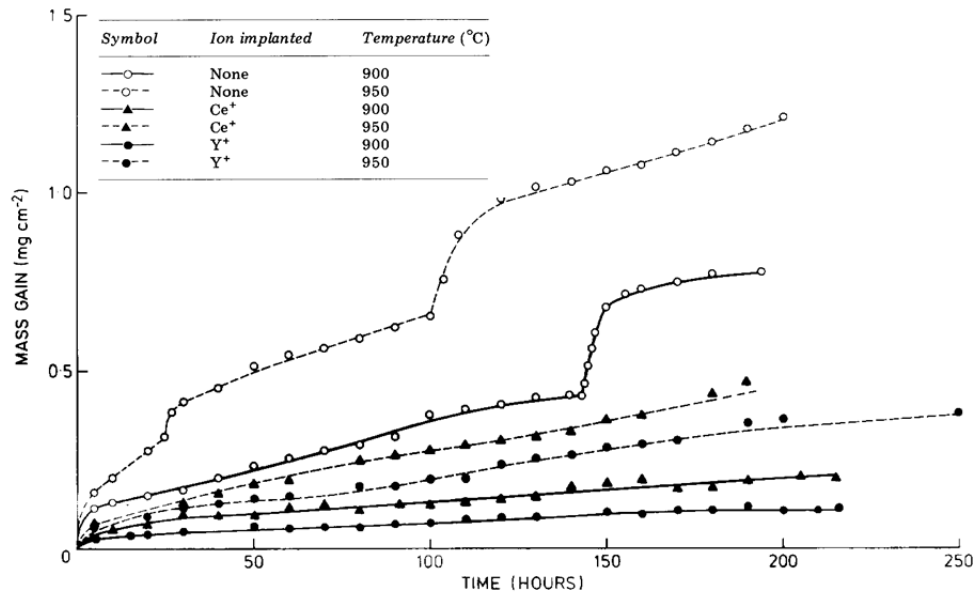
Figure 2.10. Influence of the implantation of 1017 Ce + cm $^{-2}$ or 1017 Y+ cm $^{-2}$ on t h e oxidation of 20Cr-25Ni-Nb stainless steel in carbon dioxide at 900 and 950 °C [42].
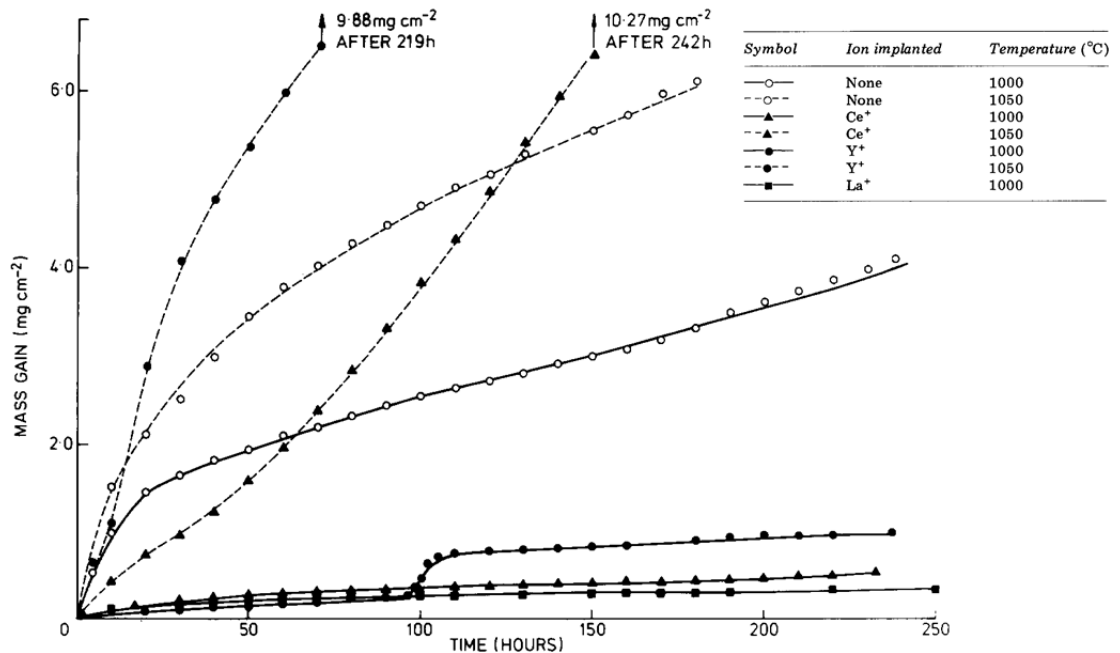
Figure 2.11. Influence of the implantation of 1017 Ce + cm $^{-2}$, 1017 Y+ cm $^{-2}$ or 1017 La + crn $^{-2}$ on the oxidation of 20Cr-25Ni-Nb stainless steel in carbon dioxide at 1000 and 1050 °C [42].

44

It can be seen that for the temperature range 900 - 950°C (Figure 2.10), both Y and Ce aid the formation a protective scale. This is also true for 1000°C (Figure 2.11), a slight increase in mass gain can be observe for the Y implanted material, though this then plateaus after approximately 10 hours. However, at 1050°C (Figure 2.11) both Y and Ce implanted coatings show a much greater rate of oxidation via mass gain on the sample. When cooled, the amount of spalled material was measured for the different samples. It was found that after treatment to 950°C the amount of material lost for Y and Ce implanted samples was 0.01 mgcm^{-2} and 0.14 mgcm^{-2}, respectively. Conversely when isothermally treated to 1000°C the mass spalled for Y and Ce was 0.68 mgcm^{-2} and 0.14 mgcm^{-2}, respectively. This data implies that for cutting tool applications where the contact temperature is $\geq$ 950°C, Y inclusion may be more beneficial at increasing tool lifetime by reducing spallation in between uses. However, if the contact temperature is above this value, Ce may be the better choice of additive for improving tool lifetime [42].

2.2.2.4. Mechanical properties of Y Inclusion

As has been discussed the addition of small amounts of Y can increase the oxidation resistance of a material but too much inclusion (>2 atom%) is less effective. The same is true for the mechanical properties of the coating. The segregation of Y to grain boundaries and the rapid formation of protective Cr and Al oxides via Y nucleation sites, improves the adhesion of the formed scale. Scratch test of AlTiCr coatings gave a Critical load for failure after oxidation of 17 N, the addition of Y improved this value to 29 N, this is attributed to the small grain sizes reducing the roughness of the scale and hence the induced stress at grain boundaries of the scale therefore improving adhesion [41]. However increasing the Y content above 2 atom% induces a change in the structure of the coating to accommodate the large Y atoms and a hexagonal wurtzite structure becomes dominant. This new structure gives a lower hardness value than the fcc-NaCl structure and also results in a lower elastic modulus [39].

Yttrium has been shown to be a successful reactive element addition to coatings that require high temperature oxidation resistance. Small addition of less than 2 atom% allow the coating to remain in the fcc-NaCl structure, changes the texture to {100} via the formation of small equi-axed grains from Y nucleation sites, and most importantly the 'plugging' of grain boundaries inhibits the diffusion of cations out of the coating towards the surface, therefore switching the driving force of oxidation to inward oxygen anion diffusion, reducing the rate of oxidation. These factors are beneficial for high temperature applications and do not compromise the mechanical properties if tailored correctly.

2.3.   Coating Architecture

Many well established protective coatings are single monolithic layer (sometimes also a base layer for improved adhesion) of a material that has advanced properties to the bulk substrate material, for example oxidation resistance or improved hardness. For cutting tools, the first generation of successful protective coatings was based around TiN, other elements have since been added, for example, Al and Cr replace Ti atoms in the TiN lattice improving oxidation and wear resistance, these coatings have been labelled second generation. Further development into the improvement of thin deposited coatings has led to the synthesis of third generation multilayer structure [43].

There are different types of layered structures and their classifications determine the potential benefits; if the materials are non-isostructural the layering structure acts to prevent the large scale columnar growth by interrupting the growth mechanism with the deposition of new layer. In addition to this one can combine the properties of two materials to increase the overall performance, for example, a hard layer deposited up on a lubricious layer would create a coating with low coefficient of friction and high hardness. Increasing the number of layers has the effect of creating more interfaces, and hence more volume of atoms occupying interface regions; these act as energy dissipation zones and can aid in crack deflection; the increased number of layers has a similar effect to that of increasing the number of grain boundaries by decreasing the grain size. If however, the two deposited layers are isostructural where the lattice sizes and atomic radii are similar they form a superlattice. A superlattice provides the benefits of those described above through layering but also can produce coatings with properties not achievable by the individual layer materials alone [44].

In 1987, Helmersson et. al. synthesised the 1st nanoscale multilayered PVD coating, TiN/VN [45]. They sequentially sputtered Ti and V in an Ar and N_2 gas mix with an elaborate shuttering mechanism to shield areas of the target. By varying the exposure time of each element they could vary the thickness of the layers and the l_{MN}/λ ratio, where l_{MN} is the thickness of the metal nitride layer and λ is the bilayer thickness. The l_{MN}/λ ratio was maintained at 0.5 and the $l_{TiN}/l_{VN} = 1$, increasing the λ value to test how it affected hardness. As can be seen in Figure 2.12 there is a distinct sharp increase in hardness when introducing the multilayered structure compared to TiN and VN coatings individually. It was seen that the hardness reached a maximum value of 5560 kgmm^{-2} for a bilayer thickness of $\lambda = 5.2$ nm, further increase led to a decrease in hardness but still improved [45]. The max hardness value measured is a factor of 2 larger than that of TiN or VN alone and thus indicated the potential improvement in coatings properties through architecture design and the application of multilayered structures.
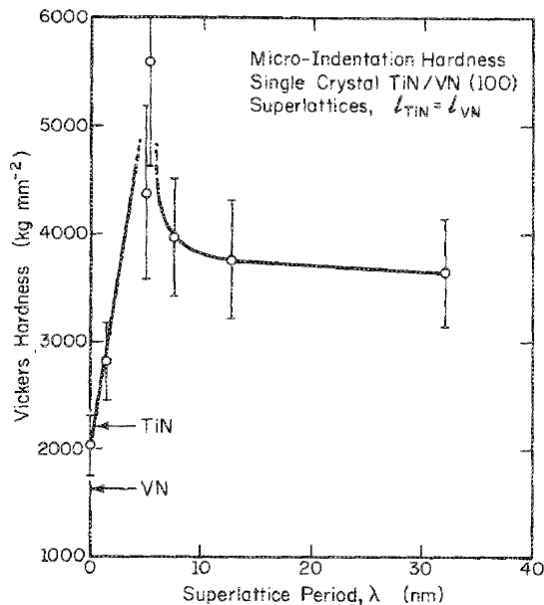
Figure 2.12. The effect of increased lattice period on the measured hardness. For reference, the hardness of TiN and VN coatings have also been included[45].

The hardness of the multilayered coatings is clearly determinable via control of process parameters during deposition to design a coating with specific multilayer lattice periods. Munz et. al [46] developed a method of up-scaling the process to an industrial production level by sequentially subjecting samples to target material and a Hauzer 1000-4 PVD system. The set-up involved 4 cathode targets operated in either steered cathodic arc or unbalanced magnetron modes and a 3-fold rotational substrate carousel; the primary rotation speeds controlled the length of time a sample was exposed to a target, as the sample passed a layer of that target would form, upon passing the next target a new layer of that target could grow. This allowed control of the layer thickness by varying the time exposed to each target. The secondary and tertiary rotation speeds helped homogeneous growth of the coating on complex geometry samples. Another variable was the power of the cathodes; by increasing the power the sputtering rate increases and hence the deposition rate, therefore forming a thicker layer, this was seen by measuring performing Low Angle X-ray diffraction scans on coatings with increasing cathode power, the single peak observed indicates the bilayer thickness and this was seen to increase with increased cathode power. The study demonstrated that the production of multilayered coatings with improved properties over monolithic coatings was not only controllable and reproducible, but also that it could be applied to industrially sized equipment [46].

2.3.1. The Mechanism behind Improved Properties

Increasing the number of interfaces is known to increase the toughness of a material and improve its resistance to crack propagation; the increase in toughness has the effect of reducing the brittleness, particularly important in the production of hard ceramic materials which have notoriously low yields to plastic deformation [44]. The improved hardness and wear resistance of nanoscaled multilayer coatings has been observed (described above) but the mechanism behind it was not entirely known. Luo et. al. performed cross section TEM analysis on 3 coated High Speed Steel samples to determine the wear mechanism that occur. Monolithic TiAlCrN, Monolithic TiAlCrYN, and mulitilayered TiAlN/CrN coatings were deposited on High Speed Steel, wear tests were performed under identical conditions for all 3 coatings and the worn surfaces compared [43]. It was found that the TiAlN/CrN multilayer coating had the best wear resistance but all 3 coatings showed improved wear resistance compared to uncoated samples. Cross sectional TEM indicated that the top few layers of the multilayer coating delaminated producing a loss of material down to a depth of approximately 8 nm, the multilayer structure however is maintained throughout the coating and is not destroyed via frictional heating effects as shown in Figure 2.13., interestingly cracks are visible however they propagate vertically down column boundaries and are not sufficient on their own to remove large amounts of material.
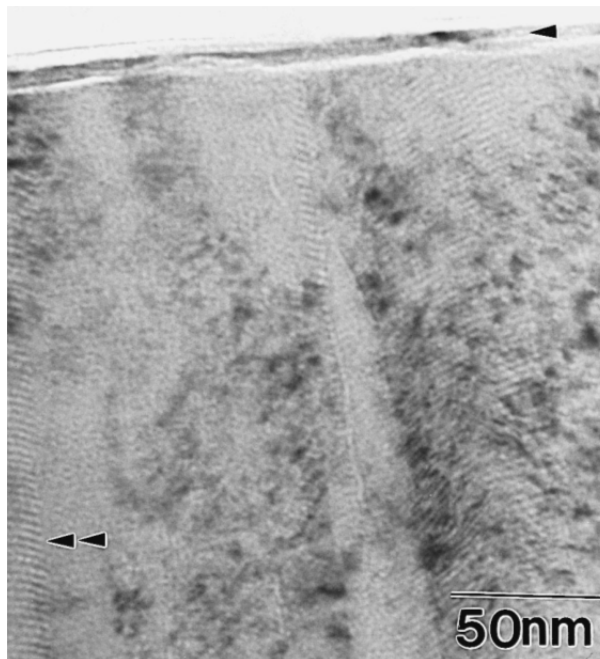
Figure 2.13. Cross sectional Bright Field TEM image of the wear on a multilayered TiAlN/CrN coating after wear tests. The single arrow indicates the delaminated top surface layers and the double arrows indicate the presence of the multilayer structure

In comparison the monolithically grown coatings show evidence of plastic deformation at the surface, bending the columns in the direction of sliding. This behaviour is not observed in the multilayered coating and clearly indicates a different wear mechanism. Cracks parallel to the worn surface begin to form at the base of the deformation areas and it is from this point, causing large pieces of material to be removed, approximately 50 nm compared to 8 nm delaminated layer of the multilayered coating. Figure 2.14 is a schematic that nicely demonstrates the different wear mechanism involved between monolithic and multilayer coatings and the benefits multilayers have on improving the wear resistance by retarding dislocation flow down through the coating to the substrate.
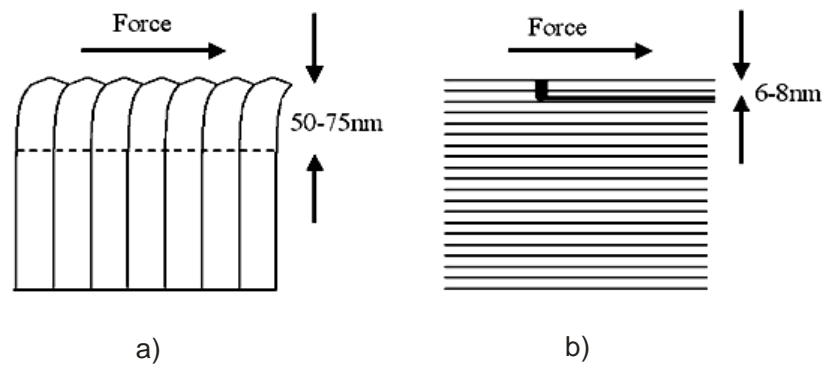
Figure 2.14. Schematic of mechanical failure during wear of a) monolithic and b) superlatiice coatings[46].

Further evidence to support the mechanism of improved hardness and wear resistance was realised by Karimi et. al. in 2002 [47]. They investigated the cracking of multilayered Si and C containing TiAlN coatings under load as a comparison with non-multilayered coatings. It was seen from the load-unload curves of nanoindentation measurements that the nanoscale multilayered coating exhibited 'kinks' in the curve at certain loads indicating the formation of nano and micro-cracks. In comparison the non-multilayered coatings gave a much smoother reading for the curve, however, large 'kinks' indicative of large cracks occur at much lower loads than for the multilayered coating. It is deduced from these results that the formation of small cracks in the multilayered coating act to delay the formation of large cracks. This increases the toughness of the hard coatings and reduces brittleness [47].

2.4. Previously Established Coatings

2.4.1. CrAlYCN/CrCN

2.4.1.1. Coating Development

Traditionally Titanium Nitride (TiN) was used as a protective coating to improve the lifetime of tools. The addition of Aluminium (Al) to the lattice, replacing Titanium (Ti), improved the hardness. Increasing the Al content increases the hardness up to approximately 70% Al, $((Ti_{0.3}Al_{0.7})N)$, after which the lattice changes its structure from the fcc NaCl structure to the wurtzite type due the abundance of the smaller sized Al atoms.

There is a continuous decrease in the lattice parameter and the Me-N bond length with increased Al content (up to 70% Al) due to the smaller ionic radius and mass of Al compared with Cr. The reduced bond length alters the energy of the wavelength emitted by the CrAlN lattice during Raman spectroscopy; there is a continuous wavenumber downshift of all spectral bands with increased Aluminium content, as observed in Figure 2.15 [48].
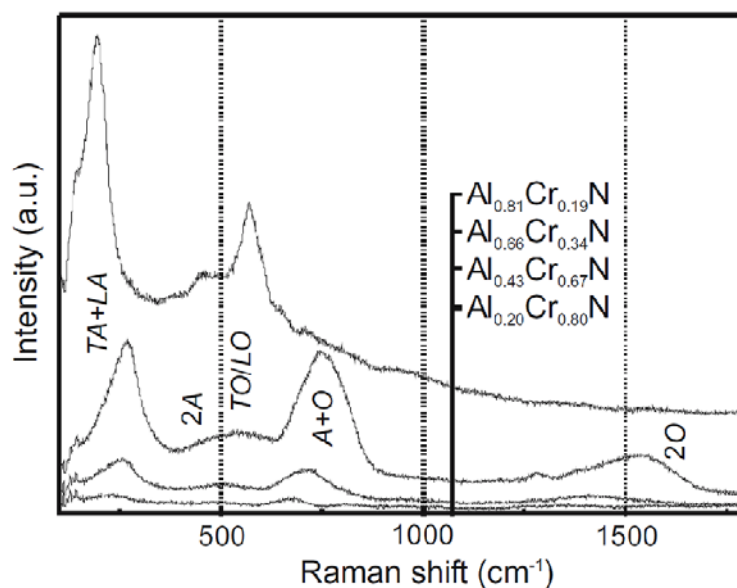
Figure 2.15. Raman spectra of CrAlN coatings with increasing Aluminium content.[48])

Al also forms a dense protective oxide scale which increases oxidation resistance. Many coatings on the market today are TiAlN based and it has proved to be a very effective coating. However, despite the high oxidation resistance generated by the addition of aluminium, a coating is only as strong as its weakest constituent; Titanium is known to form relatively porous oxides and therefore provides oxidation pathways down through the coating to the substrate. A study by Tien and Duh (2006) looked at the mass gain in air of CrN/AlN and TiN/AlN coatings. Figure 2.16 indicates that, with prolonged exposure times, oxide growth is linear for Ti-based, the oxide contuse to grow with time. However, for the Cr-based coating, the oxide layer acts to prevent further oxidation and the oxide growth plateaus [49].
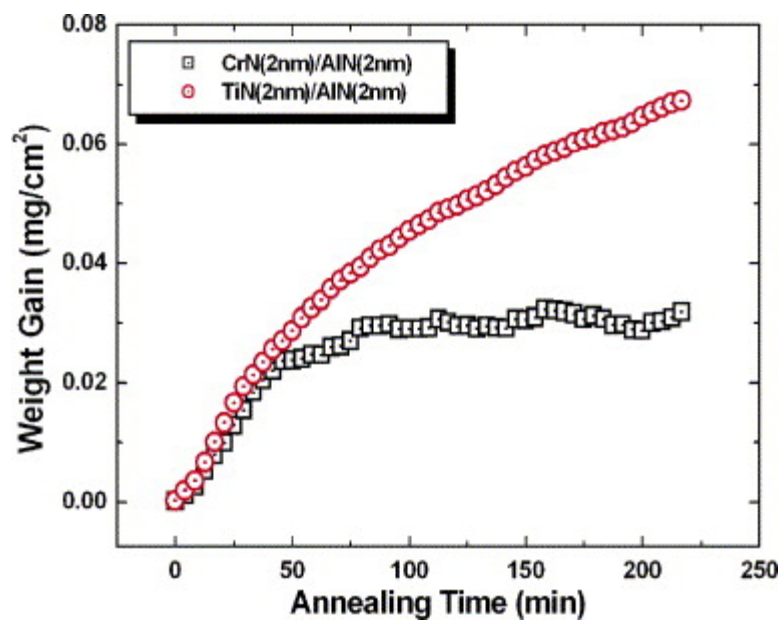
Figure 2.16. TGA weight gain during isothermal heat treatment to 850°C of TiN/AlN and CrN/AlN coatings [49].

To combat these issues and increase the oxidation resistance chromium is being used a substitute; CrAlN also forms an fcc NaCl lattice structure with a similar change occurring with increased Al [50]. CrAlN has been shown to have superior high temperature oxidation resistance to its predecessors, TiN, CrN and TiAlN, maintaining only a single oxide presence of Cr_2O after annealing up to 1000°C [51], outperforming the other coatings and showing coating stability up to and above temperatures often

observed in dry-high speed machining. Another important factor is that CrAlN also shows greater hardness values at elevated temperatures, decrease in hardness observed after annealing to 800˚C compared to 600˚C [52] for TiAlN and 500˚C for TiN and CrN [51]; thus highlighting the benefits of Ti-free coatings for oxidation resistance and inclusion of Al for hardness.

Further development of oxidation resistance coatings led to the introduction of Yttrium as a dopant. Yttrium segregates into grain boundaries 'plugging' oxygen diffusion paths; this migration increases the high temperature oxidation resistance of the coating. There has been a natural progression to combine these elements in the evolution of the coatings to increase oxidation resistance. The development of the architecture proved a useful tool in combatting wear resistance; the nanoscale multilayer design produced by a rotating substrate holder carousel sequentially exposes the substrates to different targets for brief periods allowing layer by layer growth of the target material. For example when the sample passes a Cr target with N_2 as a reactive gas, a CrN layer is deposited. Upon passing a CrAlY target a CrAlYN layer is then deposited on top as depicted in Figure 2.17.
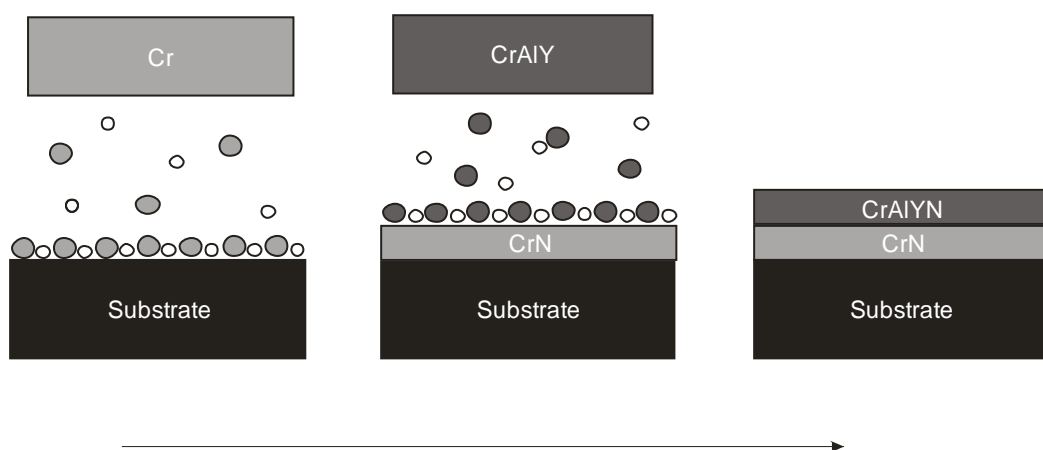
Figure 2.17. A linear representation of the sequential coating process for a multilayer structure, the empty circles represent dissociated Nitrogen reactive gas and the coloured circles are the target material.

As described in section 2.3, the nanoscale multilayer architecture provides an alternative mechanism for wear by the removal of layers as opposed to large sections of the coating, the interfaces help to divert crack propagation laterally rather than down through the coating increasing hardness and also the layer interfaces act as Oxygen diffusion barriers improving the high temperature oxidation resistance. In addition to the multilayer structure a base layer is often deposited; nanoscale multilayers are inherently highly stressed due to the individual lattices of the layers being forced into forming a common lattice, therefore, deposition directly onto the substrate would cause a highly stressed interface and result in poor adhesion. The base layer is a large layer (in comparison to nanoscale multilayers) with a single lattice structure for example CrN; the deposition of the base layer onto the unstressed substrate creates a stress at the interface but lesser than the multilayer construct, therefore providing a stress gradient over the entire architecture.

Introducing HIPIMS as the method for the etching step showed improved adhesion of coatings; the highly ionised, metal ion rich plasma created by HIPIMS means that the implantation rate is greater than the sputter rate, resulting in an extremely clean surface with metal atoms implanted into the surface [53]. The implantation provides a template for local epitaxial growth (LEG) over large surface areas and results in good adhesion of the subsequently deposited base layer and nanoscale multilayer structure. In addition to the etching step, HIPIMS has also been employed in the coating step; the presence of metal rich, highly ionised, droplet free plasma has been shown to give fully dense coatings with low surface roughness, globular growth (as opposed to columnar) and coatings free from voids and defects.

The development of the coatings elemental properties, deposition technique and coating architecture gave rise to the CrAlYN/CrN nanoscale multilayer PVD coating

deposited by HIPIMS-UBM and HIPIMS-HIPIMS techniques [1], [53]–[55]. Further to this, Carbon has been successfully added to the structure [56] with the application of coating tools used for the machining of Al alloys which react with the tool causing a build-up of work piece material on the tool surface and also form highly abrasive Al-based oxides; the addition of Carbon reduces the coefficient of friction during wear, and also the segregation of Carbon during growth into the layer boundaries gives low inter-layer shear strength aiding the layer-by-layer wear mechanism and reducing the build-up on the tool [56].

2.4.1.2. Oxidation Resistance and High Temperature Stability

In order for a coating to retain its protective properties at the elevated temperatures experienced during cutting applications they must maintain high temperature stability and act to delay the onset of rapid oxidation. In 2006 Hovsepian et. al. developed the CrAlYN/CrN superlattice coating [1]. A Cr etch was performed using a HIPIMS power supply, then a CrAlN base was deposited followed by the CrAlYN/CrN coating both deposited using the power supplies in UBM.

The coating was subjected to high temperature testing involving thermogravimetric analysis and Isothermal heating; the onset of rapid oxidation occurred within the temperature range of 950-98 0˚C, comparing this with TiAlN/CrN (900 ˚C) and monolithic TiAlYCrN (920-950 ˚C) shows that this coating outperforms Ti-based coatings. Low angle XRD analysis of coatings heated to 1000 ˚C for 1 hour Isothermal testing gave Cr_2O_3 and Al_2O_3 peaks from the surface scale and also reflections from the CrAlYN/CrN lattice below, in addition, there was no substrate oxides detected indicating that the coating is still structurally sound with inhibited diffusion of the substrate into the coatings and also the dense oxide layer helps to reduce further oxidation down to the substrate. Figure 2.18 shows the layered structure of the

coating after heat treatment - there is an Al rich layer at the surface with a mixed Al and Cr oxide scale below, the increased performance is due to the formation of dense oxide compared to Ti-based coatings, segregation of Yttrium in grain boundaries and the multilayer structure.
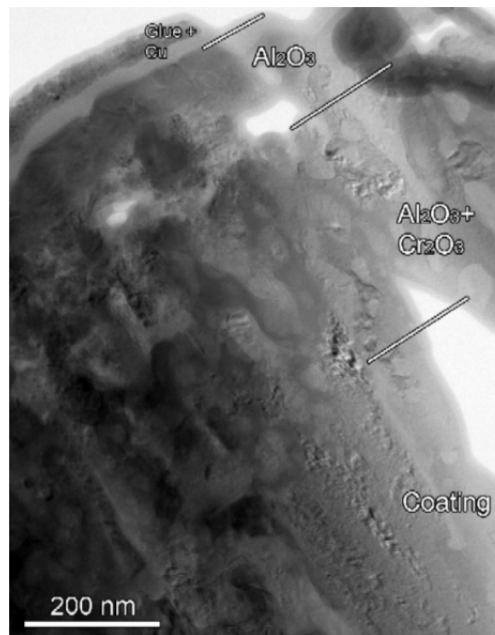
Figure 2.18. A cross sectional TEM image of the CrAlYN/CrN superlattice coating after heat treatment of 1000 ˚C in air for 1 hour. Highlighted are the layers of the original coating plus the oxide scale areas[1].

Further study of the oxidation properties of this coating was undertaken [55], the coating was heated to 850 ˚C, 900 ˚C, 950 ˚C and 1000 ˚C and the coating structure analysed using LA XRD and XTEM. Before heat treatment the coating was observed to have 2 distinguishable peaks in LA XRD indicating a superlattice structure with layer thicknesses of 4 nm, the second peak indicates sharp layer transitions. Upon heating to 850 ˚C the second peak is no longer visible; the superlattice structure is still evident, however, there is some diffusion between layers - this is confirmed by TEM. 900 ˚C shows the first evidence of an oxide scale, Cr_2O_3 peak detected by XRD. At 950˚C more oxides are present; Cr_2O_3, $(Al_{1-x}Cr_x)_2O_3$, Cr_2N and AlN, coating structure can be

58

seen to losing its integrity by the degradation at the base of the columns. Finally, at 1000 ˚C the superlattice structure has been destroyed, Figure 2.19 highlights the diffusion of material within the coating; an Al rich layer forms at the surface, with a Cr rich layer below - near the coating. Substrate oxide peaks were, again, not observed in XRD scans indicating the effective oxidation resistance of the coating at high temperatures.
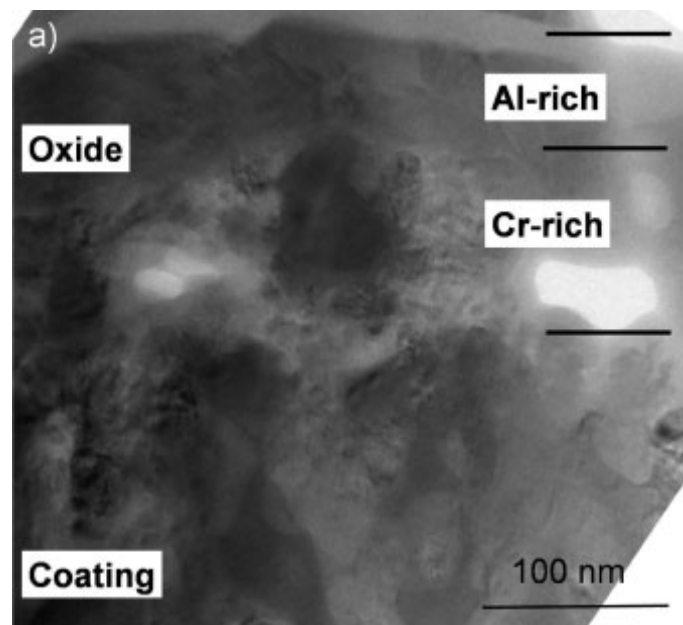
Figure 2.19. A bright field XTEM image showing the layered structure and layer composition of the oxide scale formed after heating to 1000˚C for 1 hour[55]*.*

The mass gain of CrAlYN/CrN during heating to 750 ˚C for 1000 hours was seen to be superior to a TiAlCr coating and an uncoated γ-TiAl sample [53], as shown in Figure 2.20. The oxidation resistance properties are described in the paper to be due to the dense Al scale formed at the surface creating an oxygen diffusion barrier and the multilayer superlattice structure which provides many interfaces to inhibit oxygen diffusion [53]. Despite the improvements stated in the study, it can be seen from Figure 2.17. that the mass change for the Y-containing coating is steadily increasing, whereas,

for the Y-free coating the mass change has almost plateaued. Based on the trends, it may be the case that at higher temperatures (than that studied in this paper) the mass change of the Y-containing coating exceeds that of the Y-free coating.
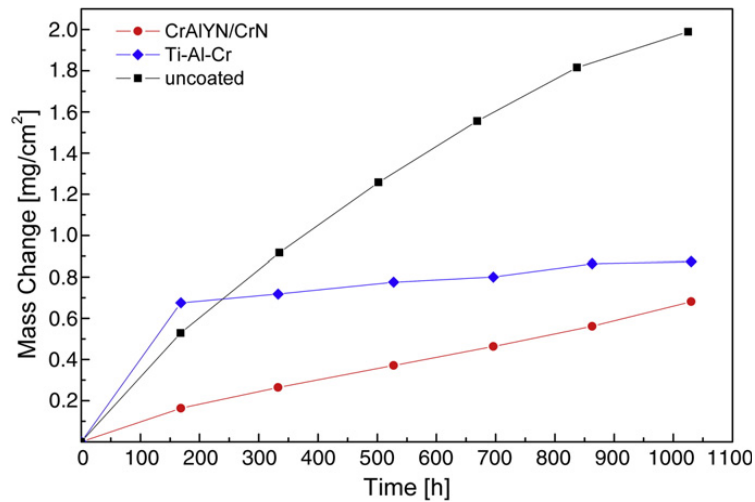
Figure 2.20. The mass gain vs. exposure time of γ-TiAl samples, uncoated, TiAlCr coated and CrAlYN/CrN coated[53]

The introduction of Carbon into the coating architecture to help reduce the coefficient of friction [56] did not affect the oxidation resistance; the onset of rapid oxidation occurred at 940 ˚C (950-980 ˚C for CrAlYN/CrN [1]), there are also dense Cr and Al rich oxide scales forming at the surface providing protective barriers as seen for the carbon-free coatings.

Another study utilised the HIPIMS power supply as part of the deposition process as well as the etching step, known as HIPIMS-HIPIMS technique [54]. The HIPIMS-HIPIMS coatings showed further advancement in the oxidation resistance properties of CrAlYN/CrN multilayer; γ-TiAl coated with CrAlYN/CrN via HIPIMS-HIPIMS technique, HIPIMS-UBM technique and uncoated samples were heated to 2000 ˚C, after 1000 hours the HIPIMS-HIPIMS coating had a mass gain lower than

HIPIMS-UBM by a factor of 2 and uncoated by a factor of 6. This again shows the excellent performance of the CrAlYN/CrN multilayer coating under high temperature conditions and also that HIPIMS can be successfully applied to the coating step during the process to improve the properties further.

At High Temperatures the coatings begin to crack due to differences in the thermal expansion coefficient between the substrate, base layer, coating and also the individual layers in the multilayer system. Oxygen can then diffuse into the cracks, and form oxides further into the coating. Evidence of cracking can be seen in Figure 2.21. The literature shows that at high temperatures the superlattice structure begins to breakdown with interlayer diffusion, crack propagation is now not diverted laterally but can proceed down towards the substrate allowing for substrate-oxides to form and coating failure.
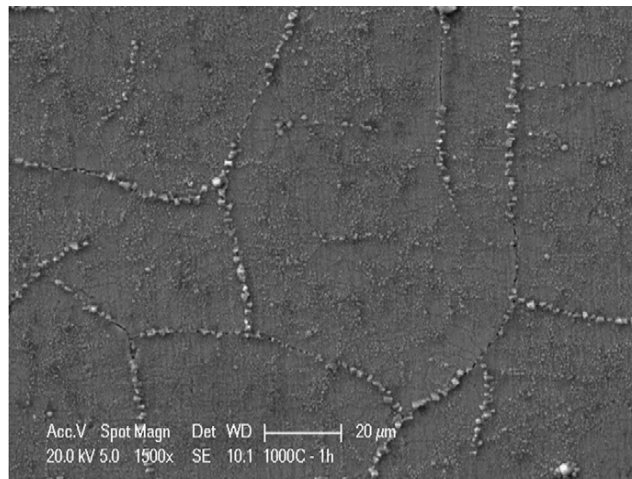
Figure 2.21. SEM image of oxides formed on the coating surface as well as within cracks.[56]*.*

Cracking has been shown to be reduced by employing the HIPIMS-HIPIMS technique as shown in Figure 2.22, the nanolayers deposited by HIPIMS prove to be better diffusion barriers than UBM deposited layers, this is down to the reduced

waviness of HIPIMS layers and, sharp layer interfaces and the elimination of growth

defects from UBM deposition [54].
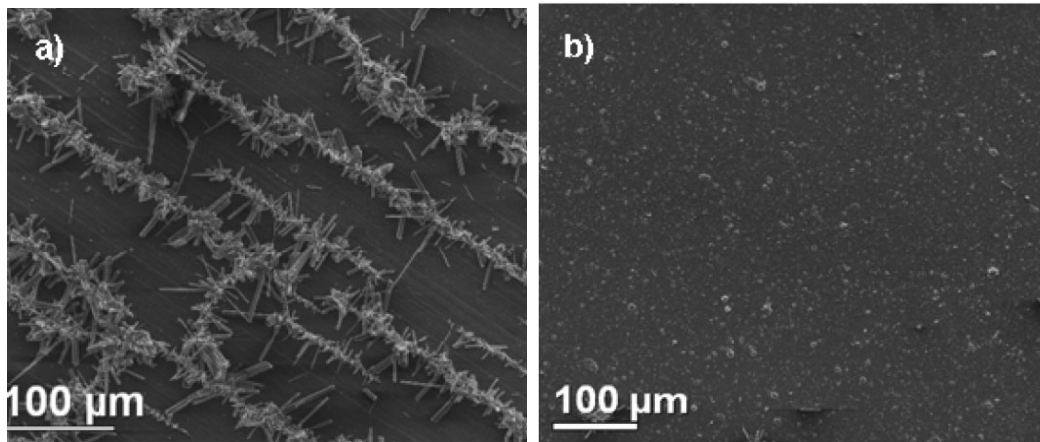
Figure 2.22. An SEM image of a CrAlYN/CrN coating deposited by HIPIMS-UBM (a) and HIPIMS-HIPIMS technique (b). (a) shows evidence of oxides forming in cracks however, in (b) only the surface oxide scale is present.[43]

2.4.1.3. Phase and Microstructure

XRD of the CrAlYN/CrN multilayer coating has a single phase NaCl fcc

structure [1][53][54][56] the peaks are positioned between that of AlN and CrN

indicating a weighted average position of the composition of the layers, typical for

superlattice coatings [1]. The maximum solubility of Al within the CrN lattice is 77%

and thus so long as the Al content does not exceed this value, the structure will remain

NaCl fcc and will not change the wurtzite structure.

The preferred texture of the coating is controlled by the energy of Ion

bombardment; at low substrate bias (-75 V) the {111} orientation dominates, however

at higher bias (>-95 V) the {220} orientation is preferred; this simultaneously causes an

increase in the compressive stress within the material [1][54]. The {220} orientation has

also been observed in the CrAlYCN/CrCN coating, in this study the texture is attributed

to the strong influence of the CrN layers and also the presence of H^+ and CH^+ in the plasma, used as the precursors for the inclusion of C into the coating [56].

HIPIMS-UBM technique gives nanoscale multilayer coatings with sharp, distinguishable interfaces, this allows for corroboration of the layer thickness using LA XRD with XTEM imaging. It can be seen from Figure 2.23 a) the layers have a waviness to them but still maintain the multilayer structure. When Carbon is added to the coating structure it segregates to column boundaries and layer interfaces, this causes the layer to be discontinuous however overall the layer structure is still visible (Figure 2.20 b)) [56].
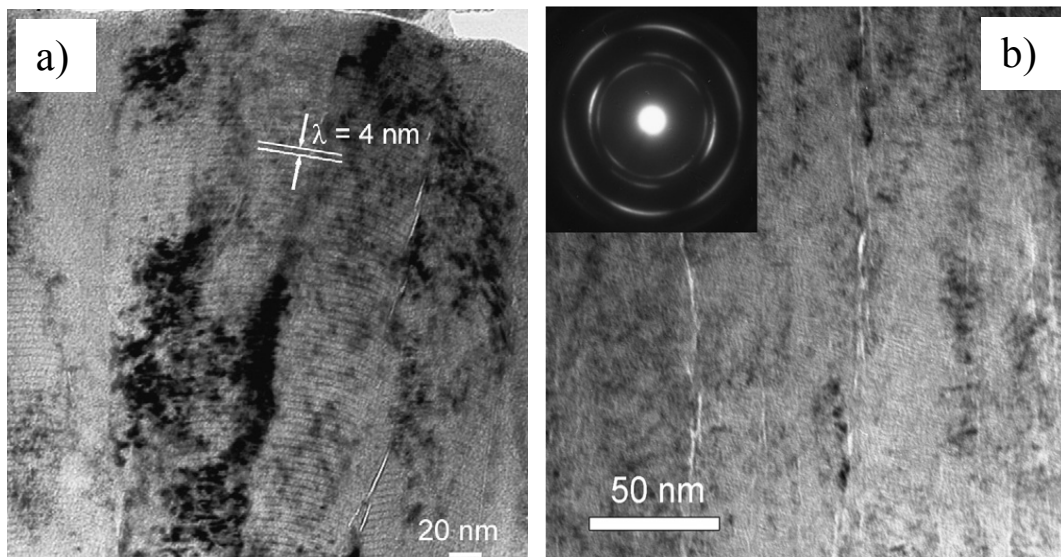
Figure 2.23 a) shows the nanolayer structure and layer thickness of CrAlYN/CrN deposited by HIPIMS-UBM technique and b) shows the 'broken' nanolayer strucutre of the CrAlYCN/CrCN coating[56].

In the study [56], the brighter areas of the cross-sectional transmission electron microscope (XTEM) image (Figure 2.23 b)) were confirmed to be carbon by electron energy loss spectroscopy (EELS). The selected area diffraction pattern (inset of Figure 2.23 b)), indicated a (200) orientation of the individual layers.

Deposition of CrAlYN/CrN by HIPIMS-UBM technique has shown to improve the coatings; the HIPIMS etching step gives a very sharp and clean surface, free from macroparticles and high metal implantation content. This has been seen to give fully

dense columnar structures and the coatings show evidence of LEG over large surface areas [1]. High resolution imagining was performed to study the interface between the substrate and the base layer [53]; Cr implantation was clearly visible at the interface to a depth of 5 nm into the substrate. Atomic resolution Images showed atomic column alignment along the interface indicating registry between the 2 lattices. Furthermore, Selected-Area Electron Diffraction (SAED) patterns of the substrate and base layers show identical cube-on-cube phase orientation; the Cr implantation helps to template the base layer growth [53].

The waviness of the layers can be greatly reduced by employing HIPIMS during the coating process. HIPIMS-HIPIMS CrAlYN/CrN coatings were seen to have very clean, sharp, distinguishable, dense and free from voids nanolayers with virtually no waviness and shown in Figure 2.24. This is important for the improvement of coating adhesion.
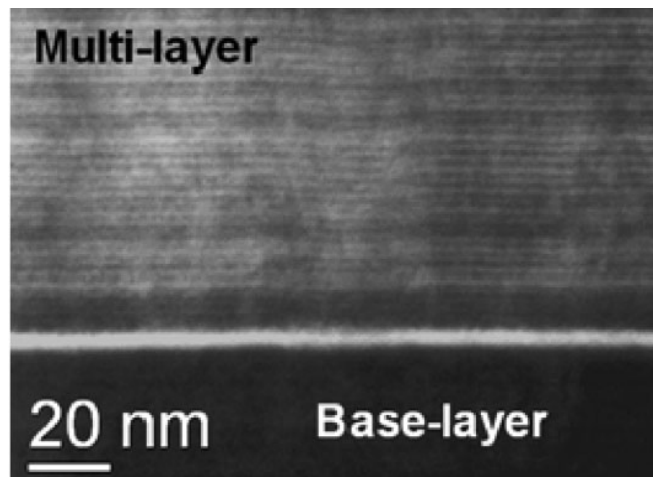
Figure 2.24. The architecture of a CrAlYN/CrN coating deposited by the HIPIMS-HIPIMS technique, the base layer, base layer-coating interface and the nanolayer superlattice are clearly visible[54].

2.4.1.4.　Mechanical and Tribological Properties

Deposition onto M2 hardened steel with Rockwell hardness scale C, HRC = 58 utilising HIPIMS and arc pre-treatment showed HIPIMS to be the superior method. The surface roughness, R_a, reduced from 0.05 μm with ARC to 0.036 μm with HIPIMS, also the critical load during a scratch test, L_c, increased from 56 N for ARC to 65 N for HIPIMS. The difference in adhesion and roughness is attributed to HIPIMS creating clean, sharp, macroparticle-free interfaces and the promotion of LEG over large surface areas [1].

CrAlYN/CrN is classed as a superhard coating ($H_p \geq 40$ GPa) with a hardness of $H_p = 42$ GPa, determined by nanoindentation to eliminate plastic deformation effects of the substrate [1]. The hardness is seen to decrease however upon the introduction of carbon into the coating, nanoindentation gave a hardness of $H_p = 39$ GPa [56]. The carbon-containing coating is almost classed as superhard and the reduction is likely to be caused by the segregation of carbon into the layer interfaces making the less defined and reducing its ability to withstand deformation.

The behaviour of the coefficient of friction, μ, is interesting as temperature is increased during a pin on disk test with an Al_2O_3 ball counterpart. At room temperature μ ≈ 0.5, it then increases as temperature is elevated to approximated 100 ˚C, however, upon further increase, in temperature past 600 ˚C the coefficient of friction is observed to reduce down below the value at room temperature. This has been observed for CrAlYN/CrN deposited on both M2 hardened steel and γ-TiAl [53][54]. This behaviour can be explained by lubricants; with the initial increase in temperature surface moisture is evaporating, eliminating the lubricant between coating and counterpart and thus increasing the friction. At higher temperatures, a lubricious oxide, Cr_2O_3, forms on the surface of the coating due to localised flash temperatures. This works to lubricate the

surface of the coating and thus bring down the coefficient of friction at high temperatures. The coefficient of friction is seen to be reduced further by the introduction of C, μ = 0.42 at room temperature. This occurs due the Carbon segregation into the layer interfaces creating low shear strengths between individual layers, therefore during wear the nanolayers are easily removed and the coating acts as a solid lubricant[56].

The high hardness, low coefficient of friction, good adhesion, high temperature stability and excellent oxidation resistant properties of these coatings developed through the progressive addition of beneficial elements and the employment of HIPIMS both as an etching and coating technique have given rise to coatings that not only perform well in laboratory testing, but also in cutting tests.

2.4.1.5.   Cutting Performance

For the CrAlYN/CrN coating 8 mm end mills were coated in 2 separate studies and showed superior performance. In the study [1] cutting test were performed on a workpiece material of Hardened A2 steel (58 HRC) using a MAZAK FJV-25 milling centre, the cutting speed was 385 m min^{-1}, the depth of cut was 3.8 mm and the feed rate per tooth was 0.4 mm. Tool lifetime is based on an industry standard 0.25 mm flank wear. CrAlYN/CrN with Arc etching is seen to have a longer lifetime than a range of other coatings tested as shown in Figure 2.25, except TiAlCrYN. Upon using the CrAlYN/CrN coating with HIPIMS etching it was found to last 9 minutes longer than it's Arc etched sister coating and 8 minutes longer than the TiAlCrYN coating.
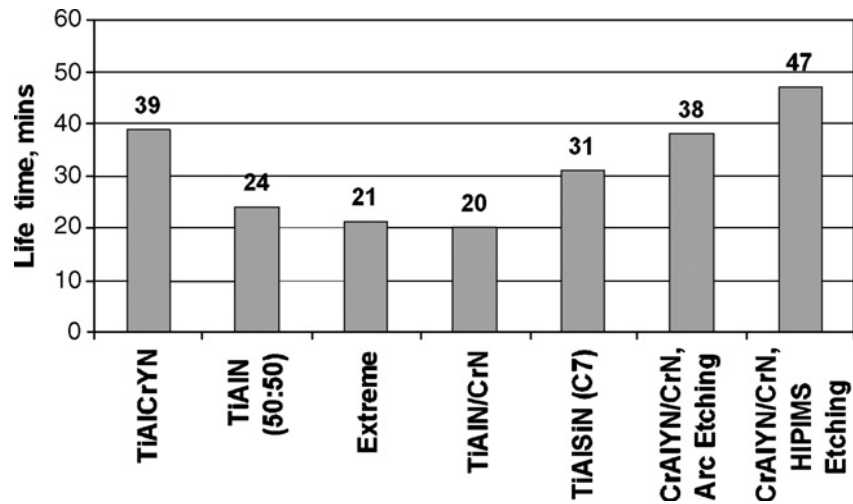
Figure 2.25. A comparison of lifetimes of coated end mills in A2 Hardened Steel.[1]

In the study [55], a comparison was made between the CrAlYN/CrN coatings with Arc and HIPIMS pre-treatment with a TiAlCrYN coating. This time the lifetime was compared at a cutting speed of 385 m.min^{-1} and 500 m.min^{-1}. Again, the HIPIMS pre-treated coating outperformed its competitors at both speeds, illustrated by Figure 2.26.
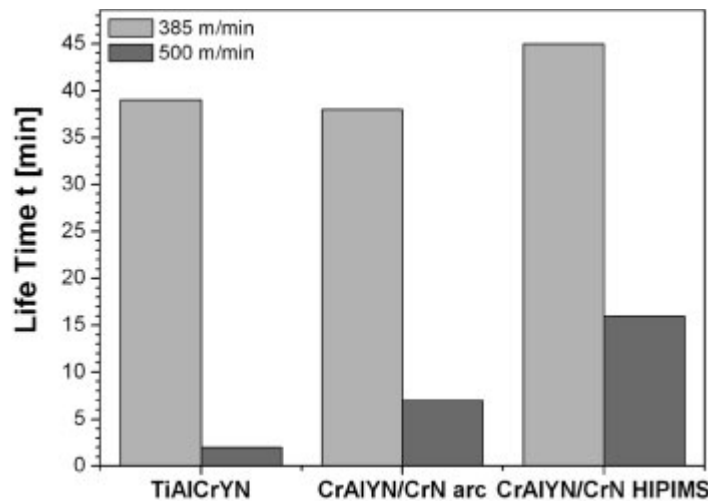
Figure 2.26. A comparison of coating lifetimes at different cutting speeds.[45].

The application of the Carbon-containing CrAlYCN/CrCN coating was to reduce the built up edge when machining Al alloys, the coating was able to remove 2.5% more material than an uncoated tool and SEM images showed very little build up on the flank of the tool [56].

These coatings have shown excellent performance both in lab based testing and cutting test. The application of HIPIMS greatly improves the adhesion, hardness and oxidation resistance of the coating by creating smooth interfaces and a coating free from macroparticles and voids. Combining this technology along with the nanoscale, multilayer, superlattice architecture and detailed knowledge of the properties of the coatings constituent elements has led to the development of a protective coating with lots of potential in the cutting tools industry.

Further improvements can be made however and inspiration arose from the oxidation resistance and high temperature stability properties of coating containing Silicon and Boron which form very dense oxides.

2.4.2.   SiBCN

Quaternary, amorphous Si-B-C-N has emerged as a suitable material for protective coatings among other applications. The compound has many of the desirable properties required for the cutting tool industry; very high temperature stability, high temperature oxidation resistance, good mechanical properties, low thermal conductivity and low thermal expansion coefficient. The ability to control the properties of a material is essential for the production of materials designed for a specific purpose application.

Si-B-C-N coatings and its predecessors were originally deposited via thermolysis of polymer based precursors. However, this technique requires high process temperatures in order to break the strong hydrocarbon chains; releasing the active elements. This limits the substrate selection to materials that can withstand the high temperature and thus reduces the field of application. A further disadvantage of using polymer precursors is the abundance of Hydrogen that becomes included into the coating during growth, causing defects and porosity. Reactive magnetron sputtering addresses these issues by allowing (relatively) low process temperatures. It eliminates the need for polymer precursors and can provide accurate control of the coating properties due to the direct relationship between process conditions and coating structure/properties. To elaborate on this, the effect of Si content in the coating on the properties and also the gas mixture partial pressures have been studied and will now be discussed.

2.4.2.1. The Effect of Si and Ar Content

An initial paper in 2003 studied how controlling the Si and Ar content affected the coating properties of SI-C-N [57]. The deposition process used magnetron sputtering of graphitic target embedded with Si strips along the racetrack, in an Ar and N_2 atmosphere. To test the effect of Si, the gas mixture was maintained at 50% at. N and 50% at. Ar, and the concentration of Si in the target was increased. It was found that increasing the Si content of the target increased the amount of Si incorporation in the coating, observing a corresponding reduction in the C content and an increase in the nitrogen. The strong affiliation between Si and N means that increasing the amount of Si improves the inclusion of N. Furthermore, it was found that increasing the Ar partial pressure at a fixed Si target composition induced preferential sputtering of Si over C, therefore increasing the Si content of the coating. Interestingly, despite the partial pressure of N_2 being reduced, there was not a notably observable reduction in the N content of the coating; this is again attributed to the strong affiliation between Si and N [57].

At constant partial pressure of the gas mix, increasing the Si content did not alter the hardness, it did however increase the coefficient of friction. Increasing the Ar partial pressure at constant Si content did not alter the coefficient of friction but did increase the hardness. This paper showed that controlling the content of the target and the gas mix, a coating with tailored properties can be developed via reactive magnetron sputtering.

2.4.2.1.1.   Oxidation Resistance and Thermal Stability

Boron containing silicon carbo-nitride coatings have shown excellent high temperature stability in inert gases and high temperature oxidation resistance in air. Varying the gas mix partial pressure demonstrated that the oxidation resistance of SiBCN coatings could be controlled. With a Si target content maintained at 75% coatings were deposited by reactive magnetron sputtering in an Ar and N_2 atmosphere, the effect of changing the partial pressure of Ar from 50% to 75% was studied [58]. The coatings were annealed in air to 1700 ˚C in a thermogravimetric analyser and the change in mass due to oxidation measured; the 50% Ar gas mix showed no mass change up to 1400 ˚C and only a small change after 1600 ˚C as shown in Figure 2.27, in comparison it can be seen that increasing the Ar content to 75% reduces the oxidation resistance of the coating.
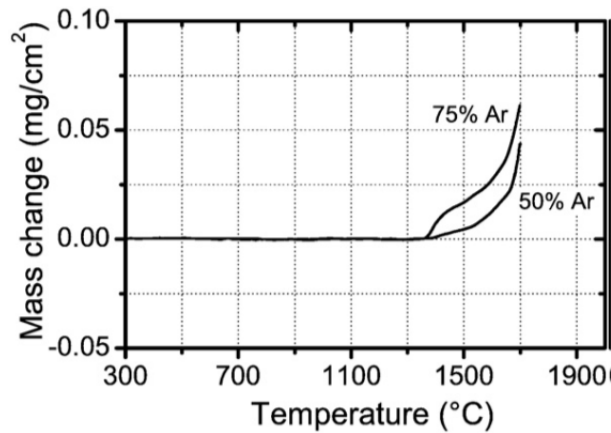
Figure 2.27. Mass gain of coatings prepared in 50% and 75% Ar gas mixture[58]*.*

XRD analysis showed that at 50% Ar a protective SiO_2 layer formed on the surface which accounts for the mass gain after 1600 ˚C but remains amorphous underneath. Comparatively, the coating at 75% Ar gave reflection from Si crystallisation; crystals provide oxygen diffusion pathways at their boundaries, explaining the reduction in the oxidation resistance [58].

The same study tested the thermal stability of the coating when annealed in inert gases; this provides detail of the coating behaviour at high temperatures without oxidation effects occurring. The 50% Ar coating remained amorphous up to 1600 ˚C whereas the 75% Ar coating became unstable above 1250 ˚C. Further study of the thermal stability of SiBCN coating has been performed by Zemen et. al [59] the results of which are summarised in Table 2.1.

Table 2.1. Thermal stability of SiCBN coatings prepared at 50% and 75% Ar gas mix at elevated temperatures

Temperature (˚C)	Partial Pressure of Ar as % of total Ar/N_2 gas mixture (%)	
	50	75
1400	No mass Change/Amorphous	Mass loss due to N release/Si Crystal phases
1600	Amorphous	Crystallised
1700	Si Crystals present but poor crystallinity	Increase in Si peak indicating formation of Si-Si bond and release of N

The oxidation resistance and thermal stability observed in these studies have been attributed to the N:(Si+B+C) ratio within the coating. It has been seen that increasing the partial pressure of Ar enhances the sputtering of Si, it therefore increases the silicon content of the coating, and hence, the coating prepared at 75% Ar has a lower ratio than the 50% coating [58]–[60]. The importance of this is the preferential bonding

of N with Si, B and C means there is an absence of the Si-Si bond; this bond has a melting point of 1414 ˚C. At elevated temperatures this bond breaks, mobilising Si atoms through the coating which are free to make new bonds which causes crystallisation and reduced oxidation resistance

This is also supported by a study into the thermal conductivity of SiBCN coatings [61]. Coatings produced at 50% Ar had an almost constant thermal conductivity at room temperature, annealing to 1300 ˚C and also 1400 ˚C, approximately 1.40 $Wm^{-1}K^{-1}$. Similarly for the 75% Ar coating at room temperature and 1300 ˚C the thermal conductivity was approximately 1.6 $Wm^{-1}K^{-1}$, however, increasing the temperature to 1400 ˚C resulted in a drastic increase in the thermal conductivity. The authors suggest this is again due to the crystallisation of the material at higher temperature due to the abundance of Si-Si bonds.

2.4.2.1.2. Mechanical properties

The amorphous structure of SiBCN coatings makes their surfaces extremely smooth; at 50% Ar the coatings had roughness values of R_a = 1 nm and RMS = 0.5 nm (indistinguishrable from the silicon wafer substrate) [60]. In addition to this the partial pressure of Ar did not appear to make a significant difference to the hardness (22 GPa, 50% Ar vs. 24 GPa, 75% Ar), Young's modulus (164 GPa, 50% Ar vs. 191 GPa, 75% Ar), the elastic recovery (72%, 50% Ar vs. 74%, 75% Ar) or the compressive stress (0.6, 50% Ar vs. 1.06, 75% Ar) [59]. Furthermore, plasma assisted deposition showed a low coefficient of friction, μ = 0.32, under Pin on Disk testing believed to be due to the formation of nano carbon phases at the sample surface acting as a solid lubricant [59].

2.4.2.2. Microstructure Before and After Heat Treatment

A recent paper [62] studied the microstructure of SiBCN coatings prepared with an Ar partial pressure of 50% of the total gas mix, and a B_4C target containing Si strips along the racetrack contributing to 75% Si content of the target erosion area. The aim was to investigate how the microstructure evolves when annealed in He to 1400 ˚C and in air up to 1700 ˚C in an attempt to determine a mechanism for the oxidation [62].

XPS analysis showed no change in the peak pattern between the room temperature as-deposited sample and the sample annealed to 1400 ˚C. However at 1700 ˚C only Si and O peaks are observed with a notable absence of B and N peaks, therefore B and N are being oxidised and released in gaseous form. The peak shifts observed of Si and B in the film, indicated that they existed as nitrides again emphasising the preferential bonding with N and inhibiting the formation of Si-Si bonds.

TEM of the as-deposited coating showed the microstructure to be homogeneous and uniform throughout, the 1400 ˚C coating showed similar features and both were confirmed to be amorphous via XRD indicating that heating to 1400 ˚C has no effect of

the structure.   However, upon increasing the temperature further and exposing the coating to air 3 distinct layers develop, Figure 2.28.
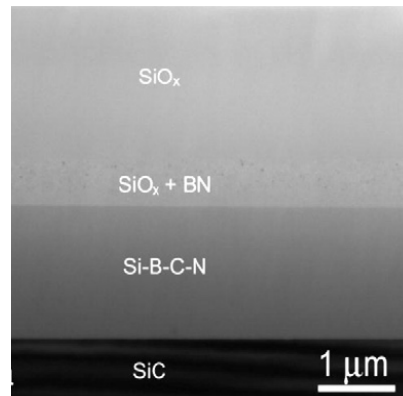
Figure 2.28. The layer separation of the SiBCN coating on a SiC substrate upon annealing in air to 1700℃. [62].

The base layer is consistent with the original coating, an amorphous SiBCN structure. The top layer is an amorphous SiO_x layer, and in the intermediate layer BN nanoparticles can be seen to have formed in a SiO_x matrix, increasing in size towards the top layer. The suggested mechanism is that O diffusion occurs; oxidising Si and the BN nanoparticles precipitate and increase in size as they migrate towards the coating surface where they become oxidised and are released as gases, hence the BN free top layer. Precipitation of BN at the base layer-intermediate layer interface forms a thin BN rich layer which acts as a diffusion barrier [62].

The evidence discussed in this section shows that SiBCN coatings have very good high temperature stability and oxidation resistance. The reason for this is the ability for the coating to remain amorphous at high temperature due to the preferential bonding of Si, B, and C to N, this eliminates the Si-Si which when broken allows the mobility of Si atoms through the coating, forming new bonds and crystallising the structure.

2.3.4.   CrAlSiN

We have seen throughout this chapter the effect elemental additives can have on improving the performance of coatings; one such improvement has been investigated through the addition of Si into the CrAlN lattice [63]–[67]. It was found that Si reacts with N to form an amorphous Si_xN phase which segregates to grain boundaries improving oxidation resistance by increasing the length of diffusion pathways [63], it was later postulated that the amorphous Si_xN phase acts to inhibit grain growth [64]. With smaller grains there is an inherent increase in mechanical hardness due to the Hall-Petch relationship where an increased concentration of grain boundaries acts to inhibit dislocations and disrupt the propagation of cracks [67].

All coatings investigated were measured to have high hardness, with the Author's classing them as 'superhard'. The CrAlSiN quaternary coatings develop a surface passivation layer consisting of dense Cr and Al oxides which protect against extensive oxidation. It has been reported [66][67] that the CrAlN structure remains stable up to 900 ˚C, after which, it dissociates into Cr_xN and AlN species with N_2 being released, at this temperature the passivation layer cannot protect against oxygen penetration and therefore it begins to grow initially, increasing the mass of the coating measured by TG. This thicker layer then protects against the onset of rapid oxidation to higher temperatures until 1050 ˚C, further increased in temperature results in extensive oxidative mass gain and coating failure.

The addition of Si proved successful in improving oxidation resistance via segregation of amorphous phases to grain boundaries, without being detrimental to the mechanical properties seen for CrAlN.

2.4.   Growth of Cr$_2$O$_3$

The growth of a thin, dense chromia passivation layer on the surface of a material acts to prevent further oxidation of the bulk material, prolonging oxidation resistance and increasing a tools performance at high temperatures. Through studying the oxidation of Cr-containing steels, it has been suggested that Cr$_2$O$_3$ forms a duplex system; initially a spinel of Fe$_2$CrO$_4$ grows at the surface and secondly, with increased oxidation via exposure to high temperatures for an extended amount of time [68][69], a crystalline Cr$_2$O$_3$ scale develops. Raman spectroscopy has been a useful tool in the determination of this mechanism as it can easily detect and quantify both crystalline and spinel phases.

Figure 2.29 shows the evolution of Raman peaks detected when a samples of HT-9 steel was exposed to a temperature of 700 ˚C in air for increasing lengths of time. There is a clear peak at approximately 685 cm^{-1} which is attributed to the spinel Fe$_2$CrO$_4$ species and with increased exposure the Cr$_2$O$_3$ peak at approximately 549 cm^{-1} appears.
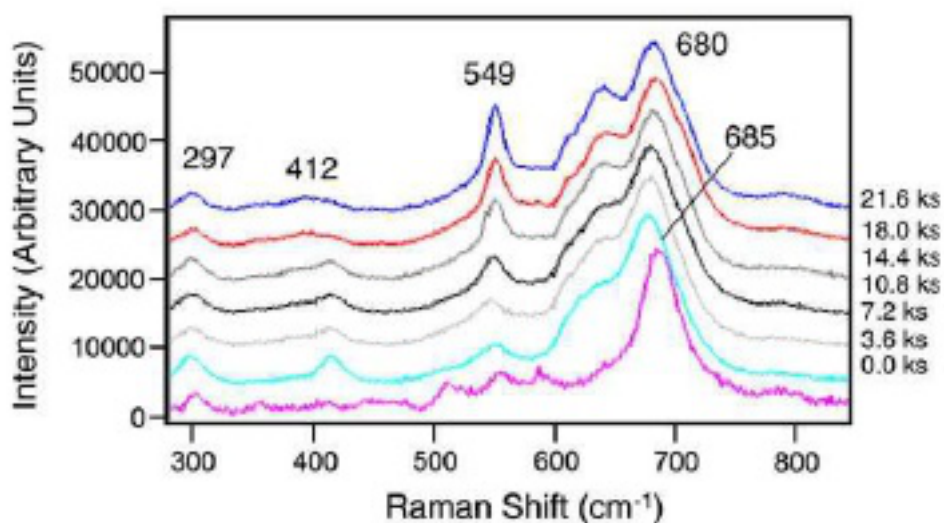
Figure 2.29. Raman spectra of corrosion products on HT-9 sample without YSZ coating as a function of time of heating at 973 K in air [69].

The study by Windisch et. al. compared the uncoated HT-9 sample with one coated in yttria-stabilised zirconia. It was found that coating acted to inhibit the growth of the Cr_2O_3 peak at 549 cm^{-1}, there was however presence of peaks associated with α-Fe_2O_3, as the iron species in the substrate diffuses through the coating to the surface [69].

Raman spectroscopy is a useful tool for the identification of the phase of grown chromia scales. A number of studies[70]–[76] have reported the presence of the CrO_2 phase; they found that the Raman peaks for CrO_2 are centred at 570 and 670 cm^{-1}. Broadening of the 670 cm^{-1} band is associated with a highly disordered CrO_2. The chromia scale was seen to exist in mixed phases depending on the conditions, Baranov et. al. report the presence of a highly disordered CrO_2 layer on an untreated Cr sample; increasing the intensity of the oxidation conditions during film growth caused an increase in peak intensity and peak narrowing suggesting a decrease in the disorder and a thickening of the layer. Further increase led to the development of the characteristic Cr_2O_3 peak at 549 cm^{-1} [77][78] occurring simultaneously with a decrease in the CrO_2 peak intensity. It was postulated that with increased exposure to an oxidative environment CrO_2 would transform into Cr_2O_3 [76].

The formation of Cr_2O_3 on the surface of coatings provides high wear resistance and low friction coefficients due to the thin, passivating, self-healing layer. The dense oxide grown from a reaction between Cr in the coating and oxygen in the environment, is hard dense and highly adhesive as it has used the Cr as a template for growth minimising stresses at the interface. The film acts as a barrier between the coating and the work piece (usually steel) therefore preventing material transfer between the two

sliding surfaces. It suppresses this adhesive transfer that occurs during adhesive wear by providing an incompatible, insoluble surface [79].

2.7.   Novel CrAlYBCN/AlSiCN

A novel coating is being designed and implemented in this study, utilising the beneficial features of the techniques, elements and coatings discussed in this literature review. The proven benefits of HIPIMS during coating aim to give a fully dense coating with excellent adhesion. The nanoscale multilayer architecture provides oxidation resistance by increasing the number of diffusion barriers, and increasing the wear resistance by providing a lateral, layer-by-layer removal mechanism. The addition of yttrium helps to block diffusion pathways via its segregation into grain boundaries. Combining these advantages with knowledge of the properties of the three previously developed coatings, CrAlYCN/CrCN, SiBCN and CrAlSiN, we aim to develop the nanoscale multilayer CrAlYBCN/AlSiCN coating. The coating will have high hardness, good adhesion high temperature stability and oxidation resistance; suitable for the coating of cutting tool designed for the application of dry high speed machining of abrasive materials.

3.   Methodology

3.1.   Experimental Details

The experiment performed in this project was carried out in the Sheffield Hallam University Centre for Nanotechnology and PVD research, the industrial sized Hauzer 1000-4 PVD system (Figure 3.1) will be the primary machine used for plasma production, etching studies, hysteresis generation and coating deposition. The system is fitted with a 250 m^3/h roots pump and a 500 m^3/h rotary vane pump, in addition to 2 Blazers TPH 2200 turbo molecular pumps used to evacuate the chamber.
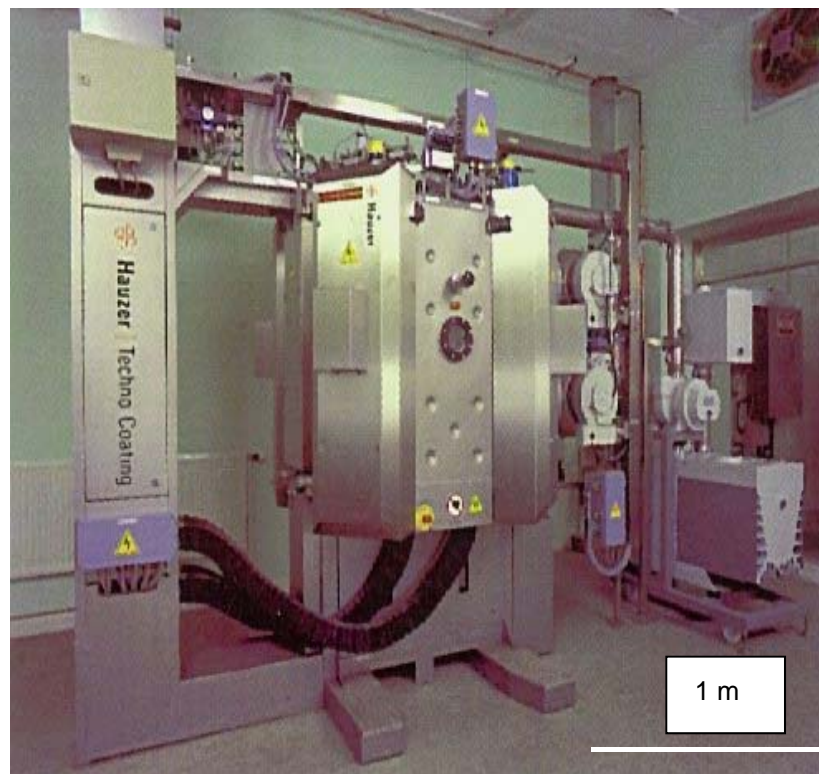
Figure 3.1. A photo of a HTC 1000-4 PVD system

The system contains four power supplies that operate in UBM mode, two of which are also capable of operating in HIPIMS mode using a Huettinger HMP2/4 power supply. Each section of the system is electrically insulated from each other. The power

supply is fitted with an arc suppression system which detects sudden rises in current associated with arcing and shuts off the supply. Targets of desired etching/coating material are bolted onto a copper plate that is used as a cooling element connected to the cathode and the targets used are of size 200 x 600 mm^2. There is also a sample holder carousel which operates with 3-fold orbital rotational motion, illustrated in the schematic given in Figure 3.2. The chamber has a volume of 1 m^3, there are 2 heating elements located on the inside wall of the chamber doors, in between targets 1 and 2, and the other between targets 3 and 4. Gas inlets allow the use of Ar as a sputtering medium, and N$_2$ and CH$_4$ as reactive gases during deposition.
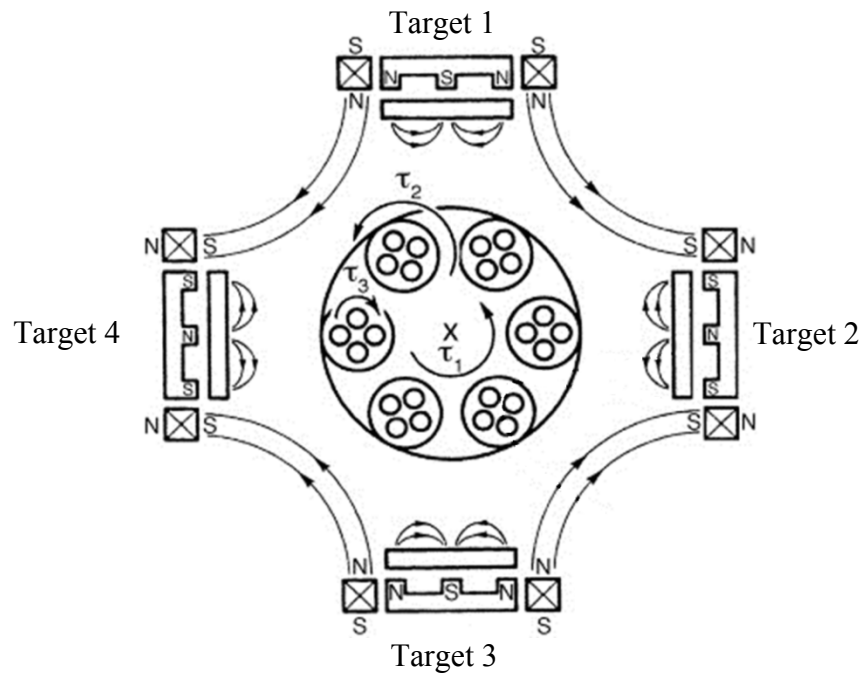
Figure 3.2. Top down cross sectional view of the Hauzer 1000-4 PVD system highlighting the linked magnetic field lines of the 4 UBM cathode arrangements.

The different types of substrate used were:

-      304L Stainless Steel 30 mm (diameter) coupons

-      High Speed Steel M2 30 mm (diameter) coupons

- Tungsten Carbide inserts (WC)

- Silicon (001) wafers

- Rolled 316L Stainless Steel square samples

Sample preparation involves two steps; polishing and cleaning. The HSS and SS samples are mirror polished progressively decreasing the feature sizes using grinding pads and then polished with a 1 µm diamond paste; this reducig surface defects on the coatings improving epitaxial, homogeneous growth. Half of the WC samples used are also polished in this way to provide samples suitable for some laboratory tests (polished), the rest are representative of the unpolished samples often used in industry. All the samples are then put through the cleaning line; an automated process alternating between detergent and water washes, with a final de-ionized water wash, followed by drying in a vacuum furnace. This is essential to remove any residual dust, dirt and grease that may be present on the surface of the samples; presence of such contaminant can lead to defects during coating growth.

The standard experimental process can be broken down into the following steps:

- *Sample Preparation*

As described above samples are ground and mirror polished. They are then put through the cleaning line to remove any residuals on the surface and dried using a vacuum furnace. The samples are then loaded into the chamber of the Hauzer 1000-4 PVD system. The steel coupons are orientated so that the polished surface faces the targets. The polished WC inserts are arranged in the same way and the unpolished WC insert are mounted onto pins with separators to replicate and industrial process.

- *Evacuating the Chamber*

The chamber must be vacuum pumped to remove any gases in the chamber that may collide with process gases or sputtered material and potentially contaminate both targets and substrates. The pressure is reduced to 8 x 10^{-2} mbar using the roots and rotary vane pumps, once this pressure is reached the turbo pumps are activated to reduce the pressure further down to 7.5 x 10^{-5} mbar.

- *Heating*

During plasma diagnostic processes where no substrates are loaded into the chamber, the temperature is maintained at 100 ˚C to protect the sensitive instruments. During processes containing samples however, the temperature is increased to 450 ˚C; temperature is monitored using a thermocouple inside the chamber at the substrate position. Heating causes out-gassing of components within the chamber and thus increases the pressure; the pressure must be allowed to reduce back down to approximately 7.5 x 10^{-5} mbar before target cleaning can begin.

- *Target Cleaning*

Native oxides form on the target during storage and also if previously used in reactive gas deposition. There may be a Nitride or Carbide compound formed on the surface; these inhibit the sputtering efficiency of the target and could lead to unwanted gas phase element inclusion in the growing coating. The targets are therefore sputtered with Ar at high cathode voltages in two steps of 5 minutes, increasing the voltage in the second step. This is performed with shutters in front of the targets to prevent etching or

deposition of unwanted contaminants onto the substrates. The AlSi targets become heavily poisoned during the coating process with a compound layer forming on the surface; they must therefore be cleaned manually in between depositions using a metal wire brush.

- *Etching*

Etching is a highly important step in the coating deposition process. Ar gas is used as a sputtering medium and it is a method of cleaning the substrate of any surface impurities before deposition. Also, the high energy particles ejected from the target can implant into the surface; the etching step is performed using only one of the targets, implantation forms an interface layer of material that will also be in the base layer and thus helps to improve the adhesion of the subsequent layers that are deposited [80]. Etching is performed at a high Voltage in order to produce the high energy species. Conventionally the charge is ramped from 0 to 16 for 20 minutes and then held at max charge 16 for 20 minutes in order to reduce the rapid changes that occur in the target when increasing the cathode current. The charge stated is the integral of the current which ensures each impulse has the same charge despite any other variations in the pulse. Operating the cathode in HIPIMS mode during this step has been proven to increase the adhesion of coatings compared to conventional UBM modes [81]–[86]. The increased number of highly energetic metal ions present in the plasma implant into the substrate surface. The effect of this process on the plasma generated and on the substrate surface will be investigated in chapter 4 and optimal process condition decided upon. For chapters 5 to 8, the etching step conditions remain unchanged; the CrAlY target is operated in HIPIMS mode with an average cathode power of 6 kW, a charge of 16, a pulse frequency of 92 Hz and pulse duration of 200 µs. During the etching step to

accelerate the ion towards the substrate for bombardment the substrate bias is set to − 1000 V. The optimal conditions investigated in chapter 4 concluded that the optimal ramping and holding times were 10 minutes and 20 minutes, respectively, and thus these times were implemented in all coatings.

- *Base Layer*

A base layer is deposited in a N_2 and Ar gas mix and is performed at a lower voltage than the etching step, minimising the amount of re-sputtering of deposited material by highly energetic bombarding ions at the substrate. A monolithically grown metal nitride base layer is deposited to act as a stress gradient between the unstressed substrate and the highly stressed multilayer superlattice structure to be deposited. The intermediate layer acts to improve the adhesion. Base layer process conditions for all coatings in chapters 5 to 8 remain constant; the CrAlY target is operated in HIPIMS mode with an average power of 8 kW, a charge 10.4, a pulse frequency of 400 Hz and pulse duration of 200 μs. The CrB target is operated in conventional DC, UBM mode with a constant power of 8 kW. The AlSi targets were operated in conventional DC, UBM mode with a constant power of 1 kW to reduce the deposition of material during this coating step. The substrate was biased at − 60 V and the chamber pressure was maintained at 3.5 x 10^{-3} mbar.

- *Multilayer Coating*

The multilayer coatings are deposited using all four targets. In all depositions the CrAlY target is operated HIPIMS mode, the CrB targets and the AlSi targets are operated in conventional DC, UBM mode. Coatings are deposited in a reactive gas mix

of Ar, N_2 and CH_4, with a $N_2{:}CH_4$ flow ratio of 3:1. As the substrate passes a target via the rotating carousel a thin Metal Carbo-Nitride layer of that target material is deposited, upon exposure to the next target a new layer forms of that target material, the constant deposition of new material prevents columnar growth and thus a multilayer is formed. Unless otherwise stated the substrate is biased to -40 V and the process time for this stage of coating is 4 hours. Chamber pressure varies for the different investigations within this study; they are described explicitly within each specific chapter.

- *Poisoning control*

For the coating series 3 to 10 the extent of target poisoning was controllable through employment of the Gencoa Speedflo Mini V2.8. This instrument utilizes a control algorithm capable of extremely fast and accurate feedback for reactive gas inlet control [87]. The instrument can be set to detect the optical emission line of a species within the plasma, for this study it was programmed to detect metallic species (Cr and Al) as a method of measuring the target poisoning level. With increased gas species the target become increasingly poisoned reducing the OES signal of the metal species, initially the gas flow was ramped from 0 to 280 sccm and back down to 0 sccm measuring the OES and producing a hysteresis for poisoning. From this, specific OES signal intensities could be selected to deposit at. The feedback loop control maintains the OES signal intensity by controlling the gas flow; if the signal reduces slightly, the target is becoming more poisoned and the controller reduces the gas flow and vice versa.

3.2. Characterisation Techniques

3.2.1. Flat Probe

Within this study a flat probe is used to determine the ion flux within the plasma. A flat probe is a form of Langmuir probe. The probe is connected to a power supply to enable a voltage to be supplied to it, information about the plasma such as electron density, electron temperature and ion flux can then be determined through analysis. Inserting a probe into a system disturbed the plasma and electron ions and atoms collide with it; electrons travel much faster than atoms due to the difference in weight and so during a plasma process reach the probe first. This causes a negative charge to build up on the surface inducing a floating potential between the probe and the quasi-neutral plasma. The floating potential creates a distance around the probe where oppositely charged ions will be accelerated towards, the surface, the area at which this affects the plasma is known as the sheath region. At zero voltage the probe will register a current due to the influx of electrons to the surface. Application of a negative bias voltage will repel incoming electrons and attract ions to the surface up until a saturation point, giving a current reading on an attached oscilloscope [88][89]. The magnitude of the current reading during one pulse will be used to estimate the total ion flux to the substrate.

3.2.2.   Optical Emission Spectroscopy

Optical Emission Spectroscopy (OES) allows atomic species to be identified by observing the spectra emitted by atoms in the gaseous state. If energy is transferred to an atom via an inelastic process, electrons within the atom are elevated to higher energy levels and the atom is said to be excited. In this excited state the electron is unstable and will 'fall' to a lower energy level. To allow for the conservation of energy, the potential energy loss of the electron is emitted as electromagnetic radiation as depicted in Figure 3.3. Each electron transition has a specific energy due to the quantisation of electrons in an atom, given by the relationship:

$$E_1 - E_0 = h\nu \qquad\qquad \text{Equation 3.1.}$$

and,

$$\lambda = \frac{c}{\nu} \qquad\qquad \text{Equation 3.2.}$$

Where E_0 is the ground state energy level, E_1 is a higher energy level, h is planck's constant, ν is the frequency, c is the speed of light and λ is the wavelength [90]. Therefore, the emitted radiation from an atom has a discrete number of wavelength possibilities depending on the energy level transitions of said atom and hence each atomic species has a fingerprint of emission spectra to identify it; this process is illustrated in the schematic of Figure 3.3.

1. Energy Transfer to atom via collisions or incident electron

2. Electron in ground state excited to higher energy level, electron is unstable in this state

3. Electron decays to the ground state, potential energy loss emitted at electromagnetic radiation
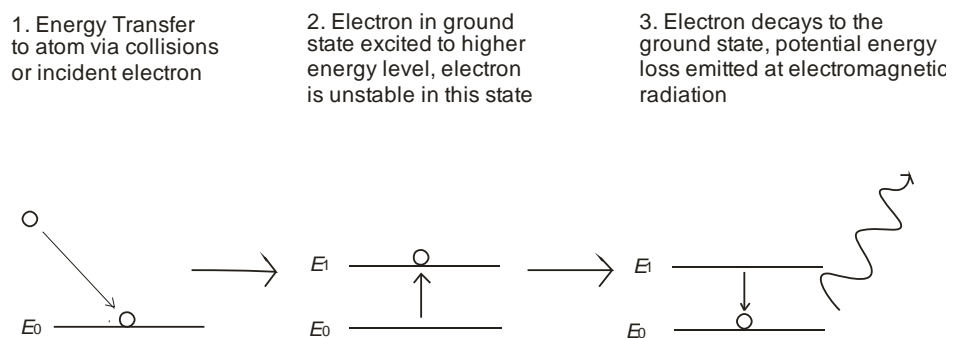
Figure 3.3. A schematic of the emission process within an atom.

The radiation emitted by the plasma passes through an optical fibre, it is reflected off a mirror onto a grating where the light is scattered into its wavelengths, they are then reflected off another mirror and onto a CCD detector which converts the intensity of photons into a current and thus gives a spectrum of the wavelengths contained within the collected light. Setting the detector to measure a range of wavelengths it will output spectra of the emission peaks within that range; from this the species within the plasma can be determined [90]. For this study the Jobin Yvon Triax 320 Spectrometer from Horiba was employed.

3.2.3. Quartz-Crystal Microbalance (QCM)

A Piezoelectric material is something that can convert an electric signal into a mechanical one and vice versa, e.g. the application of an electric field to a piezoelectric will induce a stress [91]. The Piezoelectric property of Quartz crystal is used to measure the mass gain of the device and can therefore be used as a measurement for deposition rates and coating thicknesses.

The structure of a microbalance is a disk of quartz crystal mounted with two metal electrodes, one on each face. Applying an alternating electric field across the quartz crystal induces oscillating stresses within the piezoelectric creating an acoustic wave with a frequency specific to that crystal; importantly, the frequency is directly proportional to the mass of the crystal:

$$\Delta f \; \alpha \; K.\Delta m$$ Equation 3.3.

Where Δf = change in acoustic frequency, K is a constant relating to the properties of the crystal and device and Δm = mass change [92].

Therefore, a measured decrease in the frequency of the device indicates an increase in mass. Applying the device and crystal properties as a substitute for K, the equation becomes:

$$\Delta f = \frac{-2\Delta m f^2}{A(\mu \rho_q)^{0.5}} = -C_f \Delta m \qquad\qquad \text{Equation 3.4.}$$

Where f is the intrinsic crystal frequency, A is the area of the electrode, ρ_q is the density of the quartz crystal and μ is the shear modulus. Combining these constants gives the device sensitivity C_f [93].

3.2.4.   Profilometry

Contact profilometry uses a diamond stylus to measure the topological features of a sample. The tip is moved vertically onto the sample and can be moved laterally across the surface, the tip is attached to a cantilever and the height of the tip is recorded as it proceeds by bouncing a laser off the top reflective surface of the tip, the position of the laser is measured as a voltage and changes in its position indicate height creating a profile. In this study profilometry is used to determine the step height between a masked and unmasked area during the etching process, the profile produced by the stylus will there provide information on the amount of material removed during etching. A schematic of the stylus motion over a surface feature is illustrated in Figure 3.4.
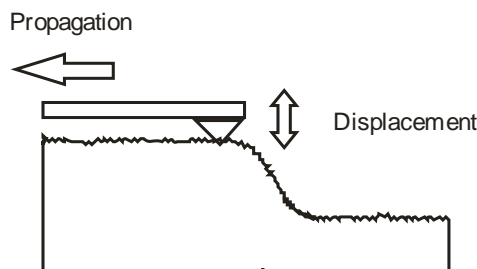
Figure 3.4. A schematic of a profilometer tip in contact with a surface as it processes; the displacement due to the topology of the sample is recorded.

For this study the stylus profilometer used was the Dektak 150 by Vecco Instruments, having a lateral resolution of 33 nm. This instrument was used to

determine the wear track depth after pin on disc testing and for whole coating thicknesses. The thickness measurements were later measured using calowear testing (section 3.2.11) in order to distinguish between base-layer and multilayer thicknesses.

3.2.5. Scanning Electron Microscopy

The resolution of features in optical microscopy is limited by the wavelength of the incident light; if the feature is smaller than the wavelength it cannot be resolved. As the wavelength is much smaller for an electron than it is for a photon of the same energy, an electron microscope has better resolution and so can see finer details at higher magnifications.

Scanning Electron Microscopy (SEM) scans a beam of electrons across a surface and uses a detector to collect deflected and emitted electrons to map the topology and chemistry of a sample. Scanning involves diverging the beam laterally along the x-axis from the origin to a set distance, the beam then returns to the origin in the x position but increments its distance from the origin in the y-axis and another scan is performed. This is repeated until a 'frame' is completed and then restarts. The slower the frame rate the better the image, however fast frame rate in environmental chambers can be used to effectively video the movement of molecules such as proteins and DNA.

The beam of electrons is generated by passing a current through a triangular shaped tungsten filament. The filament becomes extremely hot and the electrons at the tip of the triangle have sufficient energy to escape. As the electron are negatively charged and the filament is now ionised an anode is used to accelerate the electron away from the tip and channelled into a beam. The chamber must be kept in vacuum in order to reduce interaction with atoms in the air. A current is passed through metal coils in order to generate a magnetic field, this applies a force upon the charged electron as they pass through it, given by:

$$F = BevSin\theta \hspace{4cm} \text{Equation 3.4.}$$

Where F = Force on the electron, B = magnetic field Strength, e = charge on the electron, v = velocity of the electron and θ = the angle between the magnetic field lines and the direction of motion of the electron.

Altering their direction and focusing them to a point on the sample as depicted by Figure 3.5. The manipulation of the electron beam in this way is also useful in changing the focal length; by increasing the current the B field is increased and hence electrons change direction by a greater angle, decreasing the focal length [94]–[96].
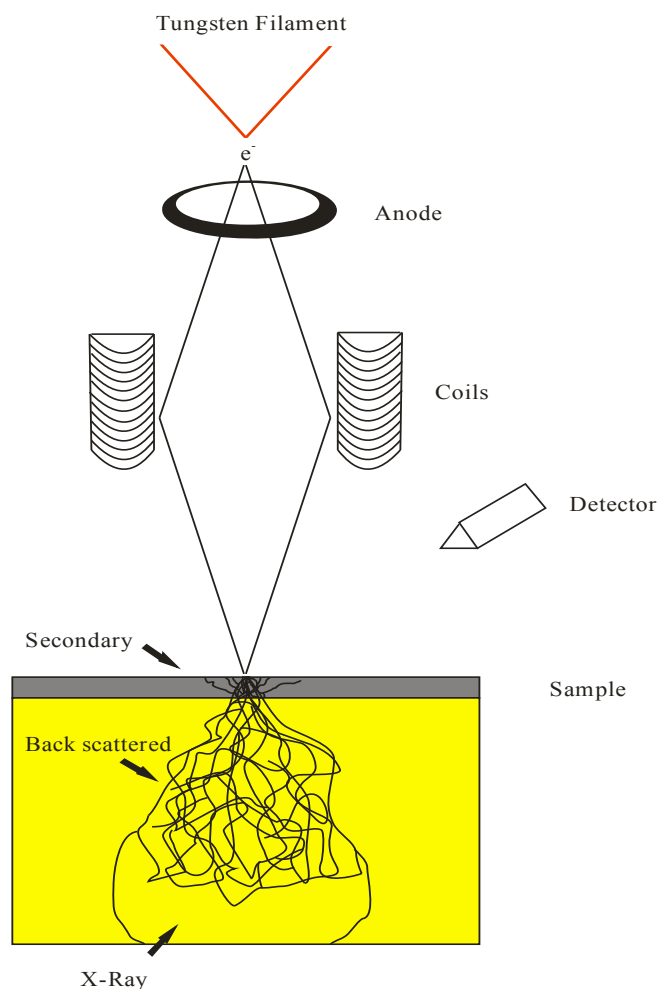
Figure 3.5. A schematic of an electron microscope, highlighting the electron production from a Tungsten filament, the beam focusing using magnetic fields generated by passing a current through coils and how the electrons are scattered when in contact with a sample.

The electron beam interacts with the sample surface after which a detector is used to collect the electrons, using their intensities to produce an image. Electrons can interact with a surface in a number of ways;

Elastic Scattering

Backscattered electrons: Electrostatic interaction with atoms can cause deflection of the electron by an angle greater than 90° without energy loss, known as backscattered electrons. A flat area will give a higher intensity of backscattered electrons than a defect or an edge - the surface feature changes the angle of deflection, hence the relative intensities allow for a contrast image where the features angled away from the detector appear darker.

Inelastic Scattering

Secondary electron Emission: This occurs when an incident electron collides with an atom-bound electron in the sample, transferring energy. If the collisional energy is sufficient an electron can be ejected from the atom. These electrons have relatively low energies, therefore to be able to escape from the sample and be detected they must come from atoms at the surface. This allows for not only a topological image of the surface to be generated but is also an indication of density; if two areas have different densities, there will be fewer collisions for an electron to undergo in the less dense area, giving a higher intensity and a brighter image. The mean free path of an electron increases with reduced density.

X-ray Emission: The removal of electrons from atomic shells as described above leaves holes that must be filled by electrons in higher energy levels to increase stability, alternatively an atom may become excited by an incident electron but not ionised and the electron returns to its original state. The change in potential energy of the 'falling'

electron is emitted as an X-ray with a discrete wavelength. This can be used to map the relative chemical composition of the sample by Energy Dispersive X-ray Spectrometry (EDX); comparing the emission lines with known lines from a built in database, elements can be identified and their intensities used to obtain elemental ratios [94][95].

The SEM device used in this study was the FEI NOVA 200 NanoSEM.

3.2.6. X-ray Diffraction (XRD)

X-ray diffraction as a characterisation technique is derived from Bragg's law which is given in equation 3.5.

$$n\lambda = 2dsin\theta \qquad \text{Equation 3.5.}$$

Where n is the whole number, λ is the wavelength, θ is the angle of diffraction and d is the spacing between neighbouring atomic planes.

An incident X-ray onto a crystalline structure will penetrate through the material. Where the wave interacts with an atom it will become reflected by an angle equal to the incident angle. When two waves interact interference occurs; whether it is constructive or destructive depends if the waves are in or out of phase, respectively. For the waves to be in phase the wave that penetrates further must have travelled an extra distance 2dsinθ, as shown in Figure 3.6 [97].
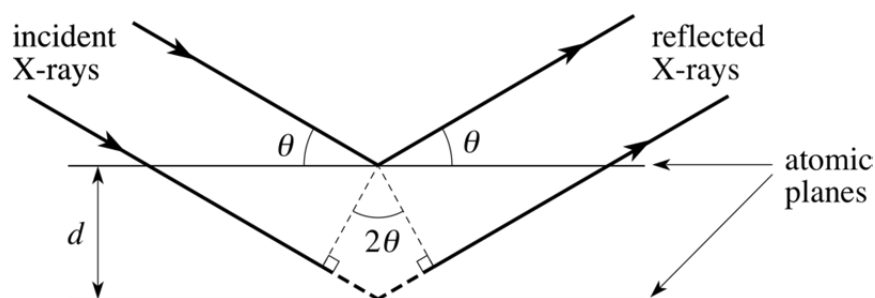
Figure 3.6. A representation of X-rays scattering from planes of atoms. [97].

This phenomena results in a discrete diffraction pattern being formed where incident waves have constructively interfered. The angle at which the incident waves are diffracted to is directly proportional to the spacing between atoms. As each material is different, the three dimensional atomic spacing's are therefore specific to that material; this allows each material to have its own unique diffraction fingerprint that can be used to identify it [97].

The reflections considered are from a series of parallel planes within the crystal lattice; the orientation of these planes is defined by three indices [h,k,l], which slice through the a, b and c axes of the unit cell, respectively, as shown in Figure 3.7.
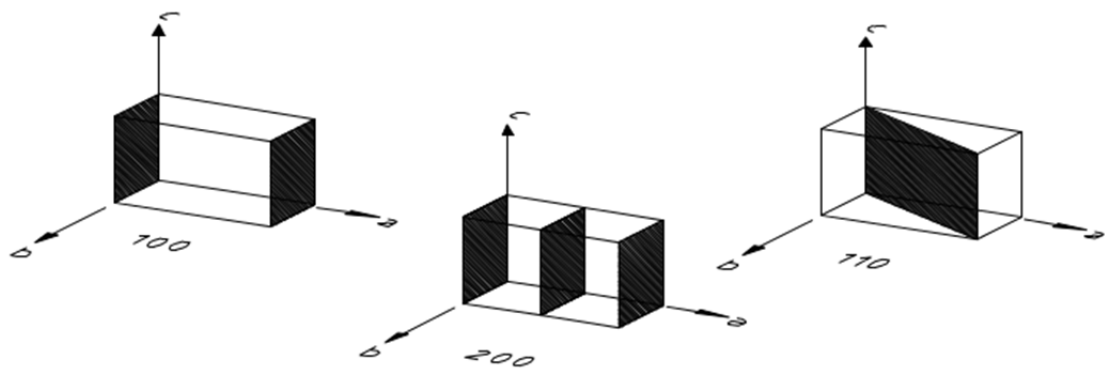
Figure 3.7. Illustration of the [100],[200] and [210], within a unit cell of a crystal lattice[98].

From Figure 3.7 we can see that the a-axis of the unit cell is cut once, reflections from this plane are termed [100]. when the a-axis is cut twice the reflection from this plane is termed [200] and when the reflection is from a diagonal plane that cuts the a and the b axis it is terms [110], and so on [98]. Using this model, the crystal structure of a material can be determined; databases of materials are stored within the software of the instrument to allow identification of the peaks.

The instrument used within this study is the PANalytical Empyrean diffractometer [99] which generates X-ray from a copper source with a wavelength of $\lambda = 1.54$ Å. The instrument set up in 2*Theta goniometer mode - this method keeps the sample stationary in the horizontal plane, with the X-ray tube and the detector moving simultaneously over the angular range, theta. This method is known as Bragg-Brentano and spans a range of $2*\theta = 0 - 140°$, a schematic of the set-up and a picture of the instrument are given in Figure 3.8a) and b), respectively.

a)

b)
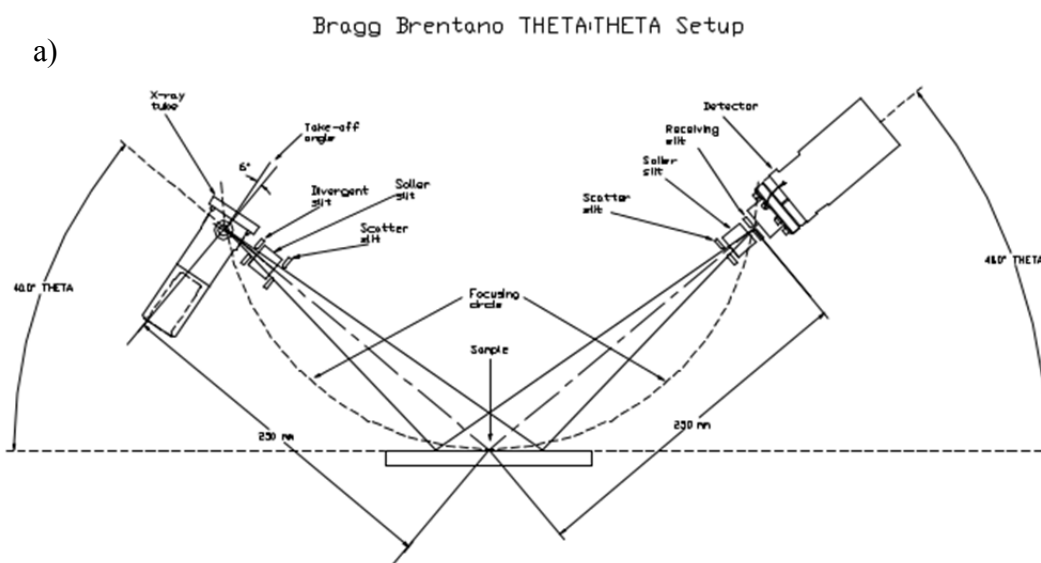
37. Figures 3.8 a) and b) show a schematic of the Bragg-Brentano set-up of the instrument and the instrument itself, respectively[98][99]*.*

The holders also contain Soller slits, inserted after the source and before the detector; these are an arrangement of parallel gratings that only allow light waves normal to the slits through, reducing the noise on the diffraction signal.

The Bragg-Brentano method increases the source to high angles therefore increasing the penetration depth of the incident waves. For thin coatings like those deposited in this study diffraction peaks from the 304 SS substrates may be detected causing convolution of some peaks. To eliminate this effect glancing angle scans were performed whereby the Omega angle (angle between the horizontal plane of the sample and the incident wave [100] is set to 1˚, and in this arrangement only the detector moves through angles $2*\theta = 0 - 140$. Test scans of $\Omega = 2˚, 5˚$ and $10˚$ were also performed, however showed traces of substrate peaks and are therefore not shown in the report.

Low angle x-ray diffraction is also implemented where the Bragg-Brentano configuration is set to only scan a range of $2*\theta = 0 - 10˚$; within this range it is possible

to measure reflections from the interfaces between layers within a multilayer coating. For coating 1 and 2 the peak positions were used to calculate the bilayer thickness, *d*, using Bragg's law (Equation 3.5).

Another application of XRD that has been applied to coatings 1 and 2 is the grain size calculation; this is not strictly a measurement of grain sizes but a calculation of the relative volumes of grains that have a specific orientation. The grain size is proportional to the broadening of the peak whereby increased peak width suggests decreased grain size determined using the Scherrer Equation 3.6:

$$B = \frac{k.\lambda}{L.cos\theta}$$

Equation 3.6

Where B = peak broadening, k = Scherner constant (0.94), λ = 1.54 Å and θ = peak diffraction angle [101].

The instrument has some inherent broadening which must be accounted for; a scan of a reference crystalline Si sample was performed to find the instrumental broadening to remove from the FWHM of the coating peaks. For XRD the broadening increases at higher angles of diffraction so these were plotted and an equation of the line of best fit found. After approximately $2*\theta$ = 107 ˚ the gradient of the altered and therefore to calculate the effect of instrumental broadening two linear equations were applied; pre and post $2*\theta$ = 107˚. This calculation allowed the relative volumes of grains with different crystallographic orientations was determined.

3.2.7.   Raman

When monochromatic light is incident onto an atom it scatters; if this scattering is elastic the detected light will have the same energy as the incident wave, this is known as Rayleigh scattering. However not all interactions are elastic; each atom within the material is bonded to its neighbour, these bonds can be modelled as springs which resonate when energy is input. Atoms within the lattice can therefore vibrate around their bonds [102].

These vibrational modes can be quantised like energy levels of electrons with v_0 being the ground state. Inelastic scattering from the ground state increases the vibrational mode of the atom(s) to a higher virtual state; relaxation of the atoms to another vibration al mode (higher than the ground state) emits radiation. This wave has a reduced energy equal to that absorbed by the atom generating the Stokes peak in Figure 3.9. If the atom is originally in a no ground state when the incident waves scatters then the energy released from the virtual state back down to the ground state will be greater than that of the incident wavelength, giving rise to the higher energy Anti-Stokes peak (Figure 3.9). At room temperature most atoms are in the ground state and hence the intensity of the Stokes peak is generally much greater than the Anti-Stokes. and therefore more useful for measurements. In practice, during calibration, the Rayleigh line is centred at zero and the Stokes peaks detected are described as being Raman shifted in wavelength (cm^{-1}) from the zero point [103].

The vibrational modes of a molecule are dependent on bond strength, atomic size and molecular orientation giving rise to specific vibrational modes for different bonding atoms; a fingerprint of the material under investigation specific to its bonding atoms is produced and can therefore be used for identification analysis.
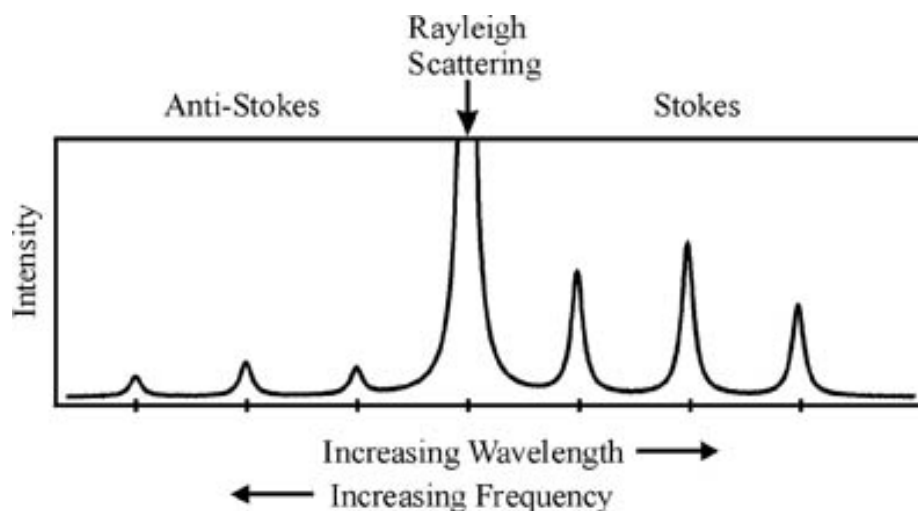
Figure 3.9. Raman scattering highlighting the elastically scattered Rayleigh line with the high intensity, low energy Stokes peaks and the low intensity, high energy Anti Stokes peaks [104].

Whether or not a vibration emits radiation through Raman scattering depends on the influence of the incident wavelength on the type of vibration. If the interaction caused a change in the molecular dipole moment, i.e. a change in the charge position, the vibration is invisible in Raman. However, if the incident light induces a change in the polarisation of the molecule, i.e. a stretching or compressing of the electron cloud, then the vibration is visible in the Raman [105]. This makes Raman a very useful tool for surface phase characterisation as bonds which may be invisible to other techniques such as IR absorption, are visible in Raman. Also the scattering of water is very weak minimising any signal noise or false coating peaks due to surface condensation [103].

Raman can be used for qualitative and quantitative applications, to detect simply the presence of a specific molecule, to determine the phase of a material and to give an idea of the amount of each phase present. The band areas are directly proportional to concentration and therefore via comparison of peak ratios it is possible to state the dominate phase of the material.

Raman is used extensively in this study to measure the surface phase of the as-deposited coatings, the compounds formed within the wear track of pin on disc tests, to investigate the effect temperature has on surface phase and also to determine the dominant phase of the material that grows within coatings cracks. The instrument employed is the Horiba Jobin Yvon, LabRAM-HR800, with a 100 mW, 532 nm laser. The spectra were acquired with a 100 x objective lens, a 100 μm pinhole aperture and a 25% power filter set to allow maximum signal with minimum surface damage by the laser. The samples used for measuring spectra of as-deposited coatings on 314L SS substrates, the high temperature tests were performed with coatings deposited onto 304 SS substrates and subsequently studied using Raman, finally the investigation into the wear track were performed using coatings with HSS as a substrate.

3.2.8. Optical Microscopy

The purpose of an optical microscope is to use visible light and a series of lenses to create a magnified image of an object. The Olympus BX51M is a compound microscope which uses an objective lens close to the object to collect and focus reflected light. The light is focused to a point creating an inverted image of the object; an eye piece lens is then placed behind the image position which acts to create a virtual magnified image of the object [106]. Figure 3.10 is a schematic of the compound microscope lens arrangement illustrating the action of light focusing and image generation.
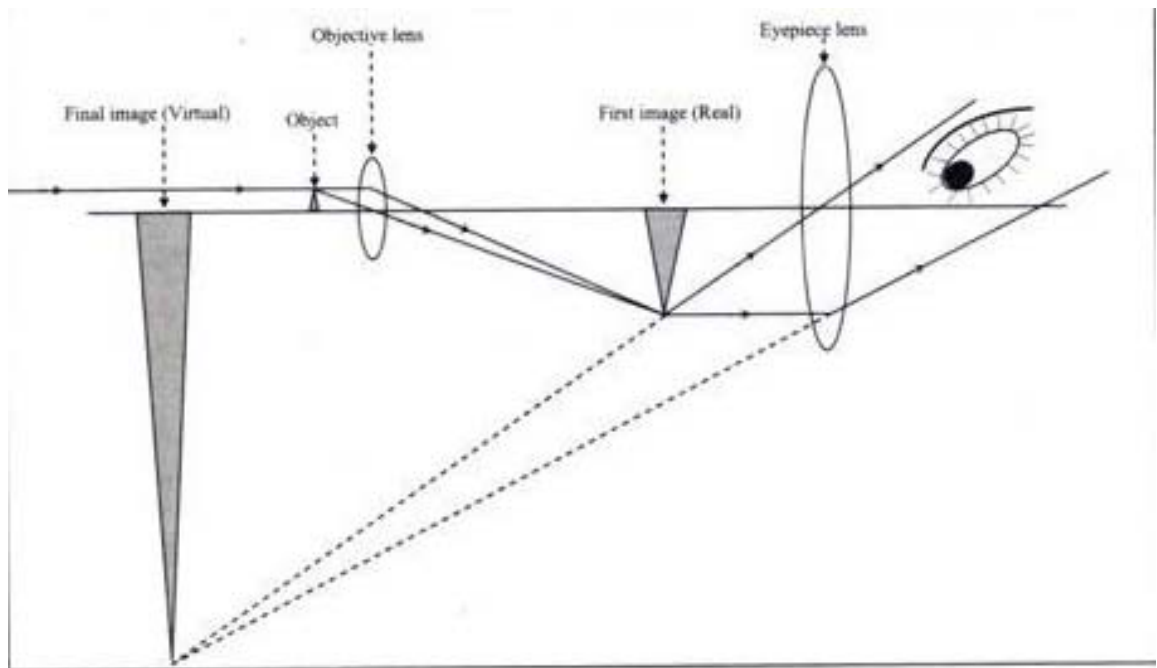
Figure 3.10. Schematic of the lens arrangement and image generation for a compound optical microscope [107].

The optical microscope is used in this study to evaluate the surface damage due to mechanical testing and hence assess the adhesive and wear properties as well as for measuring layer thickness after calowear testing. The instrument has a magnification of up to 100 x and uses CCD camera to generate an image onto the connected PC.

3.2.9.   Knoop Microhardness

Knoop microhardness is a measure of a materials hardness using an elongated pyramidal diamond tipped indenter. The geometry of the tip are displayed in Figure 3.11, the indenter has an aspect ratio of 7:1. It is generally used for brittle materials where only a small indentation into the surface is possible. The diamond tip is pressed into the surface with a known load for a specific dwell time; the indentation is then measured using optical microscopy. The hardness of the material can then be calculated from the length of the indentation using equation 3.7:

$$HK = \frac{P}{L^2 C_p}$$
<div align="right">Equation 3.7.</div>

Where L = Length of indentation, C_p = Correction factor related to shape of indenter = 0.07 and P = Load.
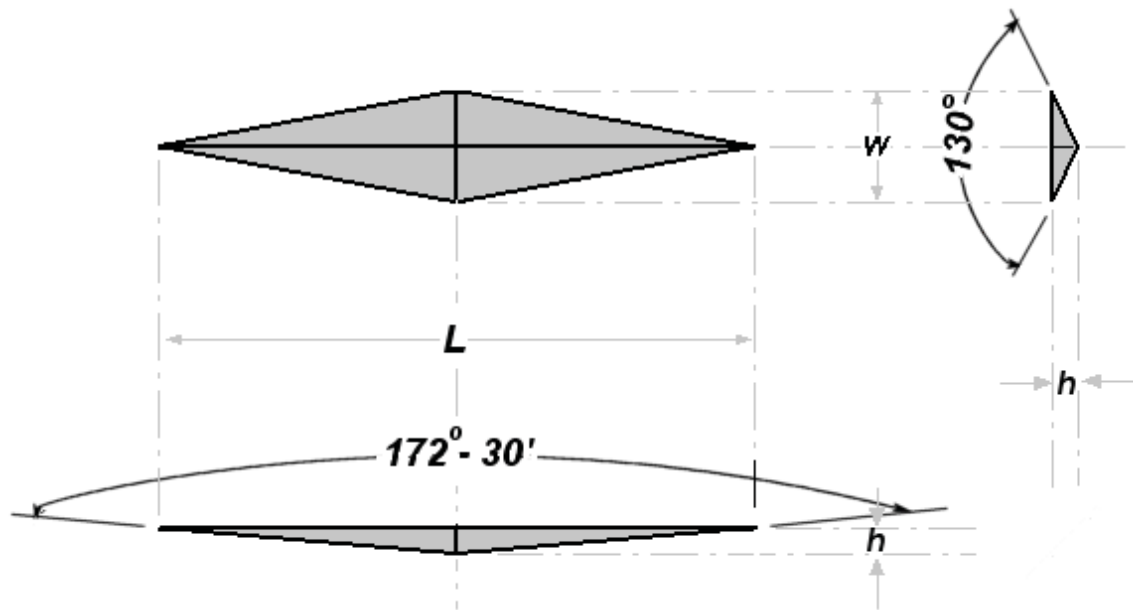
Figure 3.11. A schematic of the diamond tip dimensions taken from top, front and side view [108]

In order to successfully observe the indentation into the surface, the material should have a good surface finish. For this study the Mitutoyo MicrowizHard, HM220 was used with a load of 0.25 N. The instrument was capable of measuring the length of the indentation via the computer software and also manually using the eye piece. To minimise errors in calculating measurements, the hardness of each coating was measured 9 times at points spread across the whole sample, both manually and with the software; the 18 measurements were then averaged.

3.2.10.   Scratch Test

A progressive load scratch test involves moving a stylus across a specimen with a linearly increasing load until failure occurs at a critical load, L_c. The adhesion of the coating can then be analysed using optical microscopy to establish the type of failure and at what load it occurred.

With increased load there is sufficient stress to initiate crack formation at defect sites either within the coating or at the interfaces leading to failure. The failure mechanisms for scratch testing can be separated into two categories: cohesive failure occurs by tensile stress behind the stylus as it propagates across the coating. Tensile stress accumulation occurs within the thickness of the coating and hence leads to cohesive failure. Adhesive failure is due to a compressive stress accumulation in front of the stylus; stress builds up at the interfaces and the coating separates from the substrate either by cracking, and lifting (buckling) or by full separation (spallation) [109].

The various types of cohesive and adhesive failure modes are depicted in tables 3.2 and 3.3, respectively. These mechanisms, along with the international standard ISO 20502:2005 [110] are used to determine the L_c values of the coatings deposited. A CSM, REVETEST was used in this study; the diamond tip was lowered into the coating with a

load of 5 N, the tip then moves along the surface with a progressive load of 10 N per mm to a maximum of 100 N. The samples used were deposited on HSS substrates, three scratches were made on each coating an average L_c calculated.

Table 3.1. Cohesive failure mechanisms during scratch testing

Brittle Tensile Craking	Hertz Cracking	Conformal cracking
Micro-cracks, open in the direction of the scratch; linear and semi-circular formations	Circular micro-crack formed within the scratch	Micro-cracks, open in the opposite direction to the scratch; formed while coating tries to conform to the scratch
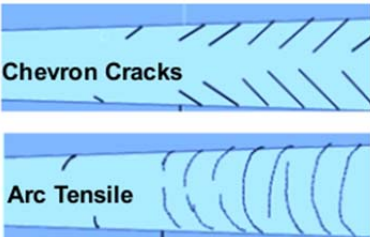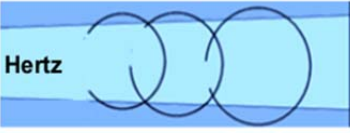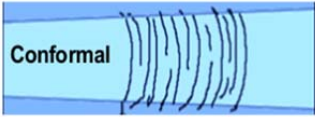
Table 3.2. Adhesive failure mechanisms during scratch testing

Buckling	Wedging	Recovery	Gross Spalation
Irregular wide arced areas missing; occurs ahead of the stylus, open away from the scratch direction	Regular, circular removal extending beyond the edges of the scratch; delaminated region ahead of the stylus	Elastic recovery behind the stylus and plastic deformation in the substrate causes spallation at the edges of the scratch	Large detached areas with substrate exposed.

3.2.11. Rockwell Indentation Test

The adhesion of ceramic coatings can be evaluated using Rockwell indentation testing; a diamond tip is pressed into the coating with a load of 1471.5 N (150 kgf) and the indentation is then viewed using an optical microscope to determine which category the coating can be classed as. An Avery 6402 instrument was used to indent coatings deposited on HSS substrates. The class evaluation of the coatings is performed to the international standard BS ISO 26443:2008; drawing of the 4 classes used for coating evaluation are depicted in table 3.1.

Table 3.3. International classes for evaluating coating adhesion by Rockwell indentation.

Class 0	Class 1	Class 2	Class 3
No Cracking and no adhesive delamination	Cracking without adhesive delamination of the coating	Partial adhesive delamination of the coating	Complete adhesive delamination

Delamination can occur by cohesion or adhesive coating failure; adhesive failure reveals the substrate underneath, clearly distinguishable from the coating. Whereas cohesive delamination occurs within the coating and the substrate is still covered by the remaining coating on top of it [111].

3.2.12.   Calowear Test

A steel sphere is rotated onto the surface of the sample with a 1 μm diamond paste acting as the grinding medium; erasing material from the surface. Ball-cratering creates a scar on the surface that can be used to determine coating thicknesses. After the crater has formed the sample is cleaned and viewed using an optical microscope. The coating layers appear as rings on the surface, illustrated in Figure 3.12; by measuring parameters X and Y, with a known sphere diameter Ø , the coating thickness, D, can be calculated [112].

$$D = \frac{X \times Y}{\phi \, ball}$$
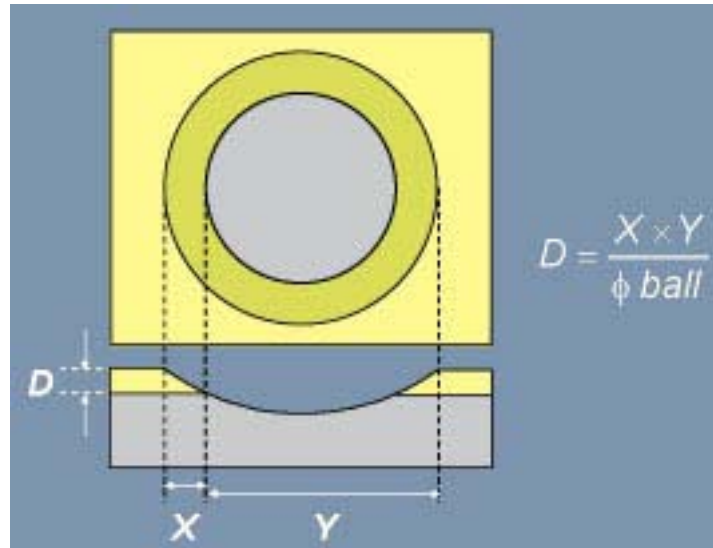
Figure 3.12. Schematic of the crater created during calowear testing and the relationship used to calculate thicknesses [112].

A CSEM Calowear testing instrument was used during this study to calculate the various layer thicknesses for each coating deposited. The coatings tested were deposited on the HSS substrates.

3.2.13.   High Temperature Tribometer

Pin-on-disc testing is method of measuring the tribological properties of a coating as a preliminary, lab-based test, to cutting applications; a disc sample is secured into a holder and an Al_2O_3 ball is held on the surface under a normal load of 5 N, the disc is then rotated with a linear speed of 0.1 ms^{-1} creating a circular scar on the surface known as the wear track. The CSM (Anton Paar) High Temperature Tribometer (Figure 3.13) is fitted with double sensors on the arm holding the ball in place which measures the tangential force and hence the coefficient of friction. The instrument is capable of performing tests at room temperature and also at elevated temperatures of up to 800 ˚C to simulate cutting conditions. The automated arm can be programmed to descend onto the sample and begin taking measurements only once the desired temperature has been reached; it is also equipped with a closed loop water cooling system that allows for temperature control [113].
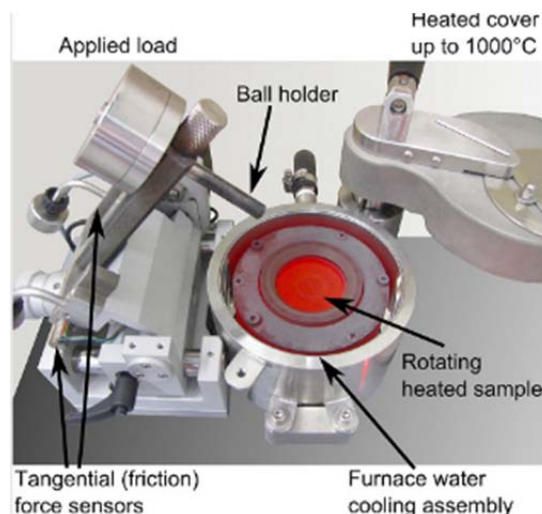
Figure 3.13. High temperature pin on disc instrument for tribological testing by CSM (Anton Paar) [113]

The tests are run for all coatings at room temperature for 10,000 laps (unless stated otherwise); the radius at which the ball is in contact with the coating varies between tests and therefore the sliding distance will be different for each coating however as each position within the wear track has experience the contact 10,000 times this will not affect the wear rate. In order to calculate the wear rate the volume of coating removed from the wear track was measure using a profilometer; the stylus was dragged along the width of the wear track and the software allowed area removed to be measured. Multiplying the area by $2\pi r$ gave the volume removed within the wear track. This value was then inputted into equation 3.8 to give the wear rate:

$$k = \frac{V}{P.d} \hspace{4cm} \text{Equation 3.8}$$

Where k = wear rate coefficient, V = volume of material removed, P = Normal load and d = sliding distance.

There are three main wear mechanisms to consider; adhesive, abrasive and oxidative, all of which may be occurring simultaneously. Adhesive wear involves contact between asperities on both the counterpart (Al_2O_3 ball) and on the surface of the coating. Even the most meticulously polished sample has a slight roughness and where these peaks in material contact the counterpart, plastic deformation and intermetallic adhesion occurs. A cold welded micro-junction is formed followed by tangential shearing resulting in coating transfer from the tops of the asperity onto the counterpart. The shear force required is high, resulting in flash temperature at the micro-junction and an increase in the coefficient of friction. The result of this is that the wear track becomes smoothed in the direction of sliding and the contact more wear is now between coating material on the surface and transferred coating material on the counterpart (Figure 3.14).
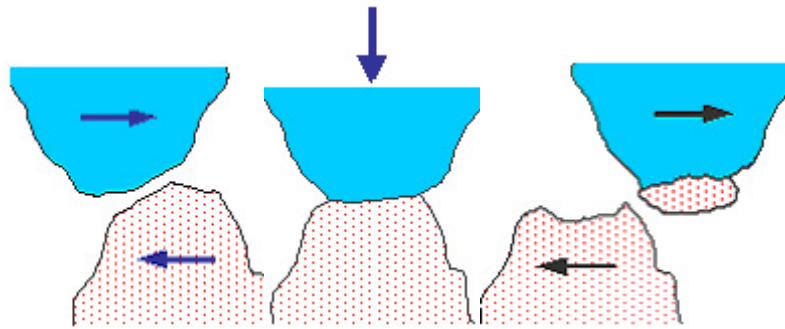
Figure 3.14. Illustration of the abrasive wear mechanism [114]

Abrasive wear can occur by two mechanisms. Firstly, what's known as 'three-body' wear which involves a hard particle becoming trapped between the coating and the counterpart resulting in material removal by the debris (Figure 3.15 a)). The second is 'two-body' abrasion which occurs when asperities of the counterpart plough through the surface of the coating; the counterpart effectively acts to grind through the surface (Figure 3.15 b)).
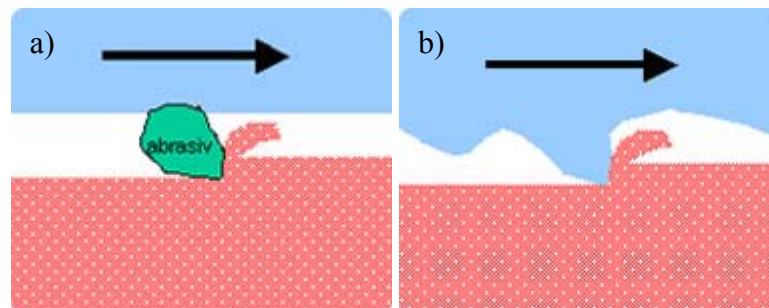
Figure 3.14. Illustration of the abrasive wear mechanism [114].

Oxidation wear occurs due to the cyclic formation and removal of an oxide layer. Many materials form a passivating oxide layer on their surface when exposed to the environment, during wear this layer is removed exposing the material underneath which again becomes oxidised, reforming the layer. However, as discussed in adhesive wear, the process may generate flash temperatures which cause much more severe oxidation of the surface and potentially cause further oxidation of the bulk material (Figure 3.16).

110
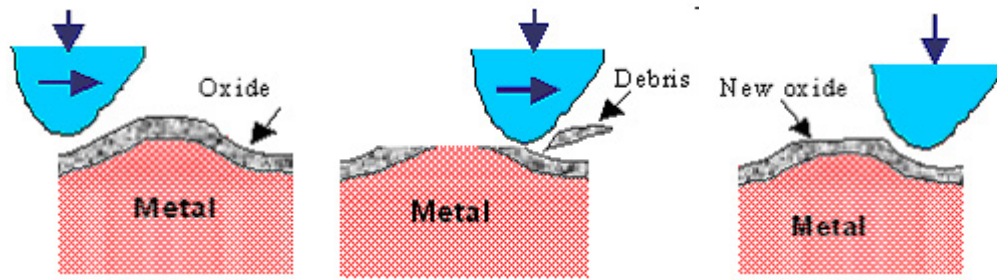
Figure 3.16. Illustration of the oxidation wear mechanism [114].

3.2.14.   **Furnace**

Coatings for cutting test applications undergo high temperatures during machining, to simulate such temperatures an atmospheric furnace by Lenton Thermal Designs LTD heated the samples to elevated temperatures in an air atmosphere. The samples tested were deposited on rolled 304 SS substrates and placed in the furnace at room temperature. The temperatures investigated were 600 ˚C, 800 ˚C, 1000 ˚C; once the samples had been placed inside the furnace the temperature was increased to the desired temperature (e.g. 600 ˚C), kept at that temperature for an hour and then allowed to cool with the door remaining closed. New as-deposited samples were used for each coating at each temperature setting.

3.2.15.   Thermogravimetric Analysis

Thermogravimetric analysis (TGA) is a technique whereby the mass of a sample is monitored as a function of temperature. A sample of 316L rolled stainless steel is suspended inside a furnace via a wire; supported by a precision balance [115]. The furnace can be used with either an inert (Ar) or air atmosphere. During heating a sample may begin to decompose, releasing material and causing it's mass to decrease with increased temperature. With an air atmosphere the coating may begin to oxidise, increasing the samples' mass, allowing for the point of the onset of rapid oxidation to be determined by extrapolating a tangential line from the largest gradient down to the x-axis as illustrated in Figure 3.17.
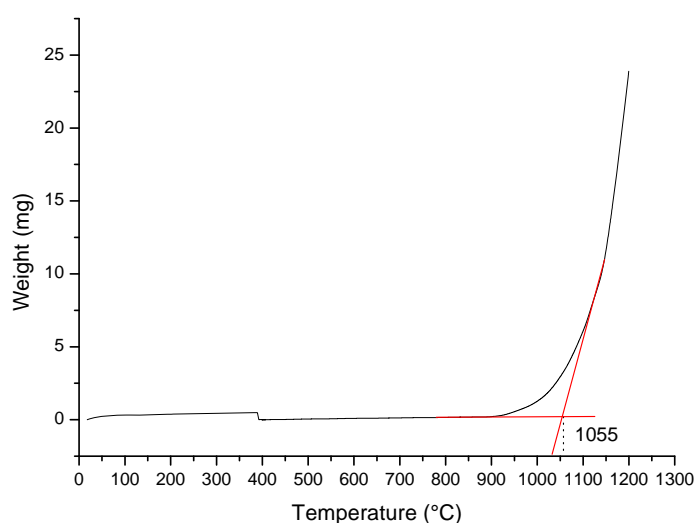
Figure 3.17. Example of determining the point of rapid oxidation from a TGA curve with weight gain plotted against temperature.

In this study a Setaram Setsys evolution instrument was used; the temperature was ramped from 400 ˚C to 1000 ˚C at 1˚C min^{-1} in an air atmosphere and the net weight gain of the sample was measured.

3.2.16.   Cutting Tests

Cutting tests were performed using a Mazak FJV 25 CNC machine; the specifications are as follows; maximum spindle speed = 25,000 rpm, maximum feed rate x, y and z axes = 30 m/min, 21 station tool carousel, 25 kW spindle motor, HSK63 A tool holding, shrink fit tooling capability available in 6, 8, 12, 20 and 25 mm diameters (up to 25,000 rpm) and collet tool holding in most standard diameters (up to 7,000 rpm). The WC-Co inserts, product number: 627793, were coated for cutting tests in P20 tool steel. The inserts were fixed to a face-milling attachment capable of holding seven inserts at once, to test the effectiveness of each individual insert however, only one was fixed at a time. The cutting parameters were provided by Sandvik who suggested a roll entry with a cutting speed, V_c = 100 m/min, an axial depth of cut, A_p = 0.1 mm, a radial depth of cut, A_e = 56 mm and a cutting feed rate V_f = 0.1 mm/rev. The tests were performed dry, without lubrication.

3.2.17.   Coating Series Parameters and Compositions

During this work, the properties of a series of coatings will be presented and discussed. The justifications for any changes in variables in deposition parameters will be given in the chapter related to that coating. For reference, the process parameters for each coating are tabulated in this section in table 3.4 and the chemical compositions measured via EDX are given in table 3.5.

Table 3.4. Process parameters for coating 1 to 12

Coating	Chamber Pressure (mbar)			Power on the Cr-based targets (kW)				Substrate bias (V)		Control Type
	2.7	2.8	3	8	7	6	4	-40	-60	
1			✓				✓	✓		Chamber Pressure
2			✓				✓		✓	Chamber Pressure
3	✓			✓				✓		Speedflow 33% N
4	✓					✓		✓		Speedflow 27% N
5		✓		✓				✓		Speedflow 23% N
6		✓			✓			✓		Speedflow 21% N
7		✓		✓				✓		Speedflow 18% N
8		✓		✓				✓		Speedflow 16% N
9		✓					✓	✓		Speedflow 20% N
10		✓					✓	✓		Speedflow 20% N
11			✓				✓	✓		Chamber Pressure
12			✓				✓		✓	Chamber Pressure

Coating	Relative At. %			
	N	Cr	Al	Si
1	55.5	31.3	12.0	1.3
2	55.5	31.3	12.0	1.3
3	17.5	35.6	43.4	3.5
4	22.8	33.2	40.2	3.9
5	44.2	28.7	25.4	1.7
6	37.4	29.6	30.0	3.0
7	47.4	28.6	21.9	2.0
8	39.8	31.5	26.6	2.0
9	47.1	24.7	25.8	2.3
10	54.3	18.8	24.3	2.6
11	56.8	19.3	21.8	2.1
12	62.0	16.1	20.0	1.9

4. Chromium Plasma Pre-treatment of Tungsten Carbide and Steels by HIPIMS

4.1.   Motivation

HIPIMS generates highly-ionised metal-rich plasma. By applying a large bias to the substrate holder carousel these ions can be accelerated. The surface bombardment removes native oxides and contaminants providing a clean surface for deposition. Implantation of metal ions into the surface creates a stress gradient between the unstressed substrate and the highly stressed multilayer coating, helping to improve adhesion between the substrate and coating base layer.

The removal of surface material via etching increases the roughness and provides binding sites for coating particles. Plasma sheath narrowing at edges increases bombardment and thus increases material removal rate. An optimum point must be established between successful cleaning and minimal material removal, to avoid blunting.

During etching the charge on the cathode is ramped from nominal 0 (min) to 16 (max) and then held at that point. In this study the plasma is characterised at each point during the ramping process to study the metal and gas ion evolution. Secondly the effect of etching on WC and Steels is investigated to analyse the effect ramping and holding times have on the etching rate on the surface and near to the edge of the substrate.

4.2.　　　　Experimental details

The chamber of the Hauzer 1000-4 PVD system was loaded with a CrAlY target without substrates. Figure 4.1 depicts the positions of the diagnostic tools used; a fibre optic was placed inside the chamber to measure OES, insulated from the chamber to prevent charging. The aperture was orientated to face down so that it detected the light from plasma at the substrate area.   In addition a piezo-electric quartz crystal microbalance (QCM) was inserted close to the target to measure the deposition rate. Finally a flat probe was inserted into the chamber facing the target connected to the carousel to measure ion flux at the substrate.
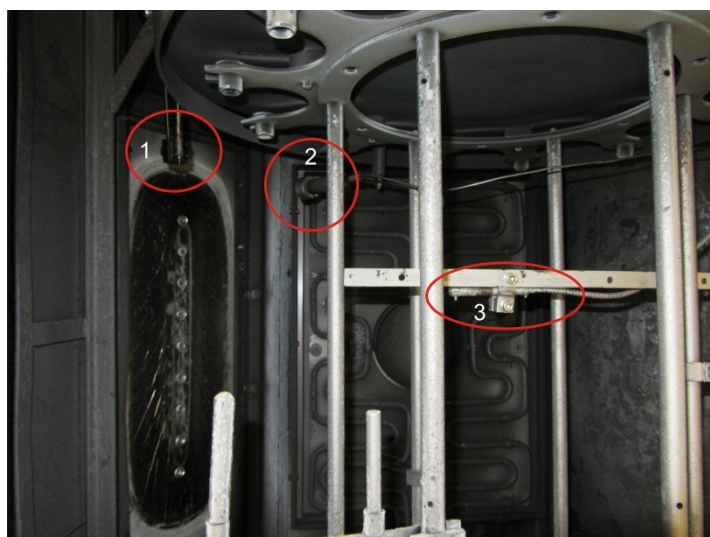
Figure 4.1. The set-up of the plasma diagnostic devices inside the chamber. 1, 2 and 3 indicate the positions of the QCM, the flat probe and the optical fibre for the OES.

The QCM settings were density = 4.50 gcm^{-3}, tooling = 100, z factor = 1 and time = 10 minutes, after 10 minutes the deposition thickness was recorded. The flat probe was biased to -100 V and the OES settings were; Exposure = 2 s, Accumulations = 5, CCD range 200 nm-850 nm and 400 nm-850 nm (filter off and on respectively) and the front entrance slit = 0.08 mm

The Hauzer chamber had a base pressure of 9.1×10^{-6} mbar, the voltages for target cleaning steps 1 and 2 and etching step were 800 V, 1300 V and 1200 V

117

respectively with the Temperature set to 100 ˚C to ensure the delicate diagnostic equipment did not become damaged. Cathode voltage was kept constant at 1050 V, the charge of the cathode was increased from 0 to 16 in 12 steps (0, 1, 2, 3, 4, 5, 6, 8, 10, 12, 14, 16, the peak current I_d increased from 992 A to 1667 A.

Known emission patterns for ArI, CrI and CrII [116] were used to locate spectral lines from the OES data; using a photomultiplier tube and an oscilloscope the species intensity signals were recorded for analysis.

To study surface material removal rate the process conditions above were maintained and the cathode charge set to 16. The test variables were the ramping and holding times as described in table 4.1.

Table 4.1. The Ramping and Hold time variables used for each run.

Run	Ramp Time (min)	Hold Time (min)
1	20	20
2	10	20
3	5	10
4	10	10

The chamber was loaded with stainless steel and high speed M2 steel 30 mm disc and also Tungsten Carbide (WC) cutting inserts both polished and unpolished. All the samples were masked with TiO_2 to provide areas that remained untreated for comparison with the etched areas and also to create a step height for measurement of the amount of material etched away. The polished WC insets were also masked in a way to study geometrical edge effect in plasma, a diagonal mask was placed from the cutting

edge to the centre of the insert to determine material removed as a function of distance from the cutting edge as shown in Figure 4.2, each run was performed at 400 ˚C.
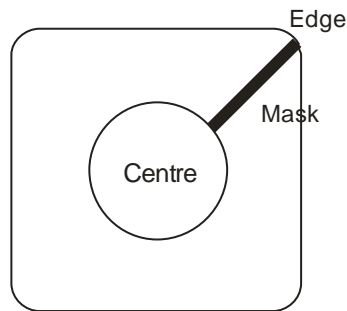
Figure 4.2. A schematic of the masked area of the polished WC inserts used to create a step for material removal analysis by profilometry.

4.3. Characterising Cr Plasma

4.3.1. Flat Probe

The flat probe measured the flux of ions within the plasma close to the target. Increasing the charge increases the intensity of the Ion Flux but does not alter the mechanisms involved as the shape of the curve for each charge is the same, illustrated by Figure 4.3. However there is a time shift to the right; as the charge is increased it takes longer to reach the peak value. The data for charges 0 and 3 was corrupt and so has not been included in the graph, the peak ion flux increased from 0.077 A at 77 µs for charge 1 up to 0.127 A at 79.2 µs for charge 16. It also indicates there is a secondary plasma release from around the target by the increase in ion flux intensity seen at the end of the pulse after the Voltage has been turned off. The ions located close to the target are no longer bound by the magnetic field lines and migrate towards the negatively bias substrate area.

119
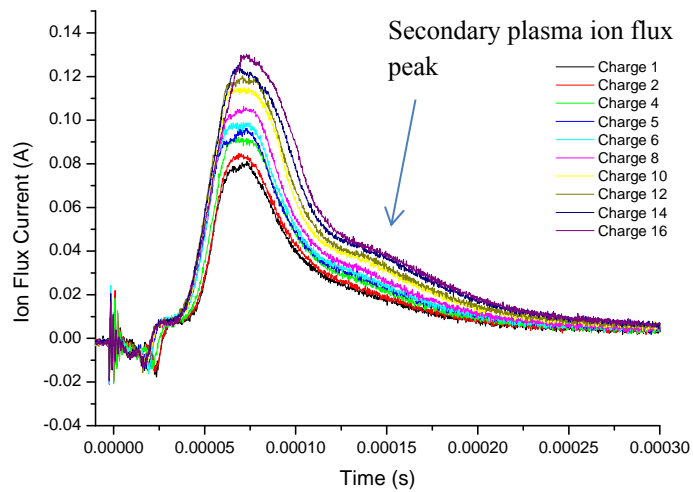
Figure 4.3. The trend of Ion flux during the pulse time for the varied charges.
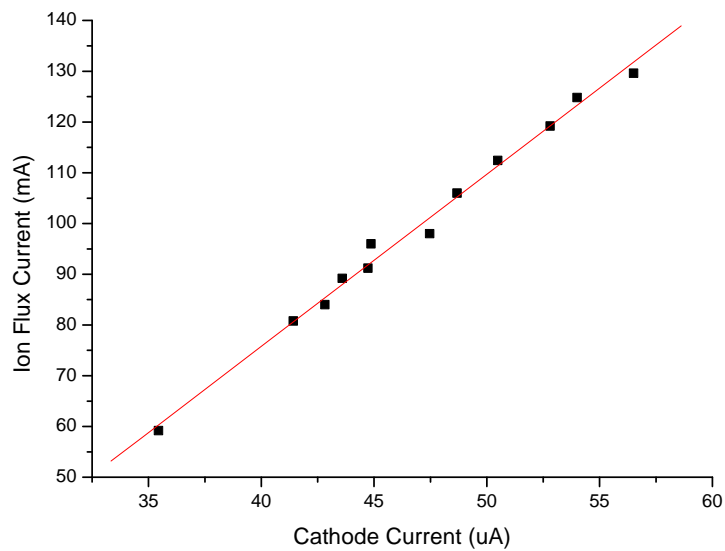
Figure 4.4. The relationship between the ion flux current measured on the flat probe and the cathode current.

The cathode current is directly proportional to the charge variable being tested. By plotting the Ion flux current against the values measured for the cathode current (Figure 4.4) it can be seen that increasing the charge increases the flux of ions detected on the flat probe and that there is a linear relationship.

4.3.2. Quartz-Crystal Microbalance (QCM)

The weight gain on the QCM within a given amount of time was measured to calculate the deposition rate as charge was increased. Increasing the charge increased the width of the cathode current during a single pulse, it can be seen from Figure 4.5 that the increase in cathode current width increases the deposition rate onto the QCM with a linear trend. This indicates that increasing the charge increases the number of atoms in the plasma and hence the rate of deposition. We also observe the same trend in increased deposition rate as a function of ion flux current as shown in Figure 4.6.
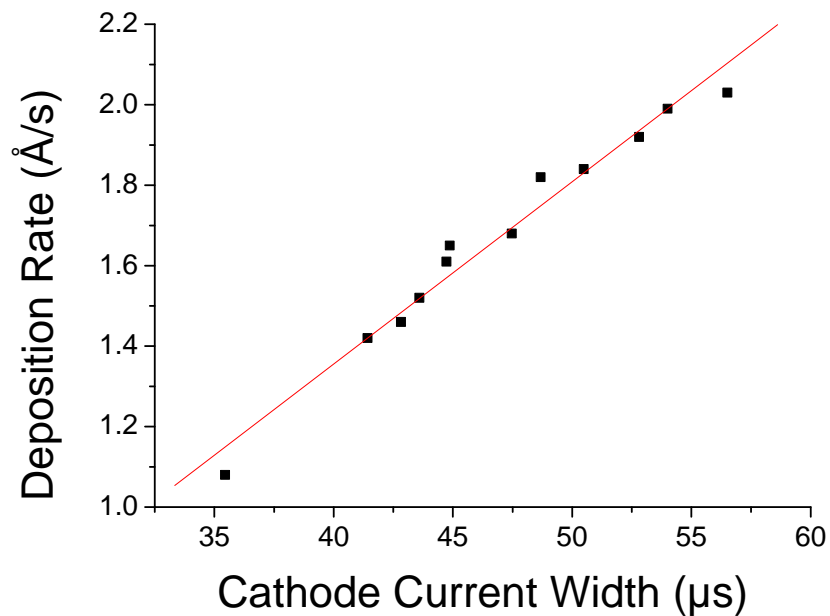
Figure 4.5. Deposition rate as a function of cathode current width within a pulse.
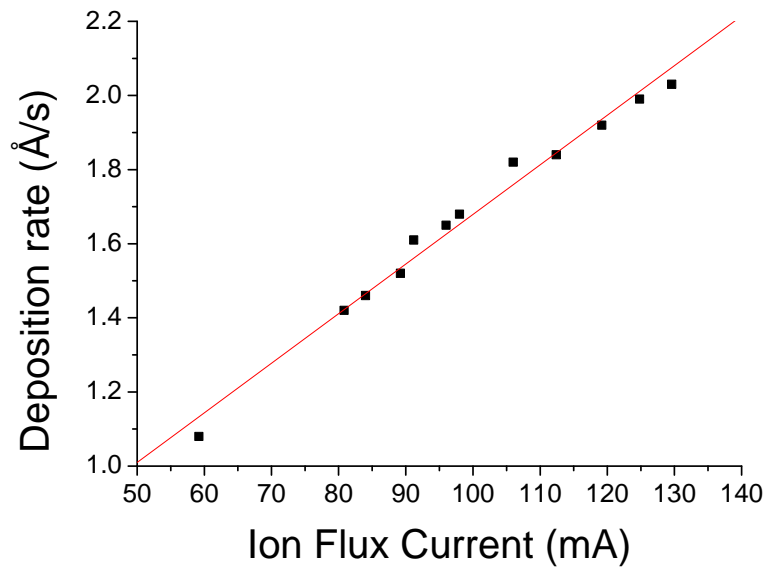
Figure 4.6. Deposition rate measured on the QCM as a function of increased ion flux.

4.3.3. Optical Emission Spectroscopy (OES)

OES was employed to study the intensities of the different ionic species of the plasma. Using a Chromium target in an Argon sputtering medium the OES spectra detected was used to identify the ion peaks for ArI, CrI and CrII, those lines were identified as having wavelengths 748 nm, 421.8 nm and 333.25 nm respectively. Taking into account the offset of the device these lines correspond to the actual emission peaks and are given in table 4.2. The peaks for each species are shown in Figure 4.7.

a)

b)
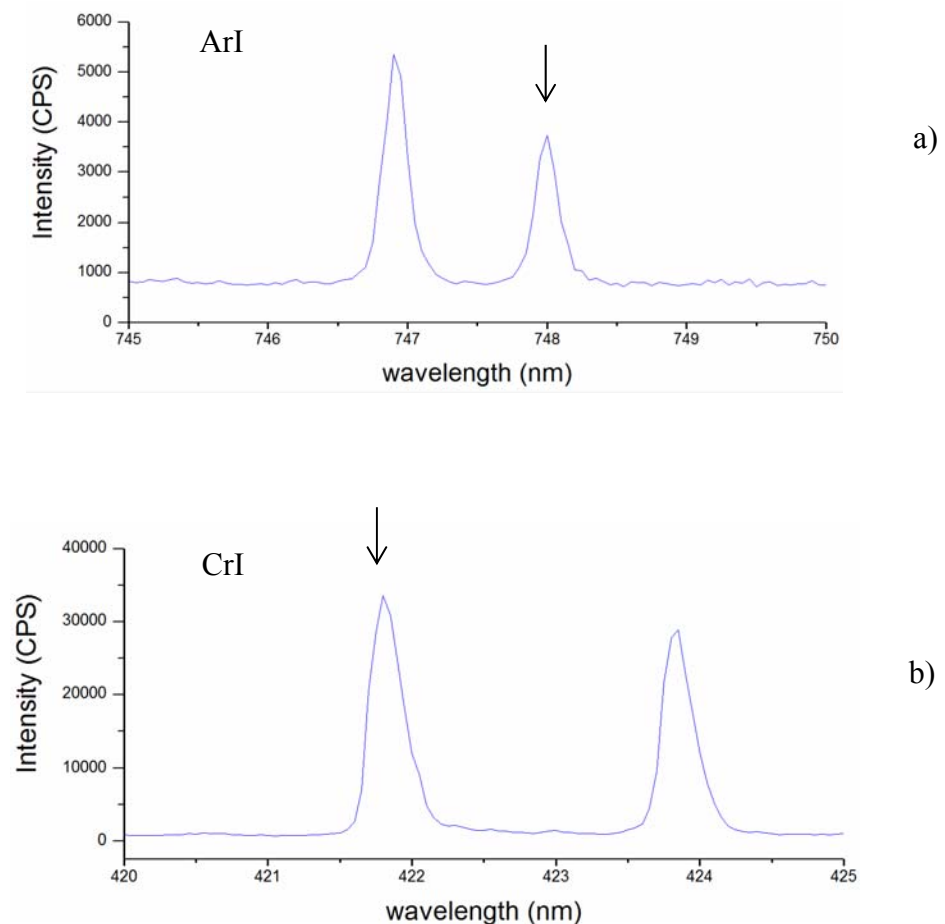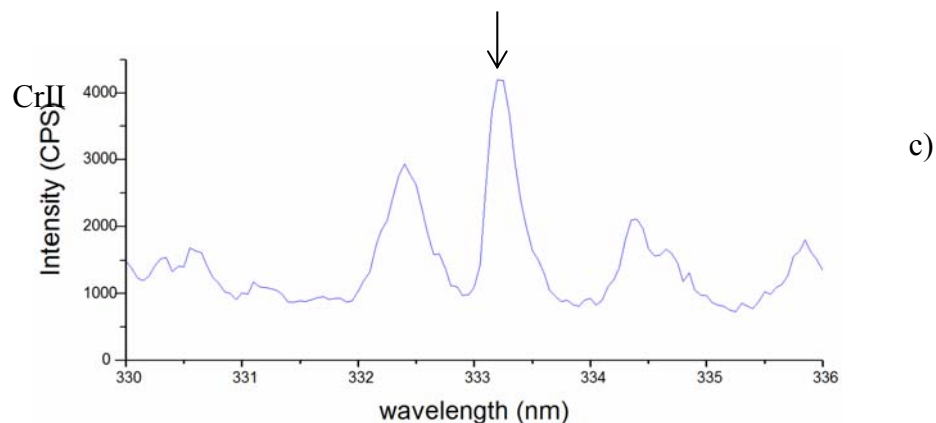
Figure 4.7. The OES spectra for Cr and Ar plasma. Peaks for Ar atom, Cr atom and Cr1+ ion are indicated in a) b) and c) respectively and the specific peak arrowed.

Table 4.2. Table describing the measured peak values and actual peak values read from the NIST database highlighting an offset of approximately 3 nm for our measurement s [117].

Species	Measured Peak Wavelength (nm)	Actual Peak Wavelength (nm)	Lower Energy Level (cm^{-1})	Upper Energy Level (cm^{-1})
ArI	748	751	93751	107054
CrI	421.8	425	0	23499
CrII	333.25	336.8	not in database	not in database

The selection of these peaks is important for studying the evolution of the different species during a process. The OES has a Photomultipier Tube (PMT) attachment which was selected to look specifically at the 3 lines of ArI, CrI and CrII. The OES was connected to an Oscilloscope and the signals from each peak emission set to a different output as well as having an output of the cathode current. The charge

value was increased from 0 to 16 in 12 steps and at each charge the current amplitude during a pulse was recorded.
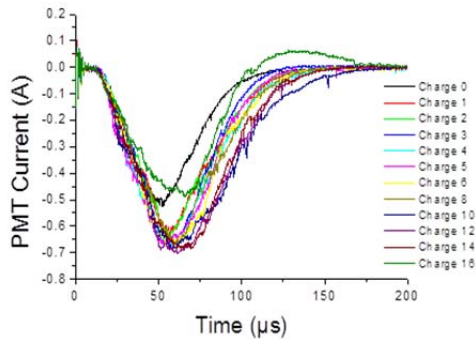
a) Argon I   b) Chromium I
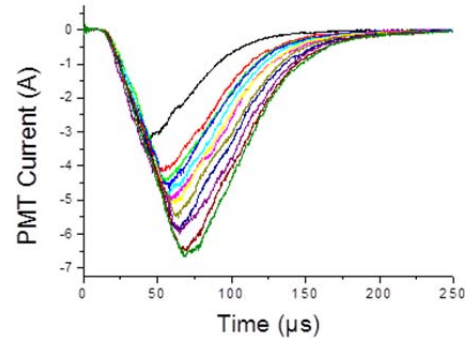
c) Chromium II
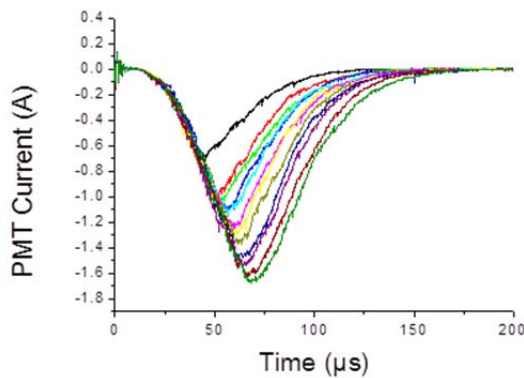
Figure 4.8. The current reading on the oscilloscope from the PMT as a function of time during 1 pulse for the selected wavelengths of a) Argon neutral, b) Chromium neutral and c) Chromium 1+ ion, for each charge.

It can be seen from Figure 4.8 that increasing the charge increased the peak current measured for all species, indicating an increase in the intensity of light at those specific wavelengths and suggesting denser plasma. Similar to Figure 4.3, the shape of the graphs is maintained with increased charge however the peak current increases, the rate of increase is the same for each charge and thus this forces the peak to occur at a later time. For ArI the peak increases from -0.526 A at 52 μs to -0.691 A at 61 μs, for CrI -3.208 A at 44 μs to -6.666 A at 67.6 μs and finally CrII increases from -0.719 A at 44.2 μs to -1.679 A at 68.2 μs. The CrI current peak is nearly an order of magnitude

larger at charge 0 than ArI and CrII suggesting that Cr atoms are very easily sputtered into the plasma. The rate of increase in peak value with increased charge for ArI is slow in comparison to Cr species suggesting that most of the Ar atoms are in an excited state at low charges. Finally the steady increase in peak value for CrII suggests that ramping to high charges is effective in increasing the amount of ions present in the plasma.

a) Charge 0   b) Charge 14
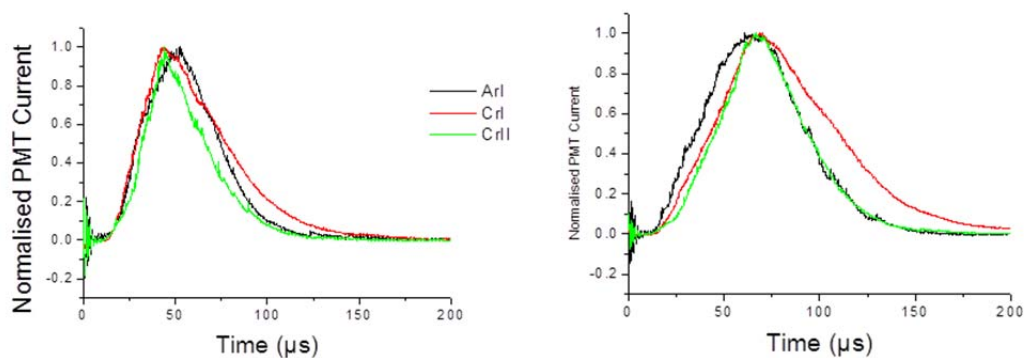
Figure 4.9. The PMT current signals normalised for each species and plotted as a function of time.

In order to observe a direct comparison between species at the same charge, the PMT currents were normalised and plotted at the lowest and highest charges (14 max due to an anomaly in the data for Ar at Charge 16), the results of which can be seen in Figure 4.9. At Charge 0 all 3 species appear at a similar time, increasing to their peak value at a similar rate. However, at Charge 14 there is a time delay for the production of Cr species. The delay is attributed to the increased gas heating at higher charges causing gas rarefaction; the reduced gas density at the target reduces the sputter yield and thus during one pulse it takes longer for Cr species to be ejected into the plasma and collide with electrons to emit light. In the early stages of the pulse there is a reduced metal content at high charges than at low, however, it was observed from quantification of OES emission that increasing the charge increases the metal content of the plasma.

Plotting the time integral of the PMT current signal against the cathode current time integral on logarithmic scales gave positive linear relationships for all species studied as shown in Figure 4.10.
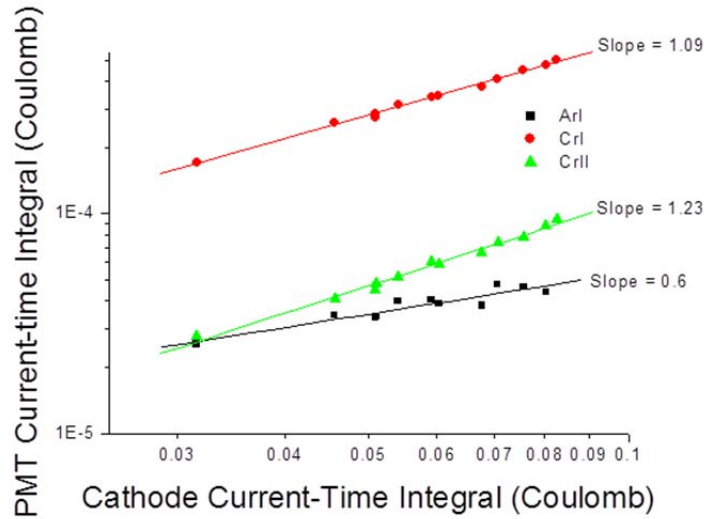
Figure 4.10. The relationship between recorded PMT current-time integral and the cathode current-time integral for the Ar neutral (ArI), Cr neutral (CrI) and Cr ion (CrII) emission lines.

In 1989, Rossnagel and Saenger devised and confirmed a model based on the processes involved in the production of optical emission during a metal plasma processes with Ar gas [118]. The emission intensity, $I_{emission}$, is related to the cathode current density, I_d, by an exponent constant, K, that is related to the number of processes involved, this relationship is given by equation (4.1).

$$I_{emission} = I_d^K \hspace{3cm} \text{Equation 4.1}$$

By plotting $I_{emission}$ vs. I_d on a logarithmic scale as shown in Figure 4.10 the K value becomes the slope of the lines. The model showed that the integer value K indicated the number of process, for example, Ar gas is present in the system before the cathodes are ignited and so to excite the Ar to produce the ArI line there is only 1 collisional energy transfer from 1 electron and therefore K = 1. The metal neutral line arises in 2 steps; first the metal must be sputtered and 2nd collide with an electron to

excite the atom, K = 2. To produce an ion the metal must be sputtered, excited and then ionised giving K = 3. These processes are described below:

-        K = 1, 1 Step. (gas)

$Ar + e^- \rightarrow Ar^* + e^-$
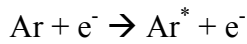
-        K = 2, 2 Steps (excited metal)

$Ar + Target \rightarrow M \qquad\qquad \rightarrow M + e^- \rightarrow M^* + e^-$

-        K = 3, 3 Steps (metal ion)

$Ar + Target \rightarrow M \qquad\qquad \rightarrow M + e^- \rightarrow M^* + e^- \rightarrow \qquad M^* + e^- \rightarrow M^+ + 2e^-$
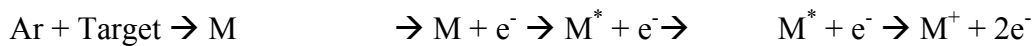
Whilst validating their model it was observed Ar produced a value of K = 0.5 rather than K=1; a result of Ar gas rarefaction. This model and method was used to produce Figure 4.10, it can be seen that the K value for Ar is also less than 1, in agreement with what Rossnagel and Saenger saw suggesting that gas rarefaction also occurs in our system, supporting the gas rarefaction explanation for the Cr species delay in Figure 4.9. The K values for Cr are quite interesting, they are also less than the predicted K = 2 and K = 3 values that would be expected. Following the same reasoning as for Ar there must be some Metal rarefaction occurring within the plasma to reduce these values to approximately K = 1 and K = 1.5 for CrI and CrII respectively. Notice however that K = 1.23 for CrII, the non-integer (or half an integer for rarefaction) suggests there is a combination of processes occurring to produce the ion emission line; both 2 and 3 step processes. This means that there is enough energy in the system to also create ions in a single step after sputtering, as depicted below:

$Ar + Target \rightarrow Cr \qquad\qquad Cr + e^- \rightarrow Cr^+ + 2e^-$
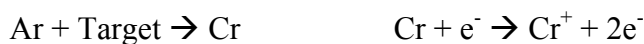
The emission intensities require quantification in order to estimate the ion content of the Cr plasma. The emission intensity data for Ar neutral (ArI), Cr neutral (CrI) and Cr ion (CrII) is used to estimate the ion content; the number of Cr ions, n_{Cr^+}, in the plasma is proportional to the number of Cr atoms, n_{Cr^0}, and the emission

intensity of the Cr neutral line, I_{CrI}, is also proportional to the number of Cr atoms, n_{Cr^0}:

$$n_{Cr^+} \propto n_{Cr^0} \propto I_{CrI}$$ Equation 4.2

and therefore,

$$n_{Cr^+} \propto I_{CrI}$$ Equation 4.3

Using this knowledge of proportionality between emission spectra and number of ions we can build a picture of the plasma content.

Mass spectrometry of Cr plasma in Ar using a HIPIMS power supply at maximum charge (charge = 16) has previously been published by Hovsepian et al. and is shown in Figure 4.11 [53]. As stated above the number of ions is proportional to the atomic emission intensity, so we can assign the ArI emission intensity at charge 16 to the % given in Figure 4.11 for Ar^{1+} (23%), similarly the CrI data at charge 16 can be assigned the % for Cr^{1+} (60.5%), furthermore, the CrII data can be assigned the % for Cr^{2+} (14%).
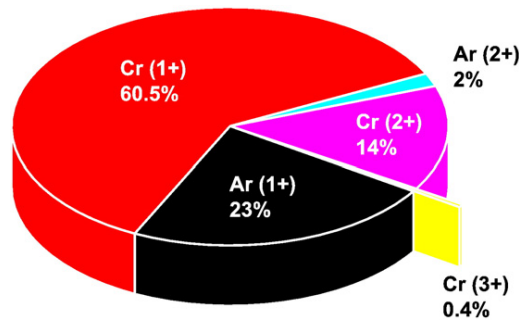
Figure 4.11. A graph of the ion species and relative composition within a Cr and Ar plasma created by a HIPIMS power supply at maximum cathode charge (charge 16)[53]*.*

By extrapolating the percentages down through the intensities measured for charge 0 to 14 the evolution of the plasma ion content with increase cathode charge can be determined. The results are given in Figure 4.12, the metal ion content % of the

129

plasma is seen to increase with increased cathode charge, corresponding to a decrease in

the Ar ion content. This is highlighted by the blue trend which indicates an increase in

the Metal ion:Gas ion ratio.
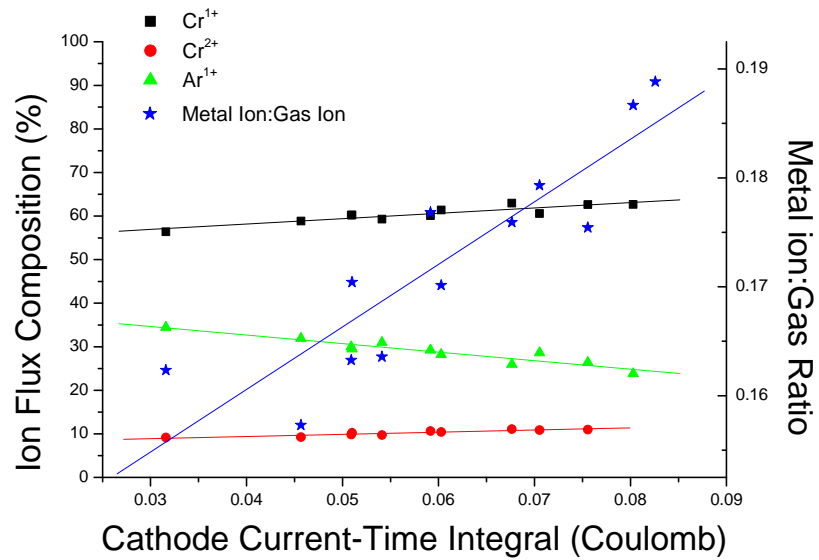
Figure 4.12. The ion flux percentage composition as a function of cathode current-time integral for Ar^{1+}, Cr^{1+} and Cr^{2+} ions. Also plotted on the right hand axis is the metal ion:gas ion ratio as a function of cathode current-time integral - the values pf Cr^{-+} and Cr^{2+} are combined to give a total metal ion content.

4.3.4. Implantation Depth Simulation

The results indicate that through HIPIMS a metal-ion rich plasma is generated. Ions are accelerated from the plasma towards a biased substrate due to the potential difference across the sheath. These ions therefore have high energies and not only clean a substrate but would also become implanted into the surface aiding adhesion. The depth of implantation for each species can be estimated using the data collected and a Dynamic TRIM simulation.

The values obtained for the probe-current integral of each species allowed the calculation of the number of ions in each pulse, this was then multiplied by the total number of pulses during the process and values used to determine the Input dose for Dynamic TRIM simulations. The simulation only allows for a maximum of 4 elements to be studied, in light of this, only W and C of the WC-Co matrix are considered in a 1:1 ratio, the simulation estimates the composition of the substrate surface as a function of depth.
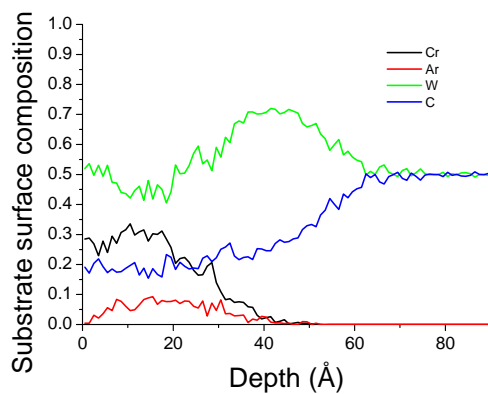
a) Charge 1   b) Charge 16
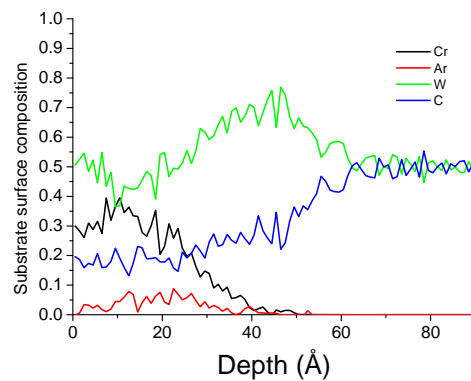
Figure 4.13. The depth profiles produced via Dynamic TRIM simulation for charge 1 and charge 16, a) and b) respectively.

131

The depth profile (figure 4.13) indicates that C is preferentially removed from the surface over W and it shows that we have implantation of Cr and Ar to a depth of 5 nm. There is an observed increase in W above its original 50% composition, this is due to the removal of C therefore increasing the relative composition of W it does not mean that we have gained more W. Comparing the charges there is an increase in the composition of Cr and a slight decrease in Ar which concurs with previous results suggesting that the plasma is more metal ion rich at higher charges.

4.4. Etching Effects

The Second part of this study involved investigating how the ramping and holding times of the cathode charge affected the amount of material removed from the surface of the samples.

4.4.1. Profilometry

The step heights for the varied ramping and holding conditions tested were measured using a profilometer and plotted on a XYZ graph to observe which variable had a greater effect on the material removed. Using the data measured the trends were extrapolated to determine an estimate of the ramping and holding times not tested to complete the matrix, table 4.3 shows the measure and estimated variables.

Table 4.3. Ramp and Hold times for cathode charge during etching. The red x's are measured and the black x's are estimated from the measured data to complete the matrix.

	Ramp 5 mins	Ramp 10 mins	Ramp 20 mins
Hold 5 mins	x	x	x
Hold 10 mins	x	x	x
Hold 20 mins	x	x	x

The results of the profilometry measurements are given in Figure 4.14. It can be seen that for all sample types both the ramping and holding period of etching causes material to be removed from the surface, increasing either causes an increase in step height, however it is clear that the holding time has a far greater influence by the steeper trends.
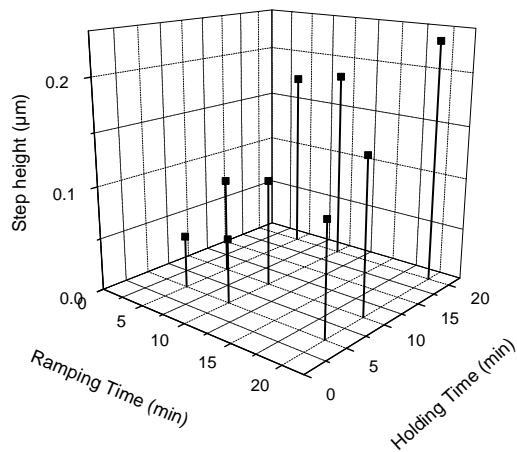
a) HSS   b)SS
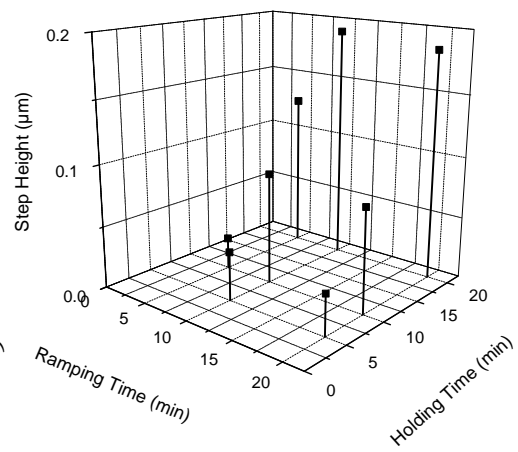
c) WC insert
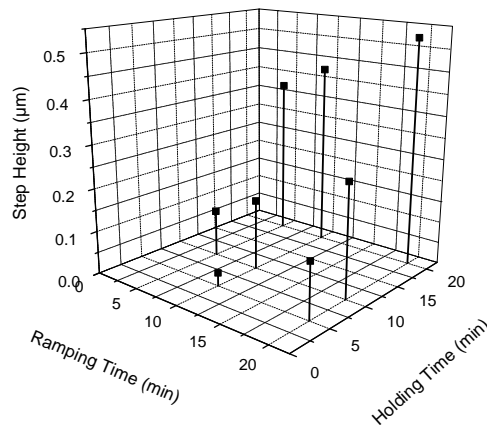
Figure 4.14. Graphs a) b) and c) plot the step height after etching as a function of holding and ramping times for HSS, SS and WC insert respectively.

In addition to this, a polished WC insert was masked from a corner to the entre to study how the geometry of a sample effect the amount of removed material.
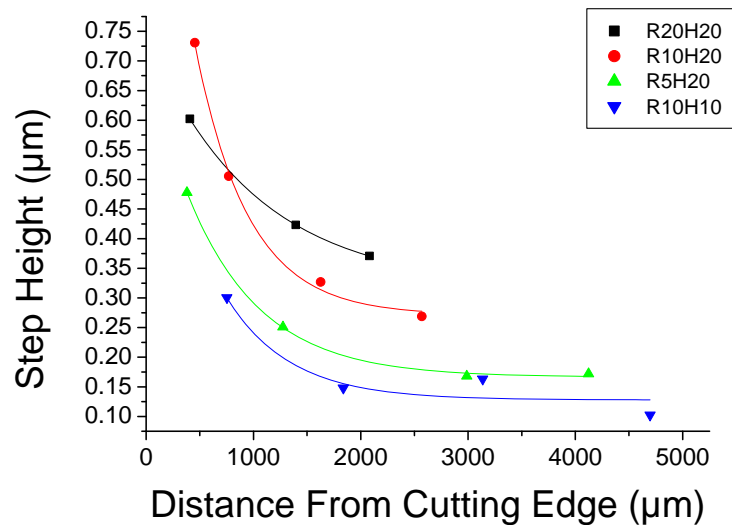
Figure 4.15. The step height as a function of distance from the cutting edge for the 4 conditions tested.

It can be seen in Figure 4.15 that the step height reduces at an exponential rate with increased distance from the cutting edge. The high hold times remove the largest amount of material and for each variable there is approximately 2 times more material removed at the cutting edge than at the centre. This can be explained by the geometry of

134

the insert; at edges the sheath surrounding the sample becomes curved and narrower, this increases the area from which the ions are collected form the plasma, increasing the ion flux and accelerating the bombarding particles towards the sample at a greater rate than on the flat. The bombarding particles also arrive at the surface at an oblique angle rather than normal (at the flat), this increases the sputter rate and thus more material is removed from the edge [16]–[18].

Controlling the substrate surface sputter rate is important for tools as some may become blunted due to edge rounding if over etched, or in some applications edge rounding may be desirable and thus understanding and control of the etching step is highly important.

4.4.2. Scanning Electron Microscopy

SEM was performed on the polished WC inserts to observe the difference in the microstructure between masked and unmasked and how etching affected the surface. Figure 4.16 is an image showing clearly the step between masked and unmasked substrate.
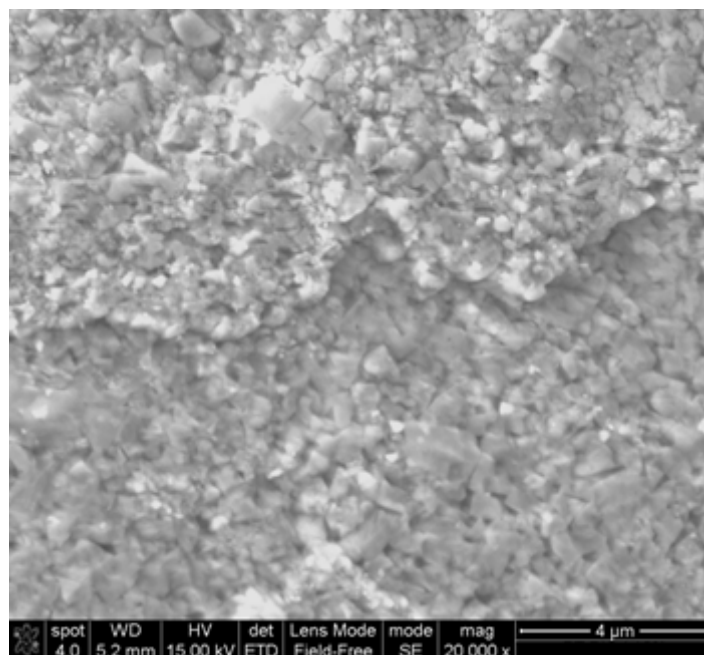
Figure 4.16. An SEM image of the step region of a polished WC insert at 15000x magnitude.

It can be seen from the image that etching the surface removes the smaller, loosely bonded grains on the surface. The removal of these grains provides a strongly bonded surface to deposited onto, reducing weak spots in the overall coating adhesion The etching will also begin to remove the Co binder between the large WC grain and thus exposing the larger grains more. The exposure of the grains is important for subsequent coating growth as it provides nucleation points.

4.5. Summary

The etching step of a deposition procedure has been investigated utilising a HIPIMS power supply and a Cr target. During this step the standard operation is to ramp the cathode current charge from arbitrary 0 (minimum) to 16 (maximum) for 20 minutes to reduce rapid changes in the target and then hold the charge at 16 for a further 20 minutes. Using the plasma diagnostic techniques OES, QCM and a flat probe, the plasma evolution during the ramping period was investigated. The main conclusions are as follows:

- Increasing the cathode current charge increases the total number of ions in the plasma.

- There is an increase in the Metal Ion:Gas ion Ratio and also an increase in the Metal Ion:Metal neutral ratio. The high energy, Cr ion rich plasma causes implantation which is known to improve adhesion of subsequent coatings.

- At high cathode current charge there is a delay in the production of metal species emission showing gas rarefaction and reduced sputtering.

- Cr plasma emission spectroscopy was used to model the plasma composition by comparison to mass spectroscopy data under the same conditions.

Ramping and holding times investigated the effect on the material removal of various substrates. The main conclusions were:

- Increased Ramping and Holding times increased the amount of surface material removed. Holding time was the dominant factor for all substrate tested.

- The microstructure of WC inserts after HIPIMS Cr etching was imaged using SEM and it was found that etching removed small, loosely bonded surface grains, exposing the larger grains; which is expected to increase coating adhesion.

- The amount of material removed by HIPIMS Cr etching decreased by a factor of 2 as a function of distance away from the WC insert cutting edge, this was true for all values of R and H time tested.

5. Initial Coating Development

5.1. Motivation

Chapter 4 showed that the use of a HIPIMS power supply was successful in generating highly ionised metal-rich Cr plasma that could be successfully used to etch the surface of a substrate. The plasma was seen to be stable at maximum power, additionally, it was found that the holding time was the dominant factor in material removal; ramping the power had a much smaller effect on amount of material removed. Once the optimum settings for etching had been established the coating composition and architecture could be designed.

5.2. Experimental Details

5.2.1. Coating Deposition

To create the proposed CrAlBYCN/AlSiCN multilayer coating the Hauzer 1000-4 PVD system was utilised. Four targets (CrAlY, CrB and two AlSi) were secured to the cathodes within the chamber. The C and N gas elements would be introduced via inlets into the chamber of CH_4 and N_2. The rotation speed of the carousel was used to control the nanolayer thicknesses, a fast speed produces a small layer and a slow speed a large one; controlling the amount of time the substrate is exposed to each target as it passes dictates the thickness.

The chamber was heated to 400˚C and had a base pressure of 7.6 x 10^{-5} mbar. The targets underwent a cleaning process in Ar gas behind the shutters to remove any surface compounds resultant of previous use. The coating were then deposited in a 3 step process onto samples of mirror polished 304 stainless steel, high speed steel, polished and unpolished tungsten carbide inserts. The samples were cleaned via a series of ultrasonic baths in detergent and de-ionised water. In the first step only the CrAlY target was used, operating in HIPIMS mode to etch the surface of the substrate, cleaning it and implanting metal ions with the aim of improving adhesion. The charge on the target was ramped from 0.4 to 16.4 over 10 minutes and then held at maximum charge for a further 20 minutes (settings determined by preliminary results obtained in chapter 4). The cathode voltage was set to 1200 V, the current was pulsed at a frequency of 104 Hz with pulse duration set to 200 μs; each pulse had a width of 50 μs. The peak current was measured to be 2.2 kA, the average current was measured to be 4 A and this generated an average power of 5.9 kW. The Ar gas flow was 77 sccm and the pressure reading was 1.14 x 10^{-3} mbar. To increase the etching effect the substrate was biased to 1000 V.

Secondly, a base layer was deposited in Ar and N reactive gas mix with a ratio of approximately 1:1, using that same CrAlY target in HIPMS mode to improve the adhesion; the base layer material binds with metal ions previously implanted into the substrate surface during the etching step. The charge on the cathode was set to 10.4, the pulse frequency was set to 400 Hz and the pulse duration was 200 μs with a pulse length of 92 μs. The cathode had a charge of 600 V and an average current of 12.2 A, generating an average power of 7.4 kW. The use of the same target as used for the etching step increases wetability and creates a stress gradient at the interface. The base layer itself also acts as a stress gradient between the unstressed substrate and the highly stressed multilayer coating by increasing the distance between unstressed and stressed areas. In addition, the CrB target was operated in UBM mode with an average power of 7.7 kW to increase the Cr content of the base layer. The two AlSi targets were also operated in UBM at a much lower average power 0.9 kW to prevent a build of coating from the Cr-based targets. The base layer deposition time was 30 minutes, the substrate bias was set to 75 V and the chamber pressure was 3.4×10^{-3} mbar.

Finally, to deposit the proposed multilayer structure all four targets were operated fully in an Ar, N_2 and CH_4 gas mix with the ratio of reactive:inert being 1:1 and N_2:CH_4 being 3:1. The CrAlY target again operated in HIPIMS mode with a charge of 8.4, a pulse frequency of 224 Hz, pulse duration = 200 μs and pulse width = 112 μs. The voltage was set to 600 V and the average current was 6 A, which generated an average power of 3.9 kW. The other three targets were maintained at an average power of 5 kW in UBM mode. The mulitlayer coating deposition time was 4 hours, the substrate bias was set to 60 V and the chamber pressure was 3.5×10^{-3} mbar. The 3-fold planetary rotation of the carousel means that as a sample passes a target it is coated by that material, it then moves past the next target, and so on, with subsequent layers building up of target material.

5.2.2.   Coating Characterisation

The coating microstructure, chemical composition, thermal stability and mechanical properties were investigated using coated 30 mm 304 SS coupons for as-deposited coatings, 30 mm HSS coupons for mechanical testing and rolled 304 SS samples for thermal testing, masked silicon wafers were also used to determine coating thickness. The FEI Nova NanoSEM 200 was used in ETD and BSED modes to study the surface morphology of the as-deposited coating as well as looking at how that morphology is affected by isothermal heat treatment and tribilogical testing. The instrument was also capable of performing EDX scans which were used to measure the chemical composition of the coating after thermal and mechanical testing. The EDX scans were performed at a working distance of 5.3 mm with beam energy of 20 keV. The PANalytical Empyrean diffractometer was used in glancing angle mode with Omega = 1 ˚ 2θ = 20-140 ˚ to determine the phase composition of the coating, the value of Omega was kept low to reduce the overlap between substrate and coating peaks. The average grain size could then be determined from the peak broadening via the Scherrer equation (3.6). In addition, a low angle scan in the range 2θ = 1-10 ˚ determined the nanolayer period.

Silicon wafers were masked with a TiO_2 paste during sample preparation; the mask was then removed with acetone after coating, resulting in a 'step' between coated and uncoated areas. The Dektak 150 profilometer measure the step height and hence coating thickness was determined. Mechanical tests were performed on the coating: adhesion was evaluated by optical microscopy after Rockwell indentation (Avery 6402, 150 kg) and critical load, L_c, scratch testing (CSM, REVETEST). Pin on Disk (CSM (Anton Paar), High-Temperature Tribometer) tests were performed at room temperature and 200 ˚C over 5000 laps with an Al_2O_3 ball as counterpart. A 5 N load was applied to the arm of the tribometer and the linear speed was set to 0.1 ms^{-1}. The area removed was

then converted to a volume removed by multiplying by the circumference of the track, the wear rate coefficients was then calculated using Archard's equation. The wear scar was also studied using SEM.

Finally, the thermal properties were investigated via isothermal heating in a furnace with an air atmosphere. Three separate tests increased the furnace temperature to 600 ˚C, 800 ˚C and 1000 ˚C, the temperature was then held for an hour and the samples were allowed to cool to ambient. Raman spectroscopy and SEM imaging analysed the effect of heat treatment on the coatings thermal stability and oxidation resistance. TGA (Setaram, Setsy evolution) was implemented to further study the oxidation resistance of the coating and determine a point for the onset of rapid oxidation; the temperature was ramped from 400 to 1000 ˚C at 1 ˚C min^{-1} in an air and Ar environment and the net weight gain was measured.

5.3.   Results and Discussion

5.3.1.   Microstructure

The coating in this chapter will be assigned the label 'coating 1'. The coating was measured to have a thickness of 1.43 μm using masking and profilometry. SEM imaging of coating 1, seen in Figure 5.1a), revealed a surface microstructure consisting of rounded and elongated features. The inset of Figure 5.1a) indicates that the elongated features also consist of smaller rounded ones. Cross-sectional SEM of the coating deposited on a Si-wafer (Figure 5.1b)) confirms these features are the tops of columns. During growth, some columns collect together/merge forming elongated features. Although the grouping of the columns into their elongated features seems ordered the directional distribution is random.
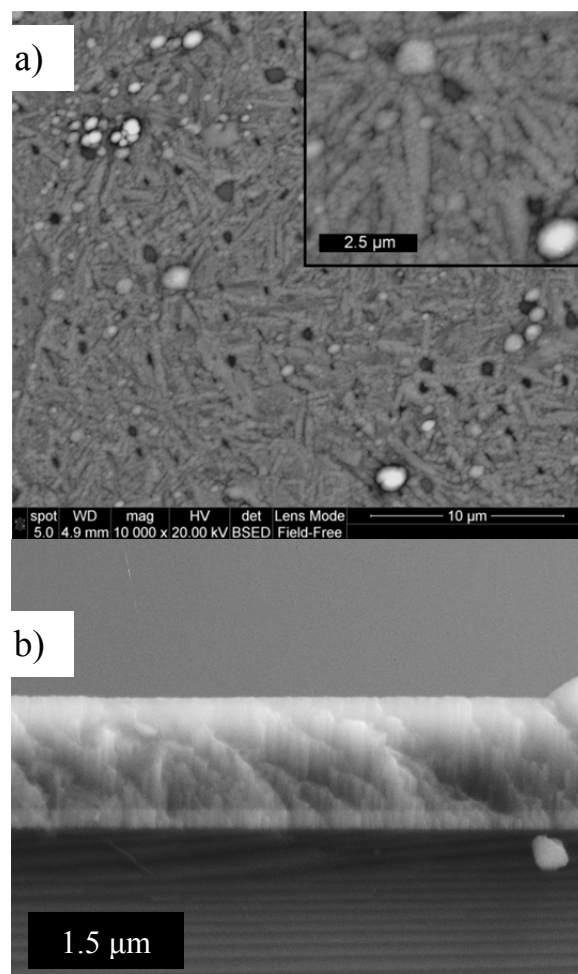
Figure 5.1. a) SEM image of the surface structure for coating 1.b) cross-sectional SEM image of coating 1 deposited on a Si wafer.

Glancing angle X-ray diffraction scans revealed the coating phase composition; at low angles peaks from the substrate are not detected allowing us to be confident that the coating predominantly has a cubic CrN lattice. There are also peaks related to Cr_2N, which would account for the high intensity of the peaks that convolute.

Low angle XRD scan of the surface revealed a peak at 2.66 ˚ which corresponds to a d-spacing of 33.2 Å. This clear peak confirms the coating has a multilayer architecture with a bi-layer thickness of 3.32 nm.

Table 5.1. The measured peaks, positions and crystal sizes associated with the orientation.

Peak Position (2θ)	Peak	Average crystal domain size, τ (nm)
37	111	15.7
43	200	9.8
62	220	7.5

The peaks measured from glancing angle XRD scans were used to calculate the average crystal domain sizes using equation (3.6) and are given in table 5.1. Each different crystallographic plane may be present within each grain. The data may also originate from several randomly orientated grains. What the data does tell us however, is an average of how much internal space is occupied a crystal domain of a particular orientation; the (111) orientated crystal domain occupies the most amount of volume,

followed by the (200) crystal crystal domains and finally the (220) crystal domains occupy approximately half the volume of the (111) crystal domains.

In the context of this work stoichiometry will be described as the point where metal and nitrogen composition have a ratio of 1:1. For example, the prominent compound detected in the Raman spectroscopy for the series of coatings presented in this thesis was CrAlN, with Al replacing atoms of Cr in the CrN lattice. Under-stoichiometric refers to coatings where the nitrogen content is lower than the metal content and over-stoichiometric will refer to when the nitrogen content is greater than the metal content of the coating. Statements as to which category the coating falls under will be based on EDX chemical composition data.

Chemical composition was determined by EDX scans of the as-deposited coating. As seen in table 5.2. a Cr:Al ratio of 2.6:1 can be determined suggesting an fcc-NaCl lattice structure. The Metal:Gas ratio of 0.7:1 indicates a significantly over-stoichiometric structure. There is also a significantly higher percentage of nitrogen than oxygen with a N:O ratio of 7.7:1, the oxygen present is likely a protective surface oxide acting as a passivation layer.

Table 5.2. Coating chemical composition determined by EDX analysis

Element	At. %
O	6.7
N	51.8
Cr	29.2
Al	11.2
Si	1.2

RAMAN spectra of the as-deposited coating in Figure 5.2 indicated a predominant CrAlN structure with peaks at 250 cm^{-1}, 710 cm^{-1} and a broad peak in the range 1200-1700 cm^{-1} (Kaindle, R 2007). At low Al content the height of the broad peak is relatively small indicating that the size of the peak is due to the presence of carbon within the coating; the indistinguishable disordered (D) and graphitic (G) phase peaks indicates that the carbon is disordered. The clear CrAlN pattern indicates a template structure of CrAlN. The periodic sequential deposition of layers consisting of different materials as the substrate passes the targets creates layers dominated by different structures. It is likely that as the substrate passes the CrB target a CrN-based layer is deposited giving rise to the CrN peak. C segregation between the CrAlN and CrN based layers in a multilayer architecture would be a possible reason for D and G presence in the RAMAN spectrum.
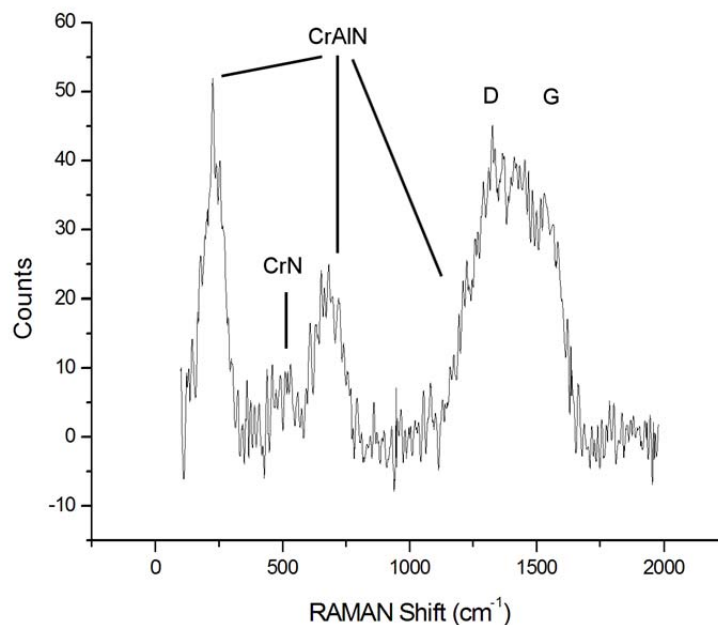
Figure 5.2. RAMAN spectrum of the as-deposited coating on 304 SS.

5.3.2. Mechanical Properties

Knoop microhardness was measured to be 3965 HK allocating the 'superhard' classification to this coating. Under scratch test the critical load for adhesion was found to be 26 N. A Rockwell indentation test classified the adhesive property of the coating; with HSS as the substrate, microcracks appear around the edge of the indentation, there is no evidence of extensive spallation and so can be described as class 0 - 1. With polished WC as the substrate similar microcracks are observed with no extensive spallation, however, larger cracks have formed which contribute to class 1 - 2.

The coefficient of friction and wear rates at room temperature and elevated to 200 °C were investigated. With a coating thickness of 1.43 μm, the room temperature wear test created a scar with average depth 0.26 μm indicating the coating survived up to 5,000 laps (277 m) with an average coefficient of friction μ = 0.61. Figure 5.3 depicts a smooth pattern with little noise present. During the 200 °C test a steady state of friction occurs up to approximately 30 m sliding distance, after which the pattern becomes extremely noisy indicating the wear depth has penetrated through to the substrate, confirmed by the average depth of the wear scar being 3.16 μm. During the coating wear phase (up to ≈ 30 m) there was an average coefficient of friction μ = 0.78. Increasing the temperature increases the coefficient of friction and, the wear rate coefficient, k, was seen to increase by two orders of magnitude from $k = 1.58 \times 10^{-15}$ to 1.54×10^{-13}, as such, material is removed at a far greater rate causing the scar to penetrate down through the base layer and into the substrate causing the coating to fail.
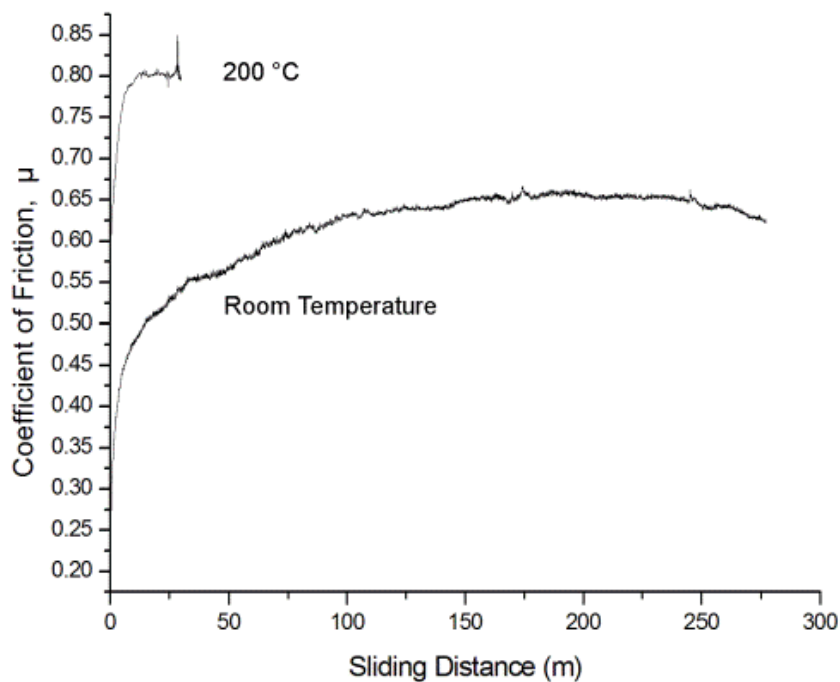
Figure 5.3. Coefficient of friction as a function of sliding distance for room temperature (bottom) and 200 ˚C (top).

SEM of the wear track (Figure 5.4) produced during room temperature testing shows a number of interesting areas and features. There is clearly a build-up of material within the wear track, as indicated by Figure 5.4 (a); the morphology of this area appears rough especially in comparison to other smooth areas highlighted by Figure 5.4 (b). The smoothing wear mechanism is nicely shown in Figure 5.4 (c) where the transition between the untouched, as-deposited coating and the wear track can be seen. This mechanism also causes a densification of the coating. A further feature to note is the snowflake-like structures visible in the areas surrounding the wear track; these patterns are attributed to arcing occurring on the surface of the sample during the coating process.
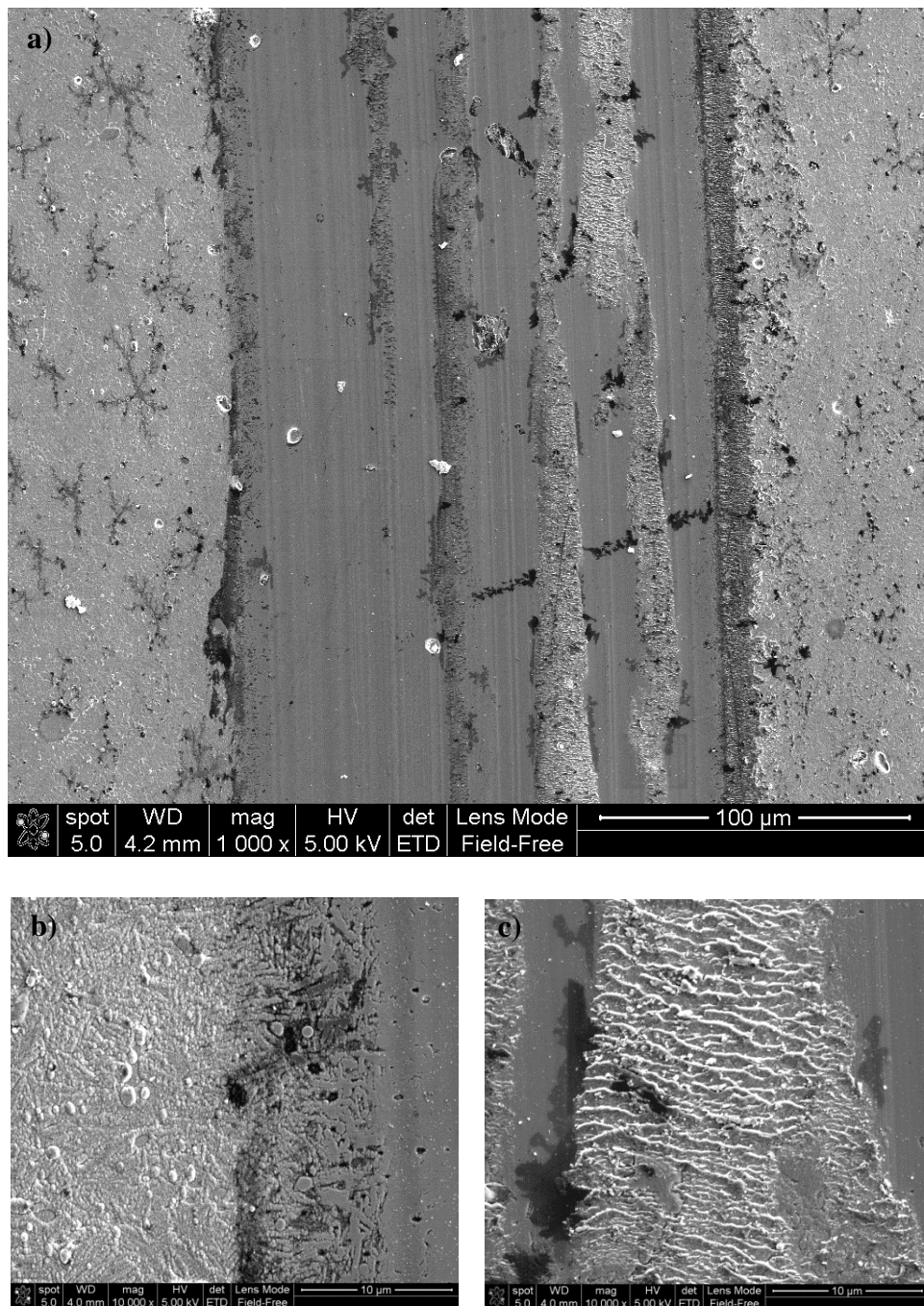
Figure 5.4. SEM image (a) of the wear scar created during pin on disk testing at room temperature. b) is of the smoothed edge of the wear track and c) is of the build-up within the wear track.

The chemical nature of the coating within the wear track was investigated at three different areas using Raman spectroscopy. The specific areas are labelled on an optical image of the wear track and their corresponding Raman spectra are displayed in Figure 5.5. Area 1 gave two strong peaks at 912 cm^{-1} and 1169 cm^{-1} associated with the Si-O vibration of Andalusite (Al$_2$SiO$_5$) [78]. The CrAlN pattern observed for the as-

149

deposited coating in Figure 5.4 is no longer present and the D and G carbon bands have also disappeared. The chemistry and high hardness of the coating is likely causing high spot temperature at the contact point.
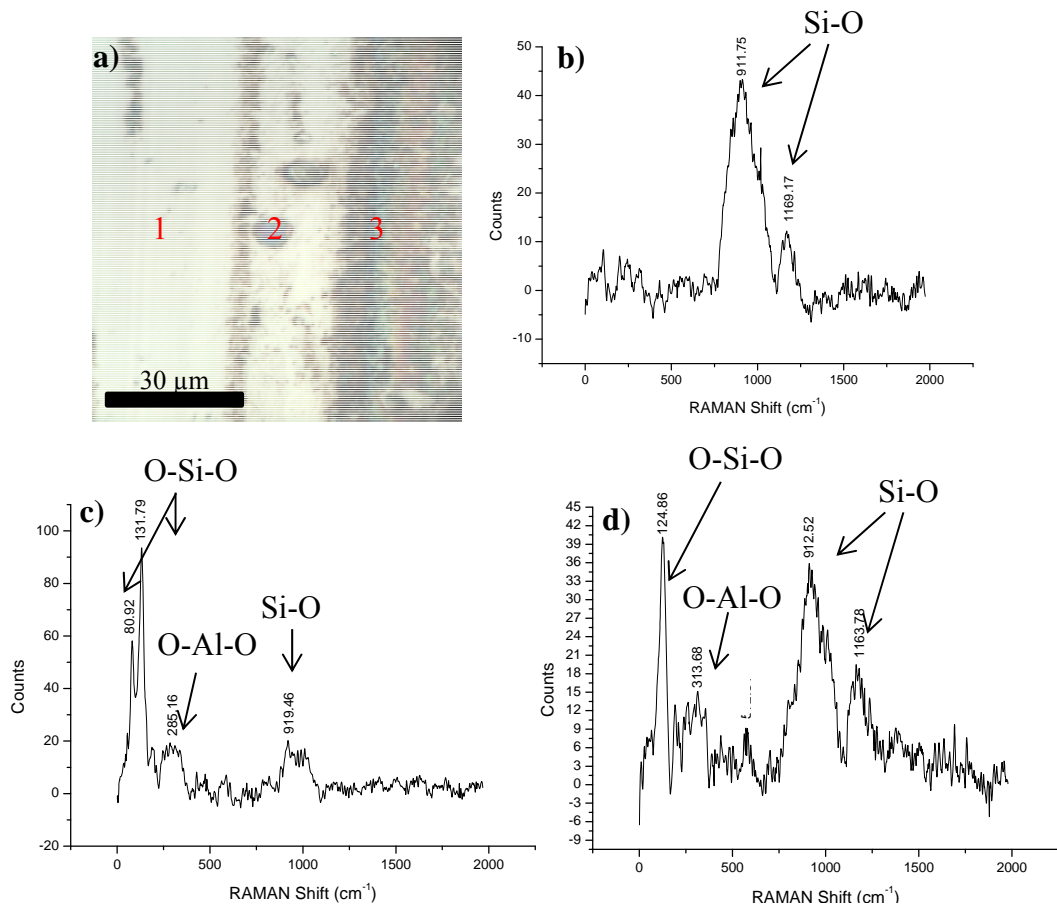
Figure 5.5. Optical image of the wear track after room temperature tribo testing (a), The Raman spectra are also given at positions 1 (b), 2 (c), and 3 (d).

The Raman spectrum for area 2 is shown in Figure 5.5 (c). The Al_2SiO_5 peak is much less prominent in this area and the spectrum is dominated by strong peaks at 80 cm^{-1} and 132 cm^{-1}; peaks in this region are associated with the symmetric bending of the O-Si-O and O-Al-O groups of Dickite ($Al_2Si_2O_5(OH)_4$) [119]. During the deposition process it was observed that the AlSi target became quickly poisoned and arcing on the target surface was rather frequent. Area 2 is a droplet formed via target arcing; the Raman spectrum indicates that this particular droplet must have originated from the AlSi target and thus highlights how target poisoning can affect the coating.

150

The spectrum for area 3 shown in Figure 5.5 (d) appears to be a superposition of the spectra for areas 1 and 2 suggesting that the build-up is a combination of two oxides: Al_2SiO_5 and $Al_2Si_2O_5(OH)_4$. During wear, friction causes high temperatures at the contact between the coating and the counterpart. We wanted to investigate how the coating behaved at such high temperatures in a controlled environment and at what temperature the oxides observed were being formed; this would give an insight into the temperature at the contact during wear.

5.3.3. Thermal Properties

SEM imaging of the coatings after isothermal treatment of three separate samples at 600 ˚C, 800 ˚C and 1000 ˚C revealed how the coating was able to withstand high temperatures. At 600 ˚C the surface morphology has clearly undergone a change; the column tops present in Figure 5.1 are no longer visible, what we observe (Figure 5.6 (a)) is a relatively smoother surface therefore annealing the coating has an improved densification effect. The grain structure of the 304 SS substrate is clearly visible indicating the significance of HIPIMS etching in exposing the faceted structure of austenite. A higher substrate roughness due to etching provides an increased number of binding sites for coating growth and thus aids adhesion. Also, visible on the surface are droplets; Raman spectra from the tribo test indicated that these droplets originated from the AlSi target due to arcing during deposition. The densification of the coating around the droplets makes them appear more prominent compared to the as-deposited coating (Figure 5.1).

At 800 ˚C further densification in the surface can be observed with the morphology in Figure 5.6 (b) appearing very smooth; this is highlighted by the clear faceted austenite structure that formed the template for coating growth. At 800 ˚C the

thermal stability of the coating is good, it remains in-tact and has not delaminated from the substrate.

Isothermal testing at 1000 ˚C caused catastrophic damage to the coating. Figure 5.7 is an SEM image of the sample highlighting a region of failure. The darker contrast area is the coating still attached to the substrate and the lighter contrast area is the substrate. It is clear that coating delamination has occurred at this temperature.
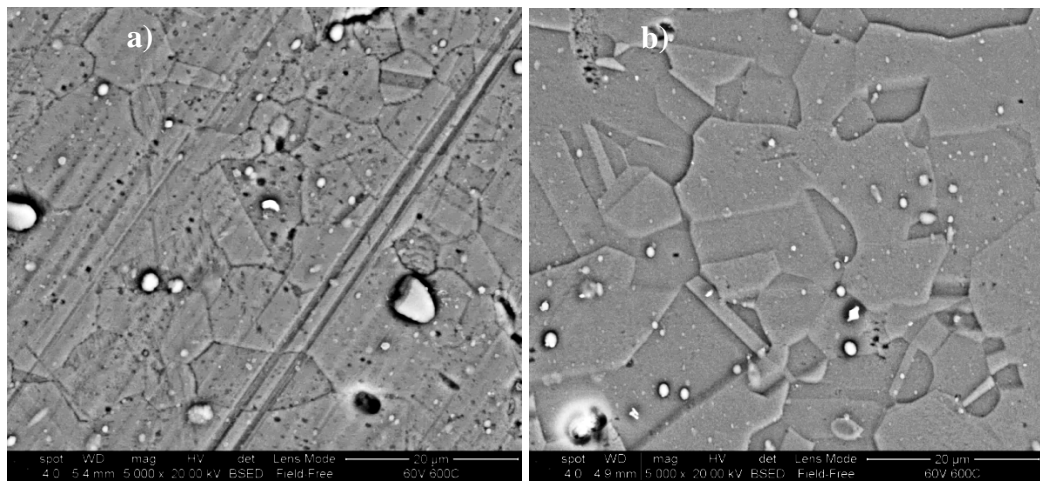
Figure 5.6. SEM images of the surface of coating 1 after isothermal heat treatment to 600 ˚C (a) and 800 ˚C (b).
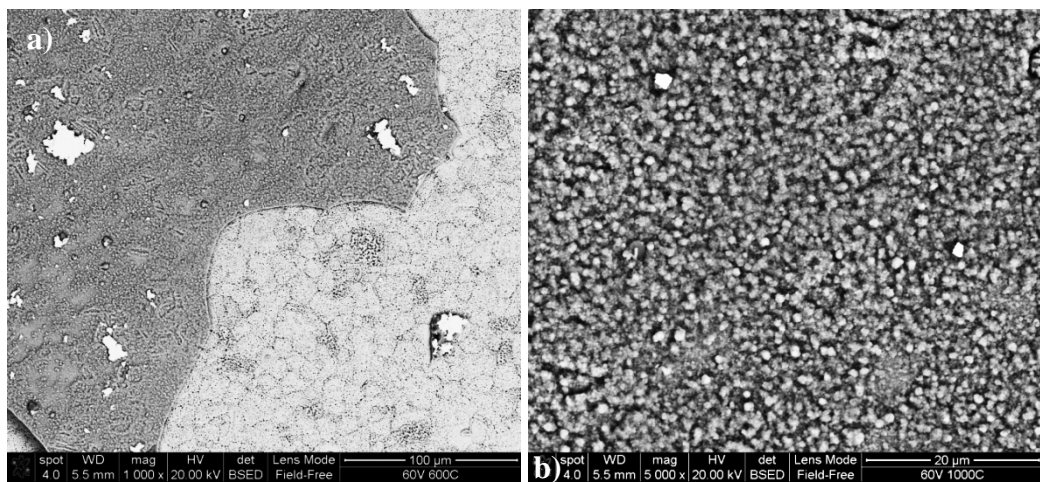
Figure 5.7. SEM images of the surface of coating 1 after isothermal heat treatment to 1000 ˚C. Image (b) is a magnification of the coating area (darker) of (a).

Magnification of the coating area in Figure 5.7 reveals surface crystal formation (Figure 5.7 (b)) across the entire area. The nature of these crystals and the coating chemical compositions at all isothermal temperatures tested was investigated using EDX.

EDX analysis of the coatings after heat treatment is presented in table 5.3 and indicates that at 600 ˚C and 800 ˚C the protective surface oxide layer (also present on the as-deposited layer) is preventing any further oxidation; the metal:gas ratio is maintained at approximately 0.6. There is a light increase in the oxygen inclusion from 600 ˚C to 800 ˚C causing the N:O ratio to decrease from 8.7 to 5.5, however, as observed by the SEM images of the surface at these temperatures the oxidation is not extensive.

Table 5.3. Chemical composition of the coatings after isothermal heating to 600 ˚C, 800 ˚C and 1000 ˚C, via EDX.

Element	At. % at 600 ˚C	At. % at 800 ˚C	At. % at 1000 ˚C
O	6.3	9.1	65.2
N	55.3	50.3	0
Cr	23.9	25.5	25.5
Al	13.2	13.8	8.4
Si	1.3	1.2	0.9

At 1000 ˚C, the metal:gas ratio has decreased further to approximately 0.5. EDX indicates no presence of N within the coating and an O content of 65 at.%, indicating

complete replacement with oxygen in the crystal lattice. At this point coating is fully oxidised and is likely the cause of the delamination observed. It is also noticed that the Cr:Al ratio increases to 3 at 1000 ˚C suggesting that the surface oxide crystals observed in Figure 5.7 will be chrome-based.

To further investigate the surface after heat treatment and to more accurately determine the nature of the observed oxide crystals, Raman spectroscopy was performed on the three samples. At 600 ˚C, the spectrum (Figure 5.8 a)) is almost identical to that of the as-deposited spectrum shown in Figure 5.2; the peaks associated with a CrAlN structure are dominant with the disordered and graphitic carbon peaks increasing the intensity of the broad peak in the range 1200 - 1700 cm^{-1}. At 800 ˚C we begin to see a change in the peak patterns; the CrAlN fingerprint is still visible however the spectrum is now dominated by the carbon region.

Raman spectra of the samples heated to 600 ˚C and 800 ˚C indicate no significant oxide formation on the surface; therefore, the surface reconstruction must be due to the movement of the most mobile atoms. As N content is highest among the non-metals, it forms a host lattice with Cr and Al. C is a replacement atom with a lower bond strength which may diffuse to the surface, plugging grain boundaries, giving a smooth, dense surface. This difference is observed when comparing the as-deposited coating (Figure 5.1) with the heat treated samples (Figures 5.6 and 5.7). The Raman spectra (Figure 5.8) support this hypothesis as the peak ratios of the disordered carbon to the CrAlN increases suggesting C migration to the surface. Within the temperature range approx. 400-1400 ˚C the diffusion coefficient of C is larger than that of N in steel, at temperature outside this range, N has a larger diffusion coefficient. If we assume a similar behaviour for diffusion within our coating then this helps to explain the C dominance at high temperatures [120].
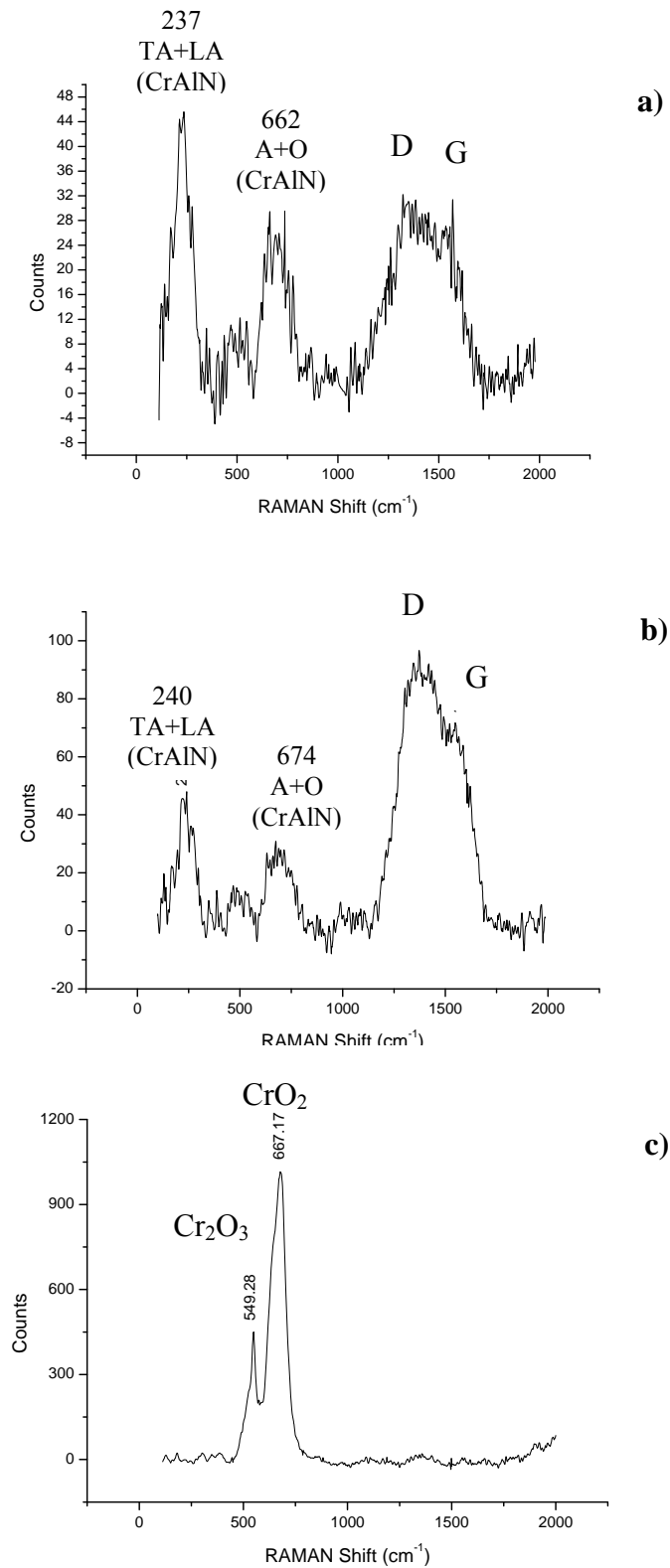
Figure 5.8. RAMAN spectra of the isothermal tests at a) 600 ℃, b) 800 ℃ and c) 1000 ℃. a) and b) contain CrAlN peaks along with a broad carbon peak, c) displays peaks associated with chromia scales.

At 1000 ˚C, the coating was seen to delaminate; in some areas the coating was still attached to the substrate and so it was possible to perform Raman scans for analysis. There are no longer any remnants of the peaks associated with CrAlN, CrN or disordered carbon suggesting thermal decomposition of the CrAlN lattice. The peaks observed are indicative of Cr_2O_3 [78]; the peak centred at 550 cm^{-1} can be attributed to Cr_2O_3 phase and the strong peak at 667 cm^{-1} is an indication of CrO_2 [70]–[76]. The ratio of the peaks tells us that we have a very strongly crystalline oxide formed on the surface of the coating. The Raman spectrum of the coating heated to 1000 ˚C supports the EDX findings that nitrogen is completely displaced by oxygen to form a chromium-based oxide.

TGA was performed on the as-deposited coating to determine its oxidation resistance and the results are displayed in Figure 5.9.
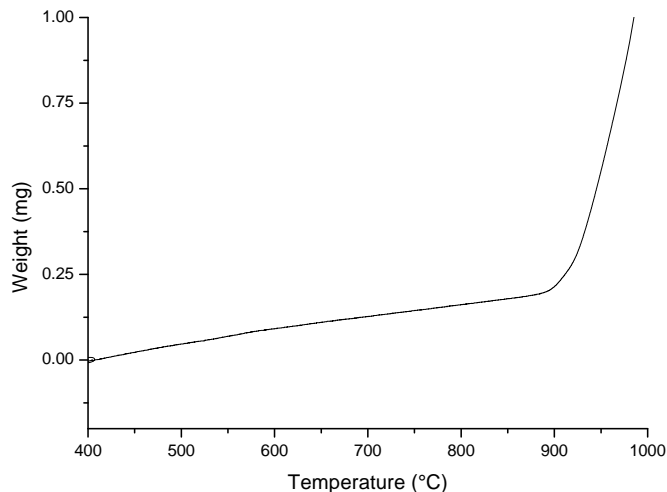
Figure 5.9. TGA; weight gain of a coating sample as a function of increased temperature in an air atmosphere.

At approximately 900 ˚C the gradient of the curve begins to increase indicating the point at which the coating is experiencing the onset of rapid oxidation; it is at around this temperature the beginning of coating failure occurs. The isothermal testing

suggested that at some point between temperatures 800 ˚C and 1000 ˚C the coating failed, through the use of TGA we are able to narrow down the region of coating stability and can say with confidence that the coating is thermally stable up to 900 ˚C. It has been seen in the literature that the CrAlN structure dissociates after 900 ˚C [65]–[67], which would align with the TGA results we have observed.

5.3.3. Wear Mechanism

Analysis of the wear scar after room temperature pin on disk tribological testing revealed the formation of aluminium silicon oxides. During adhesive wear, welding of the coating material and the counterpart creates micro-junctions; these require large forces to break and thus generate high flashpoint temperatures at the junction. These temperatures are high enough to cause oxidation of the surface material. It was thought that isothermal testing and analysis would reveal the temperatures being reached at the contact point to create such oxides. However, only chromium oxides were observed - even at the point of coating failure (1000 ˚C) there was no indication of aluminium silicon oxides via Raman spectroscopy. Therefore there must an additional process occurring at the contact point during wear.

The proposed mechanism is that the initial stage of wear smooth's the coating and exposes droplets embedded in the coating due to arcing of the AlSi target. The exposed droplets then become a contact point for welding and the formation of micro-junctions. The high temperatures at these specific points cause the droplet material to oxidise forming the aluminium silicon oxide species measured. Droplets are loosely bound within the coating; there are vacant areas surrounding the droplets causing them to be easily removed. Aluminium silicon oxide transfers onto the counterpart due to adhesive wear causing these oxides to spread. The large volume of droplets present enhances this effect and creates a layer of aluminium silicon oxide on the surface of the

coating. As the wear scar has only penetrated 0.26 μm down into the full thickness of the coating (1.43 μm), the surface measured is still within the multilayer coating region when performing the Raman scans. With the as-deposited coating being predominantly CrAlN in structure but there being a distinct absence of chrome oxide peaks it may be possible that the aluminium silicon oxide layer is protecting the oxidation of chrome species and therefore enhancing the resistance to wear.

5.4. Summary

- The proposed CrAlBYCN/AlSiCN mulitlayer coating was successfully deposited using combined HIPIMS/UBM technology. Raman spectroscopy identified a CrAlN structure; a Cr:Al ratio of 2.6:1 and a metal:gas ratio of 0.7:1 were determined by EDX

- Room temperature pin-on-disk tests, analysed by Raman spectroscopy, indicated the formation of aluminium silicon oxide species during wear

- Isothermal heat treatment and TGA showed high temperature stability up to 900 ˚C; Raman of the heated samples displayed clear chromium oxide peaks at 1000 ˚C but not before. Surface reconstruction after annealing generated a much smoother coating and revealed the faceted austenite grain structure of the substrate

- A mechanism was proposed for the appearance of aluminium silicon oxide species on the surface during tribo testing whilst being absent after the isothermal heat treatment.

6. The effect of Bias on structure and wear

6.1.　　　Motivation

Chapter 5 saw the successful deposition of the proposed CrAlBYCN/AlSiCN coating. Cathode instability due to target poisoning and excessive arcing led to droplets landing on the coating during growth which create point defects which can be detrimental to cutting performance. To reduce the number of droplets and to improve cathode stability the power on the AlSi targets was increased - increasing the metal content of the plasma and reducing target poisoning. This also introduces more metal species into the coating which was previously seen to be over-stoichiometric.

The deposited coating was super-hard with a Knoop Hardness of 3965 HK. Such high hardness is induced by stresses within the multilayer structure of the coating. Although hardness is beneficial for cutting, too high hardness can cause the material to be brittle. In addition, stresses at interfaces cause poor adhesive properties. It has been well reported that substrate bias has a direct effect on the stresses within a coating therefore, in an attempt to improve coating performance, this chapter studies the effect of reducing the substrate bias.

6.2.　　　　Experimental Details

The Hauzer 1000-4 PVD system was again used to deposit a coating using the parameters and methodology for deposition and sample preparation previously described in chapter 4 (unless otherwise stated). The base pressure of the chamber was 7.6 x 10^{-5} mbar. The CrAlY target operated in HIPIMS mode with an average power of 6.5 kW performed an etch on the substrate surface. The base layer was then deposited for 30 minutes using the CrAlY target in HIPIMS mode and the CrB target in UBM mode with powers of 7.9 kW and 7.8 kW respectively. This was deposited in a 1:1 Ar:N gas mix at a pressure of 3.5x10^{-3} mbar. The AlSi targets were kept on during the base layer deposition but with only a power of 1 kW to prevent a Cr contamination to their surface.

Finally the multilayer coating was deposited. All four targets were used in a reactive gas mix of Ar, N_2 and CH_4 with a N_2:CH_4 ratio of 3:1. The 3 UBM targets operated at a power of 8 kW and the CrAlY HIPIMS target had an average power of 4 kW.

6.3. Results and Discussion

6.3.1. Microstructure

The coating in this chapter will be assigned the label 'coating 2'. The surface grain morphology of coating 2 is a combination of rounded and elongated column tops. It can be seen from the lower magnification SEM image Figure 6.1a) that there is not a dominant direction for the elongated column tops. It can also be seen that the rounded features are generally clustered together with fewer in the areas between clusters. Further magnification indicates that both types of features (spherical and elongated) consist of similar shaped smaller grains as seen in the inset of Figure 6.1b). In some cases column boundaries can clearly be seen, resulting in round features. In others, the intercolumnar boundaries are densified resulting in elongated column tops. Similar surface morphology features of the as-deposited coating were observed for coating 1.
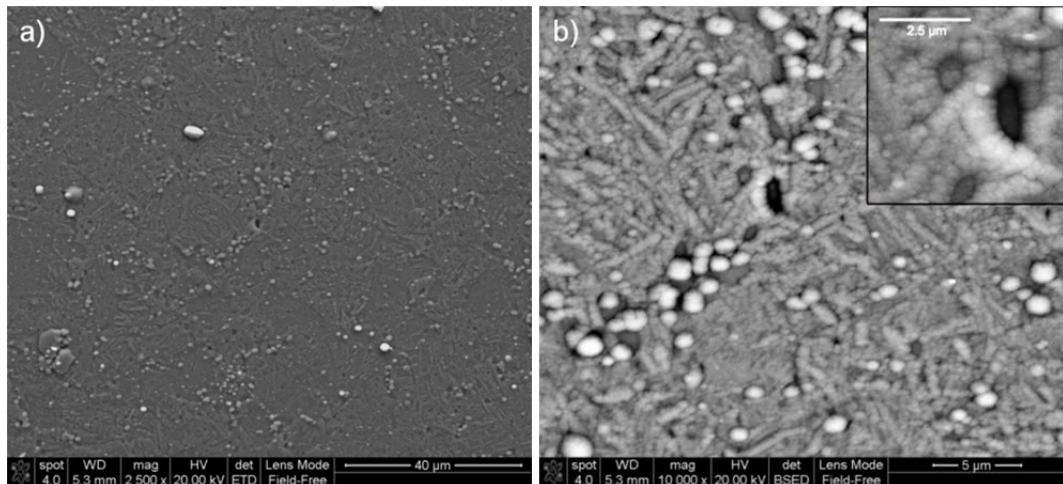
Figure 6.1. SEM images of the coating surface structure. a) is at 2.5k times magnification, b) is at 10k times and the inset of b) is at 20k times.

Glancing angle X-ray diffraction scans revealed the coating phase composition; low incident angle scans have a shallow penetration depth, therefore, the substrate contribution to peak intensities is minimal. There is a predominant cubic CrN lattice structure with additional peaks associated with Cr_2N peak convolutions cause an increase in intensity where they overlap as seen in Figure 6.2. Compared to coating 1,

decreasing the substrate bias to 40 V has had no effect on the lattice structure; the cubic CrN peak pattern remains.
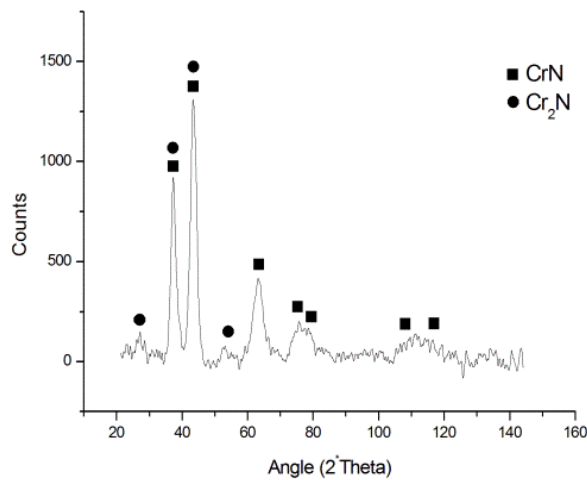
Figure 6.2. Glancing Angle Omega = 1° X-ray diffraction pattern.

Low angle XRD scan of the surface revealed a peak at 2.51 ° which corresponds to a d-spacing of 35.2 Å. This clear peak confirms the coating has a multilayer architecture with a bi-layer thickness of 3.52 nm, which is slightly larger than coating 1 (3.32 nm) and can be attributed to the increase in power for the targets operated in UBM mode (AlSi and CrB).

Glancing angle XRD was also utilised to measure peak positions and estimated grain sizes were calculated using the Scherrer equation (3.6) and are shown in table 6.1. It can be seen that within each column the (111) and (200) orientated grains occupy approximately the same average volume as each other and twice as much as the (220) orientated grains.

Table 6.1. The measured peaks, their positions and the grain size associated with that orientation.

Peak Position (2θ)	Peak	Grain Size, τ (nm)
37	111	11.2
43	200	11.1
63	220	6.6

Table 6.2 chemical composition of the coating determined by Ion Beam Centre University of Surrey.

Element	Mol. %
C	8.5
N	38.1
Cr	34.2
Al	17.5
Si	1.7

The chemical composition indicates a Cr:Al ratio of 2:1 and a Metal:Gas ratio of 1.2:1 indicating slight under-stoichiometry, this is due to chromium targets being difficult to poison and therefore giving a high metal content. Comparing the Metal:Gas

ratios of coatings 1 and 2, the effect of increasing target powers is clear; increasing the power attempted to achieve stoichiometry however it has been 'over-shot' - we have progressed from over to under-stoichiometric. There is a low Al content relative to Cr therefore CrN acts as a host lattice which is consistent with an fcc-NaCl lattice structure found by XRD. Ion beam analysis was not sensitive to the light element Boron (Anon., Personal Communication with Surrey Ion Beam Centre).

Raman spectroscopy revealed 3 peak shifts indicative of a CrAlN structure at around 250 cm^{-1}, 710 cm^{-1} and a broad peak in the range 1200-1700 cm^{-1} also associated with disordered and graphitic carbon (Kaindl, et al., 2007). At a Cr:Al ratio of 2:1 the contributions to the broad peak from the CrAlN structure is low (Kaindl, et al., 2007) and so the intensity is dominated by carbon presence; the single broad carbon peak suggests there is predominantly disordered carbon present in the as deposited coating. The peak height ratio of CrAlN to the carbon region has increased in coating 2 compared with coating 1; increased target power introduces more metal species into the plasma and hence metal inclusion into the coating. This is also consistent with the over to under-stoichiometric conversion measured by XRD.
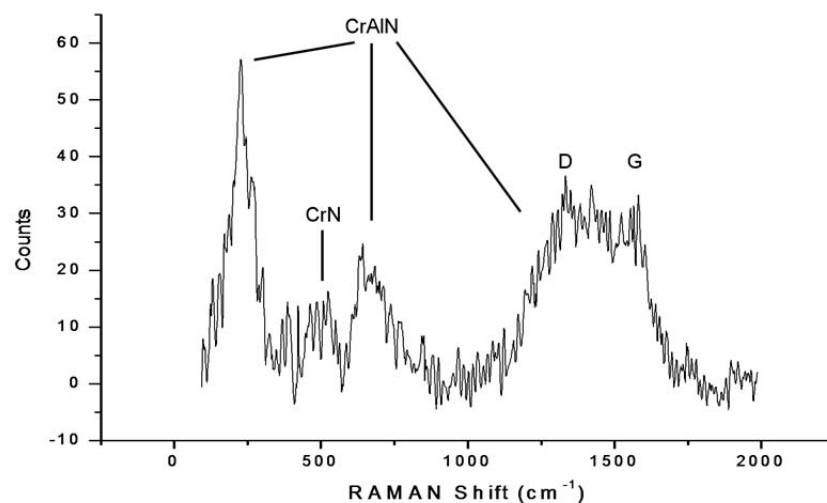
Figure 6.3. Raman spectrum of the as-deposited coating on a 304 SS 30 mm coupon. Indicated are the peak points of the CrAlN peak pattern and the D and G carbon band.

The Raman spectrum indicates a CrAlN dominated coating, carbon segregates into carbon rich nanolayers separating the CrAlN layers which would explain its strong presence in the Raman spectrum. The presence of the weak CrN peak suggests that there are likely layers of CrN that form as the substrate passes the CrB target during its rotation within the deposition chamber.

6.3.2. Mechanical Properties

Knoop microhardness was measured to be 3550 HK classing this coating as superhard. This value is a reduction from the 3965 HK hardness of coating 1, this is likely due to reduced coating stress as a result of reducing the substrate bias from 60 V to 40 V. When evaluating the adhesive properties of the coating the critical load, L_c, was found to be 43 N and is classified as class 0-1 through Rockwell indentation testing with only small edge cracking and no spallation. Rockwell indentation was also performed on the coating deposited on Tungsten Carbide, the performance of which decreased with larger cracks visible but no flaking and a classification of Tier 1-2 has been assigned. Reducing the substrate bias has had the desired effect of reducing the stress within the coating and thus improving the adhesion to the substrate.

The coefficient of friction curves generated by pin on disk wear testing over 10,000 laps are depicted in Figure 6.4.
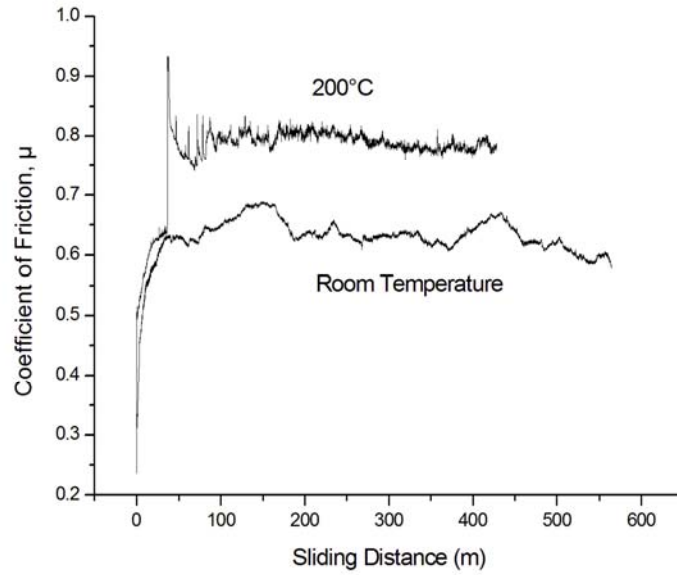
Figure 6.4. Coefficient of friction as a function of sliding distance for room temperature (bottom) and 200 ˚C (top).

At room temperature the coefficient of friction fluctuates between 0.6 and 0.7 and averages at 0.63 ± 0.04. At the elevated temperature of 200˚C there is a running in period up to approximately 50 m where the coefficient of friction increases to 0.77 ± 0.06, after which it reaches a steady state over the remainder of the 600 m. Profilometry measured the average wear track depth to determine if the test has gone through the coating, in addition the wear rate coefficients were calculated; wear scar depth, d = 0.44 µm and d = 0.3 µm, wear rates $k = 8.36 \times 10^{-15}$ Nmm^{-3} and $k = 3.89 \times 10^{-16}$ Nmm^{-3} for room temperature and 200 ˚C respectively.

Step height profilometry of the coating thickness gave value of t = 2.12 µm, the results indicate that at both room temperature and 200 ˚C the test has not worn down through to the substrate. Increasing the temperature of the test improved the wear rate by a factor of 4 and this is noted by the reduced wear track depth for the same number of laps, 0.44 and 0.30 µm for the room temperature and 200 ˚C tests respectively.

The improved adhesion is likely the reason why coating 2 survives a much longer sliding distance than coating 1 at 200 ˚C, without penetrating through to the

166

substrate. However, the reduced hardness of coating 2 has had the effect of increasing the wear rate during room temperature testing compared to coating 1.

The wear tracks were investigated further; evidence of the graphitisation caused by wear can be seen in SEM images and EDX of the scar. In Figure 6.5 a lighter (contrast) area can be seen in the centre of the wear track, with increased magnification (inset Figure 6.5) this area appears to be a build-up of material with a fibrous structure, EDX confirms that these deposits are 94% carbon.
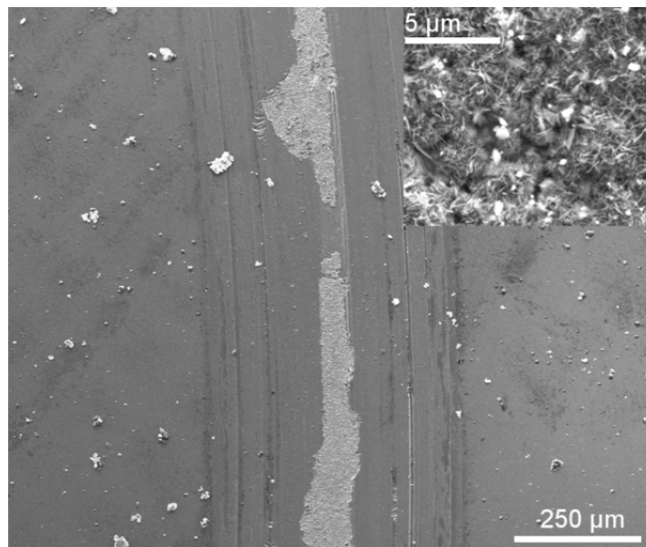
Figure 6.5. SEM image of the wear track created by room temperature pin on disk testing. Inset is a magnified image of the lighter area in the centre of the wear track.

The wear track (non-carbon area) is smooth and un-cracked indicating good coating performance under wear conditions. The wear track of the 200 ˚C sample (not shown) experienced the same build-up of carbon in the centre, as seen by imaging and EDX, but to a greater extent. This increased build-up of carbon acts as a solid lubricant and explains the improved wear rate. Another point of note is that the 'snowflake' patterns present on the surface of coating 1 do not appear on coating 2. This is clear indication that increasing the target power has improved deposition stability and drastically reduced arcing on the coating surface.

167

Raman spectra of the wear track (Figure 6.6) produced at room temperature shows evidence of the as-deposited CrAlN structure still present. The wear process and flash point temperatures cause the surface to oxidise indicated by prominent Cr_2O_3 peak; decomposition of the structure due to oxidation during wear may have caused CrAlN to dissociate as CrN peaks are seen to be more prominent. The clear separation of the carbon peaks is evidence for the graphitisation of carbon within the coating due to tribological contact, confirming the EDX analysis.
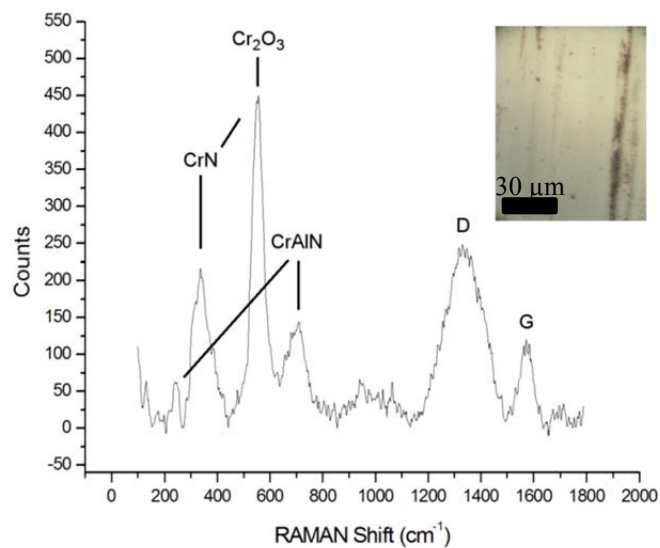
Figure 6.6. Raman spectra of the wear track created during room temperature pin on disk test. Peaks associated with CrAlN, CrN and Cr_2O_3 present, carbon band separation into disordered (D) and graphitic (G) peaks. Inset: optical microscope image of the wear track.

Optical microscopy (Figure 6.6 inset) reveals a smooth wear track in line with Figure 6.5, the unremarkable colour of the wear track and few features indicates that build up due to surface oxidation is not extensive. Interestingly, the Raman spectrum is absent of the aluminium silicon oxides peaks observed for coating 1 (Figure 5.5); this helps to support the mechanism proposed in section 5.3.3. that it is the abundance of droplets within the coating, originating from the AlSi target, that contributes to the

surface oxide during wear. The reduction in droplets for coating 2 allows protective oxides to be generated from the multilayer coating as intended.

In room temperature wear testing a thin protective tribo-layer comprising Cr_2O_3 and graphitised Carbon forms on the surface indicated by the peaks in Figure 6.6. At higher temperatures this tribo-layer becomes thicker and enriches with carbon reducing the sensitivity of the instrument to the CrAlN coating underneath which is why the associated peaks are no longer present (Figure 6.7). The dense and thick tribo-layer formed on the surface is noted by the change in surface colour of the inset of Figure 6.7 compared to the inset of Figure 6.6. This tribolayer must have a higher coefficient of friction than the CrAlN and CrN surface structures as shown by the coefficient of friction data (Figure 6.4). It must also help to improve the wear of the coating; evident by the improved wear coefficient measured at elevated temperatures by pin on disk testing.
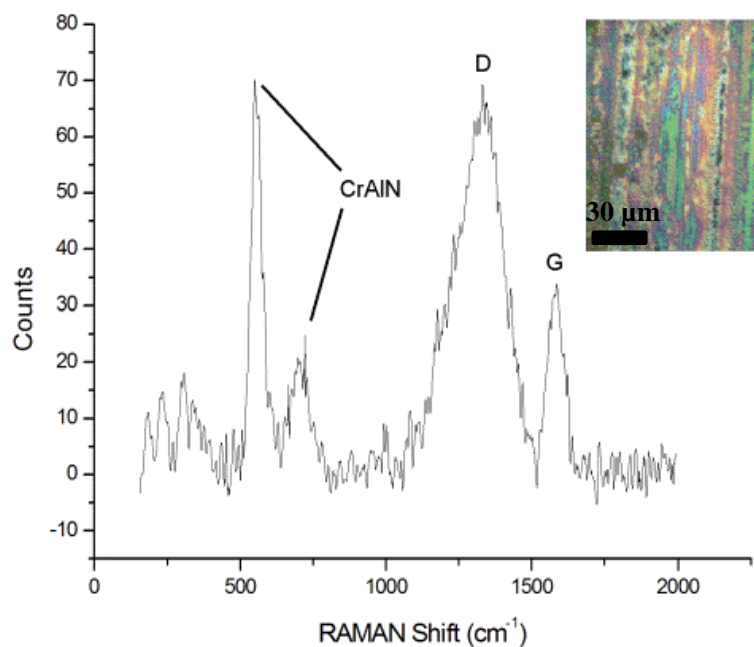
Figure 6.7. Raman spectra of the wear track created during 200 ˚C pin on disk test. Peaks associated with Cr_2O_3 present, carbon band separation into disordered (D) and graphitic (G) peaks. Inset: optical microscope image of the wear track.

6.3.3. Thermal Properties

Isothermal heat treatment of 3 separate samples of the CrAlBYCN/AlSiCN coating aimed to investigate the thermal stability of the coating and the temperature range in which it was resistant to the onset of rapid oxidation resulting in coating delamination.
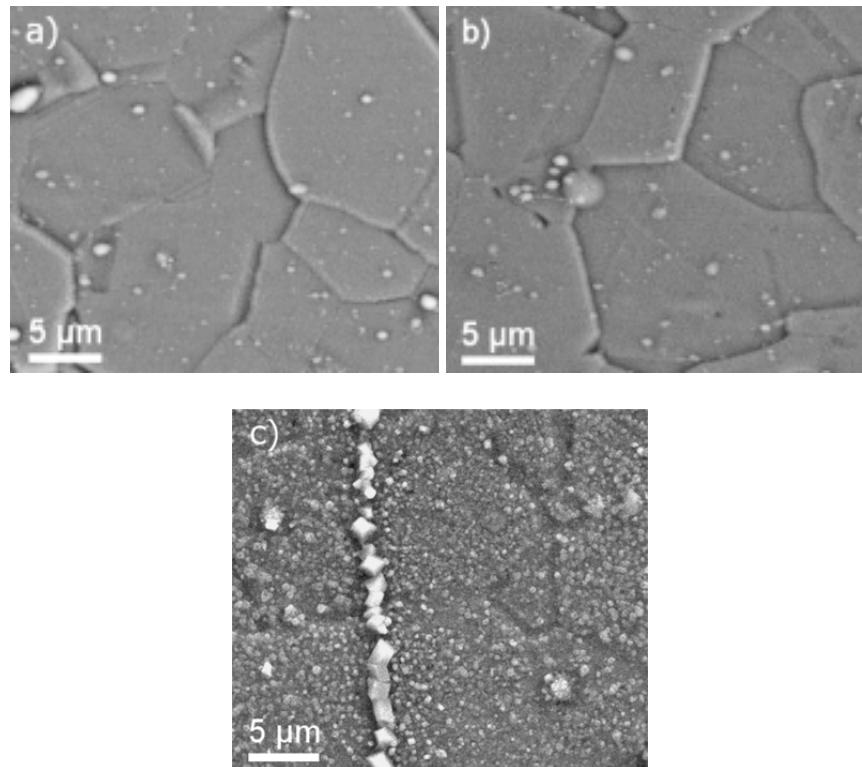
Figure 6.8. SEM images the coating surface after heat treatment in air for 1 hour at a) 600 ˚C, b) 800 ˚C and c) 1000 ˚C, images are 10,000 times magnification.

As an initial observation of Figure 6.8a) in comparison to the as-deposited (Figure 6.1), the original sphere- and rod-like features described are no longer visible, annealing the coating has an improved densification effect. The same effect was observed for coating 1 after heat treatment. The grain structure of the 304 SS substrate is clearly visible; indicating the significance of HIPIMS etching in exposing the faceted structure of austenite. The coatings heated to 600˚C and 800˚C seen in Figures 6.8a) and 6.8b) indicate no obvious difference in surface morphology. Further increase in temperature to 1000˚C (Figure 6.8c) sees the coating fail and flake off from the

substrate; failure was not observed at 800 ˚C (Figure 6.8b) therefore the onset of rapid oxidation occurs at a point above 800 ˚C. It is also noted that although the austenite grain structure is still visible through the coating, surface oxide crystals are the dominant feature. The difference in thermal expansion coefficient between the substrate and the coating causes cracking at 1000˚C, evident in Figure 6.8c, the oxidation within the cracks is clearly more extensive than the surface.

The EDX scans indicate that at 600˚C we have Cr:Al ratio of 2:1, just over 50% N present and an O content of only 6.5 at.%, originating from the thin protective oxide layer formed on the surface. The efficiency and calibration of the EDX detector cannot give reliable values for the light elements B and C; further unreliability of C At. % stems from possible surface contamination during transport and handling. In light of this, they have been omitted and the values for the other elements recalculated and presented in Table 6.1. Comparing the chemical composition of the heat treated coating via EDX analysis, it can be seen that when the temperature is increased to 800˚C the Cr:Al ratio of 2:1 is maintained however there is a slight increase in the O inclusion corresponding to a decrease in the N content; the surface is becoming more oxidised but the morphology remains stable. After heat treatment to 1000 ˚C the coating areas that remain attached to the substrate maintain the Cr:Al 2:1 ratio, however they are now completely void of nitrogen and have an O content of approximately 50 at.%.

Table 6.1. Coating element composition via EDX analysis for samples heat treated in air for 1hr at 600 ˚C, 800 ˚C and 1000 ˚C.

Element	At. % at 600 ˚C	At. % at 800 ˚C	At. % at 1000 ˚C
N	56.4	46.8	0
Cr	24.8	29.1	32.7
Al	11.1	13.4	14.0
Si	1.2	1.5	1.9
O	6.2	9.2	51.4

In order to study in more detail the wear mechanism during pin on disk test Raman

spectroscopy was performed on the Isothermal test samples.
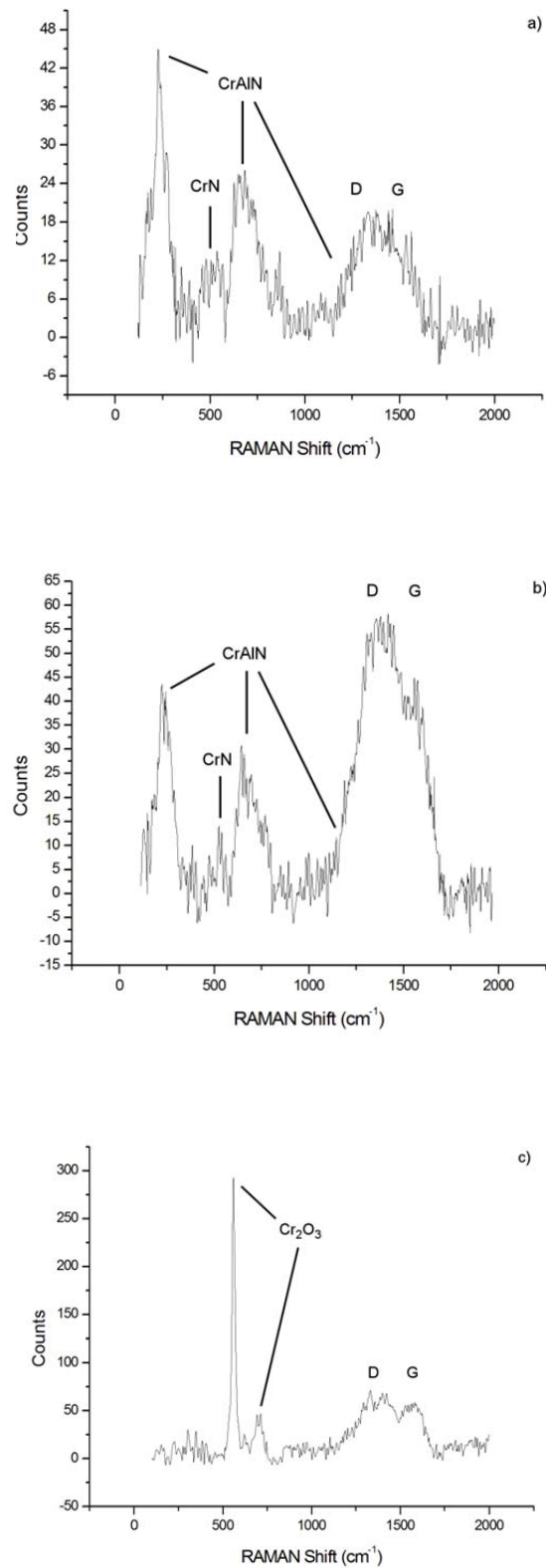
Figure 6.9. Raman spectra of the isothermal tests at a) 600 ˚C, b) 800 ˚C and c) 1000 ˚C. a) and b) contain CrAlN peaks along with a broad carbon peak, c) displays peaks associated with Cr_2O_3, slight carbon band separation into disordered (D) and graphitic (G) peaks.

After heat treatment to 600 °C and 800 °C, Figures 6.9a) and 6.9b) indicate there is little change in the spectra due to increased temperature, it is also noted that the spectra is similar to the as-deposited Raman spectra measured in Figure 6.3; a strong CrAlN presence with a broad carbon band. This supports the SEM images in Figure 6.8a) and 6.8b) which show no difference in surface morphology between the 600 °C and 800 °C samples. It is likely that the shoulder of the 2nd peaks at around 530 cm^{-1} can be attributed to Cr_2O_3 as the EDX indicates an inclusion of oxygen at the surface at these temperatures. Raman spectra indicate no significant oxide formation on the surface therefore the clear change in surface morphology that occurs after heat treatment can be explained as surface reconstruction due to the movement of the most mobile atoms.

As N content is highest among the non-metals, it forms a host lattice with Cr and Al. C is a replacement atom with a lower bond strength which may diffuse to the surface, plugging grain boundaries, giving a smooth, dense surface. This difference is observed between as-deposited (Figure 6.1) and heat treated surfaces in the SEM images (Figure 6.8a) and 6.8b)). The Raman spectra also support C mobility as the ratio of disordered carbon to CrAlN peaks increases from as-dep to 600 °C. Further increase in ratio occurs at 800 °C confirming the activation of C mobility via heat treatment. Within the temperature range approx. 400-1400 °C the diffusion coefficient of C is greater than that of N in steel. If we assume a similar behaviour for diffusion within our coating then this helps to explain the C dominance at high temperatures [120]

Figure 6.9c) confirms the change in surface morphology at 1000 °C; the characteristic CrAlN pattern is either masked or no longer present and there is a strong Cr_2O_3 peak. The Raman peak positions for Cr_2O_3 are identical to that observed for coating 1 (Figure 5.8 c)), however the peak ratios are clearly different. It was suggested

in chapter 5 that the peaks at approxiamtely 550 cm^{-1} and 660 cm^{-1} could be attributed to Cr$_2$O$_3$ and CrO$_2$, respectively [70]–[76]. The Raman spectra for coating 1 indicated it was dominated by CrO$_2$ species; however, the surface oxide for coating 2 is dominated by the Cr$_2$O$_3$ phase, a more detailed discussion of the chromia peak generation will be given in chapter 8. In addition to this, the high temperature has caused the beginnings of carbon graphitisation indicated by the individual D and G carbon peaks separating.

Thermogravimetric analysis of the CrAlBYCN/AlSiCN coating on rolled 304 SS substrate measure the coating to be thermally stable, with negligible weight gain, up to 900˚C (Figure 6.10). This supports the Raman analysis of the isothermal test (Figure 6.10), where oxide peaks are only visible in the 1000 ˚C.
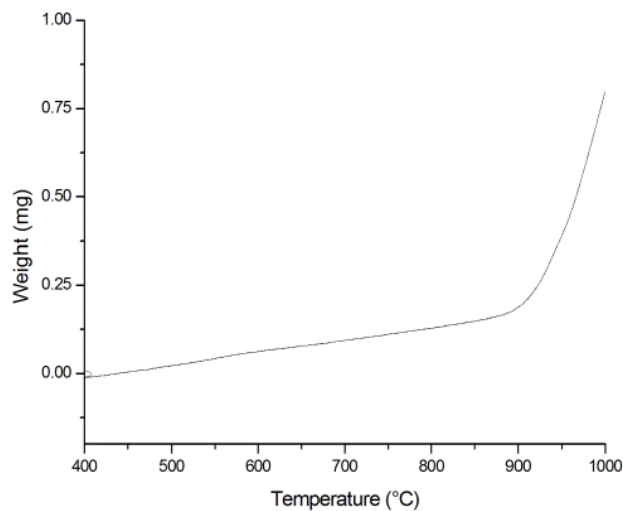
Figure 6.10. TGA; weight gain of a coating sample as a function of increased temperature in an air atmosphere.

The gradient of the curve of Figure 6.10 begins to change at approximately 900 ˚C, this now allows us to narrow the range previously stated at 800-1000 ˚C for the onset of rapid oxidation and coating failure. As with coating 1, we can now say that coating 2 is unstable in the range of 900-1000 ˚C, which is confirmed by the literature observations of CrAlN dissociation after 900 ˚C [66][67].

174

6.3.4. Wear Mechanism

The addition of 8.5% C into the coating does not cause amorphisation of the microstructure; it maintains a crystalline columnar structure. The coating's beneficial response to heat treatment can be seen even at temperatures of 600 ˚C, the densification of the surface columns via the mobility of C inhibits oxygen diffusion by decreasing the number of oxygen diffusion pathways and therefore improving the coating's oxidation resistance. Densification also generates improved smoothness; at room temperature pin on disk tests the wear track is visibly smooth, the presence of Raman oxide peaks in wear tracks indicate temperatures greater than 800 ˚C as the peaks are not visible in the 800 ˚C isothermal tests. The action of wear itself will smooth the surface if it behaves plastically but the densification for the coating due to heating will also act to improve the wear resistance.

The isothermal tests showed high temperature stability without the presence of oxides until 1000 ˚C, however, Raman of the wear track measured oxides even in the scar of the room temperature wear test. TGA proved that the coating was stable to oxidation up to temperatures of 900 ˚C and EDX of the heat treated samples indicated complete oxidation only after 800 ˚C. Raman of the as-deposited coating showed no indication of oxides forming on the surface at room temperature, however after pin on disk tests oxide peaks are clearly present; a wear mechanism must be causing very high temperatures to be generated in the wear track in order to produce the oxides observed.

During adhesive wear, asperities on the coating and counterpart weld to each other forming a micro-junction, high sheer forces are required to detach from the weld, which in turn, generates high temperatures. The coating material remains welded to the counterpart, in such that the contact points are now between surfaces of the same material. These local hotspots must have temperatures of around 1000 ˚C in order to generate the oxide formation and the carbon graphitisation observed in the Raman

analysis of the wear track. This effect is amplified at the elevated temperature wear test and helps to explain the coefficient of friction and wear rate results: the mechanism generates high forces giving high coefficients of friction. At higher temperatures more micro-junctions are forming and increased forces are required to separate them causing the increased coefficient of friction observed between room temperature and 200 ˚C wear tests. However, we see from the Raman that the production of oxides and graphitised Carbon on the surface is much greater than at room temperature, therefore the process generates a much more significant amount of lubricious chrome oxide and graphitic carbon phases which act to reduce the wear rate; the material created remains within the wear track as a solid lubricant, confirmed by the build-up of graphitic carbon in the wear track seen in Figure 6.5.

6.4.   Summary

- Increasing the target powers improved the stability of the deposition process, reducing arcing both on the substrate and on the AlSi target; as a result, the number of surface droplets was reduced. It also increased the metal content of the plasma and hence the coating; coating 2 became slightly under-stoichiometric compared to coating 1 which was over-stoichiometric

- Decreasing the substrate bias from 60 V to 40 V successfully improved the adhesion of the coating. However, the reduced stress also reduced the hardness which was detrimental to the wear rate during tribo testing.

- Isothermal heat treatment and TGA showed high temperature stability and oxidation resistance up to the range of 900-1000 ˚C; Raman of the treated samples only indicated oxide peaks at 1000 ˚C. Isothermal annealing causes a significant reconstruction in the surface morphology, generating a much smoother surface compared to the as-deposited.

- Based on the evidence we propose the wear mechanism of adhesive wear occurring at the contact during tribo tests, shearing of the cold-welded micro junctions generate temperatures of over 1000 ˚C; explaining the appearance of chrome oxide Raman peaks during low temperature pin on disk tests that are not present until 1000 ˚C in static isothermal heating.

7. The effect of target poisoning and coating development

7.1. Motivation

During deposition at constant pressure the metallic targets gradually become poisoned. Gas phase elements (C and N) react with the surface of the target, forming a ceramic compound. Subsequent sputtering of these compounds leads to non-metallic deposition. As such, a coating becomes increasingly ceramic during the deposition process time, thus creating a metal-ceramic gradient from base layer to coating surface. In order to find the optimum coating chemistry we must be able to control the metal content of our coatings; to do so the target poisoning must be controllable. This chapter sees the implementation of a Speedflo controller with an OES feedback. Monitoring the emission lines of the metal species in the plasma allowed the gas flow to be automated, with the aim of maintaining a constant metal content in the plasma.

7.2.   **Controlling Poisoning**

The initial step was to decide which target would produce a suitable poisoning hysteresis in order to successfully control the metal inclusion whilst remaining stable for the entire deposition process. Another factor in the decision process would be which target to operate in HIPIMS mode; the hysteresis curves would answer this question for us.

The CrAl target and an AlSi target were chosen to be tested. Each was operated in HIPIMS mode and in conventional DC mode at high (8 kW average) and low (5 kW average) powers totalling 4 hysteresis curves for each target. The hystereses were generated by ramping the nitrogen from 0 to 280 sccm and back down to 0 sccm over 40 minutes whilst monitoring the intensities of the optical emission lines for the relevant metal. It was observed straight away that the AlSi target was incapable of being operated in HIPIMS mode, the target arced heavily and the inbuilt safety features of the process cut the power to the target. It was clear that this target would only be operable in conventional DC mode. The target produced hysteresis with wide transition regions at both low and high power and therefore to increase coating deposition rate the high power setting was chosen as a potential candidate for process monitoring (hysteresis shown in Figure 7.1).
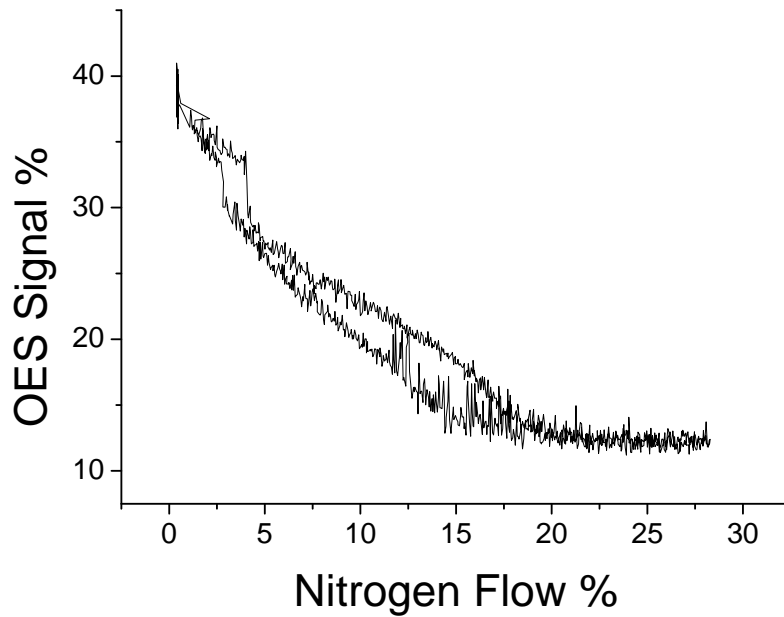
Figure 7.1. Hysteresis curve of the Al OES signal against the nitrogen flow as a % of the total flow capacity of the system (1000 sccm). AlSi target operated in HIPIMS mode at high power.

To utilise the improvements to coating properties seen through the use of HIPIMS this meant that the CrAl target needed to be operated in HIPIMS mode. It was seen to be stable for the duration of the process at both low and high powers, so again the high power setting was selected to increase coating deposition rates. However, the hysteresis curve for Cr operated in HIPIMS mode generates a 2 peaked curve as seen in Figure 7.2. The significance of this is that for any given OES intensity there could be four possible nitrogen flow rates; controlling a processes that behaves in this manner is beyond the capability of the Speedflo software.
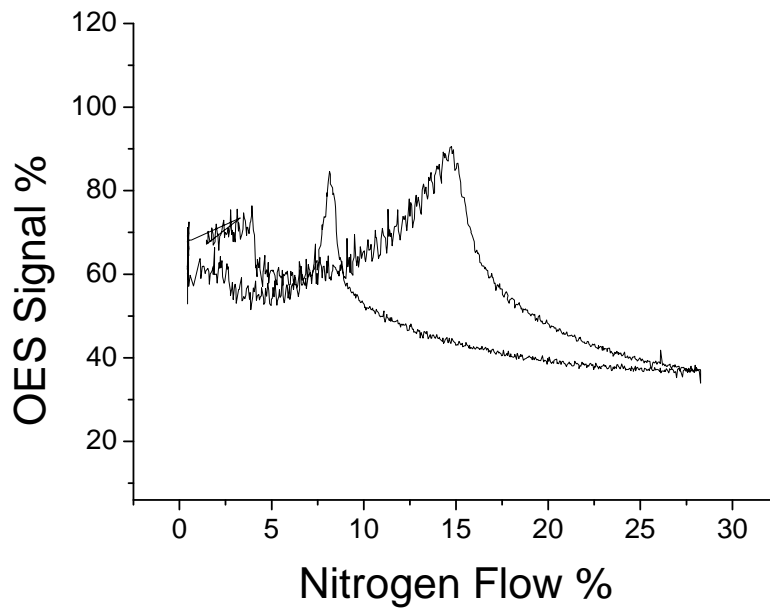
Figure 7.2. Hysteresis curve of the Cr OES signal against the nitrogen flow as a % of the total flow capacity of the system (1000 sccm). CrAl target operated in HIPIMS mode at high power.

For the reasons stated the AlSi target operating in conventional DC mode at high power was selected as a means of monitoring and controlling the target poisoning, therefore controlling the metal content of the coating. It can also be seen by comparing Figures 7.1 and 7.2 that the AlSi target becomes fully poisoned at a much lower nitrogen flow than the CrAl target. To prevent the complete poisoning of one target and hence renouncing metal content control, the target that more readily poisons is the more prudent choice.

Specific points along the hysteresis transition region were then selected to produce coatings. All four targets were operated in the same combination and process parameters (target cleaning, etching etc) set for coating 2. The AlSi and CrB targets were operated in UBM conventional DC mode with a Power of 8 kW (unless otherwise stated) and the CrAl target was operated in HIPIMS mode with an average power of 8 kW. Figure 7.3 shows the positions within the Al hysteresis loop at which the coatings

were deposited. The desired Al OES % intensity was set and the Speedflo controlled the nitrogen flow to maintain this value.
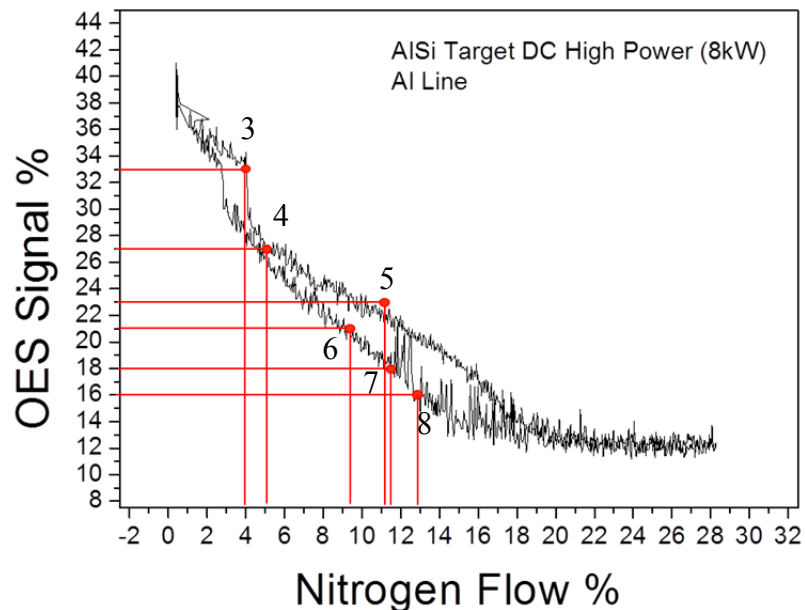
Figure 7.3. The positions within the hysteresis of Al poisoning at which coating were deposited.

The Al OES signal percentage chosen to deposit coatings were 33%, 27%, 23%, 21%, 18% and 16% which will be termed coatings 3,4,5,6,7 and 8, respectively. Although each process had the intention of maintaining a pressure of 2.7 x 10^{-3} mbar, the nature of signal control meant that pressure varied depending on gas flow required to reach poisoning levels. For coatings 3 and 4 the average pressure was 2.7 x 10^{-3} mbar however for coatings 5-8 (inclusive) the average pressure increased to 2.8 x 10^{-3} mbar. It was also intended that each target have an average power of 8 kW, in order for the process to be kept stable for the full coating duration some tailoring was required:

- The power on the Cr targets was reduced to 6 kW for coating 4.

- The power on the Cr targets was reduced to 7 kW for coating 6.

It may also be noted that coatings 6,7 and 8 had a nitrogen flow % on the reduced flow line of the hysteresis. This indicates that the coatings are being deposited

in a state where the AlSi targets are coming from an already poisoned position; the initial atoms deposited on the base layer will be metal-gas element compounds that had formed on the target surface. The AlSi targets are highly reactive and so require both manual and process cleaning. A reason for their positions on the hysteresis curve may be that the cleaning was not sufficient.

Each coating was immediately evaluated using Knoop Hardness microindentation to determine how effective the process control had been. It was found that the coatings deposited using this method showed significantly reduced hardness compared to coatings 1 and 2 (results shown later in this section). The limit of the Speedflo control had been reached. It was not possible to increase the poisoning further (OES signal % < 16%) in a controlled manner; to reach the levels of poisoning required for the desired hardness values the signal fell into the poisoned region of the hysteresis. At this point there is a range of gas flows possible to maintain the low OES signal and thus it is impossible to know the gas content of the plasma and therefore the coating.

As we have seen from the hysteresis patterns (Figures 7.1 and 7.2), AlSi targets poison far more readily than Cr based targets. In order to increase the hardness the coatings must become more ceramic and less metallic; having reached the limit of reducing the Al OES signal %, controlling the metal content of the plasma had to be switched to the Cr targets. We have already established that this was not possible via Speedflo control meaning that in order to decrease the metal content of the plasma the power on the Cr targets needed to be reduced.

To implement this change the Al OES signal % was maintained at 20% and the power on the Cr targets was reduced from 8 kW to 6 kW and then 4 kW, termed coatings 9 and 10, respectively. An improvement in the hardness was observed,

however, it was not sufficient to reach the hardness values measured for coatings 1 and 2. Therefore further process refinement was required.

Unfortunately, the metal signal process control had been unsuccessful in achieving the desired hardness values and reducing the power on the Cr targets further would be detrimental to the deposition rate. To improve the hardness more C and N needed to be included into the coating, this could be achieved by increasing the gas content of the plasma however the pressure limit had been reached via this method. The process parameters were reverted back to pressure control as for coatings 1 and 2, however this time set to 3×10^{-3} mbar compared to 3.5×10^{-3} mbar in an attempt to achieve stoichiometry. For this latest coating the power on the targets was maintained at 8 kW and 4 kW for AlSi and Cr-based respectively, the coating is termed coating 11.

7.3. Results

The series of deposition experiments discussed in this chapter was intended to observe the coating property evolution from metallic to ceramic by increasing the inclusion of gas phase elements into the coating. This section looks at how the microstructure, composition, mechanical and thermal properties developed.

7.3.1. Microstructure and composition

The microstructure and composition of each of the coatings, 3-11, were studied using SEM, EDX, XRD and Raman. Coating 3 was deposited with the metallic region of the hysteresis curve and the SEM image in Figure 7.4 shows a very dense structure with large column tops. From coating 3 to coating 6 the metal content is decreasing and the coatings become more porous with grain boundaries clearly visible. There is a reduction in the grain size with increased poisoning, a trend which continues through from coating 3 to coating 11. It can be observed that from coating 7 onwards, that in

addition to grain refinement, there is also surface densification with increased target poisoning. Increasing the gas element inclusion into the coating increases the density.

Coatings 3 and 4 show a broad peak centred on 42.4 ˚ in low angle XRD scans (Figure 7.5) associated with Cr_2N. As the metal content of the coatings decreases we observe a mixture of Cr_2N and emerging CrN resulting in a single broad peak in the range 30-48 ˚ for coatings 5-9. The most ceramic coatings (10 and 11) demonstrate the 2-1 peak pattern of fcc lattice structure with peaks at 37.4 ˚, 43.6 ˚ and 63.5 ˚. A pattern reminiscent of that measured for coatings 1 and 2, with peak intensities increasing as the coating evolution heads toward stoichiometry.
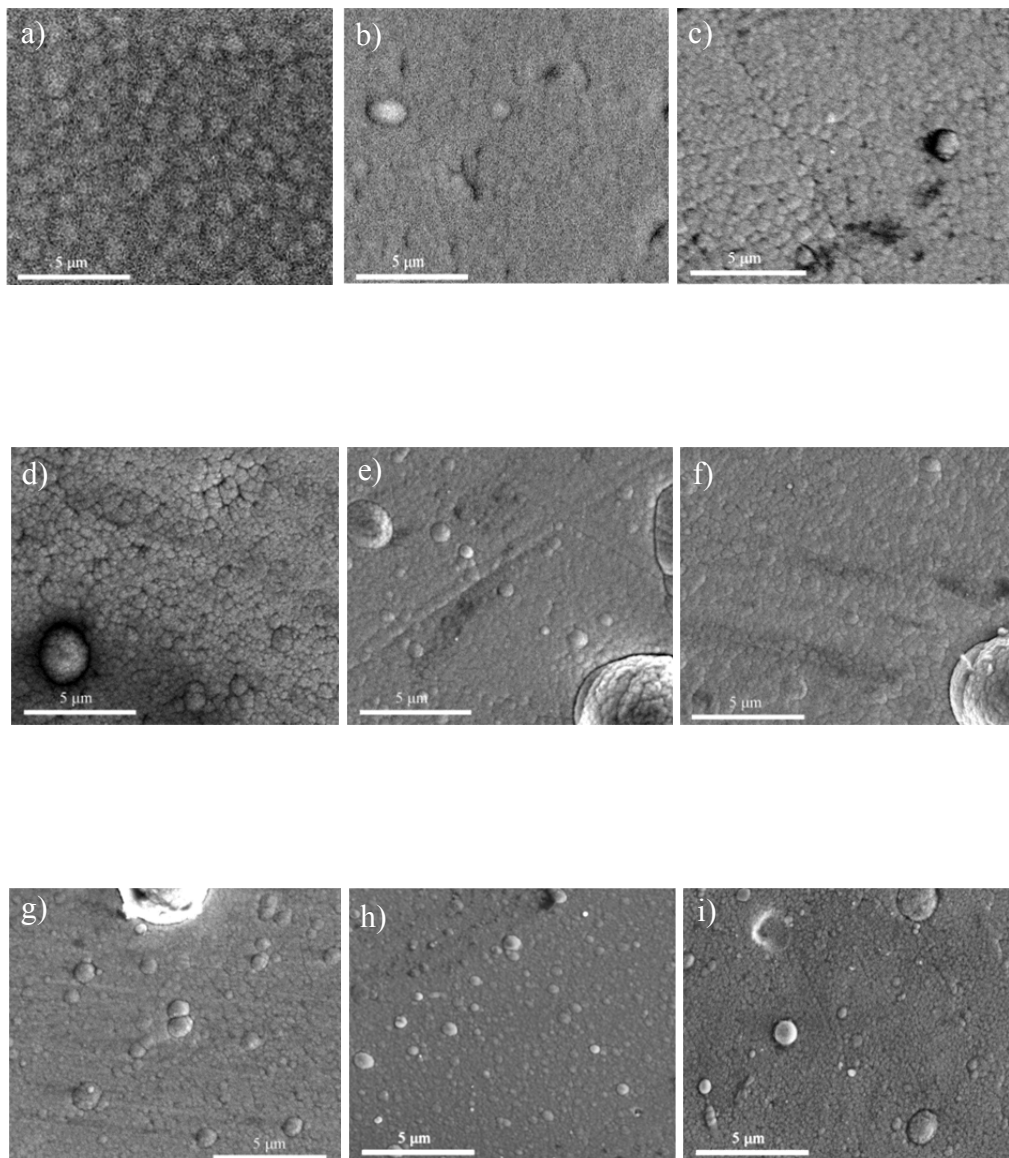
Counts
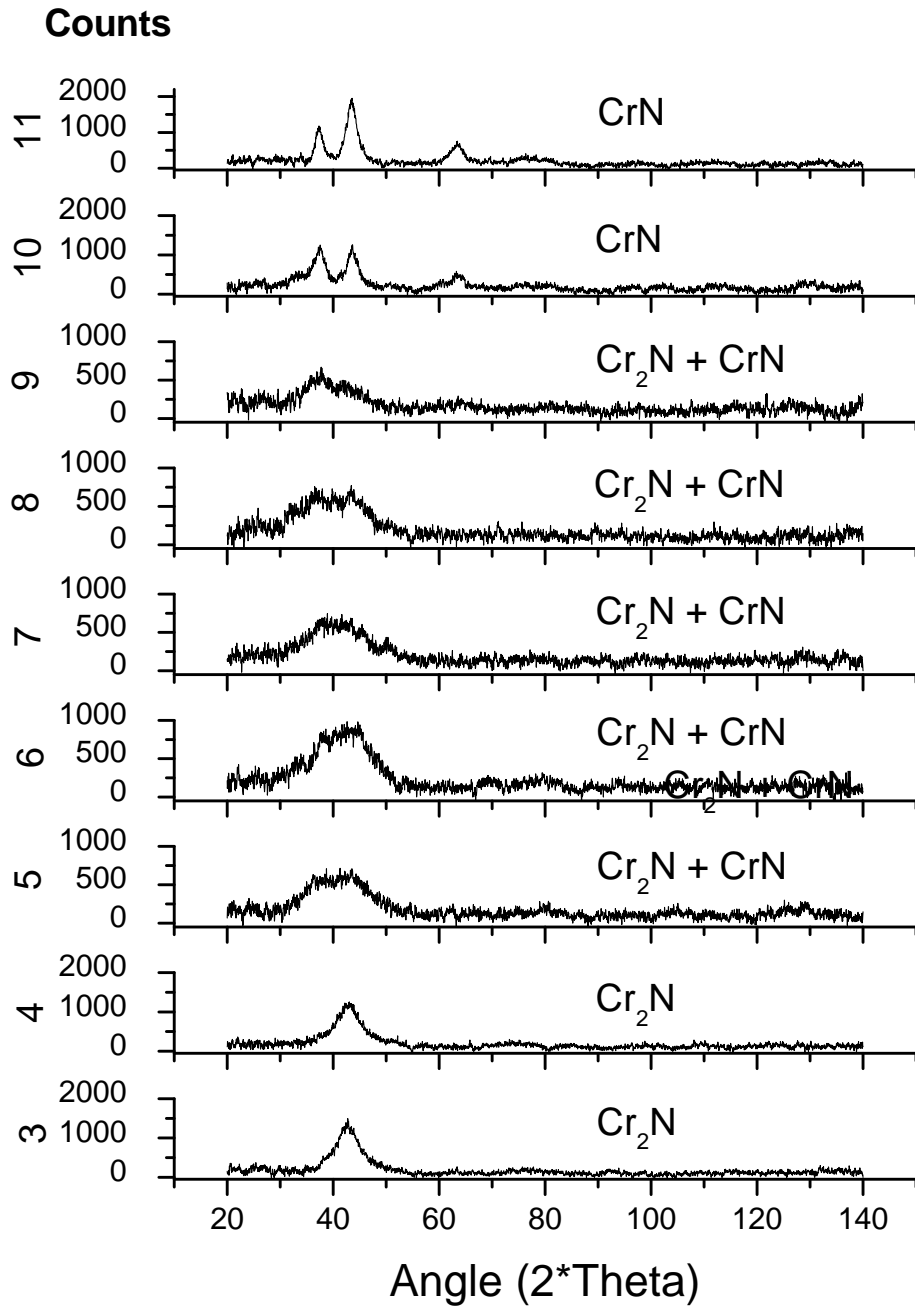
Figure 7.5. Low angle XRD patterns for coatings 3-11 over an angle range of 2θ.

Chemical composition of the as-deposited coatings was measured using EDX and is displayed in Figure 7.6. The overall trend is one in which we would expect to see; the experimental process increased the level of target poisoning which in turn increased the atomic % of nitrogen included into the coating whilst simultaneously decreasing the Cr and Al content. To achieve OES signal % lower than 27% the Speedflo control

186

caused an increase in average chamber pressure which can be seen by the sharp increase in N content and corresponding decrease in Me content between coatings 4 and 5.
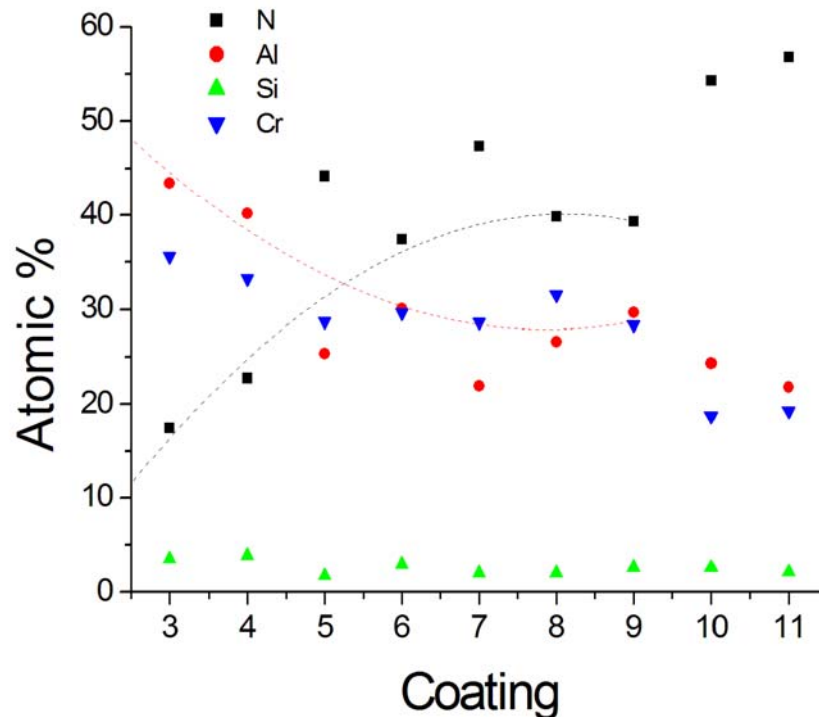
Figure 7.6. The as-deposited chemical composition in relative atomic percentage for coatings 3-11.

The two trend lines plotted highlight the relationship between increased poisoning of the Al target and nitrogen inclusion into the coatings. There is an almost linear increase in nitrogen with a corresponding decrease in Al for coatings 3, 4 and 6, after which, increased poisoning has little effect on either. Further reduction in the Al OES signal percentage did not generate an increase in gas-phase elements into the coating - a limit had been reached. Decreasing the power on the Cr-based targets to 6 kW had little effect on the nitrogen inclusion, however further reduction to 4 kW increased the N content to 54 at. %. The data supports the preliminary hardness checks and justifies the decision to revert back to a pressure controlled process without sacrificing deposition rate by further reduction in Cr-based target power. Upon doing so the N content increases again to 57 at. %.

Coatings 5 and 7 contain a higher N content than expected, this may be due to the sequence of deposition; coating 4, 6 and 8 were deposited first, followed by coatings 3, 5 and 7. The variation in nitrogen content could indicate that the target for 5 and 7 may not have been sufficiently cleaned prior to operating.

Elemental ratio can help us understand the coatings structure and properties; for example, an increase in Al in the CrAlN structure (up to approximately $Cr_{0.3}Al_{0.7}$) increases the hardness by inducing an inherent stress via increasing the lattice parameter [121]. The high metal content coating (coating 3) has a low Cr:Al ratio of 0.82 (Figure 7.7). The plasma has a high metal content at this point on the hysteresis (Figure 7.3) for this coating, with Al being in slightly higher abundance. Coating 4 is the first coating within the transition region, the Cr:Al ratio would be expected to increase at this point due to increased poisoning however it remains almost constant; it is likely that this occurred due to the power on the Cr-based target needing to be reduced to 6 kW for stability. As we move down the hysteresis further into the transition region and towards the fully poisoned tail the Cr:Al ratio increases to 1.3 for coating 7 (the dip in the trend for coating 6 to 0.9 is again due to a reduction in the Cr-based target power to 7 kW). The increase in the ratio highlights how reactive the AlSi targets are and the extent to which they are more readily poisoned the Cr-based targets.
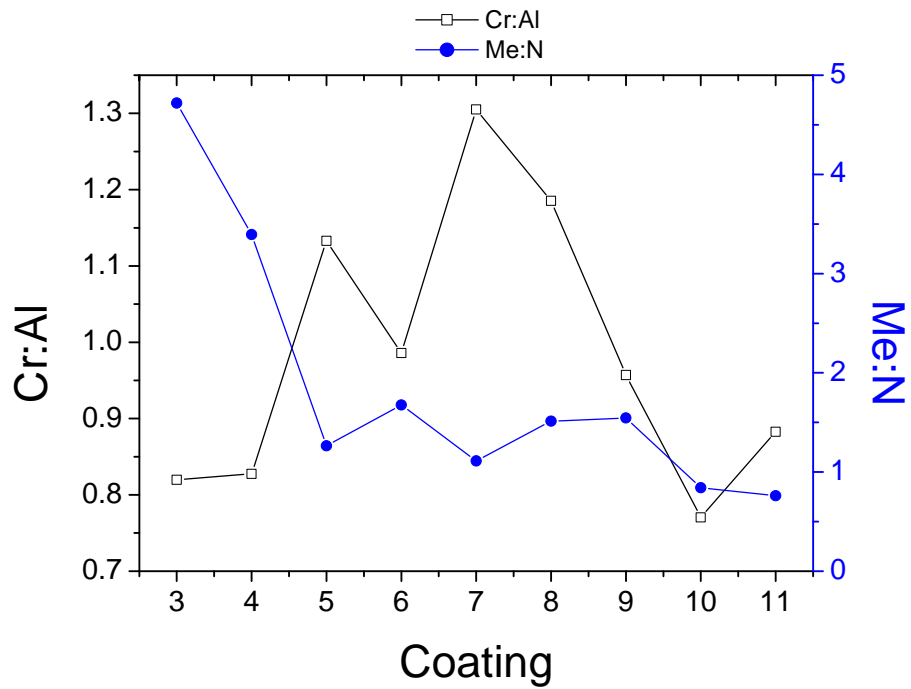
Figure 7.7. Compositional ratios for coatings 3-11. The left hand x axis shows the ratio of Cr to Al in the coating (black) and the right hand x axis shows the ratio of metal species (Cr, Al and Si) to nitrogen in the coating (blue)

There is a significant drop in the Cr:Al ratio between coatings 8 and 10 which corresponds to the reduction in power from 8 kW to 6 kW and then again to 4 kW for the Cr-based targets. The ratio increases again for coating 11 to 0.88 as the process becomes pressure controlled; no longer maintaining a constant Al OES signal % will mean the AlSi targets become increasing more poisoned through the duration of the process compared to the Cr-based coatings.

Stoichiometry, MeN, is important in nitride coatings to achieve the fcc-NaCl structure which generates harder materials compared to the hexagonal close-packed metal lattice (hcp) for Me_2N phases. hcp structures deform more easily than fcc structures and thus causes a reduction in the hardness [121]. With a Me:N ratio of 4.7, coating 3 is massively under-stoichiometric (Figure 7.7). Increasing the poisoning causes a sharp decrease in the Me:N ratio from 4.7 to 1.26 for coatings 3 to 5; at this point the coating is still under-stoichiometric however far more gas-phase elements have been included. It is at this point that we start to see reduced effect signal control

has on the nitrogen inclusion as the trend levels off. Reducing the power of the Cr-based targets to 4 kW takes the Me:N ratio under the stoichiometric line (y=1) as the plasma has a lower Cr content and the AlSi targets are relatively poisoned. Switching to pressure control and increasing the pressure to 3×10^{-3} mbar increases the nitrogen inclusion further and the coating is over-stoichiometric with a Me:N ratio of 0.76.

The chemical compositions and trend in ratios stated supports the evolution of the coatings crystal structure measure via XRD (Figure 7.5). The high metal content and massive under-stoichiometry coatings 3 and 4 would result in a hpc Me_2N structure; the XRD patterns confirm that this is in fact Cr_2N. As the targets become more poisoned and the ratios converge towards stoichiometry for coatings 5 to 9, CrN also forms; convolution between CrN and Cr_2N causes the broadening observed. With increased N inclusion the coatings become over-stoichiometric and the CrN fcc-NaCl peak pattern becomes dominant.

Raman spectra of the coating series helped to describe the change in phase composition during coating evolution. Optical microscopy images of the surface (Figure 7.8) show slight variations in colour and number of droplets but in general there is no significant change in the macroscopic topography.
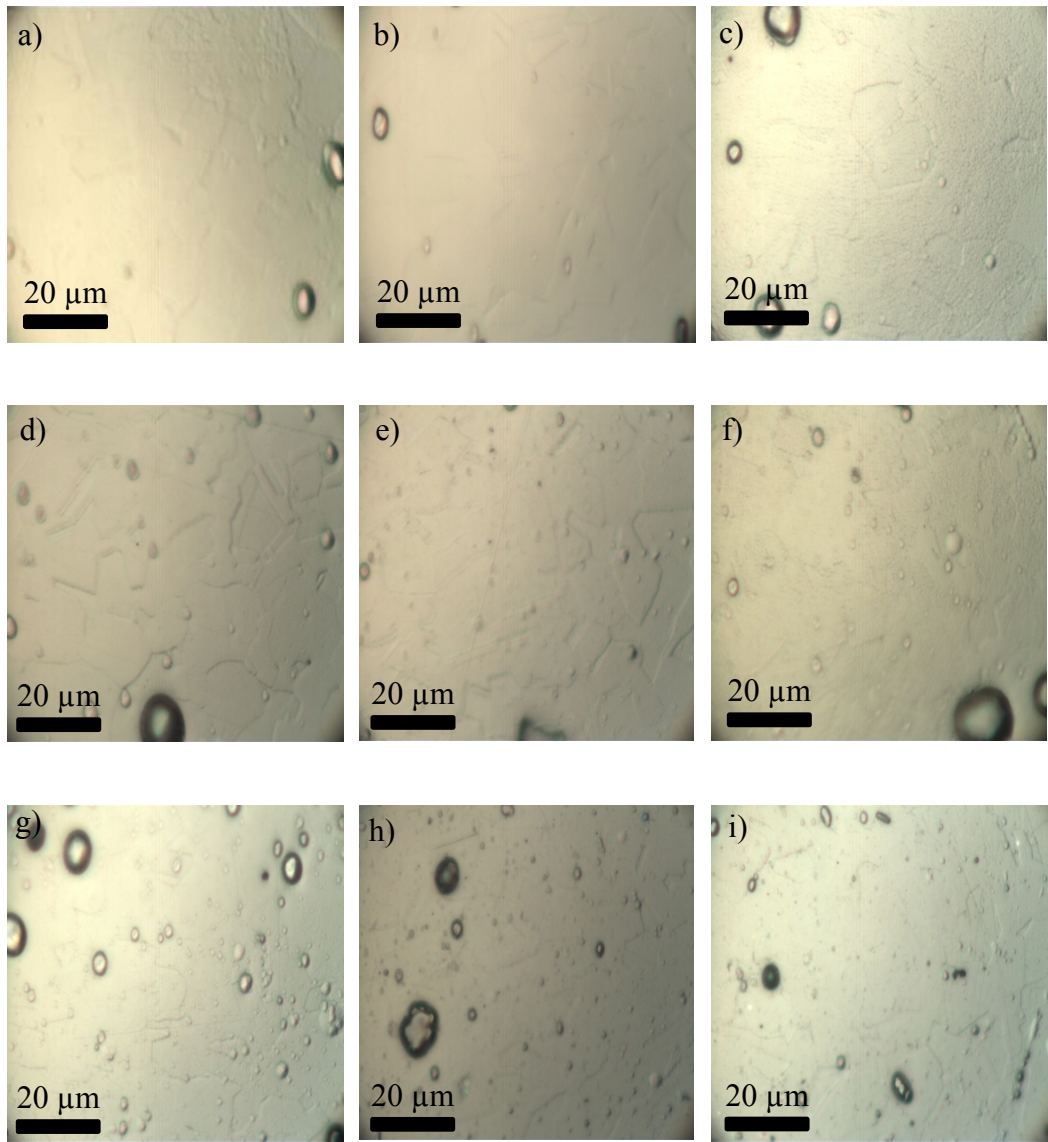
Figure 7.8. Optical microscopy images of coatings 3-11, a-i, respectively, taken through the Raman lens.
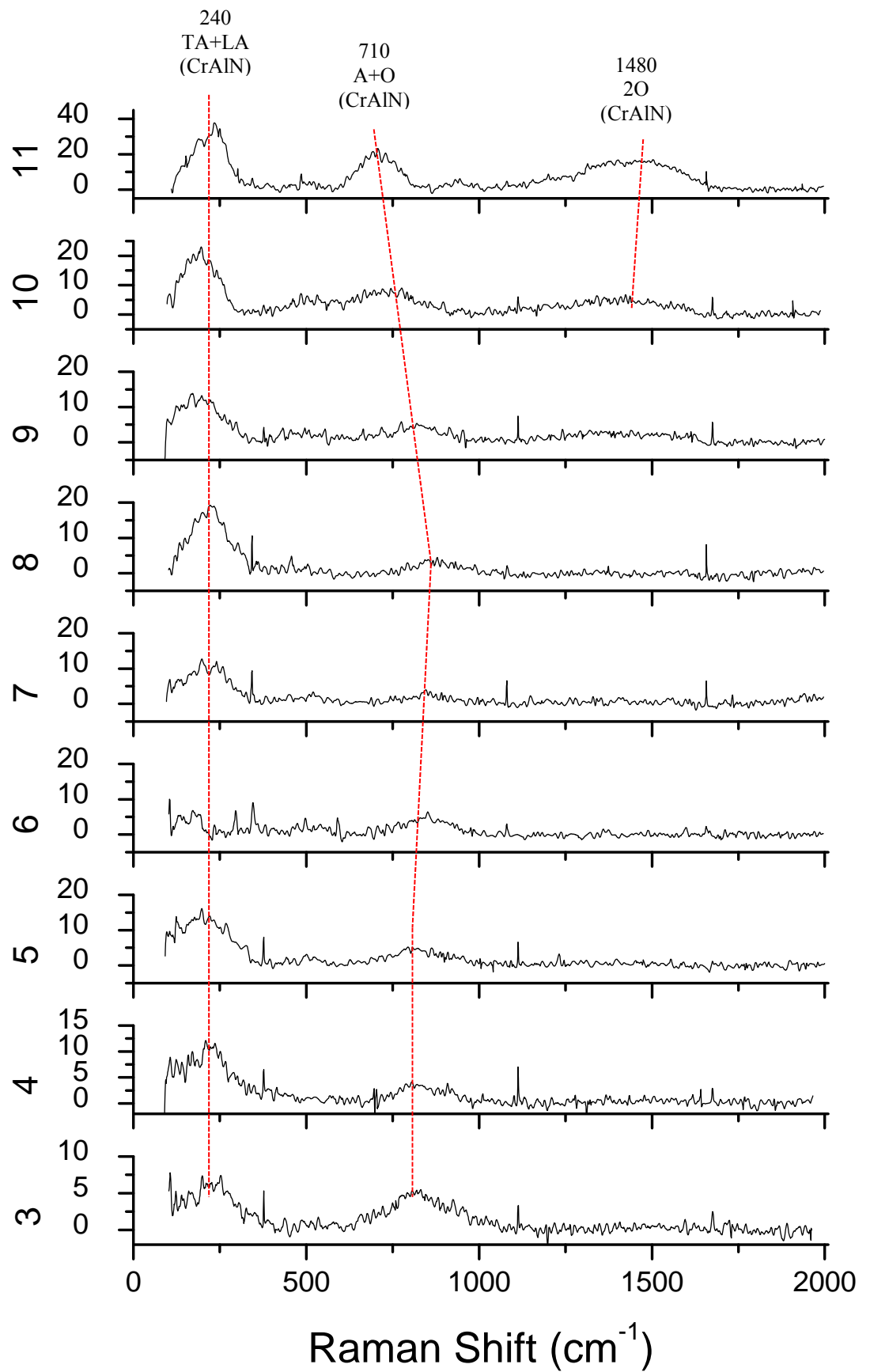
Figure 7.9. Raman spectra for as-deposited coatings 3-11. Dashed red lines included to highlight the shift in peak position for the peak at 710cm^{-1} and the appearance of the broad peak in the range 1200-1700 cm^{-1}.

The study by Kaindl et. al. [48] showed that increasing the Al content of the CrAlN lattice lead to prominence of the three peaks (labelled on Figure 7.9) that have also been seen for coatings 1 and 2 and previously described in this study. These peaks are observed nicely in coatings 3 and 4 where the Cr:Al ratio is much less than 1 (Figure 7.7). As the Al signal on the Speedflo is reduced to include less Al species into the coating the Cr:Al ratio increases and the characteristic Raman peak pattern is less recognisable. The peaks become broader and less defined for coatings 5 and 6, for coating 7 the second peak is barely visible. There is a general trend of peak shifting to higher Raman shifts from coatings 5-8. Upon reducing the power on the Cr-based targets (coatings 9 and 10) the peaks begin returning towards the lower Raman shift becoming slightly more defined. The characteristic CrAlN Raman pattern observed for coatings 1 and 2 returns for coating 11, when the pressure is increased to 3×10^{-3} mbar. We also start to see the presence of the broad peak centred around 1500 cm^{-1} begin to take shape. The intensity increase of this peak may also be due to carbon contributions; increasing the pressure for coating 11 not only increases the N content but also the C, there may be sufficient disordered C under these conditions to produce a measurable Raman signal. These results are consistent with the pattern observed by Kaindl et. al. in that lower Cr:Al ratios produce more prominent Raman peaks [48].

For coatings 10 and 11 the Raman indicates a CrAlN structure with Al replacing Cr atoms in the CrN lattice; this suggests that the CrN structure observed in XRD is not pure CrN but is in fact a fcc-MeN structure containing the two metal Cr and Al. Future reference to the CrN phase detected by XRD is or descriptive purposes only; indicating an fcc-phase.

7.3.2. Mechanical Properties

Reducing the set Al OES signal % increases reactive gas flow into the chamber and thus increases target poisoning. Increased poisoning reduces deposition rate and the effect of this can be seen in Figure 7.10. Coating thickness decreases almost linearly with increased target poisoning from coatings 3 to 8 this is a direct effect as the process times were constant for each coating. Coatings 5 and 7 stand out as having lower than expected deposition rates; this is likely an effect of the process schedule and target history resulting in targets that are operating in a much more poisoned regime during deposition. Further reduction for coating 9 is due to the reduction in power on the Cr-based coatings from 8 kW to 6 kW, a much greater effect is seen however when the power is reduced again to 4 kW (coating 10) with the coating thickness almost halving. Increasing the chamber pressure would cause further target poisoning resulting in only slight decrease in coating thickness from coatings 10 to 11.
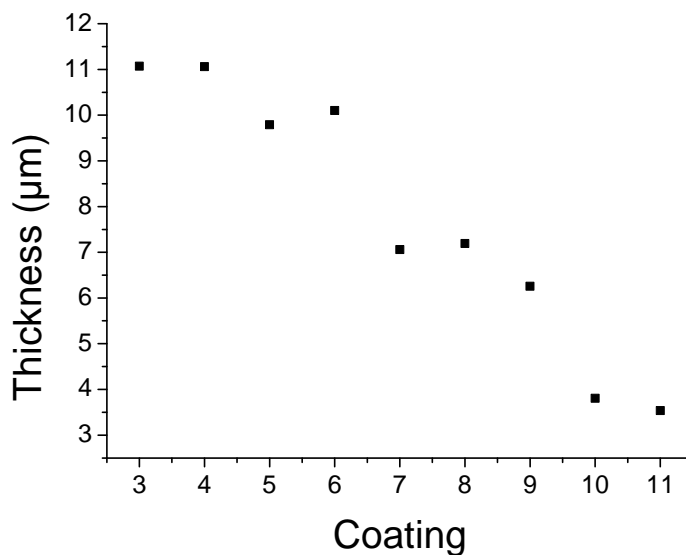
Figure 7.10. Coating thicknesses measure by calowear testing for the deposition series of coatings 3-11.

As described in section 7.2. Knoop hardness tests were performed by microindentation to provide a guide for coating development. The results of those tests are plotted in Figure 7.11. Coatings 3 and 4 show low Knoop hardness values; the coatings are soft and rather metallic, increased poisoning from coatings 3 to 4 shows no effect on the hardness.
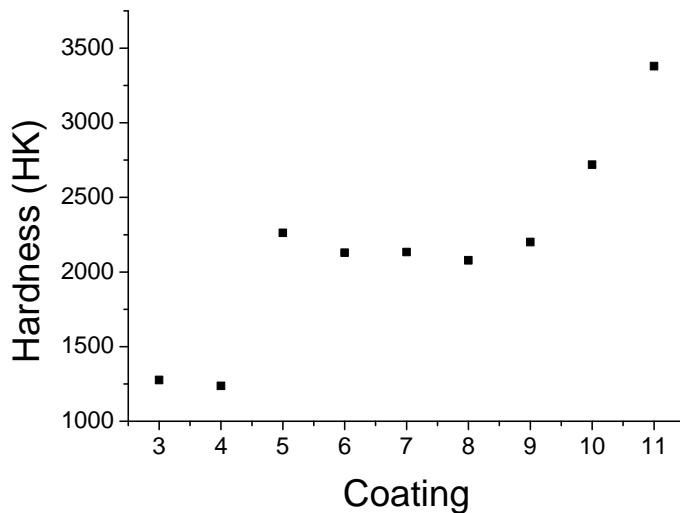
Figure 7.11. Knoop hardness (HK) for the coating series 3-11, measured by micro-indentation.

Further increase however causes a jump of approximately 1000 HK from coating 4 to 5. Hardness remains constant around this value despite increased poisoning with a slight decreasing trend until coating 9; the reduction in Cr-based target powers to 6 kW causes a slight increase in hardness from coating 8, but the effect of further decrease between coating 9 to 10 is far more significant. Increasing the deposition pressure again increases the hardness for coating 11 as the coatings become more ceramic.

Scratch test evaluates the cohesive and adhesive strength of the coatings. The critical loads for each coating are plotted in Figure 7.12. Coatings 3, 5 and 7 show a trend of increasing cohesive and adhesive failure resistance with increasing target poisoning. Coatings 4 and 6 both show improved coating adhesion with coating 6

proving to have much better cohesive failure resistance than any of the other coatings. Coating 8 performed poorly for both cohesive and adhesive strength. Coatings 10 and 11 have the highest critical load values for adhesion; the switch to pressure control causes the adhesion to suffer slightly but with an increased cohesive critical load value. Coating 11 was also tested with a WC substrate, labelled 11/WC on in Figure 7.12, the adhesion of the coating is slightly poorer with WC as the substrate compared to HSS likely due to an increased coating stress when deposited on WC, it is however, still better than or equal to all of coatings 3-9.
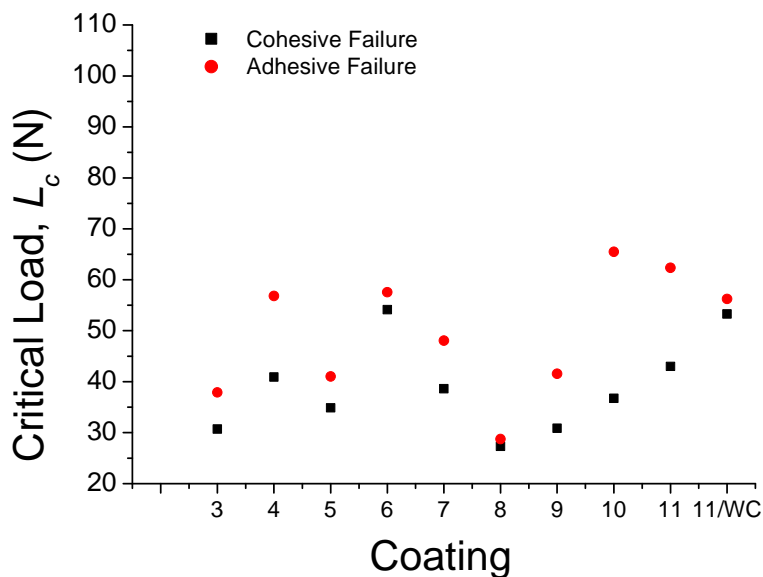
Figure 7.12. Critical Load, Lc,for adhesion and cohesion of coatings 3-11 on HSS substrates and also for coating 11 on WC substrate. Performed by scratch test and evaluated using optical microscopy.

For coatings 8, 9 and 10 we observe an increase in critical load for adhesive failure and also an increase in hardness. Hardness can develop either by a change in chemistry (becoming more ceramic) or by an increase in intrinsic stress. If the increase in hardness were due to stress within the coating, the coatings would become more brittle. Upon applying a load, an unstressed material will experience an increased compressive stress at the contact point; this will be dissipated and absorbed through the

196

material so that the stress at the coating-substrate interface remains 0. The plastic deformation region is larger for softer materials and hence the more energy can be absorbed. However, and intrinsically stressed material such as a nanolayer coating cannot dissipate the stress effectively enough, this leads to a build of stress at the coating-substrate interface and ultimately resulting in coating failure by cracking/delamination. Therefore, an increase in hardness due to increased stress would result in a reduction in adhesive strength. We observe an increase in adhesive properties, confirming that the hardness improvement is due to the inclusion of more gas phase atoms forming the CrAlN structure. Increasing the gas content further by switching to pressure control (coating 11) causes an increase in hardness but this time the adhesive properties decrease; this indicates that the further addition of gas phase elements is causing a strain in the CrAlN lattice caused by over-stoichiometry.

The pin on disk tests allowed the coefficient of friction of each coating to be measured. It could be said that the average coefficient of friction decreases with increased target poisoning from coating 3 to coating 11, as the points appears to follow that trend. However, each friction curve is very noisy and not always in steady-state. This leads to large standard deviations for each average taken and it can be seen that in actual fact all the coatings fall within each other's margin for error and so it can be said that there is little effect on the coefficient of friction with increased poisoning.
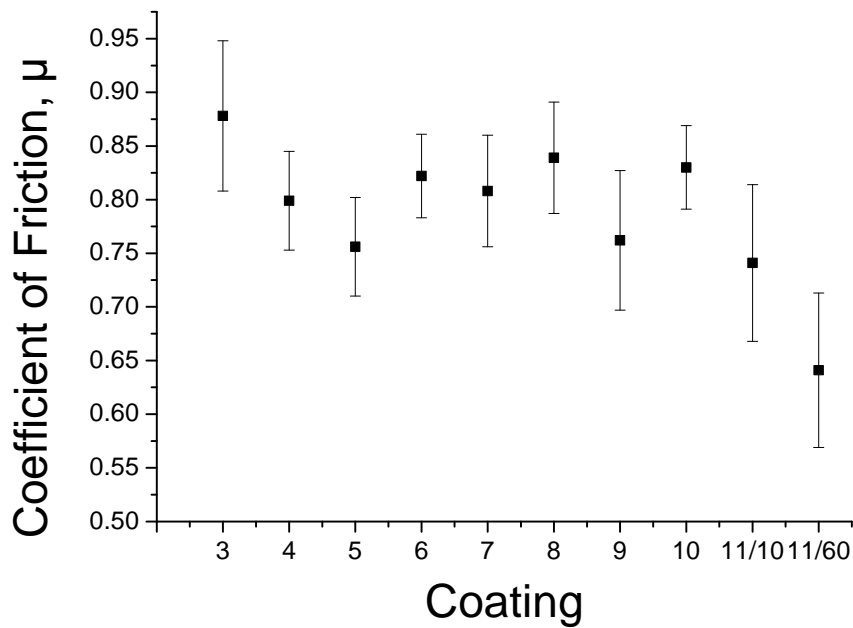
Figure 7.13. Average coefficient of friction measure by pin on disk tests for coatings 3-11 over 10,000 laps, and also 60,000 laps for coating 11.

The large variations in friction coefficient for the coatings during pin on disk testing could be due to the build-up and subsequent removal of various oxides on the surface, some of which may act as a solid lubricant (Cr_2O_3 for example), and others that may be very hard (Si-based oxides). In addition, the coatings contain carbon which is known to segregate into layers within multilayer coatings; exposure of these carbon-rich areas may lead to carbon graphitisation and brief periods of reduced friction coefficients.

As coating 11 performed very well in the wear test with a wear depth of only 0.89 μm (Figure 7.14), it was tested again for longer - 60,000 laps. It is only after increasing the sliding distance significantly that we see a marked improvement in the coefficient of friction for this coating series. The cause of this may be that there is sufficient time the solid lubricant phases that are created at the contact point to build up enough and remain within the wear track (rather than being forced out of the contact

region by the sliding action of the ball), allowing constant lubrication rather than intermittent.

It can be noted that there is an overall trend of decreasing friction coefficient with increasing nitrogen content. The literature suggests that the frictional force is caused by the shearing of micro-junctions during abrasive wear, as seen in Figure 3.14 [122], therefore the coefficient of friction is proportional to the number of points of contact leading to micro-junctions formed between the work piece and the tool. The increase in hardness measured for coatings with higher nitrogen content implies fewer surface aberrations developing from plastic deformation. If there are fewer contact points available on the coatings then the shear forces will be less; resulting in a reduced coefficient of friction [123].

The depth of the wear scar created by pin on disk testing was measured using profilometry; this was then plotted on a graph with coating total thickness and base layer thickness to determine how far through the coating the scar had penetrated. This is depicted in Figure 7.14. For samples 3, 4, 8 and 10 the coatings have not survived 10,000 laps and the wear scar has penetrated into the substrate. Coating 5 and 9 performed fairly well, with the wear scar not quite reaching the base layer, however, it is coatings 6 and 11 which show the most promise. Due to the different thickness of coatings 6 and 11 the percentage of total thickness removed was calculated: for coating 6, 40% of its total thickness was removed after 10,000 laps, however for coating 11 only 25% was lost. This indicates that coating 11 has by far performed the best during pin on disk testing. So much so, that it was tested over 60,000 laps and it can be seen that even with the increased sliding distance the wear scar is still within the multilayer structure and has yet to even reached the base layer.
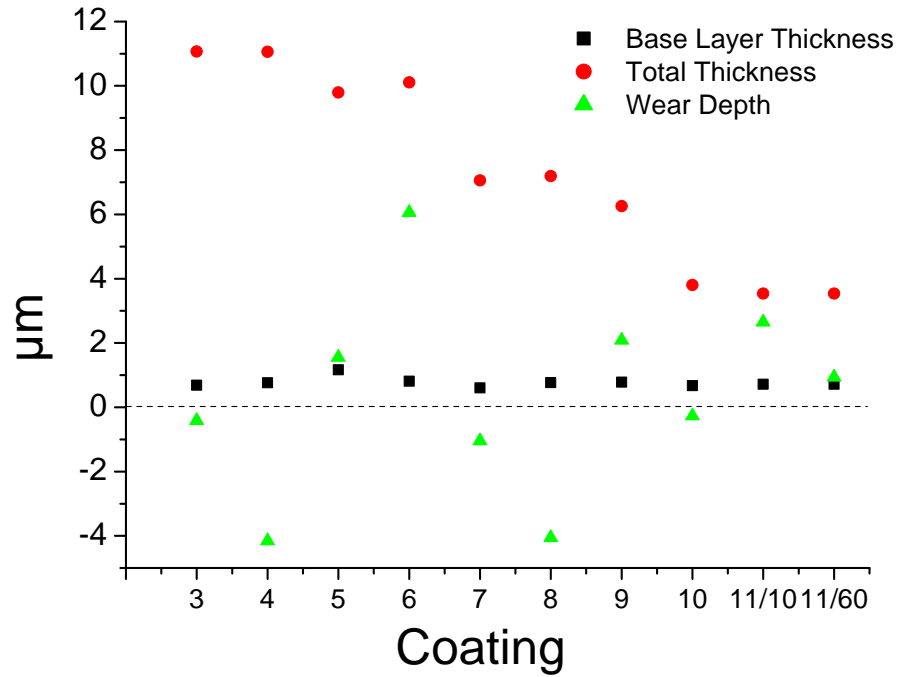
Figure 7.14. A plot of total coating thickness, base layer thickness and wear depth for each of the coatings 3-11 over 10,000 laps and also coating 11 over 60,000 laps.

The wear rates for each coating were calculated and plotted for comparison (Figure 7.15). The trend naturally follows the wear depth data (Figure 7.14) in that coatings 3 and 4 have the highest wear rates resulting in the wear depth penetrating through to the substrate. The wear rate improves for coating 5 which almost reached the base layer after 10,000 laps. Coatings 7 and 8 have a similar wear rate to coating 5, however, their thicknesses are smaller and hence why the wear scar penetrates down into the substrate and coating 5 does not. Coatings 6, 9 and 10 display similar wear rates and it is again due to coating thickness whether or not the coating survives; coating 6 is approximately 4 µm thicker than coating 9 and approximately 6 µm thicker than coating 10. If wear rates are similar then coating thickness dictates whether a coating survives in a given number of laps.

We see a pattern of increasing wear rate with hardness and cohesive failure resistance; coating 11 has the lowest (most desirable) wear rate and has the highest hardness, combining this with good cohesive and adhesive properties suggests this coating may be the most suitable of the coating series for cutting tests - based on its mechanical and chemical properties.
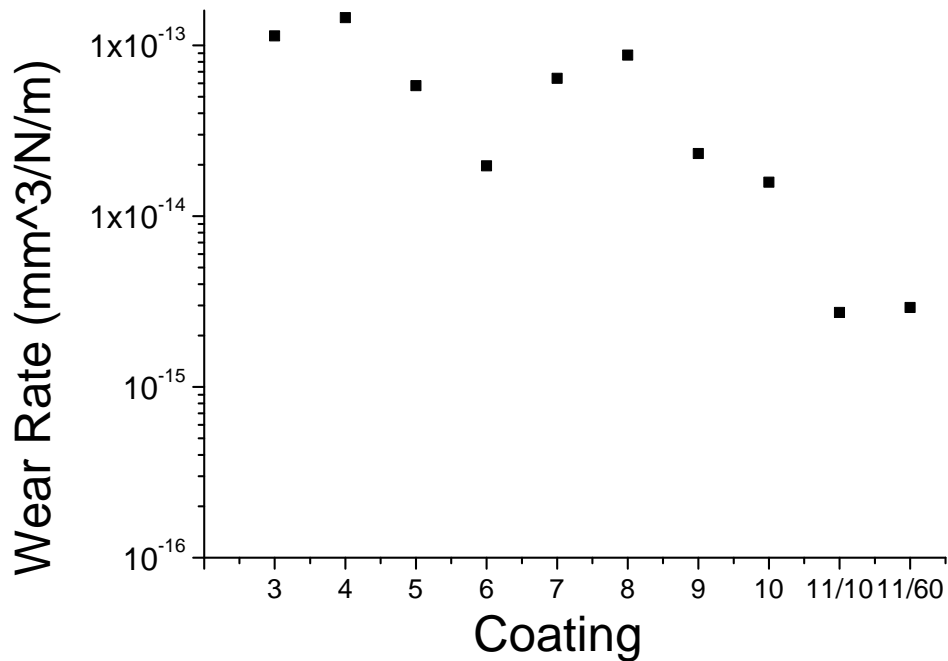
Figure 7.15. Calculated wear rates for coatings 3-11 after 10,000 pin on disk testing and also 60,000 laps for coating 11.

In general, we see that the hardness data supports the XRD, Raman and EDX quite well in that it is apparent that there are a number of coatings that can be grouped based on their properties. Coatings 3 and 4 have a Me_2N hpc structure which is known to be softer than the MeN structure; the high Me:N ratio in the coatings causes this softer structure to form. We then move into a transition period for coatings 5 to 9 where the hardness values are approximately constant at 2200 HK; the peak convolution and broadening of the XRD spectra for these coatings indicates a mixed Cr_2N + CrN lattice

structure. For this group, we have a range of coating parameters and poisoning levels which produce coatings that behave similarly. Finally, we have a third group (coatings 10 and 11) where the hardness increases towards being classed as 'superhard'; this change is attributed to the N content of the coating increasing enough to surpass stoichiometry and the Me:N ratio drops below 1. This corresponds to the CrN phase becoming dominant in the XRD patterns and the characteristic CrAlN pattern observed for coatings 1 and 2 begins to take shape.

7.3.3. Isothermal Heat treatment – A Raman study

The high temperature stability and oxidation resistance of the coating series 3-11 was studied using Raman spectroscopy. The spectra for samples isothermally treated to 600 ˚C, 800 ˚C and 1000 ˚C are presented with an optical image of the location taken through the light microscope integrated into the Raman detector. Grouping by temperature allows direct coating comparison; we shall begin by discussing the effect of heating to 600 ˚C has on the coatings. Little difference can be seen in the appearance of the coatings' surfaces by comparing the optical images of the surfaces at 600 ˚C (Figure 7.16) with the as-deposited (Figure 7.8); both the topography and colour are maintained.

We do observe some difference however when analysing the Raman spectra plotted in Figure 7.17. For coatings 3 to 9 the second characteristic CrAlN peak at approximately 740 cm^{-1} has diminished significantly and is barely detected. The most notable change in peak pattern, from as-deposited spectra, is for coatings 5 to 11; all of these coatings show an increase in the intensity of the broad peak centred around 1500 cm^{-1}. The diminished CrAlN pattern at this temperature signifies that this increase must be due to the migration of C to the surface. The absence of C in coatings 3 and 4 is likely due to low gas species included in these metal rich coatings. Interestingly, for the transition

region coatings that are a mixed Cr_2N+CrN phase (coatings 5-9) we begin to see C peak separation indicating slight C graphitisation. This effect is not observed for coatings 10 and 11, which are fcc-CrN phase; the single phase coatings restrict/delay C graphitisation.
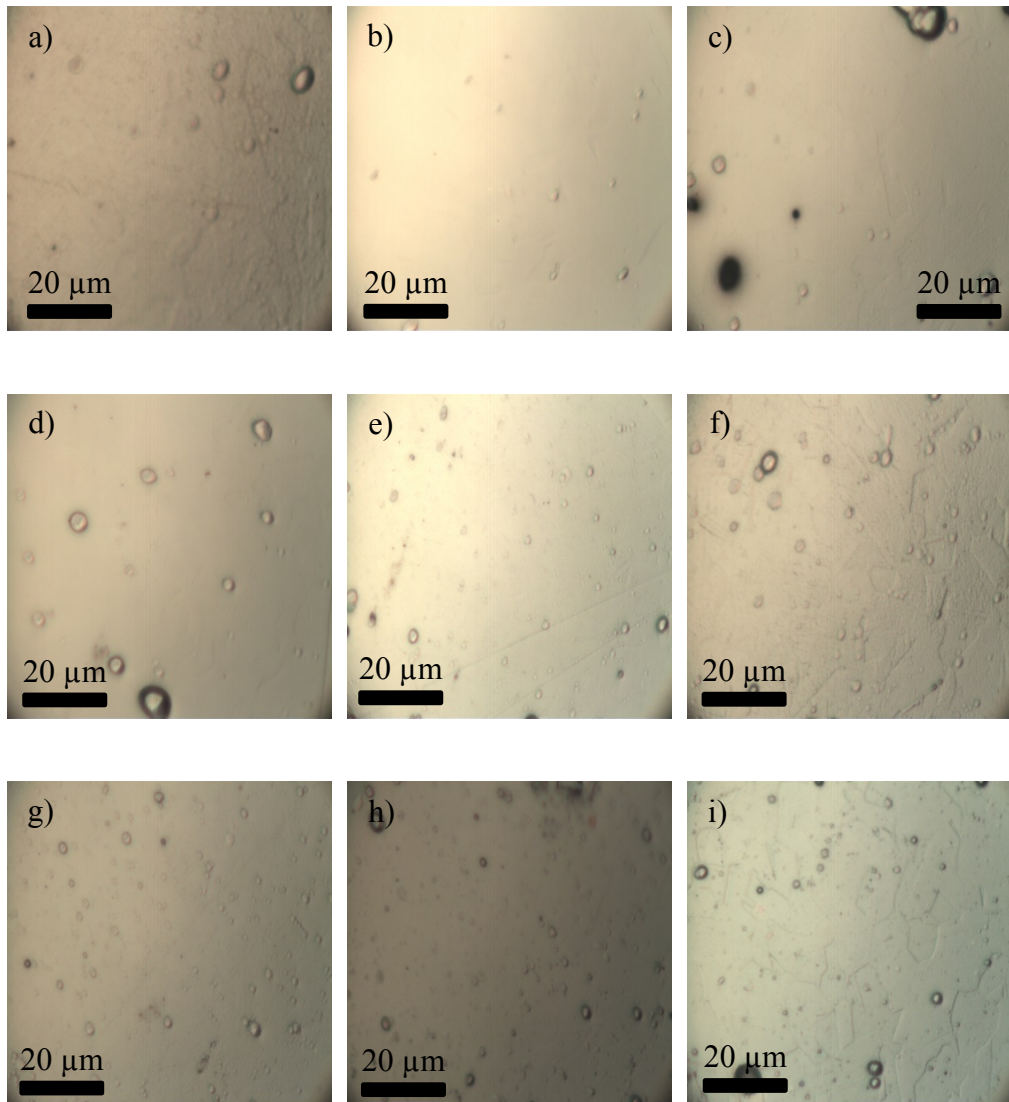
Figure 7.16. Optical images of the sample surface for coatings 3-11, a)-i) respectively, after isothermal heat treatment to 600 ˚C.
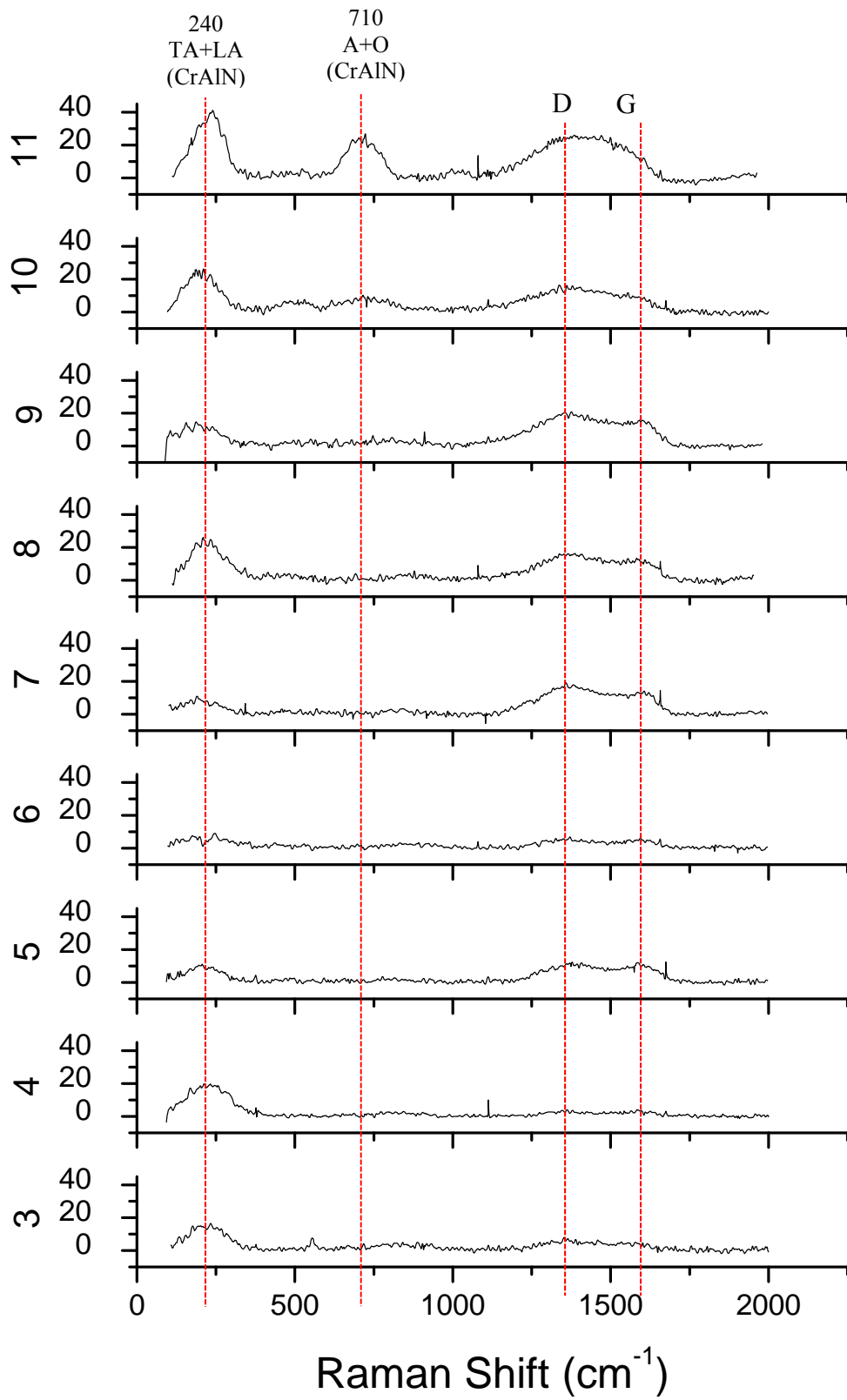
Figure 7.17. Raman spectra for coatings 3-11 after isothermal heat treatment to 600 ˚C.

At 800 ˚C, we begin to notice a change in the colour of the surface of the samples ranging from green to purple for coatings 3-10; this change of colour signifies the further development of the protective surface oxide, which acts as a passivation layer. This layer will be present at 600 ˚C however will be too thin to initiate a colour change. The observation that coating 11 appears a very similar colour at 600 ˚C and 800 ˚C indicates its improved resistance to oxidation with minimal growth of the passivation layer.

There appears to be a slight increase in roughness for coatings 3 and 4 and islands of oxide begin to grow on the surface, whereas coatings 5-11 remain rather smooth with a similar topography to the coatings treated to 600 ˚C. Coatings 5 to 10 exhibit crack formation (cracks for coating 9 not shown in Figure 7.18 but present), due to varying intrinsic stresses within the multilayer coatings and the difference in thermal expansion between substrate and coating. The process of depositing a multilayer coating inherently causes a compressive stress to develop as different layer lattices attempt to accommodate each other. As the substrate expands during heat treatment it initially relaxes the stress within the multilayer system until stresses reach 0, after which, further substrate expansion imposes a tensile stress until the energy build up is too much for the coating to withstand causing cracking. Hard ceramic coatings have very small plastic deformation regions and so the material failure occurs at lower stresses than for more metallic materials. This helps to explain why coatings 3 and 4 do not experience cracking; their high metal content increases their ability to plastically deform and absorb more of the stress energy induced through substrate expansion.
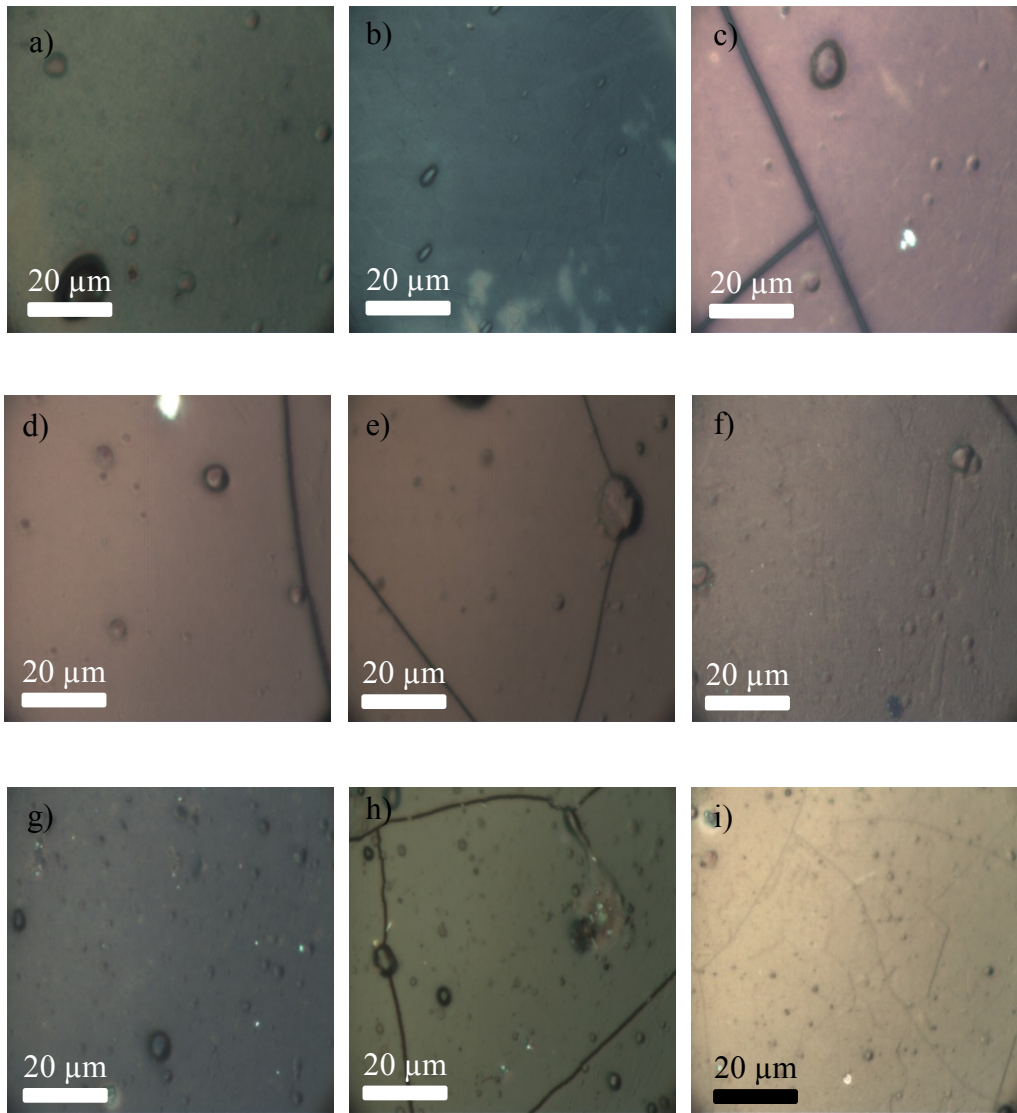
Figure 7.18. Optical images of the sample surface for coatings 3-11 after isothermal heat treatment to 800 ℃.
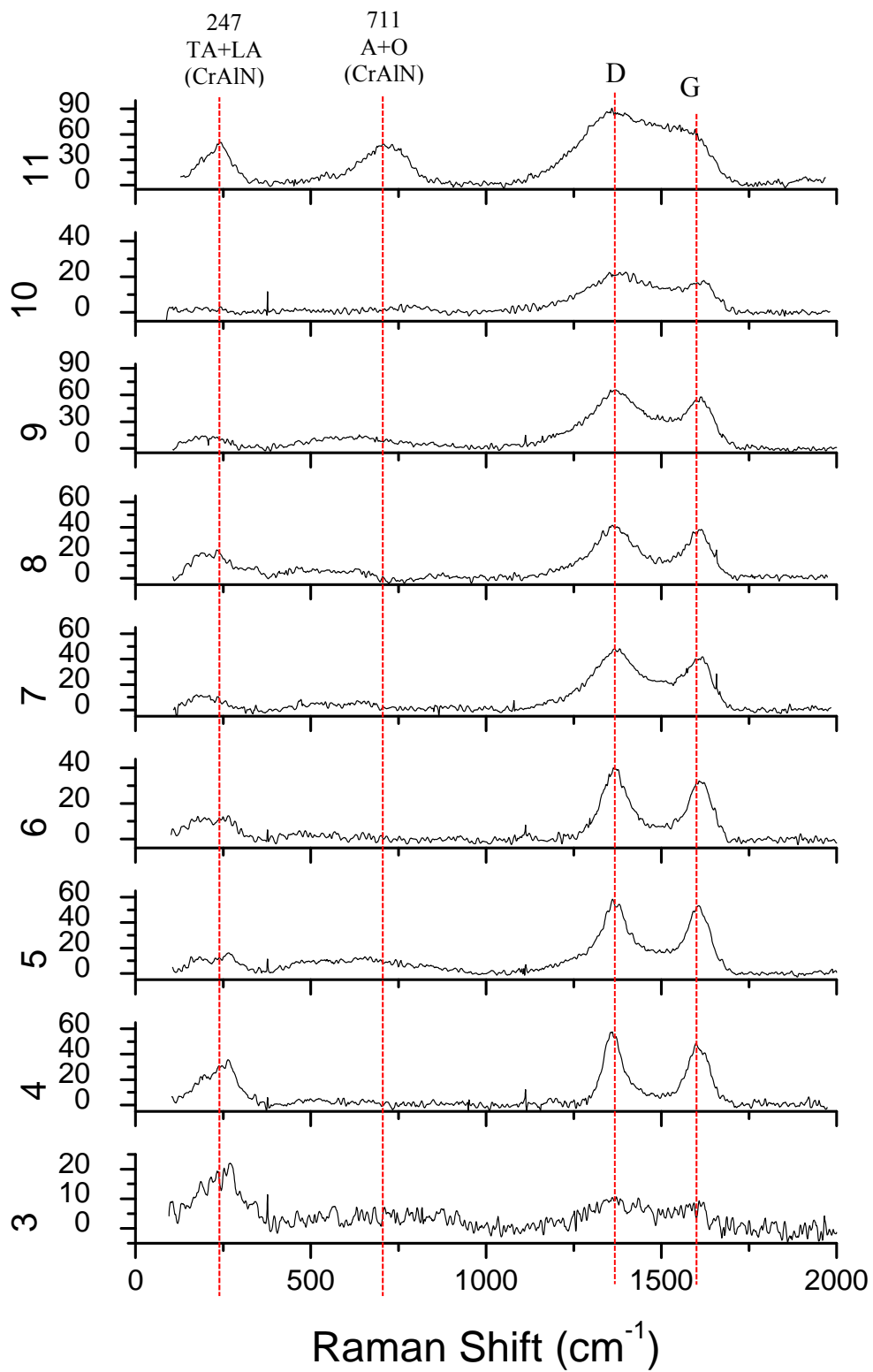
Figure 7.19. Raman spectra for coatings 3-11 after isothermal heat treatment to 800 ˚C.

The trend of an increased intensity of C peak observed for the coatings heated to 600 ˚C is again observe for those heated to 800 ˚C. High temperatures are causing C to migrate from within the coating to the surface and hence be detected. The difference however, is that at 800 ˚C the D and G peaks become distinguishable indicating carbon graphitisation. This is most prominent for coating 4 with clear peak separation, decrease graphitisation occurs with increased gas content from 4 to 11. With increased gas content it may be suspected that this would mean more C inclusion in the coating, more C migration and therefore more graphitisation at high temperatures. As this is not the case, the increased C inclusion with reduced metal content implies that the carbon is likely evaporating more easily when it reaches the surface or is forming carbides within the lattice. The weak carbon region for coating 3 supports the evidence that this coating is very metal rich with little gas phase elements included.

The characteristic CrAlN 3 peak pattern is only maintained for coating 11; the coatings ability to maintain its structure and resist cracking at 800 ˚C is promising for its survival at higher temperatures.

Optical image of coating 5 shows cracks that appear to be filled with another material, we have termed these 'walls' and a comparison between the coating area and the wall has been made via Raman spectra (Figure 7.20). The coating area shows clear carbon band peak separation indicative of carbon graphitisation, with remnants of the CrAlN peak pattern. Within the wall however the carbon peaks are not clearly separated and the disordered region is more prominent. The presence of peaks at 530 and 680 cm^{-1} indicate the presence of crystalline Cr_2O_3 and spinel, respectively [69]; as the 680 cm^{-1} peak has a greater intensity the suggestion is that the walls are dominated by the spinel, Fe_2CrO_4.
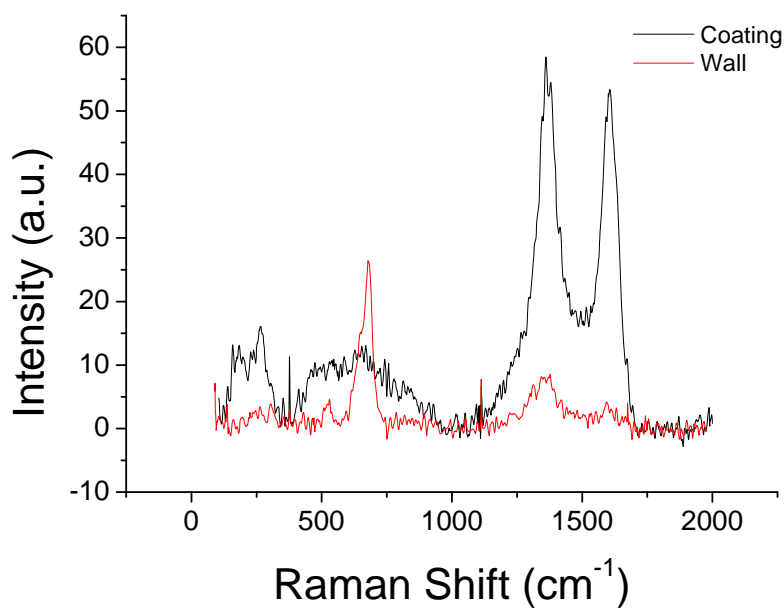
Figure 7.20. Raman spectra of coating 5 isothermally heat treated to 800 ˚C. The black line indicates and the spectrum for the coating area and the red line is that of the 'wall'.

A more detailed investigation of crack formation and development will be given in chapter 8, at this point we simply note their presence and that the 'walls' consist of Cr-based oxides. Most importantly we do not detect any Fe oxide peaks in the low shift region (297 cm^{-1} and 412 cm^{-1}) indicating that the cracks formed do not reach the substrate - this is also true for all coating cracks that develop after isothermal heat treatment to 1000 ˚C.

Increasing the isothermal heat treatment temperature to 1000 ˚C had a further effect on the coatings; coatings 5-11 all cracked whilst coatings 3 and 4 were resistant. Significant changes to surface morphology occurred for some of the coatings; reasons for these changes and the crack formation will now be discussed.
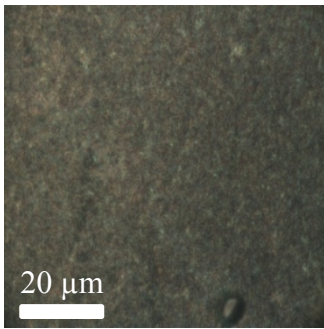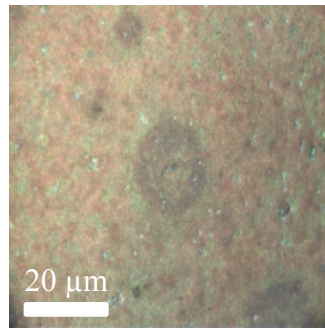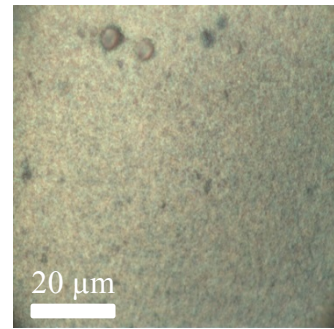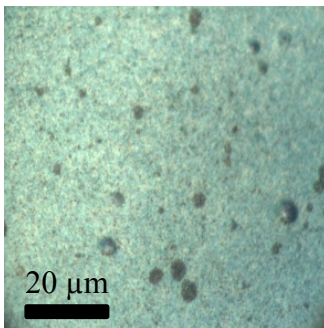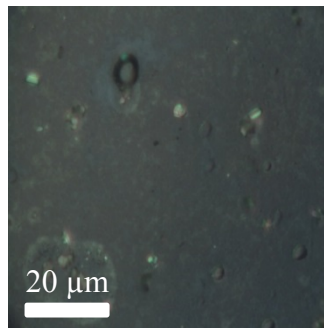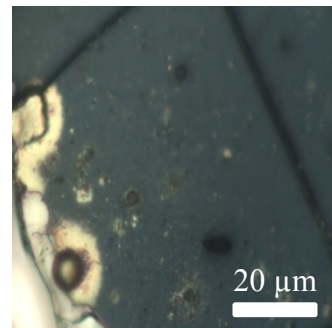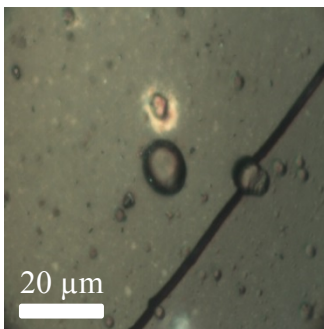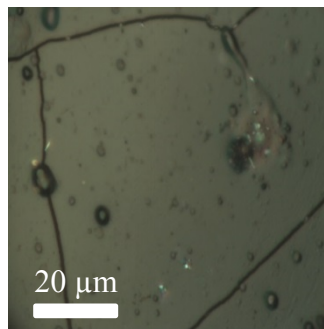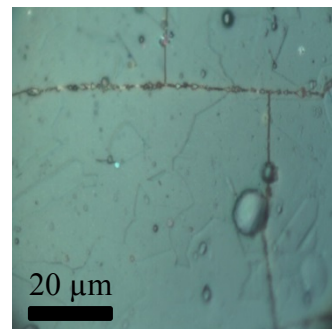
Figure 7.21. Optical images of the sample surface for coatings 3-11 after isothermal heat treatment to 1000 ˚C.
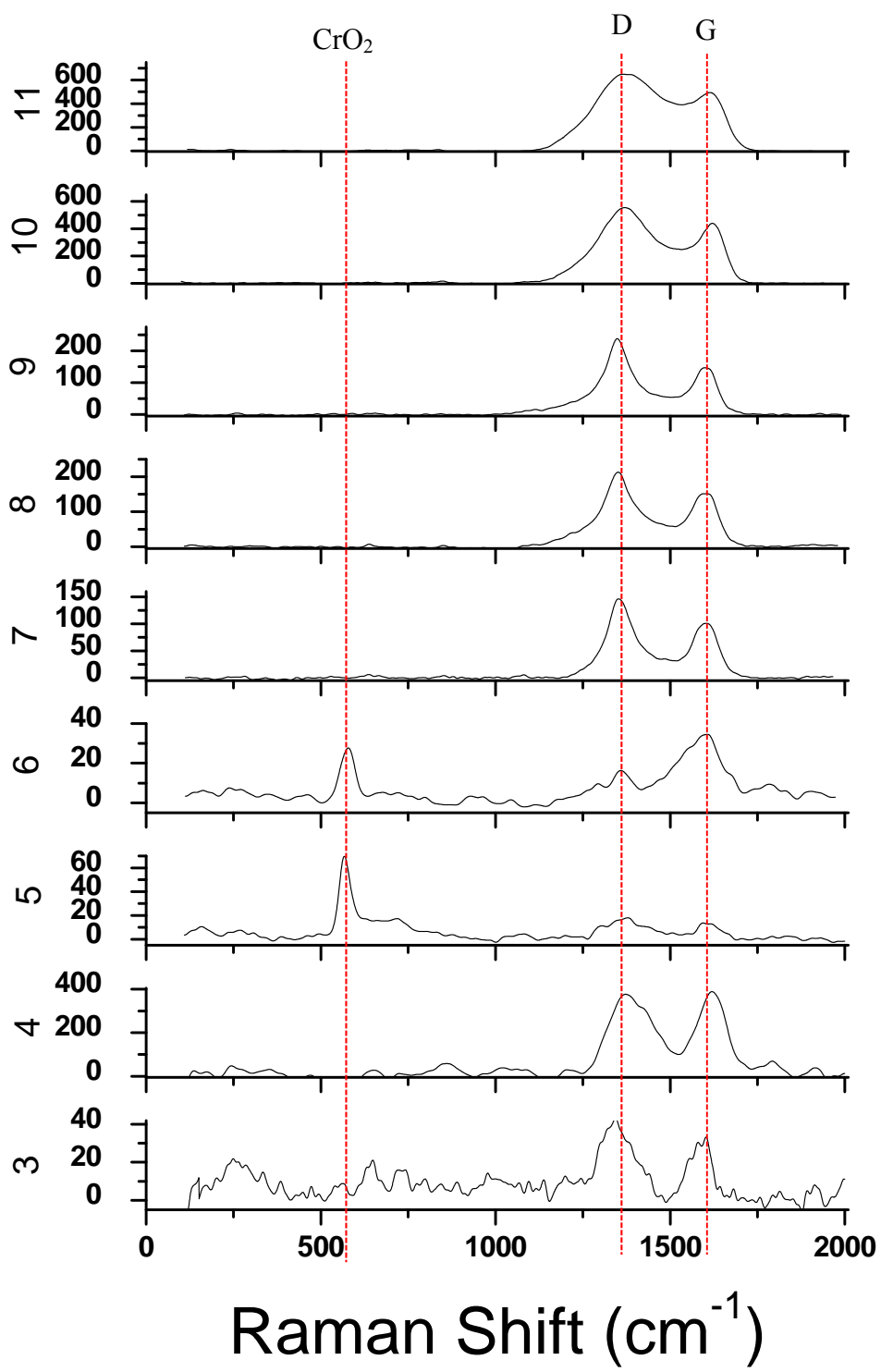
*Figure 7.22. Raman spectra for coatings 3-11 after isothermal heat treatment to 1000 ˚C.*

The carbon region for coating 3 displays clear peak separation and carbon graphitisation at higher temperatures; this separation was not evident at 800 ˚C. Coating 4 also shows good peak separation, both coatings show no oxide peaks. The surface of these coating has become rough. We have seen previously that C migration induces surface smoothing; it appears that between 800 ˚C and 1000 ˚C the C coalesces and builds up in islands on the surface causing roughness. We can be certain that this roughness is not due to the build-up of an oxide layer from the Raman spectra.

For the first two coatings of the 'transition region' (coatings 5-9), coatings 5 and 6, CrO_2 oxides are detected at approximately 570 cm^{-1} [73]. The C peaks for these two coatings is less prominent than for 800 ˚C suggesting perhaps some C is reacting with the air and being released as CO_2. Coatings 7 - 11 show increased graphitisation of carbon compared to the spectra taken after 800 ˚C; the pattern suggests that with increased gas content in the coating the higher the temperature required to graphitise the C in the coating. Coating 11 maintained its CrAlN pattern up to 800 ˚C, however, at 1000 ˚C it is no longer visible. This is an indication of significant C migration to the surface.

From the Raman spectra we suggest that C migration to the surface, when the structure is dominated by Cr_2N, initially hinders coating oxidation. With increased gas content the coating enters a transition period of mixed Cr_2N and CrAlN phases; at this point phase rather than the C migration becomes the dominant factor in oxidation resistance as coatings 5 and 6 show CrO_2 oxide peaks. With increased gas content and improved stoichiometry the coatings become increasingly resistant to oxidation [124]. The transition from mixed Cr_2N and CrAlN to single CrAlN phase also inhibits graphitisation of C.

Cracking is not observed for coatings 3 and 4; in comparison to the other coatings, they are metal-rich and soft, therefore, more able to absorb the stresses induced by thermal expansion of the substrate, plastically deforming and improving crack resistance. From coating 5 onwards (inclusive) the metal:gas ratio is reduced, the coatings become more ceramic, harder and brittle. They therefore experience cracking as they have a reduced plastic deformation region compared to coating 3 and 4. As cracking may appear to be detrimental property of a coating, it would seem as though coatings 3 and 4 would be the most desirable to use for cutting tests, however, the mechanical properties are not so promising. In addition, as previously mentioned, the cracks in the coatings appear to be filled with some material. In light of this, coating 11 has been selected for further investigation into crack formation due to its superior mechanical properties and high temperature stability.

7.4.   Summary

- Coating composition was shown to be controllable by the monitoring of the Al OES signal and subsequent gas flow control via the Speedflo controller. Al signal % was used to select a position on the AlSi target poisoning hysteresis at which to deposit CrAlBYCN/AlSiCN films

- Controlling the deposition via this method proved ineffective at acquiring coatings with the desirable mechanical properties due to their high metal content. The process control would not permit further increase in gas phase species to achieve stoichiometry

- Increasing the gas content of the coatings was then achieved by reducing the power on the Cr-based targets, and even further by increasing the deposition pressure

- With increased gas content the coatings transitioned from metal rich Cr_2N phase (coatings 3 and 4), through a mixed Cr_2N and CrAlN phase (coatings 5, 6, 7, 8 and 9), to a single phase CrAlN structure (coatings 10 and 11). The mechanical properties became more desirable for cutting tool application with increased gas content as the coatings became more stoichiometric and ceramic

- All coatings were thermally stable and resistant to oxidation after isothermal heat treatment to 600 ˚C and 800 ˚C. C migration to the surface was detected using Raman; it was seen that increasing the gas content delays the graphitisation of C to higher temperatures. Coatings 5 and 6 showed CrO_2 Raman peaks; oxidation resistance is improved with increased gas content due to increased stoichiometry

- Coatings 3 and 4 were resistant to thermal cracking due to their metal-rich composition. With increased stoichiometry the coatings became harder and therefore more brittle and less able to absorb stresses. The cracks appear to have been filled with another material creating 'walls' which will be investigated in chapter 8

- Coating 11, despite cracking at elevated temperatures, showed the most promise for cutting tool applications and was therefore selected for further investigation

8.   The effect of substrate bias on crack formation

8.1.   Motivation

From chapter 7, Coating 11 proved to show the most promise as a potential candidate for cutting test investigation. The development of this coating has seen an improved understanding of process conditions on coating performance and properties from the original coating 1. We have demonstrated how this has led to a coating with improved adhesion and wear resistance with high temperature stability and oxidation resistance. However, to improve the coating further, we investigated the formation of coating cracks at high temperatures that were observed for all coatings in chapter 7.

Crack formation during heat treatment is due to a difference in thermal expansion between the coating and substrate; the expansion of the bulk substrate induces a stress within the coating, building up energy until the coating cannot withstand any further structural deformation and cracks. Multilayer coatings are inherently stressed due to inter-layer lattice mismatch, the thermal expansion of the substrate acts to relax the coating to a zero stress state. Further expansion induces a stress until breaking point and crack formation. The inherent stress within the multilayer coating therefore determines whether cracks form or not at a given temperature. A more stressed coating will relax over a larger temperature range for the same substrate and therefore delay the induced stress and failure through cracking to a higher temperature.

In this chapter we investigate the effect of substrate bias on coating properties and crack formation to test the theory suggested. The process conditions for coating 11 are repeated however this time the substrate bias voltage is increased to -60 V; this coating is labelled coating 12.

8.2. Results

8.2.1. Microstructure and Composition

Images were taken of the as-deposited coatings using optical microscopy and SEM. There is no discernible difference in coating structure between coatings 11 and 12 when viewed through the optical microscope (Figure 8.1); both coatings are relatively smooth with similar concentrations of droplets. Droplet composition was discussed in section 5.3.2, figure 5.5 shows the characteristic Raman spectra for Al and Si-based oxides, originating from arcing of the highly reactive AlSi targets. The faceted grain structure of the austenitic steel substrate can be seen through the coating. Again, the appearance of the substrate grain structure through the coating, which has been observed in all coatings, is an indication of the substrate acting as a strong template for coating growth.
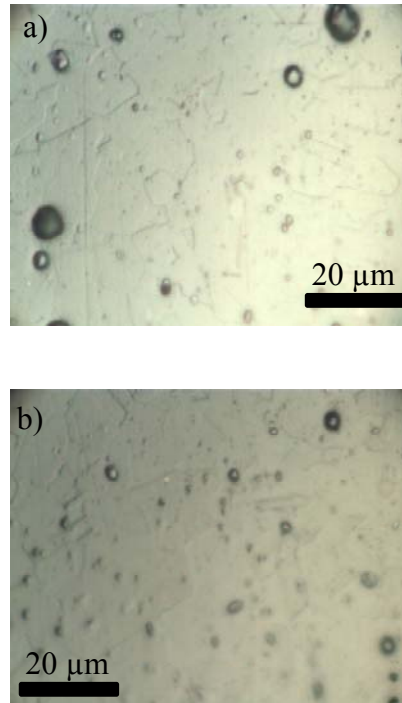
Figure 8.1. As-deposited optical microscopy images of coatings 11 (a) and 12 (b).

Images taken using the SEM (Figure 8.2) show a fine grain structure with clearly visible column tops for both test bias'. Increasing the bias from 40 V to 60 V causes the grains to elongate along a growth axis; this is an effect of densification [125] suggesting that a higher bias promotes denser coatings.
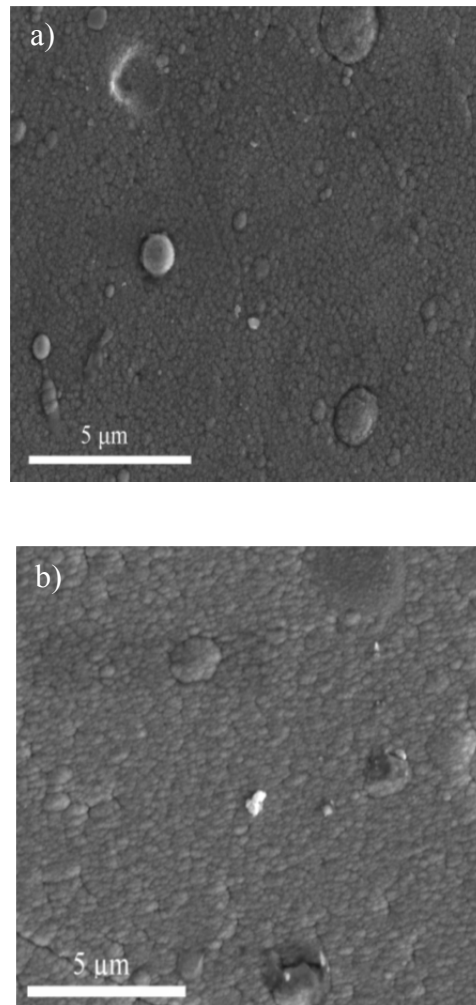
Figure 8.2. SEM images of the as-deposited coatings 11 (a) and 12 (b).

By comparing the glancing angle XRD scans for coatings 11 and 12, Figure 8.3, it can be seen that increasing the bias to 60 V has no effect on the coatings structure; both exhibit the peak pattern of the fcc-structure associated with CrN. As the substrate bias is the only variable between the two coatings, the chemistry is expected to be maintained, which XRD confirms. There is a slight peak shift to the higher angles with increased bias; 37.26 ˚ to 37.42 ˚ for the (111) peak, 43.34 ˚ to 43.66 ˚ for the (200)

peak and 63.46 ˚ to 63.50 ˚ for the (220) peak. From Bragg's law (Equation 3.5), if $n\lambda$ is constant, then up to $\theta = 90$ ˚ an increase in θ must have been caused by a decrease in d. A reduction in lattice spacing is caused by a compressive stress in the material and therefore increasing the bias induces an increased compressive stress in the coating.
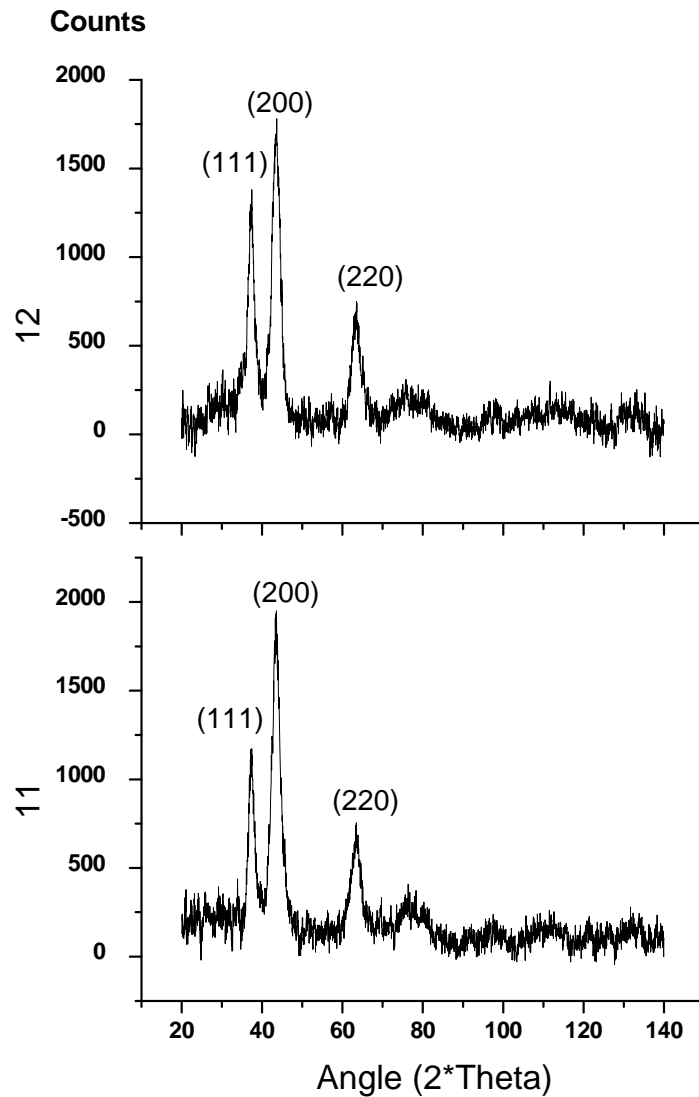
Figure 8.3. Glancing Angle XRD patterns for coatings 11 and 12, with Omega = 1 and 2θ range of 20˚ - 140˚.

Comparison of the surface phase composition determined by Raman spectroscopy shows that increasing the bias has no significant effect; the characteristic 3-peak CrAlN pattern discussed previously is clearly visible in both the spectra for coatings 11 and 12. Also note similarities in peak ratios between the two coatings, confirming phase consistency between the two. The presence of the carbon region is important for the formation of graphitic phase carbon during wear testing which acts as a solid lubricant.
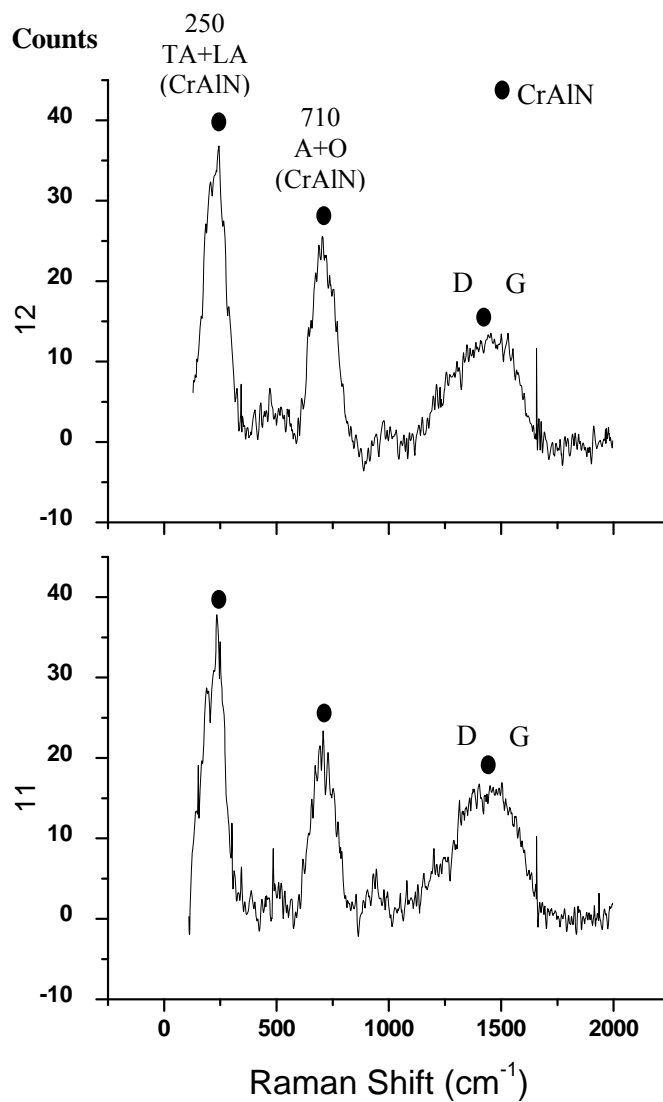
Figure 8.4.Raman spectra of as-deposited coatings 11 and 12.

220

EDX scans of the coating surfaces were taken over the areas imaged in Figure 8.2 to compare the chemical compositions of the two coatings. Light elements such as carbon and boron cannot be reliably detected in the system used due to the overlapping of peaks with other elements in the low kV range. The Yttrium content is low that it also is omitted from the comparison due to unreliability. This then leaves nitrogen, aluminium, silicon and chromium for comparison; table 8.1. indicates that an increased bias causes a decrease in the composition of Cr, Al and Si, and a corresponding increase in N content. This may be due to an increased attraction to the substrate for N as it has a much higher electronegativity than the metal elements, N (3.04) compared to Al (1.61), Si (1.9) and Cr (1.66).

Table 8.1. Elemental composition (at. %) of nitrogen, aluminium, silicon and chromium for coatings 11 and 12.

	Elemental composition (at. %)	
Element	Coating 11	Coating 12
N	56.8	62.0
Al	21.8	20.0
Si	2.1	1.9
Cr	19.3	16.1

Thus far, as expected, we have observed very little difference in the coating structure and phase with increased bias. It has however increased the gas phase element content of the coating slightly and induced densification of the coating grains/columns.

8.2.2.   Mechanical Properties

We shall now discuss the effect substrate bias has on the mechanical properties; the tests undertaken and their results are displayed in table 8.2. Increasing the substrate bias reduced the coating thickness by almost 1 μm; a higher bias accelerates ions towards the surface more greatly, meaning they arrive at the substrate with higher energies than at a lower bias. At a higher bias, some arriving ions may have enough energy to sputter atoms from the growing coating; there is therefore a competition between coating growth and resputtering. The resputtering interrupts the columnar growth of the coating and leads do the densification observed in the SEM images of the surface, Figure 8.1.

Table 8.2. Mechanical properties for coatings 11 and 12.

Mechanical Test	Coating 11	Coating 12
Thickness	3.5 μm	2.6 μm
Hardness	3379 HK	3828 HK
Critical load of Adhesion (Critical load of Cohesion)	62 (43) N	65 (34.4) N
Coefficient of Friction (10,000 laps)	0.74+/-0.07	0.59+/-0.09
Wear Depth	2.6 μm	1.9 μm
Wear Rate (10,000 laps)	2.7×10^{-15} m^{3}N^{-1}m^{-1}	1.4×10^{-15} m^{3}N^{-1}m^{-1}

There is a significant increase in the hardness of the coatings by increasing the bias, coating 12 is 450 HK harder than coating 11; the cause of this could be due the increased N content indicated by EDX, however the most significant contribution to the hardness will be that a higher bias induces an increased inherent stress in the material. With increased hardness it is expected to see a decrease in the coefficient of friction and hence an improved wear rate; this relationship is confirmed in the results of coating 12. Despite the reduced coating thickness for coating 12, the lower wear rate means that the wear scar has not penetrated through to the substrate after 10,000 laps and is still within the multilayer region.

As discussed, increasing the substrate bias voltage increases the inherent stress within the coating, the mechanical benefits of which have been described above; however, there is a drawback – brittleness. The increased hardness means the coating is less able to plastically deform and absorb the force supplied to it by the stylus of the scratch tester. The stress is therefore transferred directly to interfaces, rather than being dissipated within the material as it would for softer materials; the build-up of stress at interfaces causes adhesive failure. The interface at which this build-up and failure occurs can dictate a coatings performance. For example, coating 11 experiences cohesive failure at higher loads than coating 12, 43 N vs. 34 N respectively, however its critical load for adhesion is lower, 62 N vs. 65 N respectively. This suggests that the cohesive failure of the inherently higher stressed coating 12 is acting to delay the stress build up at the coating/substrate interface and therefore extending its critical load of adhesion   value.

8.2.3.   Thermal Properties

To study the high temperature stability, crack formation and crack development at elevated temperatures the coatings were isothermally heated in a furnace at 600 ˚C, 800 ˚C, 1000 ˚C. Optical microscopy images of coating 11 (Figure 8.5) shows a smooth surface at 600 ˚C, reminiscent of the as-deposited image in Figure 8.1. Increasing the temperature to 800 ˚C causes a very slight colour change as the surface passivation oxide layer grows, but most notably is the beginnings of crack formation, originating from droplets. With further increase in temperature to 1000 ˚C, the coating colour becomes a bright blue but maintains its smoothness – the faceted grain structure of the austenitic steel substrate that acted as a growth template can still be observed in the coating surface. The cracks observed at 800 ˚C are far more prominent at 1000 ˚C and appear to be filled with small crystals.

To now compare coating 12 after heat treatment we see also that at 600 ˚C the coating is still smooth with the substrate grains visible. At 800 ˚C there is a greater colour change than for coating 11 suggesting a thicker passivation layer has formed for coating 12, and the surface appears rougher. Notice the lack of surface cracks suggesting that the coating deposited at a higher bias is resistant to crack formation. At 1000 ˚C, the surface is much rougher for coating 12; the substrate grain structure is no longer visible through the coating and islands of surface material (likely oxides) have formed. We can also see in both coatings that cracks have formed and been filled with a material creating a 'wall' between areas of coating.
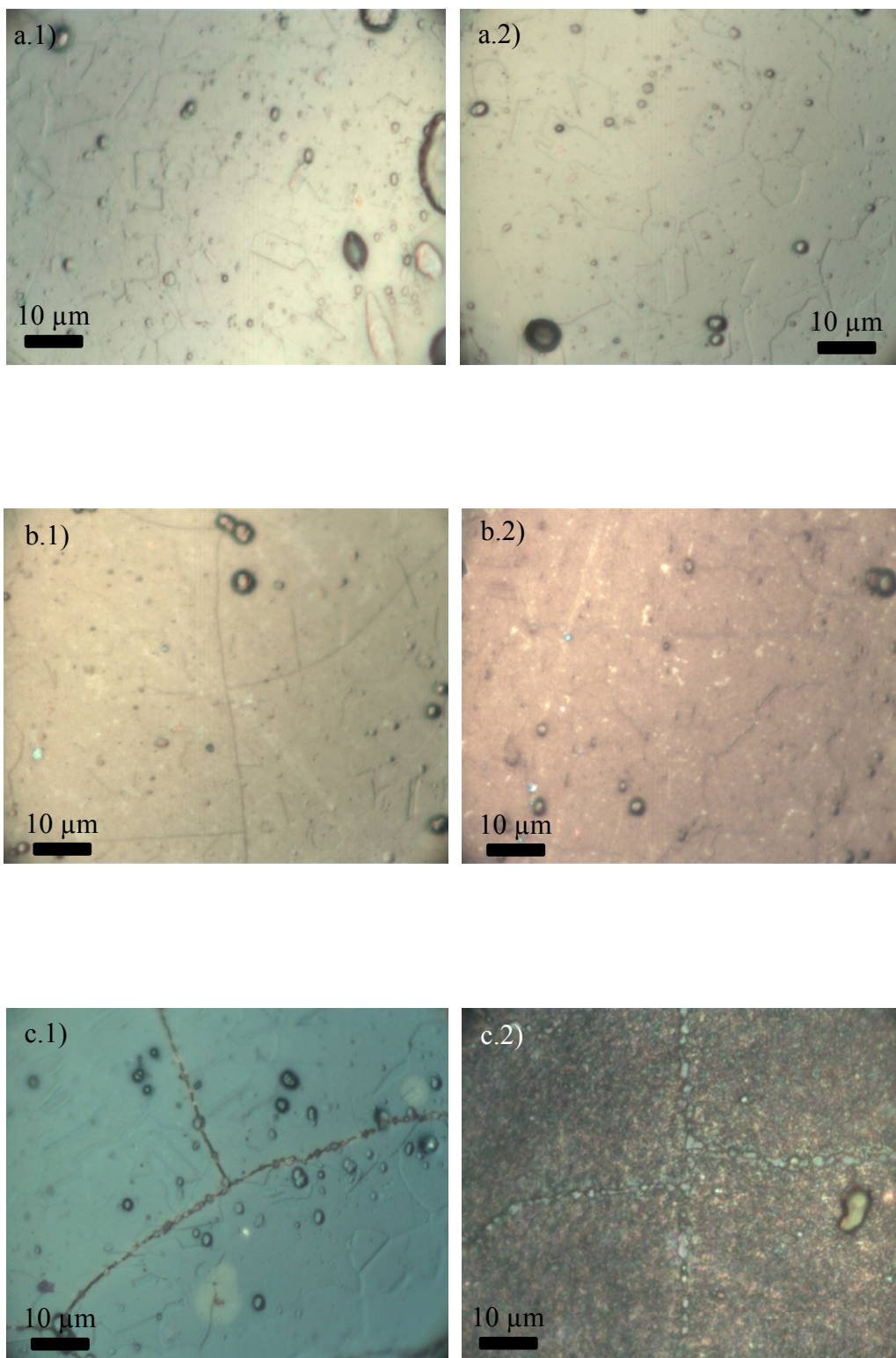
Figure 8.5. Optical microscopy images of coatings 11 (1) and 12 (2) after isothermal heat treatment at 600 ℃ (a), 800 ℃ (b) and 1000 ℃ (c).

Figure 8.6. SEM of coatings 11 (1) and 12 (2) after isothermal heat treatment at 600 ˚C (a), 800 ˚C (b) and 1000 ˚C (c).

226

As we have observed for all coatings deposited during this project, isothermal heat treatment to 600 ˚C, causes densification of the as-deposited; the grain structure and column tops observed in Figure 8.2 are no longer visible in the SEM images after 600 ˚C, we now see the austenitic steel grain structure of the substrate very clearly with a smooth surface. As with the optical microscopy images (figure 8.5) there is little evidence in SEM images of extensive oxidation or cracking at 600 ˚C.

SEM of coating 11 after 800 ˚C heat treatment highlights the crack formation mechanism; the multilayer architecture causes an inherent stress within the material, the thermal expansion of the substrate relaxes the coating to a stress of zero, after which further expansion induced a tensile stress. This stress builds up at droplets and defects until the coating must crack in order to release the energy build-up; therefore, cracks originate at droplets embedded within the coating and propagate throughout creating a network of cracks that gives the coating a pavement appearance with regular and relatively straight cracks.

These cracks are not observed for coating 12 after 800 ˚C heat treatment, another feature is prominent; pores at the surface begin to form along grain boundaries. These pores are far less regular than the cracks observed for coating 11 suggesting a different mechanisms; it is likely due to oxidative attack at the grain boundaries. We have shown in the Raman scans in chapter 7 (Figures 7.17 and 7.19) that carbon migrates to the surface during heat treatment, if it congregates within grain boundaries and reacts with oxygen in the atmosphere, CO_2 may be released leaving the pores as it is removed.

The SEM images of both coatings after heat treatment to 1000 ˚C highlights the difference in crack formation mechanism between the two; coating 11 has relatively straight, regular cracks originating from droplets creating the pavement pattern, whereas the pore formation exposing grain boundaries causes a mosaic-like pattern to develop with reduced regularity.

Table 8.3. At.% of elements in coating 11 measured by EDX.

Temperature	Elemental composition (at. %)				
	Cr	Al	Si	N	O
600 ˚C	7.04	8.84	0.76	14.06	69.30
800 ˚C	7.42	9.58	0.78	13.28	68.94
1000 ˚C	7.66	10.45	0.98	12.62	68.29

Table 8.4. At.% of elements in coating 12 measured by EDX.

Temperature	Elemental composition (at. %)				
	Cr	Al	Si	N	O
600 ˚C	6.59	9.00	0.80	14.37	69.23
800 ˚C	6.39	8.88	0.81	14.64	69.27
1000 ˚C	13.54	12.89	1.03	4.60	67.95

Chemical composition analysis via EDX for each coating is given in tables 8.3 and 8.4. The most notable change from as-deposited to heat treated in air is the presence of oxygen; for the as-deposited the O content is so low that it was taken out of the calculation however at high temperatures it becomes the dominant element within the scanned area for both coatings. Despite the high oxygen levels there is little change in the chemical composition of coating 11 with increased temperature suggesting good thermal stability, this is supported by the Raman (Figures 8.8 and 8.9) which shows no oxide peaks in the coating areas, and also the SEM images indicating little - no extensive surface oxidation.

Coating 12 is also thermally stable up to 800 ˚C, however at 1000 ˚C there is a significant drop in the at. % of N. This suggests a breakdown of the CrAlN structure at 1000 ˚C with N being released; it has been noted in the literature review, section 2, that CrAlN dissociates at temperatures exceeding 900 ˚C [65][66][67]. This breakdown must allow O to react with the metal species of the coating as oxide peaks are detected in Raman scans (Figure 8.11) of the coating area. If the O within coating only reacted with metal species then as N decreased it would be expected that the metal species and the O would increase; as O actually decreases the N must also react with O on its release, removing some O trapped within the coating.

EDX scans and mapping were also performed to test for the presence of Fe, the results gave a composition < 0.05 at. % at all temperatures and positions tested on the coating area and within the 'walls'. The results were therefore omitted from the EDX data given in Table 8.3 and 8.4, and also from the EDX mapping images given in Figure 8.7.

The 'walls' within the cracks were investigated further using SEM and EDX mapping in order to suggest the different mechanisms that lead to their formation. The SEM images in Figure 8.7 show clear differences in coating surfaces; coating 11 is smooth and dense with the column top just visible, whereas coating 12 has islands of material growing up from the surface – the topography is much rougher. The cracks themselves appear different also; coating 11 has large crystals grown within the crack, some of which protrude out of the surface. The cracks are not completely filled however as voids can be seen – the material grown within the crack does not seal it. In coating 12, similar large crystal can be seen protruding out of the surface of the crack, although in this case there are no voids, the crack has been completely sealed.

The EDX mapping in Figure 8.7 shows that for coating 11 there is little oxidation of the coating surface, it is dominated by Cr and Al, originating from the coating material. Where the crack has formed there is a large deficiency in Al, a slight reduction in Cr content and a significant increase in O suggesting the formation of chrome oxide species within the crack.
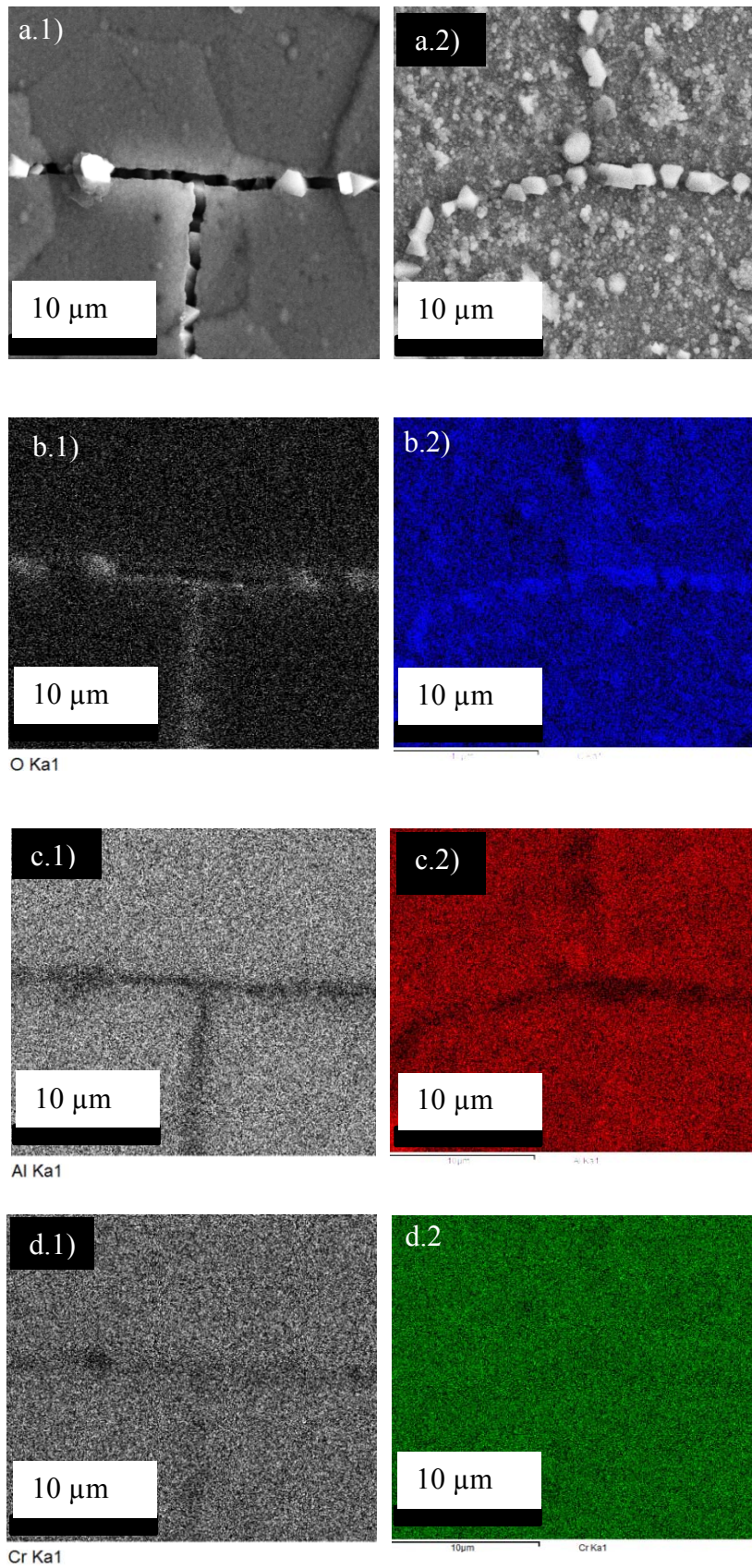
Figure 8.7. SEM Images (a) of a crack and 'wall' area on coatings 11 (1) and 12(2), accompanied by EDX mapping for oxygen (b), aluminium (c) and chromium (d).

The EDX mapping for coating 12 reveals that the growth of material covering the surface is a form of oxide, with high intensity signal from all over the surface. There is an Al signal reduction within the wall area, whereas the wall cannot even be distinguished from the coating area when looking at the Cr signal; this implies that material filling the crack and creating the wall is also chrome oxide in nature. The question remains as to why at lower bias the crack contain only large crystal oxides separated by voids, whereas at increased bias these crack are dense with material.

We have seen previously that Raman spectroscopy can be effective in identifying if the chrome oxide species is dominated by crystalline or spinel phases therefore it was employed to investigate the nature of the wall areas. Firstly we shall discuss the effect of heating on the surface phase composition up to 800 ˚C. Figure 8.8 shows how the Raman spectra develops for coating 11 with increased temperature; the peak ratio's and intensities remain constant when comparing the as-deposited signal with the signal after treatment to 600 ˚C, however after 800 ˚C the carbon region becomes dominant indicating carbon migration to the surface of the coating.

After heat treatment to 1000 ˚C (Figure 8.9) the coating area (red line) is completely dominated by carbon species, the high temperature has also instigated carbon graphitisation confirmed by separation of the D and G peaks. The characteristic CrAlN peak pattern is no longer visible suggesting thermal decomposition of the base structure, however there are no oxide peaks present, indicating oxidation resistance up to 1000 ˚C.
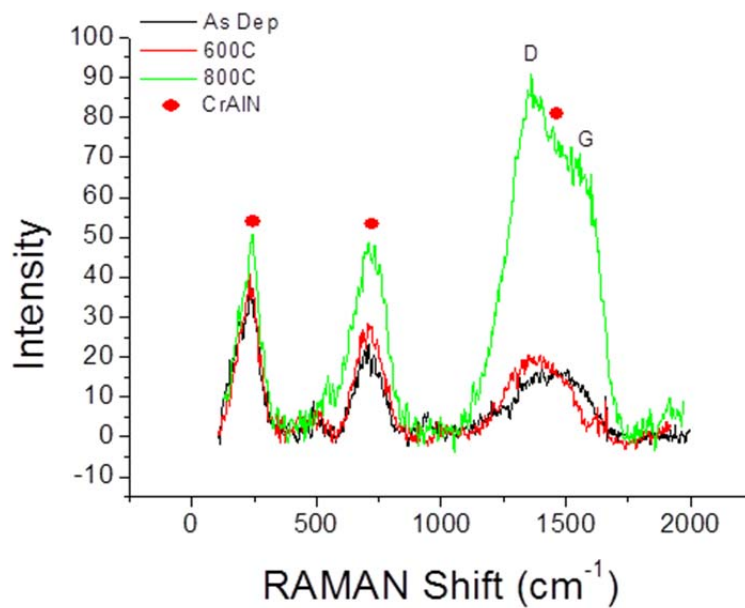
Figure 8.8. Raman spectra of coating 11 as-deposited and after isothermal heat treatment to 600 ˚C and 800 ˚C.

The Raman spectrum of a wall area is also plotted in black in Figure 8.9. The D and G peaks are present within this area with good separation indicating graphitisation; however their intensity is reduced greatly compared to the coating area. The spectrum is dominated by two chrome oxide peaks in the range 500 - 700 cm-1. For chromia species, peaks within this region could be attributed to a number of phases. For example, the presence of Fe2+Cr2O2 spinel shows a vibrational mode in the region of 690 cm-1 [68][69], the presence of this phase however, can be ruled out by the EDX data showing negligible Fe content.

As discussed in the literature review, the CrO_2 scale peak is centred around 670 cm-1 and the characteristic Cr_2O_3 peak is at approximately 550 cm-1. We see a presence of both these peaks in the Raman spectrum of the 'wall' for coating 11, though, peak convolution has caused up and down shifting of the maximum peak position for

233

Cr_2O_3 and CrO_2, respectively. The presence of CrO_2 contributes to the broadening of the peaks within this region.
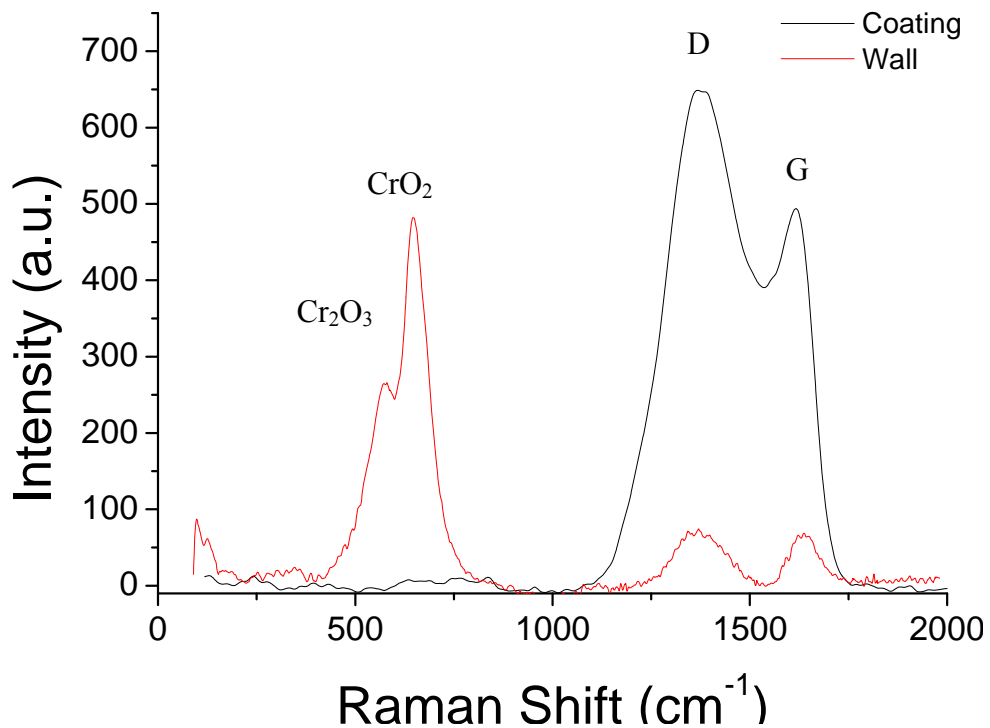
Figure 8.9. Raman Spectra of coating 11 after isothermal heat treatment to 1000 ˚C, two areas investigated were coating (red) and wall (black).

The Raman spectra evolution with increased temperature up to 800 ˚C for coating 12 (Figure 8.10) is almost identical to that of coating 11 (Figure 8.8), the only difference of note being that the intensity of the carbon region is increased slightly after 600 ˚C for coating 12 suggesting the increased bias promotes carbon migration at an earlier temperature. Where the change in bias becomes most prominent is when comparing the Raman spectra after 1000 ˚C.
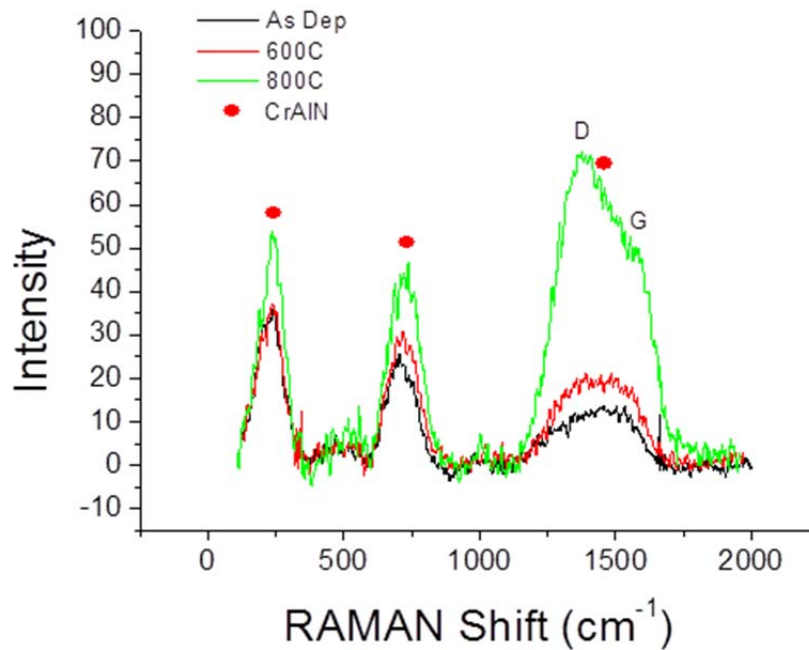
Figure 8.10. Raman spectra of coating 12 as-deposited and after isothermal heat treatment to 600 ˚C and 800 ˚C.

The coating surface area of 12 shows Raman spectra indicative of Cr_2O_3 (Figure 8.11) with a peak at 559 cm-1 [69]. The spectrum of the coating area is similar to that of the 'wall' area for coating 11, with a strong CrO_2 peak at 670 cm-1 indicating a mixed Cr_2O_3 and CrO_2 phase. Peaks in this region (coating area) were not present for coating 11 suggesting that increasing the bias causes increased surface oxidation to occur. The 'wall' area shows an increased intensity of oxide species which has become dominated by the Cr_2O_3 line at 559 cm-1.
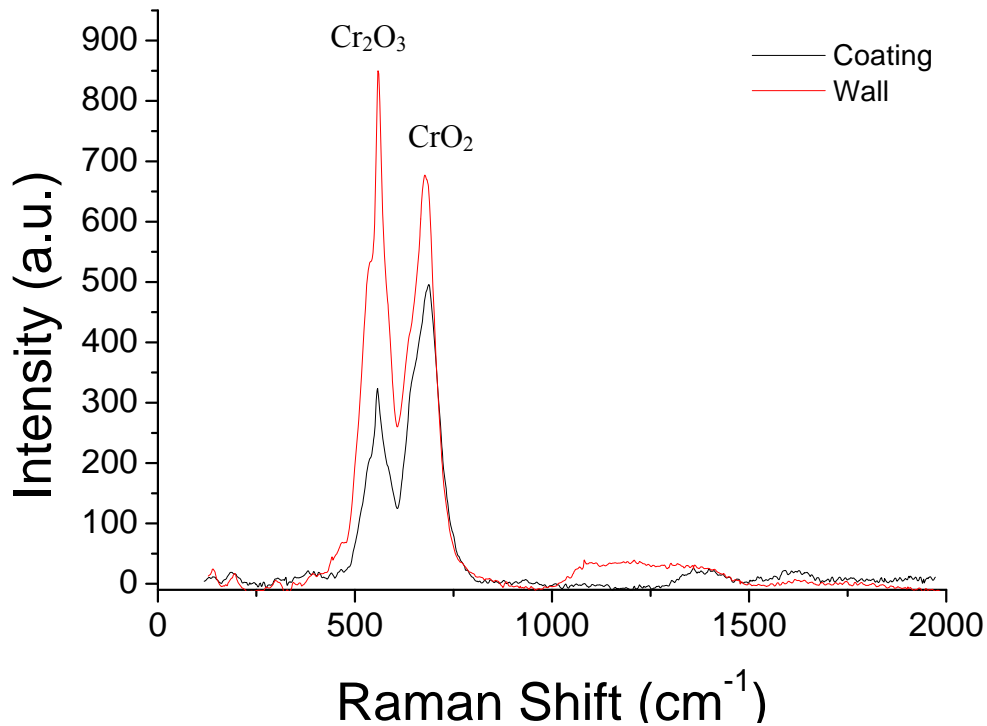
Figure 8.11. Raman Spectra of coating 12 after isothermal heat treatment to 1000 ˚C, two areas investigated were coating (black) and wall (red).

To understand the behaviour of the two coatings at high temperatures we propose the following mechanism for crack formation and oxidation:

At low bias (coating 11) the thermal expansion of the substrate causes a build-up of tensile stress to be released via cracking between 600 ˚C and 800 ˚C. The coating material within the crack is then suddenly exposed to oxygen in the air at high temperatures causing oxidation and crystallisation of the oxide species. The density of the oxides formed protects the coating against the onset of rapid oxidation.

At increased bias (coating 12) the coating withstands cracking up to much higher temperatures due to the increased inherent compressive stress, however oxidative attack occurs at grain boundaries causing pores to develop. These pores begin to expand and connect up to 1000 ˚C, an oxide grows slowly within the pore, filling it. According to the literature, the initial oxide that grows is a disordered CrO_2, with

increased exposure to an oxidative environment this scale thickens. The intensity of the peak is directly correlated to amount of substance and hence its increase indicates the thickness. This occurs until a point is reached where it begins to transform into Cr_2O_3 [69]. We propose that the coating area initially forms a thick, protective, Cr-based, passivation layer, forming a template for the growth of CrO_2 and with time transforms into Cr_2O_3. This process is delayed by the passivation of Cr diffusion out from the coating and hence explains why after heat treatment to 1000 ˚C the CrO_2 remains dominant. Further exposure would cause a change in the ratio of peaks in favour of the Cr_2O_3.

For the 'wall' area however, oxidative attack at the grain boundaries allows the CrO_2 phase to form earlier in the oxidation process, therefore also allowing the transformation of CrO_2 to Cr_2O_3 to occur earlier. This mechanism helps to explain why the dominant phase of the mixed chromia species differs between coating and 'wall' areas.

For coating 11 we have shown that the coating area indicates no oxide species (Figure 8.9) and that the 'wall' area is dominated by CrO_2 in a mixed CrO_2 and Cr_2O_3 phase. This CrO_2 dominance means that the cracks haven't yet been exposed to the oxidative environment for as long as the 'wall' areas of coating 12. Therefore, the cracks observed at 800 ˚C for coating 11 (Figure 8.6 b.1)) must occur at higher temperatures than the pores are formed for coating 12.

It is of vital importance to note the absence of any iron oxide peaks in the Raman spectra for either coating 11 or 12. If the cracks were to propagate through the coating to the substrate, it would be possible for O to diffuse through the crack, oxidising the Fe within the substrate; this would lead to the cracks being filled with Fe

oxides rather than the solely chrome oxides that we observe. The coatings are sealing their cracks and creating them from within themselves, giving 'self-healing' properties.

8.2.4. Cutting tests

Coatings 11 and 12 showed the most promise for cutting tool applications in lab-based testing; their high hardness, adhesive strength, high temperature stability and oxidation resistance are all essential properties for dry, high-speed machining of abrasive materials. In light of this, coatings 11 and 12 were selected for cuttings tests. Tool lifetime during face milling of P20 tool steel was evaluated by measuring the flank wear after each pass of the material; the results are plotted in Figure 8.12.
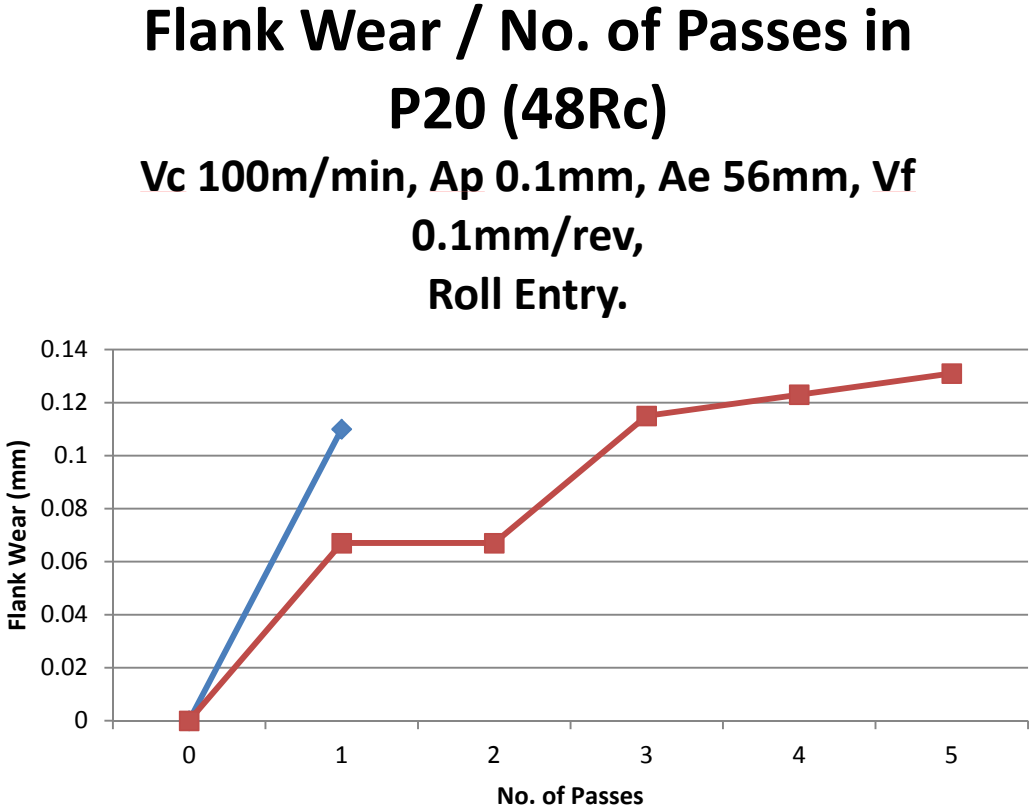
Figure 8.12. Flank wear versus number of passes for coatings 11 (blue) and 12 (red).

Coating 11 survived one pass of the material at the settings stated in the title of Figure 8.12. Coating 12, however, lasted 5 passes; the lifetime of the tool was increased 5 times by increasing the substrate bias during deposition from -40 V to -60 V. SEM and EDX were used to determine the failure mechanisms of the two coatings:

It is clear from Figure 8.13 that failure has occurred for coating 11 at the substrate-coating interface, there is no evidence of wear; instead there are large areas of coating removal at the cutting edge suggesting adhesive failure. The EDX mapping no Al above sheer edge; as both the multilayer and base layer contain Al this area therefore must be substrate. The presence of both W and Co in this area confirms the hypothesis. Areas of Cr above the sheer line and especially at the top of the image along the cutting edge indicate work-piece build up; this is supported by the presence of Fe above the sheer line also.

Importantly, there is not a build-up of Fe along the sheer line or at any area consisting of coating material. This is significant as it implies the coating chemistry is successful at preventing a built up edge during machining.

The SEM image of flank wear for coating 12 in Figure 8.14 shows a smoothed region close to the cutting edge with no indication of cracking or adhesive failure. This is evidence of abrasive wear; the difference in wear mechanism is the likely cause of the improved lifetime observed in cutting tests.
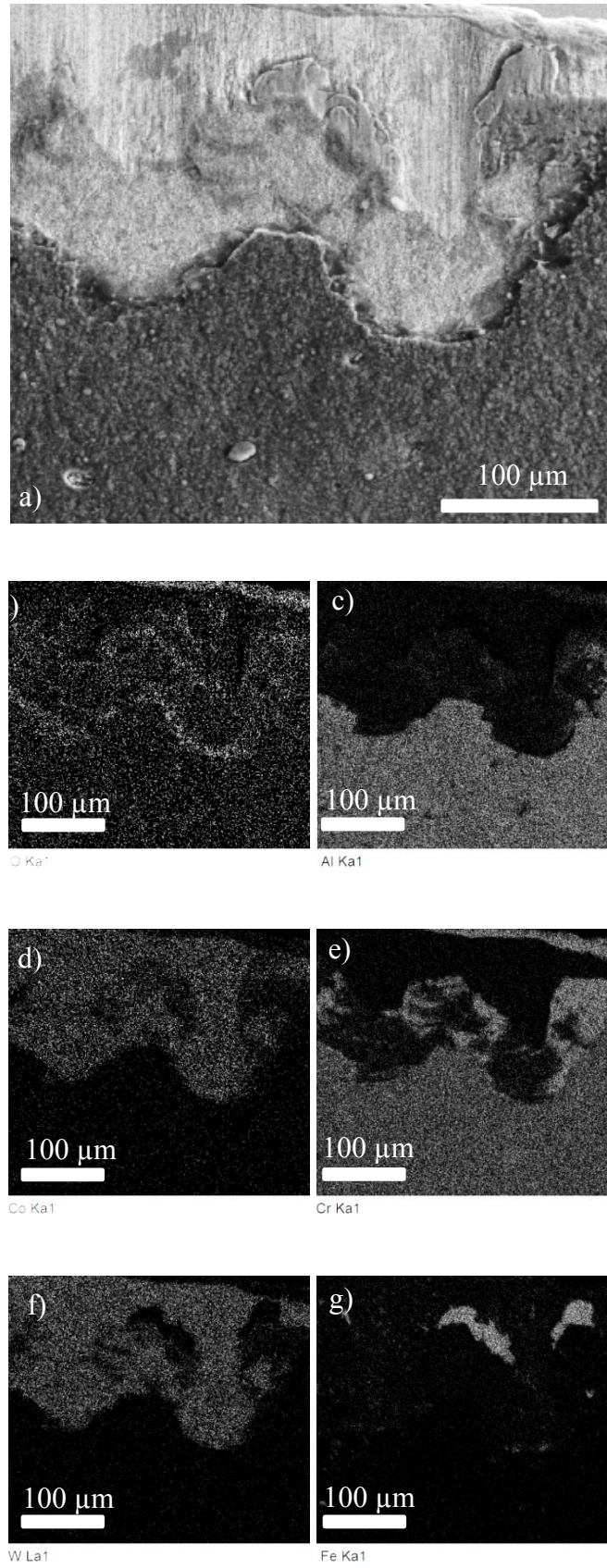
Figure 8.13. SEM image of the cutting edge for coating 11 after 1 pass (a) with EDX mapping images for O (b), Co (c), W (d), Al (e), Cr (f) and Fe (g).
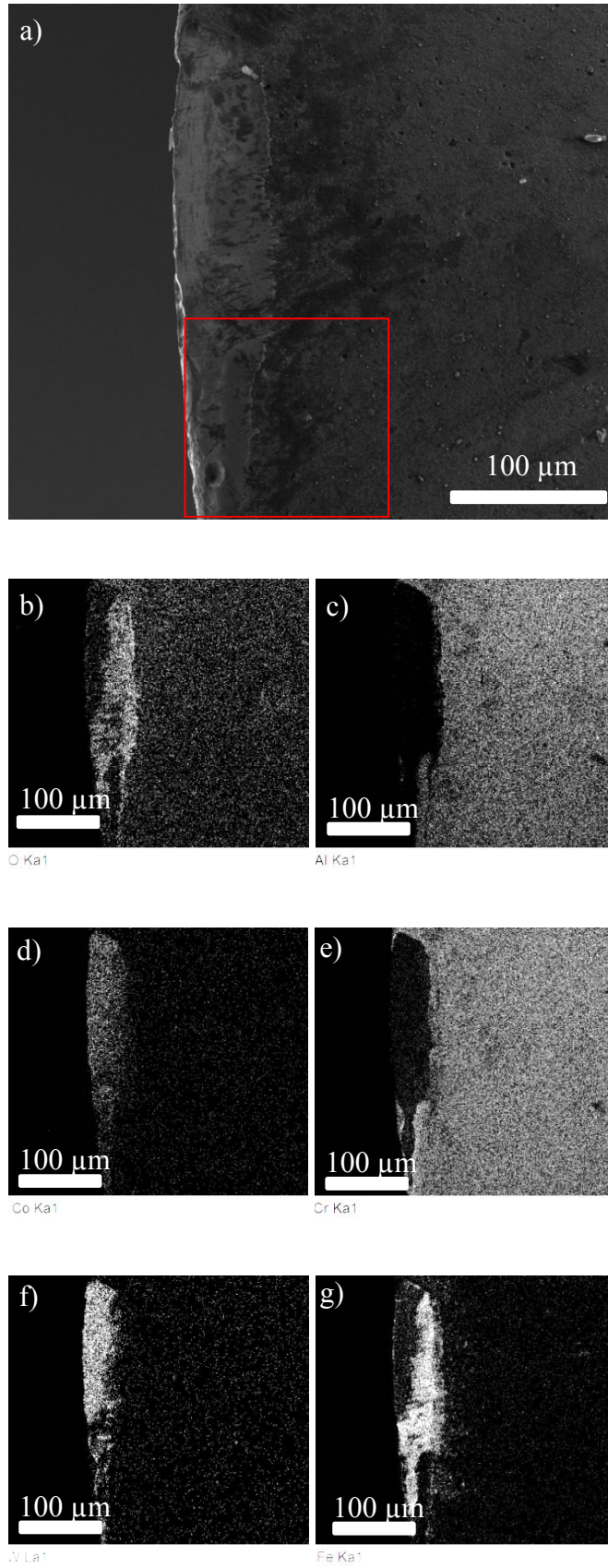
Figure 8.14. SEM image of the cutting edge for coating 12 after 5 passes (a) with EDX mapping images for O (b), Co (c), W (d), Al (e), Cr (f) and Fe (g).

The EDX mapping of the cutting edge for coating 12 shown in Figure 8.14 confirms the coating failure after 5 passes; W and Co show up in regions closest to the cutting edge indicating the substrate has been exposed. In area within the red square there is a region totally dark for Fe that is bright for both Al and Cr; this area has been magnified in Figure 8.15. It can be seen that from right to left the coating appears as-deposited, abrasively worn and then there is an edge running down the image separating coating from substrate. The absence of Fe in this worn region again supports the suggestion that the coating chemistry prevents the formation of a built up edge during cutting tests.
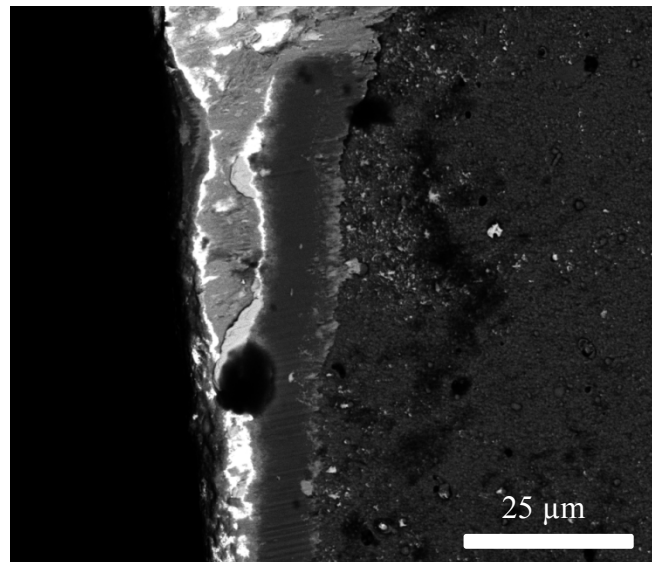
Figure 8.15. Enlarged SEM image of the area encased in the red square in the SEM image of Figure 8.14.

8.3.　　　　Summary

• Increasing the substrate bias from - 40 V to - 60 V had little effect on the coating structure and phase when measured using XRD and Raman spectroscopy. Column tops begin to elongate along a single plane - an effect of coating densification due to increased bias.

• Mechanical properties improved for coating 12, most notably, the increased hardness leading to an improved wear rate. Increased substrate bias induces a larger inherent stress which was detrimental to the cohesion of coating 12; there was however, no reduction in the adhesive strength.

• The theory that increasing the bias would delay crack formation to higher temperatures was proven by coating 12 resisting cracking of the same type/mechanism as coating 11. However, oxidative attack at the grain boundaries opened up surface pores and diffusion routes for oxidation.

• Coating 12 was seen to be less resistant to extensive surface oxidation than coating 11, the higher bias led to breakdown of the CrAlN structure at lower temperatures, causing N release and replacement and the formation of surface oxides.

• Both coatings exhibited 'self-healing' properties; Raman of the 'walls' that filled the cracks/pores showed no Fe oxide species indicating the walls grew through oxidation of the coating material only and the cracks/pores had not propagated down to the substrate.

• The phase of the 'wall' oxides was shown to be dependent on the length of time the inner parts of the coating were exposed to the oxidative environment; if the cracks opened gradually via oxidative attack at the grain boundaries the walls were predominantly Cr_2O_3, if there was a sudden exposure to the atmosphere due to cracking they were CrO_2

- The growth of wear resistant Cr_2O_3 species on the surface of coating 12 may be the reason for the 5 times improvement in cutting test lifetime compared to coating 11

9.   Conclusions

This study has been performed with the intention of developing a novel, oxidation resistant and high temperature stable coating for the application of dry, high-speed machining of abrasive materials. An appreciation of the work that has come before this study has been given in detail in the literature review; it has been through this work that inspiration was drawn to combine the beneficial chemical properties of coatings such as CrAlYCN/CrCN, SiBCN and CrAlSiN. The improvements to wear through coating architecture engineering and the deposition of a multilayer were employed. The reported increase in coating adhesion and coating density through the use of HIPIMS technology were also utilised to produce a coating that is capable of withstanding the high forces and temperatures involved in such a harsh environment as cutting tool applications.

At the end of each stage of the investigation a brief summary has been given on the discussion of the relevant results. The general conclusions of the study and the development of both the coating and knowledge will now be presented:

- The investigation of the plasma revealed that increasing the charge on the HIPIMS cathode increased both the metal ion:gas ion and the metal ion:metal neutral ratio. HIPIMS generated a highly ionised, metal rich plasma which has been reported in the

literature to increase coating adhesion when used as a pretreatment method and to improve coating density

- Holding time was found to be the dominant factor in material removal during substrate etching. Etching increased the roughness of the WC substrates by exposing the larger embedded grain and removing loosely bound surface debris; providing an increased surface area for coating growth sites and improving the adhesion by removing the chance of bonding to a loosely bound debris piece. Etching rate increased by a factor of two as a function of distance from the cutting edge, emphasising the effect of tool geometry and plasma sheath narrowing on material removal

- Combine HIPIMS/UBM technology was successful at depositing an initial CrAlBYCN/AlSiCN coating with high hardness, high temperature stability and oxidation resistance at elevated temperatures up to 900 ˚C. A mechanism for the generation of aluminium silicon based oxides during pin on disk wear tests has been proposed; it describes a surface layer being transferred around the coating during sliding wear, consisting of oxides formed from exposed droplets that originated from the AlSi target

- The effect of substrate bias on coating performance was investigated; it was found that reducing the bias from 60 V to 40 V improved the adhesive properties of the coating due to the reduced inherent stress. Stress is also linked to hardness and therefore decreasing the bias resulted in a reduction in hardness and hence an increase in the wear rate

- Increasing the target power improved the stability of the deposition process which led to a reduction in target arcing of the AlSi targets and the subsequent formation of AlSi droplets on the substrate during coating growth. This in turn generated an alternative wear mechanism than that observed for coating 1; with the number of AlSi droplets reduced the wear mechanism was now dominated by the formation of chrome

oxide species. The wear mechanism proposed involved the formation of microjunctions at the contact point of asperities on the coating and counterpart. High flashpoint temperatures generated via sheering of the coating material at the microjunction caused Cr within the coating to react with O in the atmosphere and form a protective, wear resistant chrome oxide layer

- Coating composition through gas flow control was proved effective via the use of OES monitoring and a gas flow feedback. Despite depositing coatings that were reproducible, the method was unsuccessful at achieving the desirable mechanical properties for cutting tool applications and so the process was reverted back to pressure control. This increased the stoichiometry of the coatings leading to improved mechanical properties

- By increasing the target poisoning the deposited coating transitions through 3 dominant phases; at low poisoning the coatings are metal rich, Cr_2N phase and hence soft, there is then an intermediate zone with a mixed $Cr_2N + CrN$ phase until the coatings become more stoichiometric leading to presence of CrN peaks only. The XRD phases correspond well to the EDX chemical composition data with a reduced metal content is observed with increased poisoning. Raman spectra revealed that the surface phase becomes increasing dominated by CrAlN phase with increased target poisoning

- C migration to the surface with increasing annealing temperature is observed and the graphitisation of C is delayed to higher temperatures, by the coating approaching stoichiometric composition.

- Coating 11 was determined to have the most desirable chemical, mechanical and thermal properties of the deposition series. The development of coating cracks during heat treatment was investigated through substrate bias. It was found that increasing the bias prevented crack formation however led to oxidative attack at the grain boundaries. The crack and the pores became filled with a material and this area was termed a 'wall';

these walls were investigated using Raman spectroscopy which revealed that the slow exposure of the coating via pores opening at lower temperatures allowed time for CrO_2 to transform into Cr_2O_3. The cracks for the lower biased coating developed at higher temperatures to the pores and therefore there was insufficient exposure time to the oxidative environment for Cr_2O_3 to form. Importantly, analysis found negligible trace of Fe within the cracks/pores indicating that they did not propagate to substrate - the coatings can be classed as 'self-healing' and prolong oxidation resistance

• During cutting tests coating 12, with the increased bias and reduced cracking, performed best during cutting tests; a five-fold increase in lifetime was observed compared to coating 11. Coating 12 failed due to wear after 5 passes, whereas coating11 failed due to poor adhesion after only 1 pass

This study has proven successful at achieving the objectives set out at the start of the project. A new generation, Ti-free, wear resistant PVD coating, utilising combined HIPIMS/UBM technology, has been developed for the application of dry, high-speed machining of hardened steels. To emphasise the beneficial effect this coating has on improving a tools lifetime, a WC insert was coated, cut in half and isothermally heat treated to 1000 ˚C. The coated area remained intact, whereas the exposed WC substrate experienced severe oxidation that would render the tool unusable. Results of this can be seen in the appendix. It can be said that the oxidation and wear mechanisms have been explored, current knowledge in the field has been improved and a foundation coating for future research has been produced.

10.   Future Work

As the project progressed and the improvements to the coatings became apparent it was clear that the coating chemistry, hardness, wear resistance, oxidation resistance and thermal stability were desirable for the application of dry, high-speed machining of abrasive materials. However, the cutting performance of the coatings needs improvement. We believe the most effective way to improve the cutting performance is to produce coating with superior adhesion. Suggestions for future work to achieve this would be through coating process conditions and coating architecture; for the steel substrates the base layer is deposited as a ceramic onto a metallic material, this may induce a high stress level at the interface causing the coating to delaminate. Ramping the N flow would create a stress gradient as the deposited coating transitioned from metallic to ceramic. Similarly, C is not introduced until after the base to reduce its stress inducing effects however, the coating then develops from a purely nitride material into a carbo-nitride which may again induce a stress at the base-layer-multilayer interface. A suggestion would be to also ramp the C flow during the multilayer deposition stage to again produce a stress gradient.

In terms of understanding, we have proposed a number of mechanisms both for wear and for oxidation processes. A detailed understanding and proof of these theories could be provided by thermal probe temperature measurements to determine the temperatures generated at the contact point during wear; this may also be possible via a thermal imaging camera. In situ high temperature Raman spectroscopy could be utilised to investigate the precise temperatures that the oxides generated, during isothermal heat treatment, are forming [126]–[129]. An investigation into the time of the crack formation would also be useful. This studies assumes that the

cracks and hence walls, are created during heating, they may be being formed during the cooling period. It would be interesting to use an in situ camera to record the point at which the cracks are formed. Once this is known it could then be possible, through the use of a high speed camera, to actually observe the growth of the 'walls'. A combination of all three techniques would allow a determination of the oxide growth mechanism proposed in this study to succeed.

An understanding of the effect of heat treatment on coating density, oxidation and crack formation could be developed through the use of cross sectional SEM and transmission electron microscopy; they would help to recognise which elemental migration is the driving factor behind the densification, if the grain boundaries are being plugged by Y and protective oxide species as suggested in the literature, and also could investigate the effect of C on coating multilayer architecture. Despite the benefits of C inclusion for wear, C segregation may interrupt the multilayer architecture and thus may alter the improved wear mechanism that the multilayer coating provides.

Although we have shown this coating has much promise for cutting tool application, it remains in the early stages of development and suggestions for future research have been given.

References

[1]   P. E. Hovsepian, C. Reinhard, and a. P. Ehiasarian, "CrAlYN/CrN superlattice coatings deposited by the combined high power impulse magnetron sputtering/unbalanced magnetron sputtering technique," *Surf. Coatings Technol.*, vol. 201, no. 7, pp. 4105–4110, Dec. 2006.

[2]   D. McIntyre, J. E. Greene, G. Håkansson, J. -E. Sundgren, and W. -D. Münz, "Oxidation of metastable single-phase polycrystalline Ti0.5Al0.5N films: Kinetics and mechanisms," *J. Appl. Phys.*, vol. 67, no. 3, 1990.

[3]   V. Chawla, D. Puri, S. Prakash, and B. Sidhu, "Salt fog corrosion behavior of nanostructured TiAlN and AlCrN hard coatings on ASTM-SA213-T-22 boiler steel," *Jordan J. Mech. Ind. Eng.*, vol. 5, no. 3, pp. 247–253, 2011.

[4]   X. zhao Ding, A. L. K. Tan, X. T. Zeng, C. Wang, T. Yue, and C. Q. Sun, "Corrosion resistance of CrAlN and TiAlN coatings deposited by lateral rotating cathode arc," *Thin Solid Films*, vol. 516, no. 16, pp. 5716–5720, 2008.

[5]   Z. Huan, L. E. Fratila-Apachitei, I. Apachitei, and J. Duszczyk, "Characterization of Porous TiO2 Surfaces Formed on 316L Stainless Steel by Plasma Electrolytic Oxidation for Stent Applications," *J. Funct. Biomater.*, vol. 3, no. 2, pp. 349–360, 2012.

[6]   R. R. Wang and K. K. Fung, "Oxidation behavior of surface-modified titanium for titanium-ceramic restorations," *J. Prosthet. Dent.*, vol. 77, no. 4, pp. 423–434, 1997.

[7]   D. M. Mattox, "Chapter 1 - Introduction," in *Handbook of Physical Vapor Deposition (PVD) Processing (Second Edition)*, Second Edition., D. M. Mattox, Ed. Boston: William Andrew Publishing, 2010, pp. 1–24.

250

[8]   B. Chapman, *Glow Discharge Processes*. John Wiley and Sons, 1980.

[9]   D. M. Mattox, *Handbook of Physical Vapour Deposition (PVD) Processing*, 2nd ed. Elsevier, 2010.

[10]   K. S. Sree Harsha, *Principles of Physical Vapor Deposition of Thin Films*. Elsevier B.V., 2006.

[11]   G. Bräuer, B. Szyszka, M. Vergöhl, and R. Bandorf, "Magnetron sputtering - Milestones of 30 years," *Vacuum*, vol. 84, no. 12, pp. 1354–1359, 2010.

[12]   B. Window and N. Savvides, "Charged Particle Fluxes from Planar Magnetron Sputtering Sources," *J. Vac. Sci. Technol. A*, vol. 4, no. 2, pp. 196–202, 1986.

[13]   "PVD Coatings: Unbalanced Magnetron." [Online]. Available: https://www.pvd-coatings.co.uk/theory/how-are-pvd-coatings-deposited/unbalanced-magnetron/.

[14]   Hauzer Techno Coating, "Magnetron Sputtering." [Online]. Available: http://www.hauzertechnocoating.com/en/plasma-coating-explained/magnetron-sputtering/.

[15]   V. Kouznetsov, K. Macák, J. M. Schneider, U. Helmersson, and I. Petrov, "A novel pulsed magnetron sputter technique utilizing very high target power densities," *Surf. Coatings Technol.*, vol. 122, no. 2–3, pp. 290–293, 1999.

[16]   E. B. Macak, W.-D. Münz, and J. M. Rodenburg, "Edge related effects during ion assisted PVD on sharp edges and implications for coating of cutting tools," *Surface Engineering*, vol. 19, no. 4. pp. 310–314, 2003.

[17]   E. B. Macak, W.-D. Münz, and J. M. Rodenburg, "Plasma–surface interaction

at sharp edges and corners during ion-assisted physical vapor deposition. Part I: Edge-related effects and their influence on coating morphology and composition," *J. Appl. Phys.*, vol. 94, no. 5, p. 2829, 2003.

[18] E. B. Macak, W.-D. Münz, and J. M. Rodenburg, "Plasma–surface interaction at sharp edges and corners during ion-assisted physical vapor deposition. Part II: Enhancement of the edge-related effects at sharp corners," *J. Appl. Phys.*, vol. 94, no. 5, p. 2837, 2003.

[19] J. A. Thornton, "Influence of apparatus geometry and deposition conditions on the structure and topography of thick sputtered coatings," *J. Vac. Sci. Technol.*, vol. 11, no. 4, p. 666, 1974.

[20] C. Charpentier, P. Prodhomme, I. Maurin, M. Chaigneau, and P. i Cabarrocas, "X-Ray diffraction and Raman spectroscopy for a better understanding of ZnO:Al growth process," *EPJ Photovoltaics*, vol. 2, no. 2011, p. 25002p1-25002p8, 2011.

[21] R. Messier, A. P. Giri, and R. A. Roy, "Revised structure zone model for thin film physical structure," *J. Vac. Sci. Technol. A*, vol. 2, p. 500, 1984.

[22] M. Predeleanu and S. K. Ghosh, Eds., *Studies on applied Mechanics 43: Materials Processing Defects*. Amsterdam: Elsevier, 1995.

[23] D. Dowson, C. M. Taylor, and M. Godet, Eds., *Trobology Series, 17: Mechanics of Coatings*. Amsterdam: Elsevier, 1990.

[24] K.-H. Muller, "epitaxial vapor-phase growth: A," vol. 35, no. 15, pp. 7906–7913, 1987.

[25] A. Anders, "A structure zone diagram including plasma-based deposition and

ion etching," *Thin Solid Films*, vol. 518, no. 15, pp. 4087–4090, 2010.

[26] R. Bandorf and H. Gerdes, "SVC-Tutorial C-338: Application of Reactive Sputtering." Fraunhofer IST.

[27] Reactive Sputtering, "Basic Concepts of Reactive Sputtering." [Online]. Available: http://reactive-sputtering.info/node/99. [Accessed: 17-Jul-2016].

[28] A. R. Oganov and V. L. Solozhenko, "Boron: a hunt for superhard polymorphs," *J. Superhard Mater.*, vol. 31, no. 5, pp. 285–291, 2009.

[29] S. Kouptsidis, H. Lüthje, K. Bewilogua, a. Schütze, and P. Zhang, "Deposition of c-BN films by DC magnetron sputtering," *Diam. Relat. Mater.*, vol. 7, no. 1, pp. 26–31, 1998.

[30] L. Vel, G. Demazeau, and J. Etourneau, "Cubic boron nitride: synthesis, physicochemical properties and applications," *Mater. Sci. Eng. B*, vol. 10, no. 2, pp. 149–164, 1991.

[31] M. Z. Karim, D. C. Cameron, M. J. Murphy, and M. S. J. Hashmi, "Plasma deposition of cubic boron nitride films from non-toxic material at low temperatures," *Surf. Coatings Technol.*, vol. 49, no. 1–3, pp. 416–421, 1991.

[32] G. P. Lamaze and R. G. Downing, "Analysis of cubi boron nitride thin films by neutron depth profiling," *Diam. Relat. Mater.*, vol. 3, pp. 728–731, 1994.

[33] K. Yamamoto, H. Ito, and S. Kujime, "Nano-multilayered CrN/BCN coating for anti-wear and low friction applications," *Surf. Coatings Technol.*, vol. 201, no. 9–11 SPEC. ISS., pp. 5244–5248, 2007.

[34] Y. H. Lu, P. Sit, T. F. Hung, H. Chen, Z. F. Zhou, K. Y. Li, and Y. G. Shen, "Effects of B content on microstructure and mechanical properties of

nanocomposite Ti–Bx–NyTi–Bx–Ny thin films," *J. Vac. Sci. Technol. B*, vol. 23, p. 449, 2005.

[35]   R. W. Kelsall, I. W. Hamley, and M. Geoghegan, Eds., *Nanoscale Science and Technology*. John Wiley and Sons, Ltd, 2005.

[36]   K. Przybylski, A. J. Garratt-Reed, and G. J. Yurek, "Grain Boundary Segregation of Yttrium in Chromia Scales," *J. Electrochem. Soc.*, vol. 135, no. 2, p. 509, 1988.

[37]   D. P. Moon, "Role of reactive elements in alloy protection," *J. Mater. Sci. Technol.*, vol. 5, p. 754, 1989.

[38]   D. B. Lewis, L. a. Donohue, M. Lembke, W.-D. Münz, R. Kuzel, V. Valvoda, and C. J. Blomfield, "The influence of the yttrium content on the structure and properties of Ti1−x−y−zAlxCryYzN PVD hard coatings," *Surf. Coatings Technol.*, vol. 114, no. 2–3, pp. 187–199, 1999.

[39]   M. Moser and P. H. Mayrhofer, "Yttrium-induced structural changes in sputtered Ti1-xAlxN thin films," *Scr. Mater.*, vol. 57, no. 4, pp. 357–360, 2007.

[40]   F. Rovere, P. H. Mayrhofer, A. Reinholdt, J. Mayer, and J. M. Schneider, "The effect of yttrium incorporation on the oxidation resistance of Cr-Al-N coatings," *Surf. Coatings Technol.*, vol. 202, no. 24, pp. 5870–5875, 2008.

[41]   H. N. Lee, Z. M. Park, M. H. Oh, K. Y. Kim, and D. M. Wee, "Oxidation behavior and mechanical properties of yttrium-doped L12 (Al,Cr)3Ti coating on TiAl alloys," *Scr. Mater.*, vol. 41, no. 10, pp. 1073–1078, 1999.

[42]   M. J. Bennet, H. E. Bishop, P. R. Chalker, and A. T. Tuson, "The Influence of

Cerium , Yttrium and Lanthanum Ion Implantation on the Oxidation Behaviour of a 2 0 C r - 2 5 N i - N b Stainless Steel in Carbon Dioxide at 900-1050 ° C *," *Mater. Sci. Eng.*, vol. 90, pp. 177–190, 1987.

[43] Q. Luo, W. M. Rainforth, and W. D. Münz, "TEM observations of wear mechanisms of TiAlCrN and TiAlN/CrN coatings grown by combined steered-arc/unbalanced magnetron deposition," *Wear*, vol. 225–229, pp. 74–82, 1999.

[44] H. Holleck and V. Schier, "Multilayer PVD coatings for wear protection," *Surf. Coatings Technol.*, vol. 76–77, no. 1–3 pt 1, pp. 328–336, 1995.

[45] U. Helmersson, S. Todorova, S. A. Barnett, J. E. Sundgren, L. C. Markert, and J. E. Greene, "Growth of single-crystal TiN/VN strained-layer superlattices with extremely high mechanical hardness," *J. Appl. Phys.*, vol. 62, no. 2, pp. 481–484, 1987.

[46] W.-D. Münz, D. B. Lewis, P. E. Hovsepian, C. Schönjahn, A. Ehiasarian, and I. J. Smith, "Industrial scale manufactured superlattice hard PVD coatings," *Surf. Eng.*, vol. 17, no. 1, pp. 15–27, 2001.

[47] A. Karimi, Y. Wang, T. Cselle, and M. Morstein, "Fracture mechanisms in nanoscale layered hard thin films," *Thin Solid Films*, vol. 420–421, pp. 275–280, 2002.

[48] R. Kaindl, B. Sartory, J. Neidhardt, R. Franz, A. Reiter, P. Polcik, R. Tessadri, and C. Mitterer, "Semi-quantitative chemical analysis of hard coatings by Raman micro-spectroscopy: The aluminium chromium nitride system as an example," *Anal. Bioanal. Chem.*, vol. 389, no. 5, pp. 1569–1576, 2007.

[49] S. Tien and J. Duh, "Comparison of microstructure and phase transformation

for nanolayered CrN / AlN and TiN / AlN coatings at elevated temperatures in air environment," vol. 515, pp. 1097–1101, 2006.

[50]   M. Kawate, A. Kimura, and T. Suzuki, "Microhardness and Lattice Parameter of Cr1-xAlxN Films," *J. Vac. Sci. Technol. A*, vol. 20, no. 2, p. 569, 2002.

[51]   Y. C. Chim, X. Z. Ding, X. T. Zeng, and S. Zhang, "Oxidation resistance of TiN, CrN, TiAlN and CrAlN coatings deposited by lateral rotating cathode arc," *Thin Solid Films*, vol. 517, no. 17, pp. 4845–4849, 2009.

[52]   C. Hammond, *The Basics of Crystallography and Diffraction*. New York: Oxford University Press, 1997.

[53]   P. E. Hovsepian, a. P. Ehiasarian, R. Braun, J. Walker, and H. Du, "Novel CrAlYN/CrN nanoscale multilayer PVD coatings produced by the combined High Power Impulse Magnetron Sputtering/Unbalanced Magnetron Sputtering technique for environmental protection of γ-TiAl alloys," *Surf. Coatings Technol.*, vol. 204, no. 16–17, pp. 2702–2708, May 2010.

[54]   P. E. Hovsepian, A. P. Ehiasarian, Y. P. Purandare, R. Braun, and I. M. Ross, "Effect of High Ion Irradiation on the Structure, Properties and High Temperature Tribology of Nanoscale CrAlYN/CrN Multilayer Coating Deposited by HIPIMS-HIPIMS Technique," *Plasma Process. Polym.*, vol. 6, no. S1, pp. S118–S123, Jun. 2009.

[55]   C. Reinhard, A. P. Ehiasarian, and P. E. Hovsepian, "Oxidation Behaviour of Nanoscale Multilayer CrAlYN/CrN Coatings Deposited by the Combined High Power Impulse Magnetron Sputtering/Unbalanced Magnetron Sputtering Technique," *Plasma Process. Polym.*, vol. 4, no. S1, pp. S910–S915, Apr. 2007.

[56]   P. E. Hovsepian, a. P. Ehiasarian, and U. Ratayski, "CrAlYCN/CrCN

nanoscale multilayer PVD coatings deposited by the combined High Power

Impulse Magnetron Sputtering/Unbalanced Magnetron Sputtering

(HIPIMS/UBM) technology," *Surf. Coatings Technol.*, vol. 203, no. 9, pp.

1237–1243, Jan. 2009.

[57]   J. Vlček, M. Kormunda, J. Čížek, Z. Soukup, V. Peřina, and J. Zemek,

"Reactive magnetron sputtering of Si-C-N films with controlled mechanical

and optical properties," *Diam. Relat. Mater.*, vol. 12, no. 8, pp. 1287–1294,

2003.

[58]   J. Čapek, S. Hřeben, P. Zeman, J. Vlček, R. Čerstvý, and J. Houška, "Effect of

the gas mixture composition on high-temperature behavior of magnetron

sputtered Si–B–C–N coatings," *Surf. Coatings Technol.*, vol. 203, no. 5–7, pp.

466–469, Dec. 2008.

[59]   P. Zeman, J. Capek, R. Cerstvy, and J. Vlcek, "Thermal stability of magnetron

sputtered Si-B-C-N materials at temperatures up to 1700 ??c," *Thin Solid

Films*, vol. 519, no. 1, pp. 306–311, 2010.

[60]   V. M. Vishnyakov, a. P. Ehiasarian, V. V. Vishnyakov, P. Hovsepian, and J.

S. Colligon, "Amorphous Boron containing silicon carbo-nitrides created by

ion sputtering," *Surf. Coatings Technol.*, vol. 206, no. 1, pp. 149–154, Oct.

2011.

[61]   J. J. Gengler, J. Hu, J. G. Jones, A. A. Voevodin, P. Steidl, and J. Vl??ek,

"Thermal conductivity of high-temperature Si-B-C-N thin films," *Surf.

Coatings Technol.*, vol. 206, no. 7, pp. 2030–2033, 2011.

[62]   J. He, M. Zhang, J. Jiang, J. Vlcek, P. Zeman, P. Steidl, and E. I. Meletis,

"Microstructure characterization of high-temperature, oxidation-resistant Si-B-C-N films," *Thin Solid Films*, vol. 542, pp. 167–173, 2013.

[63]   T. Polcar, T. Vitu, J. Sondor, and A. Cavaleiro, "Tribological Performance of CrAlSiN Coatings at High Temperatures," *Plasma Process. Polym.*, vol. 6, no. S1, pp. S935–S940, Jun. 2009.

[64]   H. W. Chen, Y. C. Chan, J. W. Lee, and J. G. Duh, "Oxidation behavior of Si-doped nanocomposite CrAlSiN coatings," *Surf. Coatings Technol.*, vol. 205, no. 5, pp. 1189–1194, 2010.

[65]   S. Zhang, L. Wang, Q. Wang, and M. Li, "A superhard CrAlSiN superlattice coating deposited by multi-arc ion plating: I. Microstructure and mechanical properties," *Surf. Coatings Technol.*, vol. 214, no. January 2013, pp. 160–167, 2013.

[66]   S. Zhang, L. Wang, Q. Wang, and M. Li, "A superhard CrAlSiN superlattice coating deposited by multi-arc ion plating: II. Thermal Stability and Oxidation Resistance," *Surf. Coatings Technol.*, vol. 214, pp. 153–159, 2013.

[67]   D. Chaliampalias, N. Pliatsikas, E. Pavlidou, K. Kolaklieva, R. Kakanakov, N. Vouroutzis, P. Patsalas, E. K. Polychroniadis, K. Chrissafis, and G. Vourlias, "Compositionally gradient PVD CrAlSiN films: structural examination and oxidation resistance," *Surf. Eng.*, vol. 844, no. July, pp. 1–7, 2016.

[68]   P. A. Tempest and R. K. Wild, "Formation and growth of spinel and Cr2O3 oxides on 20% Cr-25% Ni-Nb stainless steel in CO2 environments," *Oxid. Met.*, vol. 23, no. 3, pp. 207–235, 1985.

[69]   C. F. Windisch Jr, C. H. Henager Jr, M. H. Engelhard, and W. D. Bennet, "Raman and XPS characterization of fuel–cladding interactions using

miniature specimens," *J. Nucl. Mater.*, vol. 323, pp. 237–243, 2009.

[70] M. N. Iliev, A. P. Litvinchuk, C. W. Chu, A. Barry, and J. M. D. Coey, "Raman spectroscopy of ferromagnetic CrO2," *Phys. Rev. B*, vol. 60, no. 1, pp. 33–36, 1999.

[71] M. N. Iliev, A. P. Litvinchuk, H. G. Lee, C. W. Chu, A. Barry, and J. M. D. Coey, "Raman Spectra of the Half-Metallic Ferromagnet CrO 2," *phys. stat. sol.*, vol. 215, pp. 643–646, 1999.

[72] R. Srivastava and L. L. Chase, "RAMAN SPECTRA OF Cr02 AND MoO2 SINGLE CRYSTALS," *Solid State Commun.*, vol. 11, pp. 349–353, 1972.

[73] O. Monnereau, L. Tortet, C. E. A. Grigorescu, D. Savastru, C. R. Iordanescu, F. Guinneton, R. Notonier, A. Tonetto, T. Zhang, I. N. Mihailescu, D. Stanoi, and H. J. Trodahl, "Chromium oxides mixtures in PLD films investigated by Raman spectroscopy," *J. Optoelectron. Adv. Mater.*, vol. 12, no. 8, pp. 1752–1757, 2010.

[74] F. Guinneton, O. Monnereau, L. Argeme, D. Stanoi, G. Socol, I. N. Mihailescu, T. Zhang, C. Grigorescu, H. J. Trodahl, and L. Tortet, "{PLD} thin films obtained from CrO3 and Cr8O21 targets," *Appl. Surf. Sci.*, vol. 247, no. 1–4, pp. 139–144, 2005.

[75] D. Stanoi, G. Socol, C. Grigorescu, F. Guinneton, O. Monnereau, L. Tortet, T. Zhang, and I. N. Mihailescu, "Chromium oxides thin films prepared and coated in situ with gold by pulsed laser deposition," *Mater. Sci. Eng. B*, vol. 118, no. 1–3, pp. 74–78, 2005.

[76] A. V Baranov, K. V Bogdanov, A. V Fedorov, M. V Yarchuk, A. I. Ivanov, V. P. Veiko, K. Berwick, and J. Wiley, "Micro-Raman characterization of laser-

induced local thermo-oxidation of thin chromium films," *J. Raman Spectrosc.*, vol. 42, no. January, pp. 1780–1783, 2011.

[77]   H. C. Barshilia and K. S. Rajam, "Growth and characterization of chromium oxide coatings prepared by pulsed-direct current reactive unbalanced magnetron sputtering," *Appl. Surf. Sci.*, vol. 255, no. 5 PART 2, pp. 2925–2931, 2008.

[78]   "The RRUFF Project." [Online]. Available: http://rruff.info/.

[79]   J. S. Burnell-Gray and P. K. Datta, Eds., *Surface Engineering Casebook: Solutions to corrosion and wear-related failures.* Cambridge: Woodhead Publishing Limited, 1996.

[80]   M. Lattemann, A. P. Ehiasarian, J. Bohlmark, P. Å. O. Persson, and U. Helmersson, "Investigation of high power impulse magnetron sputtering pretreated interfaces for adhesion enhancement of hard coatings on steel," *Surf. Coatings Technol.*, vol. 200, no. 22–23 SPEC. ISS., pp. 6495–6499, 2006.

[81]   Y. P. Purandare, A. P. Ehiasarian, and P. E. Hovsepian, "Deposition of nanoscale multilayer CrN/NbN physical vapor deposition coatings by high power impulse magnetron sputtering," *J. Vac. Sci. Technol. A Vacuum, Surfaces, Film.*, vol. 26, no. 2, p. 288, 2008.

[82]   C. Reinhard, A. P. Ehiasarian, and P. E. Hovsepian, "CrN/NbN superlattice structured coatings with enhanced corrosion resistance achieved by high power impulse magnetron sputtering interface pre-treatment," *Thin Solid Films*, vol. 515, no. 7–8, pp. 3685–3692, 2007.

[83]   T. Film and P. Division, "Adhesion improvement of carbon-based coatings

through a high ionization deposition technique," vol. 370, no. Lawpp 2011, pp. 1–13, 2012.

[84]   Q. Luo, S. Yang, and K. E. Cooke, "Hybrid HIPIMS and DC magnetron sputtering deposition of TiN coatings : deposition rate , structure and tribological properties," pp. 13–21, 2013.

[85]   U. Helmersson, M. Lattemann, J. Bohlmark, A. P. Ehiasarian, and J. T. Gudmundsson, "Ionized physical vapor deposition (IPVD): A review of technology and applications," *Thin Solid Films*, vol. 513, no. 1–2, pp. 1–24, Aug. 2006.

[86]   K. Sarakinos, J. Alami, and S. Konstantinidis, "High power pulsed magnetron sputtering: A review on scientific and engineering state of the art," *Surf. Coatings Technol.*, vol. 204, no. 11, pp. 1661–1684, Feb. 2010.

[87]   Gencoa, "Gencoa Speedflo Technology." [Online]. Available: http://www.gencoa.com/speedflo-technology/. [Accessed: 15-Jul-2016].

[88]   R. J. Goldston and P. H. Rutherford, *Introduction to Plasma Physics*. IOP Publishing Ltd, 1995.

[89]   L. Conde, "An introduction to Langmuir probe diagnostics of plasmas," 2011.

[90]   G.L. Moore, *Introduction to Inductively Coupled Plasma Atomic Emission Spectrometry*, Volume 3. Elsevier, 1989.

[91]   The Oxford Dictionary, "Definition of Piezoelectricity." [Online]. Available: http://www.oxforddictionaries.com/definition/english/piezoelectricity.

[92]   C. K. O'Sullivan and G. G. Guilbault, "Commercial quartz crystal microbalances - Theory and applications," *Biosens. Bioelectron.*, vol. 14, no.

8–9, pp. 663–670, 1999.

[93] K. A. Marx, "Quartz crystal microbalance: A useful tool for studying thin polymer films and complex biomolecular systems at the solution-surface interface," *Biomacromolecules*, vol. 4, no. 5, pp. 1099–1120, 2003.

[94] P. J. Grundy and G. A. Jones, *Electron Microscopy in the Study of Materials*. London: Edwards Arnold, 1976.

[95] G. Lawes, *Scanning Electron Microscopy and X-Ray Microanalysis*. John Wiley and Sons, 1987.

[96] D. Brandon and W. Kaplan, *Microstructural Characterisation of Materials*, 2nd ed. John Wiley and Sons, 2008.

[97] The Open University, "The atomic basis of matter," 1996. [Online]. Available: http://www.physics.brocku.ca/PPLATO/h-flap/phys7_1.html. [Accessed: 05-Apr-2016].

[98] Scintag Inc, "Chapter 7: The basics of X-ray Diffraction," Scintag Inc., 1999, p. 7.1-7.25.

[99] Panalytical, "PANalytical Empyrean Diffractometer." PANalytical, 2012.

[100] M. E. Fitzpatrick, A. T. Fry, P. Holdway, F. A. Kandil, J. Shackleton, and L. Suominen, "Determination of Residual Stresses by X-ray Diffraction - Issue 2," in *Measurement Good Practice Guide No. 52*, Crown, 2005.

[101] P. Barnes, S. Jacques, and M. Vickers, "Crystallite Size and Strain," 1997. [Online]. Available: http://pd.chem.ucl.ac.uk/pdnn/peaks/size.htm.

[102] C. Rulli, "Raman Spectroscopy." [Online]. Available: http://www.sas.upenn.edu/~crulli/RamanBasics.html. [Accessed: 15-Jul-2016].

[103] InPhotonics Inc, "An Introduction to Raman for the Infrared Spectroscopist," 1999. [Online]. Available: http://www.inphotonics.com/technote11.pdf. [Accessed: 15-Jul-2016].

[104] Omega Optical Inc, "Raman Spectroscopy," 2014. [Online]. Available: http://www.omegafilters.com/applications/raman-spectroscopy/. [Accessed: 15-Jul-2016].

[105] J. Loader, *Basic Laser Raman Spectroscopy*, Illustrate. Heyden, 1970.

[106] Olympus Coorperation, "Optical Microscopes." [Online]. Available: http://www.olympus-ims.com/en/microscope/terms/feature10/. [Accessed: 15-Jul-2016].

[107] yourarticlelibrary, "Working Principle and Parts of a Compound Microscope (with Diagrams)," 2015. [Online]. Available: http://www.yourarticlelibrary.com/micro-biology/working-principle-and-parts-of-a-compound-microscope-with-diagrams/26509/. [Accessed: 15-Jul-2016].

[108] G. England, "Microhardness Test." [Online]. Available: http://www.gordonengland.co.uk/hardness/microhardness.htm.

[109] S. Kuiry, "Advanced Scratch Testing for Evaluation of Coatings," USA, 2012.

[110] ISO, "International Standard: Fine ceramic (advanced ceramics, advanced technical ceramics) - Determination of adhesion of ceramic coatings by scratch testing," 20502, 2005.

[111] BSI, "Internation Standard: Fine ceramics (advanced ceramics, advanced technical ceramics) - Rockwell indentation test for evaluation of adhesion of

ceramic coatings," 26443:2008, 2008.

[112] Guhring, "Calotest Principle," 2015. [Online]. Available:

http://www.guhring.com/ProductsServices/CoatingServices/Calotest/.

[113] J. Nohava, M. Morstein, and P. Dessarzin, "High temperature tribological

behavior of advanced hard coatings for cutting tools."

[114] C. X. Li, "Wear and Wear Mechanism." [Online]. Available: http://emrtk.uni-

miskolc.hu/projektek/adveng/home/kurzus/korsz_anyagtech/1_konzultacio_el

emei/wear_and_wear_mechanism.htm.

[115] PerkinElmer, "Thermogravimetric Analysis (TGA) A Beginner ' s Guide,"

2010.

[116] "Atomic Spectra Data," 2013. [Online]. Available:

http://physics.nist.gov/PhysRefData/ASD/lines_form.html.

[117] "National Institute of Standards and Technology Atomic Spectra Database."

[Online]. Available:

http://physics.nist.gov/PhysRefData/ASD/lines_form.html. [Accessed: 01-

Jan-2013].

[118] S. M. Rossnagel and K. L. Saenger, "Optical Emission in Magnetrons:

Nonlinear Aspects," *J. Vac. Sci. Technol. A*, vol. 7, no. 3, pp. 968–971, 1989.

[119] R. L. Frost, "The structure of the kaolinite minerals FT-Raman study," pp.

65–77, 1997.

[120] Association of German Ironworks, Ed., *Werkstoffkunde Steel. Volume 1:

Basics*. Springer Publishing House Berlin Heidelberg, 1984.

[121] S. Zhang, Ed., *Thin Films and Coatings: Toughening and Toughness*

Characteristics. CRC Press, 2016.

[122] C. X. Li, "Wear and Wear Mechanism," *The University of Birmingham*.
[Online]. Available: http://emrtk.uni-
miskolc.hu/projektek/adveng/home/kurzus/korsz_anyagtech/1_konzultacio_el
emei/wear_and_wear_mechanism.htm. [Accessed: 12-Jul-2016].

[123] A. J. W. Moore and W. J. M. Tegart, "Relation between Friction and
Hardnesse," *Proc. R. Soc. Lond. A. Math. Phys. Sci.*, vol. 212, no. 1111, pp.
452–458, 1952.

[124] B. Navinsek and P. Panjan, "Oxidation Resistance of PVD Cr, Cr-N and Cr-
N-O Hard Coatings," *Surf. Coatings Technol.*, vol. 59, pp. 244–248, 1993.

[125] W. J. MoberlyChan, J. J. Cao, C. J. Gilbert, R. O. Ritchie, and L. C. De
Jonghe, "The Cubic to Hexagonal Transformation to Toughen SiC," in
Ceramic Microstructures: Control at the Atomic Level, 1996, pp. 184–186.

[126] J. F. Lin, M. Santoro, V. V. Struzhkin, H. K. Mao, and R. J. Hemley, "In situ
high pressure-temperature Raman spectroscopy technique with laser-heated
diamond anvil cells," *Rev. Sci. Instrum.*, vol. 75, no. 10 I, pp. 3302–3306,
2004.

[127] E. Formo, Z. Wu, S. Mahurin, and S. Dai, "In Situ High Temperature Surface
Enhanced Raman Spectroscopy for the Study of Interface Phenomena:
Probing a Solid Acid on Alumina," *J. Phys. ...*, pp. 9068–9073, 2011.

[128] H. F. Garces, B. S. Senturk, and N. P. Padture, "In situ Raman spectroscopy
studies of high-temperature degradation of thermal barrier coatings by molten
silicate deposits," *Scr. Mater.*, vol. 76, pp. 29–32, 2014.

[129] I. Daniel, P. Gillet, B. T. Poe, and P. F. McMillan, "In-situ high-temperature Raman spectroscopic studies of aluminosilicate liquids," *Phys. Chem. Miner.*, vol. 22, no. 2, p. 74, 1995.

Appendix

To emphasise the effectiveness of the coatings for protecting against severe oxidation in real life applications a WC insert with coating 11 deposited was cut in half, thus exposing an area of the substrate. This piece of insert was then placed in the furnace and isothermally heated for 1 hour at 1000 ˚C. After the insert had cooled it was removed from the furnace; a bright blue oxide had grown from the side of the exposed substrate, but the coated areas remained intact. Figure A.1 is an SEM image of the exposed edge of the insert; it can be seen that the areas of the insert where the coating covered the WC substrate remained stable. A number of oxide islands have grown but the extent of oxidation is not catastrophic; the coating is still performing its protective function.

On the left side of the image in Figure A.1 however, we see a regular layered pattern of alternating contrast. It is from this side that the oxide grew, protruding outwards. It appears as though as the substrate oxidises it expands, when the expansion occurs at the interface between substrate and coating, the adhesion is such that part of the coating is taken with the expansion and sheers from the main coated area, exposing the substrate, which in turn oxidises and expands taking another segment of coating away. This repetition of coating separation and subsequent oxidation has created the alternating pattern.

It is clear from this test this test that the coating provides excellent protection for WC inserts against oxidation at high temperatures. Without the addition of a coating, the harsh environment and high temperatures experienced by the cutting tool would cause it to fail. Therefore the coating developed has been proved that it would be successful at extending tool lifetimes.
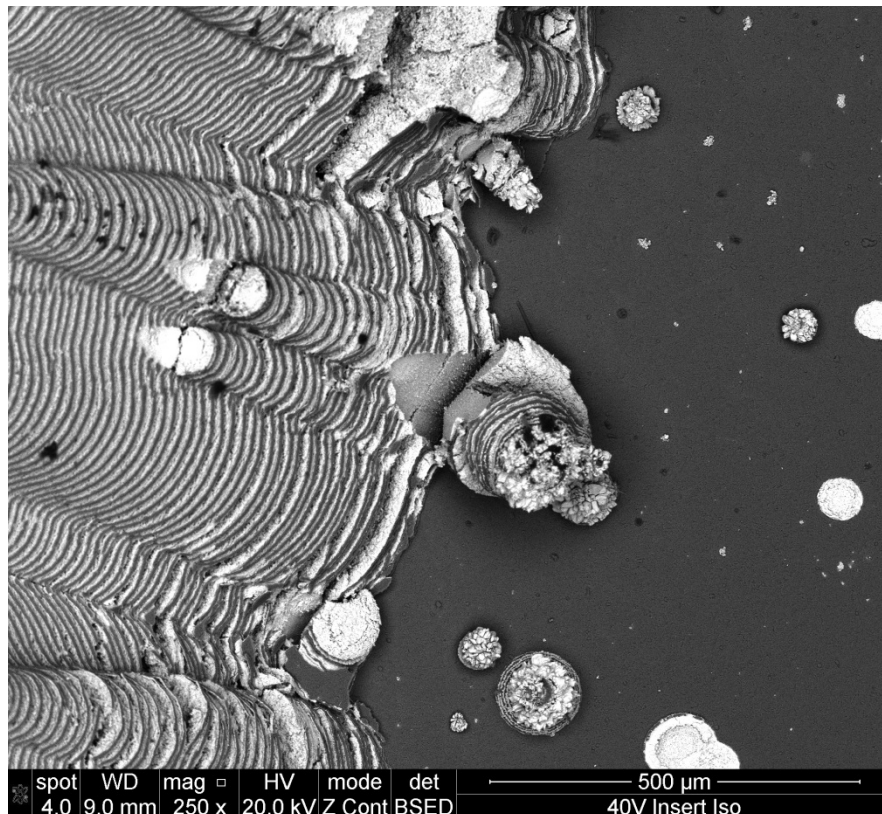

Figure A.1. SEM image taken at the cut line through the insert. The image shows the coating area on the right and the oxide that has grown from the exposed substrate on the left.